THE UNIVERSITY OF QUEENSLAND

AUSTRALIA

Interaction and growth of low frequency and high frequency wind waves

Peter Lloyd Tobin Ware

B.Eng. (Hons)

A thesis submitted for the degree of Doctor of Philosophy

at The University of Queensland in 2019

School of Civil Engineering

Abstract

The strong suppression of higher frequency (HF) wind-waves by lower frequency (LF) waves has been observed in laboratory experiments since 1966 (e.g. Mitsuyasu, 1966), but theories explaining the physical cause have varied fundamentally, all of which have aspects which may be challenged. As a result, there is no consensus as to which theory correctly describes the mechanism. This thesis presents a study which has been undertaken to determine the fundamental nature to the mechanism, through detailed measurement of the interaction between HF and LF waves. These measurements were primarily made in a laboratory wind-wave flume, with wind and paddle waves propagating in the same direction, and an array of up to 24 wave gauges distributed throughout the flume. An experiment was also performed in natural conditions in a coastal lake, with a point wave gauge providing wave records, and multiple sonic anemometers providing 3D turbulent wind velocity data.

The temporal transition in the laboratory from conditions with pure wind-waves to conditions of wind + paddle forcing has been examined in detail, through repeating a specific transition sequence 186 times. The aggregation of these measurements provided a clear representation of the precise timescale of HF wave suppression, revealing that the majority of suppression occurs too quickly to have been caused by reduced wind-input, instead indicating a mechanism of enhanced HF wave dissipation. The examination of spatial variation in HF wave energy along the LF wave phase indicated that the majority of suppression occurs on the LF wave crest, and high on the windward (rear) face, which locations are prone to experience the highest wind velocities along the LF wave phase. This observation also argued against suppression primarily by a mechanism of reduced wind-input. Quantification of HF wave suppression versus a broad range of wind velocities, paddle wave conditions and fetches did not reveal any critical dependence of suppression on either LF wave breaking or wind separation at LF wave crests, due to strong suppression occurring when neither of these was occurring. It was concluded that suppression occurs primarily as a result of enhanced dissipation of HF waves near LF wave crests, and possibly to a lesser degree from reduced wind input, the latter likely caused by wind separation at LF wave crests. The enhanced dissipation of HF waves appears correlated with locations of strong wind input, suggesting that the increased wind velocity near LF wave crests exceeds the level of forcing which HF waves of low C/u^* are able to withstand without breaking. It is concluded that HF waves experience both an excess wind forcing near the LF wave crest, and a deficit of forcing in the LF wave trough, both of which result in less HF wave energy than would be present in absence of LF waves.

In conditions of low paddle wave steepness, the distribution of energy input between LF and HF waves, and the LF waves' capacity to absorb wind input, exhibited substantial nonlinearity versus LF wave steepness and wind velocity. LF paddle waves grew negligibly below a critical steepness and wind velocity, after which they 'caught the wind', absorbing the majority of wind input, and grew rapidly. This suggests that a change in the wind flow regime occurs at the critical steepness and wind velocity, mostly likely due to wind flow separation at LF wave crests (Donelan et al., 2006). These observations suggest that the Jeffreys 1924 mechanism may be more quantitatively significant to wave growth than the commonly applied theory of Miles (1957), and also provided further argument that wind separation contributes to HF wave suppression on the leeward face and in troughs of LF waves, although secondary in magnitude and slower acting than the enhanced HF wave dissipation at and windward of LF wave crests.

HF wave growth was unexpectedly observed to be enhanced by LF waves of very low steepness, low wind velocity and short fetch. Much of this HF wave energy increase occurred at harmonic frequencies of the paddle wave, yet without being bound to the paddle wave, which is not explained by current wave theories. This suggests that LF waves and their harmonics may provide seeding to assist incipient HF waves to reach a point of Kelvin-Helmholst instability, or ripple formation, earlier. The marginally accelerated wind at LF wave crests of even very low steepness may also cause this threshold to be reached earlier.

The statement by Plant and Wright (1977), that the longest waves to grow primarily by wind input are ca. 0.1m in length, with waves longer than this growing primarily by nonlinear interactions, was challenged by measurements made in the present study. A several-fold increase in the height of wind-forced monochromatic LF waves with wavelengths of order 1m, in conditions with minimal HF wave energy from which energy could be transferred, indicated that these waves much longer than 0.1m grew as a result of wind input.

The results of the coastal lake experiment were inconclusive, with no clear patterns observed which could prove suppression to be present in nature. The range of conditions measured was limited, suggesting further insight may be gained by future experimentation with a broader range of conditions.

Declaration by Author

This thesis is composed of my original work, and contains no material previously published or written by another person except where due reference has been made in the text. I have clearly stated the contribution by others to jointly-authored works that I have included in my thesis.

I have clearly stated the contribution of others to my thesis as a whole, including statistical assistance, survey design, data analysis, significant technical procedures, professional editorial advice, financial support and any other original research work used or reported in my thesis. The content of my thesis is the result of work I have carried out since the commencement of my higher degree by research candidature and does not include a substantial part of work that has been submitted *to qualify for the award of any* other degree or diploma in any university or other tertiary institution. I have clearly stated which parts of my thesis, if any, have been submitted to qualify for another award.

I acknowledge that an electronic copy of my thesis must be lodged with the University Library and, subject to the policy and procedures of The University of Queensland, the thesis be made available for research and study in accordance with the Copyright Act 1968 unless a period of embargo has been approved by the Dean of the Graduate School.

I acknowledge that copyright of all material contained in my thesis resides with the copyright holder(s) of that material. Where appropriate I have obtained copyright permission from the copyright holder to reproduce material in this thesis and have sought permission from co-authors for any jointly authored works included in the thesis.

Publications included in this thesis

No publications included.

Submitted manuscripts included in this thesis

No manuscripts submitted for publication.

Other publications during candidature

Olfateh, M., Ware, P., Callaghan, D. P., Nielsen, P., & Baldock, T. E. (2017). Momentum transfer under laboratory wind-waves. Journal of Coastal Engineering, 121: 255-264.

Contributions by others to the thesis

No contributions by others.

Statement of parts of the thesis submitted to qualify for the award of another degree

No works submitted towards another degree have been included in this thesis.

Research involving Human or Animal Subjects

No animal or human subjects were involved in this research.

Acknowledgements

I wish to first and foremost thank my beautiful wife Alexandra for her unending patience and support as I worked towards completion of this thesis, and acknowledge my wonderful children Samuel, Liesel and Michael for the many hours that they were deprived of their father during my candidature.

I wish to thank my principal supervisor, Prof. Tom Baldock, for his continual support, patience, encouragement, wisdom and professionalism.

I also wish to thank my co-supervisors, Prof. Peter Nielsen and Dr David Callaghan, for their support, wisdom and assistance.

Thanks to the University of Queensland Hydraulics Laboratory staff, Mr Jason van der Gevel and Mr Stewart Matthews, for their assistance with construction of the wind-wave flume, using their abundant technical skills.

Thanks also to Dr Mohammad Olfateh for his work preparing for and undertaking the Lake Cootharaba experiment with myself, and to Dr David Callaghan, Dr Uriah Gravois and Ms Alice Twomey for assistance with deployment and recovery of field experimental equipment.

Financial support

This research was supported by an Australian Research Council Australian Postgraduate Award, and discovery grant DP130101122.

Keywords

wind-waves, short waves, long waves, suppression, dissipation, spectral tail

Australian and New Zealand Standard Research Classifications (ANZSRC)

ANZSRC code: 090599, Civil Engineering not elsewhere classified, 34%

ANZSRC code: 040503, Physical Oceanography, 33%

ANZSRC code: 091504, Fluidisation and Fluid Mechanics, 33%

Fields of Research (FoR) Classification

FoR code: 0905, Civil Engineering, 34%

FoR code: 0405, Oceanography, 33%

FoR code: 0915, Interdisciplinary Engineering, 33%

Contents

Nomenclature

Repeated terms

The below terms are used throughout this thesis according to the specific definitions stated here.

Higher frequency wind-waves (abbr. HF waves)

This term has been used throughout this dissertation to represent short wind-waves which develop as a consequence of wind blowing over the water surface. These waves may be generated by wind in the presence of no other forcing, or else by wind in presence of existing lower frequency (LF) waves, e.g. paddle waves or swell. In using the categorisation system of Munk (1950) (see Figure 1.1), HF waves may be classified as capillary waves or ultra-gravity waves.

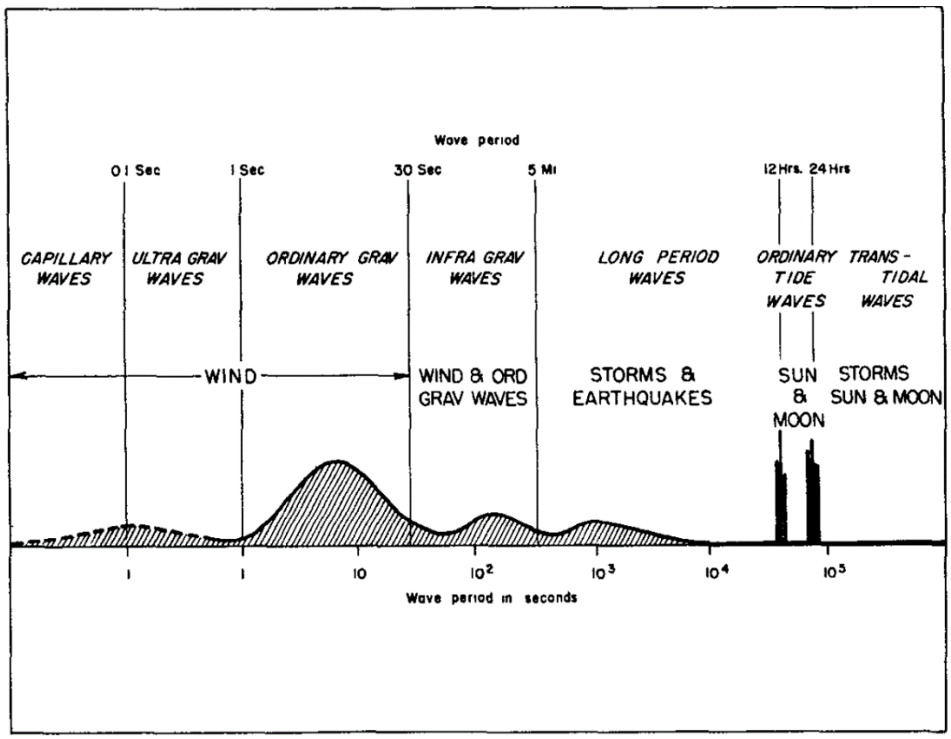

Figure 1.1: Tentative classification of waves by period, according to Munk (1950).

Lower frequency waves (abbr. LF waves)

This term has been used throughout this dissertation to represent existing swell waves, well-developed wind-waves or else laboratory paddle waves, all of which were generated elsewhere then propagated to the location in question. In circumstances where LF waves are generated by a paddle in an experimental flume, such waves are also termed paddle waves in this document interchangeably. Higher harmonics of the paddle wave, or the

proportion of energy in these harmonic frequencies which is bound to the LF waves, are also categorised to be part of the LF wave component in this thesis. LF waves may be classified according to Munk (1950) as longer wavelength ultra-gravity waves as well as shorter wavelength ordinary gravity waves. When direction is not explicitly stated in this thesis, it is implied that these waves are propagating in the same direction as the wind forcing and HF waves.

Suppression

A reduction in HF wave energy density (J/m²) caused by the presence of LF waves.

Suppression ratio

In laboratory conditions, this refers to $E_{HF_{w+p}}/E_{HF_{wo}}$, defined as the HF energy density in wind-and-paddle conditions, divided by the HF energy density in wind-only conditions with the same wind fan frequency. Chen and Belcher (2000) refer to this as E/E_0, with similar definitions for the numerator and denominator. Suppression exists when the suppression ratio is less than 1, while a suppression ratio greater than 1 indicates negative suppression, or HF wave enhancement.

Negative suppression

As mentioned above, in a minority of cases the HF wave energy density was observed to be enhanced, rather than suppressed, by LF waves. This is referred to within this thesis as either negative suppression or HF wave enhancement.

LAB2015

A batch of experiments performed in winter 2015 at the University of Queensland, described in Chapter 3 of this thesis.

LAB2016

A batch of experiments performed in winter 2016 at the University of Queensland also described in Chapter 3 of this thesis, with some variation in experimental configuration and conditions to the LAB2015 experiment.

COOTHA

The field experiment conducted in March 2016 at Lake Cootharaba, QLD Australia, described in Chapter 4.

Steepness

Wave steepness in literature has been quantified both as H/L and as ak in different studies. In this thesis, the word steepness shall refer to H/L unless otherwise stated.

Monochromatic waves

In laboratory experiments, this term refers to waves generated by a paddle programmed to output a single sinusoidal signal, although in reality the actual waves propagating through the flume were never truly monochromatic or purely sinusoidal due to inevitable formation of higher harmonic within wave trains of finite steepness.

Abbreviations

HF	Higher frequency (see Repeated terms above)
LF	Lower frequency (see Repeated terms above)
MTF	Modulation transfer function (see Section 2.2.2)
MWS	Mean water surface (elevation)
PM	Pierson-Moskowitz (spectrum)
PO	Paddle-only forcing in laboratory experiments, resulting in free waves
W+P	Combined wind and paddle forcing in laboratory experiments
WO	Wind-only forcing in laboratory experiments, resulting in pure wind-waves

Greek symbols

γ	Fractional energy growth per radian
η	Water surface elevation (m)
η_{HF}	HF component of the water surface elevation (m)
η_{LF}	LF component of the water surface elevation (m)
τ	Shear Stress (Pa)
τ_w	Shear stress between the wind and water surface (Pa)
ρ_a	Air density $(\mathrm{kg/m^3})$
ρ_w	Water density $(\mathrm{kg/m^3})$
σ	Standard deviation
σ_{HF}	Standard deviation of η_{HF} (m)
$\sigma_{rolling}$	Rolling 5-minute or 10-minute standard deviation used to eliminate spikes in COOTHA time series data (m)

ω	Angular frequency (Rad/s)
ω_P	Peak angular frequency (Rad/s)

Roman letters

a	Water surface wave amplitude (m)
C	Water surface wave phase celerity (m/s)
C/u_*	Wave age
C_D	Drag coefficient, unless otherwise stated, for wind blowing over the free water surface
E	Water surface wave energy density (J/m²)
E_{HF}	Energy density in the HF component of the water surface spectrum (J/m²)
$E_{HF_{wo}}$	Energy density in the HF component of the water surface spectrum, in wind-only conditions, with no paddle waves present (J/m²)
$E_{HF_{w+p}}$	Energy density in the HF component of the water surface spectrum in the presence of LF paddle waves, but this term does not include the LF wave energy density (J/m²)
$E_{HF_{w+p}}/E_{HF_{wo}}$	Suppression ratio (also see Repeated terms definition), defined as the HF energy density in W+P conditions, divided by the HF energy density in WO conditions of the same forcing
E_{LF}	Energy density in the LF component of the water surface spectrum (J/m²)
f_{fan}	Wind fan frequency in laboratory experiments (Hz)
f_{pad}	Sinusoidal paddle wave frequency (Hz)
f_p	Peak frequency of the wave spectrum with wind forcing only (Hz)
$\overline{H_{HF}}$	HF wave height, average using zero-crossing analysis.
H_{pad}	Wave height setting of the wavemaker paddle, usually a monochromatic setting, not to be confused with H_{LF} (m)
H_{LF}	Wave height of LF water surface waves measured in the experimental volume, varying throughout the fetch (m)
k	Wave number of the water surface wave (m^{-1})
L_{pad}	Wavelength of the paddle wave (m)

T_{pad}	Paddle wave period (s)
u_*	Friction velocity (m/s)
V_0	Reference wind velocity in laboratory experiments, measured at ca. 0.2m above the MWS at 12.15m fetch (m/s)
$V_{3.65}$	Wind velocity measured during the Lake Cootharaba experiment by the top anemometer (m/s)
V_{10}	Wind velocity at 10m above sea level (m/s)

1 Introduction

The ocean surface fluctuates in wave motions on a wide range of time scales, ranging from fractions of a second for capillary waves, to several hours for tides and storm surges. The ocean waves most commonly visible to the naked eye, such as beach breakers, are mostly caused by wind blowing over the ocean surface. The ability to predict these waves has been relevant to humankind throughout history, in naval operations, as well as for near-sea and offshore construction. As shipping operations, coastal development and offshore structures have all become more prevalent worldwide, the importance of this science has increased.

In practice, state-of-the-art wave modelling tools such as SWAN (Booij et al., 1999) currently used to forecast and hindcast wind generated waves, account for a substantial number of physical effects, but there remains significant scatter in forecasts when compared against actual measurements (e.g. Rogers et al., 2007; Groeneweg et al., 2015). This scatter suggests there are either some physical mechanisms not fully accounted for in state-of-the-art models, or else a lack of data available to models, or both.

This thesis focuses primarily on one such mechanism which has been widely observed but is not properly accounted for in models or even understood in the literature, being the effect lower frequency (LF) waves have on the evolution of higher frequency (HF) waves. In many laboratory wind-wave flume studies since the 1960's, observations have been mode of significantly less HF wind-wave energy (E_{HF}) in flumes when both wind and paddle waves are present ($E_{HF_{w+p}}$), compared with conditions of identical wind forcing without paddle waves ($E_{HF_{wo}}$) (e.g. Mitsuyasu, 1966; Hatori et al., 1981; Donelan et al., 1987). This effect is obvious when viewed with the naked eye in wave flumes. In the ocean, it has manifest itself through variations in radar backscatter measurements from the ocean surface as a result of passing swell (Plant et al., 1983; Smith, 1986), which variation is referred to as the hydrodynamic modulation transfer function (hydrodynamic MTF). However, ocean observations are far less distinct quantitatively (Chen and Belcher, 2000), with past measurements requiring sophisticated data processing techniques to separate the hydrodynamic MTF from other components of the total measured MTF.

During the past ca. 50 years, a few mechanisms have been proposed to explain this interaction, but these vary widely in physical basis. Phillips and Banner (1974) proposed two mechanisms by which dissipation of HF waves is enhanced at the crests of LF waves. Masson (1993) suggested nonlinear interaction between wavenumbers according to the

mechanism of Hasselmann (1962) causes HF energy to be transferred to the LF wave. Chen and Belcher (2000) argued that suppression of HF wave growth is caused by modification of the wind field by LF waves, with LF waves absorbing wind stress which would otherwise have been absorbed by HF waves. Each of the three main source terms used in deep-water wind-wave modelling (dissipation, nonlinear interactions and wind input) is represented by one of the above theories. However, all of the proposed theories in their suggested state have flaws, and there is no consensus in literature as to which mechanism is responsible for the interaction between HF and LF waves (Mitsuyasu, 2015).

With regards to ocean modelling, even though some source terms depend on energy at other frequencies indirectly, the calculation of spectral energy is for the most part resolved at each individual frequency independent of other frequencies, at least for the most prevalently used source terms (The Swan Team, 2018; WAVEWATCH III Development Group, 2016). Models do not adequately account for the effects that wave energy at remote frequencies has on wind input at a given frequency (Booij et al., 2001). Some empirical alternate source terms attempting to account for newer observations are beginning to appear and be tested in models (Rogers et al., 2012; Zieger et al., 2015), but these leave much unexplained regarding the physical basis of the interaction, and are not in widespread production modelling use.

An understanding of the dynamics of HF waves is important because HF portion of the wave spectrum is generally acknowledged to be the portion most influential to the roughness length and wind shear stress, and consequently affecting wind input throughout the wind-wave spectrum (Cavaleri et al., 2015). In addition, some measurements of oceanic wind velocities depend on the intensity of radar waves backscattered from HF waves (Bliven et al., 1986), and improved understanding of the hydrodynamic modulation of HF waves may enable improved wind velocity measurement, which in turn has the potential to improve practical ocean wave forecasting.

This present research study is primarily an experimental investigation. Experiments have been designed specifically to assess the validity of proposed theories to ascertain the nature of the interaction, at least to a level of pinpointing what physical effect or effects are primarily responsible. These experiments consisted primarily of wave measurements in carefully controlled conditions in a laboratory wind-wave flume, using a wide array of spatially distributed point wave gauges. In addition, a wave gauge and wind anemometers were installed in a coastal lake, in an attempt to identify and quantify suppression of HF waves by LF waves in fetch limited field conditions.

The literature related to wind-wave generation is possibly the most extensive in ocean and coastal engineering, particularly since the late 1950's, so a comprehensive literature review was required as part of the present study.

This thesis is organised as follows. The literature review comprises Chapter 2 of this thesis. At the end of this review, shortfalls in the current literature are summarised, as is the planned research activities designed to address the shortfalls. A description of the experimental methodology for laboratory investigations is provided in Chapter 3, and for field investigations in Chapter 4. The results of both laboratory and field experiments are presented in Chapter 5. Chapter 6 contains a discussion of the results, and their applicability to the topic of HF and LF wave interaction, as well as to wind-wave evolution generally. The conclusion of Chapter 7 summarises the outcomes of the present study, and suggestions for further research.

2 Literature review

Because the physics of HF wind-wave suppression by LF waves spans a broad scope of wave evolution science, a general review of wind-wave literature was necessary. Section 2.1 contains this general review. Literature focused specifically on the interaction between LF and HF waves is reviewed in Section 2.2.

2.1 General review of wind-wave evolution models and theories

There are generally considered to be three major and distinct mechanisms involved in wind-wave evolution, being

1. wind input,
2. wave dissipation, and
3. transfer of energy between frequencies via nonlinear interactions.

Each of these mechanisms has its own source terms in wave forecasting models. These three mechanisms are discussed in Chapters 2.1.1, 2.1.2 and 2.1.3 respectively.

Waves on the ocean surface are known to be distributed across a broad spectrum of frequencies. The shape of oceanic spectra is discussed in Chapter 2.1.4.

2.1.1 Wind input to waves

This section documents studies related to wind input into waves. It is arranged for the most part in approximate chronological order of research, which involves some switching back and forth between experimental and theoretical studies.

One of the earliest widely cited theories of wind input into water waves was proposed by Jeffreys (1925), who investigated wave growth by irrotational motion, skin friction and form drag, and concluded that form drag was likely the most significant mechanism contributing to wave growth. He suggested that wind separation occurs at wave crests as illustrated in Figure 2.1, before reattaching at some point on the face of the following wave before the next crest. The leeward face of waves is thus sheltered from the wind, with pressure greater on the windward face of waves than the leeward face, resulting in a net horizontal force on the waves which increases their momentum and energy. The pressure wind exerts on waves was hypothesised by Jeffreys (1925) to follow the relation

$$s\rho_a U'^2 \frac{\partial \eta}{\partial x} \tag{2.1}$$

where s in this instance is a dimensionless sheltering coefficient and U' is a reference wind velocity, which is equal to the velocity of the wind relative to the wave crests. From this equation, the temporal energy rate of change, as derived by Young (1999, p49), can be expressed as

$$\frac{\partial E}{\partial t} = \frac{1}{2\rho_w g}\, s\rho_a (U_\infty - C)^2\, (ak)^2 C, \tag{2.2}$$

where U_∞ in this equation represents the ambient wind velocity at an unspecified elevation.

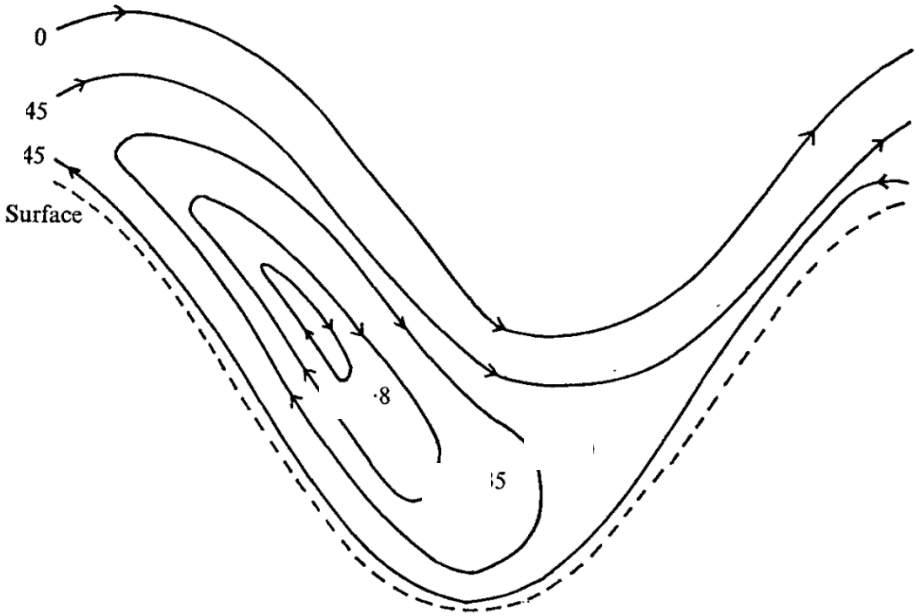

Figure 2.1: Wind flow over wave crest with separation on the leeward face. Visualisation taken from Gent and Taylor (1976).

A lot of the mathematical work of Jeffreys (1925) was focused on a minimum wind velocity that would allow waves to overcome skin friction, which was a focus for many early studies, although considered less important later. Jeffreys (1925) derived a minimum wind velocity to instigate waves equal to $0.73s^{-\frac{1}{3}}$m/s. He then fitted this simple relationship to observations by (Russell, 1844) of initial wave formulation in a river and a large pond, to arrive at a value for s in a range of ca. 0.23 to 0.32. The most enduring and widely accepted principle to come out of this work was the concept that wave growth is primarily related to form drag rather than skin friction.

Miles (1957) developed an analytical expression for growth of a sinusoidal monochromatic wave based on the Jeffreys (1925) assumption that normal pressure force is the dominant mechanism for wave growth. His derivation was based on several simplifications. Waves were considered to be pure sinusoids, with steepness sufficiently

small to assume waves were linear and assume horizontal velocity to be constant in the x direction, not varying with wave phase. The wind was treated as inviscid for mathematical simplicity, but a logarithmic shear flow in the air was imposed, with horizontal velocity varying in the vertical direction. The water was also treated as inviscid and irrotational, with any mean current ignored. The wind pressure perturbation was assumed to act on the water surface according to

$$(\alpha + i\beta)\rho_a U_1^2 k\eta \tag{2.3}$$

where U_1 is an arbitrary reference wind velocity. α and β in this formula are arbitrary coefficients dependent on U_1, phase speed c and of wave number k. It can be seen that α is multiplied directly by η according to this formula, meaning that the component of aerodynamic pressure corresponding to α, whether it be positive or negative, is in phase with the water surface. This component cannot produce any net horizontal work on the water surface and consequently cannot input energy into waves, although it may theoretically increase the force which restores water surface deformations, and hence may slightly alter the dispersion relation and wave celerity. The component of aerodynamic pressure corresponding to $i\beta$ is 90° out of phase with the water surface, meaning that it can have a maximum pressure on the windward side of the wave and minimum on the leeward side. Because the pressure acts perpendicular to the water surface, this pressure produces a net horizontal force in the direction of the wind velocity. Because of this, wind input and wave growth rate was modelled to be dependent on β and not on α. The net pressure distribution resulting from a phase shift (non-zero β in Equation 2.3) is depicted in Figure 2.2.

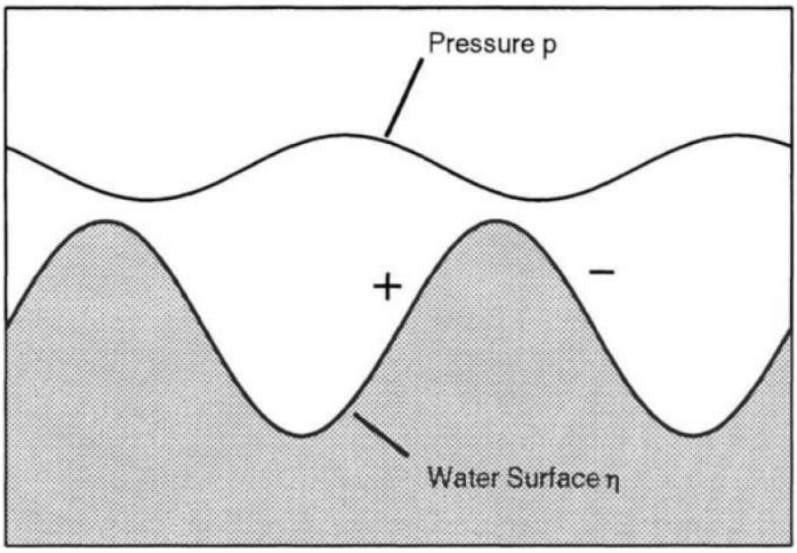

Figure 2.2: Asymmetric pressure distribution on the forward and rear face of wind forced waves, visualised by Young (1999, p47).

The rate of energy growth per radian was expressed to follow the relationship

$$\gamma = \frac{\rho_a}{\rho_w}\beta\left(\frac{U-c}{c}\right)^2 \tag{2.4}$$

where U in this case refers to the ambient wind velocity with elevation unspecified, and γ represents the fractional increase in wave energy per radian. The only unknown in this equation was the dimensionless coefficient β. Using the Navier-Stokes equations in the wind as a starting point, Miles (1957) performed analysis with dimensionless variables to determine that the stability of surface waves, or propensity to grow as a result of wind forcing, was dependent on the curvature of the vertical wind velocity profile at a critical height where wind velocity equals wave celerity. Miles (1957) then introduced the previously noted simplifications of a logarithmic wind velocity profile, wave linearity and low steepness. This enabled arrival at a series expansion expression for β of

$$\beta = \pi k y_c \left\{\frac{1}{6}\pi^2 + \log^2(\gamma k y_c) + 2\sum_{1}^{\infty}\frac{(-)^n (k y_c)^n}{n!\, n^2}\right\}^2 \tag{2.5}$$

where y_c is the height of the critical layer and $\log(\gamma)$ in this equation represents Euler's constant, which is equal to ca. 0.5772. The values of β were calculated by Miles (1957) as plotted in Figure 2.3. It can be seen that as the critical height increases, which may be expected to correlate with the wave phase velocity approaching the wind velocity, β approaches zero, resulting in wind input approaching zero.

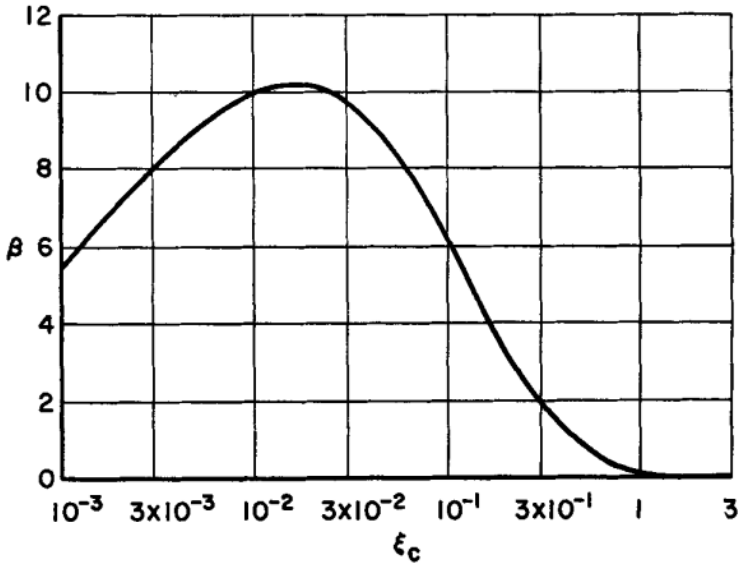

Figure 2.3: β values generated as functions of ξ_c, which in this plot represents ky_c, wavenumber multiplied by the critical height in metres. Figure taken from Miles (1957).

Miles (1957) calculated growth rates with the same order of magnitude as experimental results, but still too low (Young, 1999; Peirson and Garcia, 2008). Miles (1959) further developed this theory to improve the solution of the differential equation, which then predicted energy transfer marginally smaller than that of Miles (1957), but which he believed brought the theory better in line with experimental results up to that time. Miles (1959) also refined the model to define elevation according to distance above the wavy surface rather than the mean water surface, and included some viscous effects in the analytical solution. This reduced the number of model simplifications, but these refinements were reported to have little quantitative effect on the solution.

Miles (1957) cited earlier studies (e.g. Stanton et al., 1932) which measured wind pressure along a solid wave shaped boundary, and argued that a key improvement in his model over previous studies was the accurate elevation above the water surface at which wind velocity equals zero relative to the wave. In the case of a solid boundary, when viewed in a frame of reference following the wave, the wind velocity equals zero (i.e. equals the wave celerity) at the boundary surface, but in the case of water waves, and in the Miles (1957) theory, the elevation of zero wind velocity relative to the wave celerity occurs at the critical height, with streamlines below the critical height moving in the reverse direction to wave propagation, when viewed in this frame of reference propagating with the wave. It must also be noted that according to Miles (1957), as seen in Equation 2.3, energy input to the wave field is proportional to $k\eta$, or wave steepness.

One obstacle in applicability or calibration of the Miles (1957) theory, as seen from Equation 2.5, is that the energy input into waves was found to be dependent on the critical height at which wind velocity equals wave celerity, and this critical height is small when wind forcing is strong, often in the order of a few millimetres. Wind velocities are very difficult to measure this close to the moving water surface. Some laboratory experiments (e.g. Shemdin and Hsu, 1967; Young and Sobey, 1985), in order to obtain measurements of wind velocity close to or within the critical layer, have artificially thickened this layer several fold by means of a roughness plates at the wind inlet, which increased the critical height from a few millimetres up to the order of an inch or more. One may reason that results from an experiment with such distorted conditions must be treated with caution, and a theory in which calculations of momentum input can vary significantly due to presence of some roughness elements upwind should also be applied cautiously.

Independent of Miles (1957), Phillips (1957) also developed a theory related to wave growth as a result of wind excitation, which treated wave inception and wave growth as two

distinct mechanisms occurring at distinct stages in the evolution of waves. In the first stage, waves were theorised to form from an undisturbed surface by the turbulent air pressure fluctuations flowing over the water surface resonating with capillary waves with wavelength of order 0.017m and phase celerity of ca. 0.4m/s. This is the wavelength and celerity of waves of minimum phase celerity of an air-water free surface, which was defined by Nielsen (2009, p33) as

$$c = \sqrt{\left(\frac{g}{k} + \frac{\sigma}{\rho}k\right)\tanh(kd)} \tag{2.6}$$

where σ represents the surface tension of water, ca. 0.07N/m. Phillips (1957) theorised that ripples corresponding to the minimum possible phase celerity, i.e. waves of 0.017m wavelength, would be most affected by the resonance mechanism, and would consequently feature most prominently in early stages of the evolution of a wave field from an initially undisturbed surface. In the second stage of evolution after ripples have developed, waves were theorised to grow according to

$$\overline{\eta^2} \sim \frac{\overline{p^2}t}{2\sqrt{2}\rho_w^2 U_c g}, \tag{2.7}$$

where $\overline{p^2}$ is the mean-squared air pressure fluctuation and U_c is the velocity at which these fluctuations are blown past the waves, at an elevation above the free surface equal to the wavelength. It must be noted that wave height is not an explicit factor in Equation 2.7, and this lack of feedback of wave height to wind-input is one major difference between it and the theory of Miles (1957). Because of this apparent shortfall, the Miles (1957) theory has gained more widespread acceptance than the theory of Phillips (1957), and Young (1999, p61) stated that the latter is only generally assumed relevant in the inception and very early growth of waves.

The breakthrough work of Miles (1957) and Phillips (1957), as well as other studies of wave-wave interactions in the early 1960's (e.g. Longuet-Higgins and Stewart, 1960; Hasselmann, 1962; Pierson and Moskowitz, 1964), stimulated an increase of experimental studies in wind-wave interaction, many of which attempted the difficult task of measuring aerodynamic pressure over the top of waves.

Longuet-Higgins et al. (1963) performed measurements of wind pressure from a flat disk shaped buoy, and reported pressure fluctuations an order of magnitude smaller than those theorised by Phillips (1957). However, these results were challenged by later researchers (e.g. Dobson, 1971), who argued that the inevitable fluctuating tilt of the buoy relative to the

water surface must have polluted the pressure measurements, as it caused variation in the relative position and angle of the orifice at which pressure was measured. Young (1999 p55) pointed out that the lack of phase variation from 180° in this experiment implied zero momentum and energy transfer, and consequently labelled the Longuet-Higgins et al. (1963) experiment as largely unsuccessful.

Shemdin and Hsu (1967) sought to quantify the Miles theory by measuring pressure with a wave following sensor that was able to remain within ca. 6mm of the surface. They used the correlation and phase shift between wind pressure and wave surface slope to determine wind input to the wave. They found values that were comparable with predictions of the Miles (1957) theory, assuming that all of the momentum input entered the wave field rather than subsurface currents. As mentioned previously, the boundary layer was manipulated by a transition plate with roughness height of approximately 25mm. This was done to artificially thicken the boundary layer and increase the critical height above the water surface, from ca. 1mm without the plate, up to the order of 25mm after the plate was added, enabling measurement at and below the critical layer. As the height of the critical layer is considered to be coupled both to wind dynamics and momentum transfer (Miles, 1957), one may reason that such artificial manipulation may have altered the wind input. The boundary layer development and critical height depend on fetch, along with other factors. Natural ocean waves generally have a much longer fetch than laboratory paddle waves of similar dimensions, and hence have more room for the boundary layer to thicken and for the critical height to increase. However, in artificially manipulating the laboratory critical height, there was no way of testing whether or not this fell within a realistic oceanic range. Shemdin and Hsu (1967) did not document wave conditions in detail, nor was there mention of spatially separated wave gauges, and the latter would have provided a means to test the effects of the transition plate on actual wave growth.

Bole & Hsu (1969) performed laboratory experiments of wind over paddle waves, examining the growth of flume paddle waves under wind forcing by distributed wave gauges, and found experimental growth rates higher than predicted by Miles (1957) but of still roughly the same order of magnitude, as can be seen in Figure 2.4. They also observed that HF waves generated on top of paddle waves were often sufficiently tall to penetrate the wind critical layer discussed by Miles (1957), which shortfall in the critical layer theory was reportedly acknowledged by Miles (1957).

Dobson (1971) performed field measurements of wave surface elevation and wind pressure from a small buoy which was restrained against lateral translation. He used these

combined single point measurements to derive wind input, which was generally observed to be 5 to 8 times larger than what was predicted by Miles (1957). The growth rates compared well with some growth rates which were measured earlier by Snyder and Cox (1966).

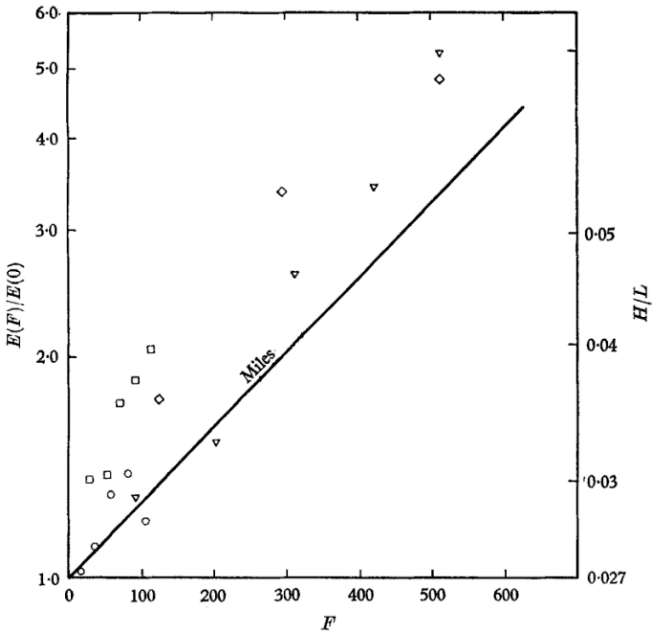

Figure 2.4: Growth of paddle waves measured by Bole and Hsu (1969), compared with Miles (1957) theoretical wind input. F, or dimensionless fetch, in this case is roughly equal to $(k^2/g)U_a\beta x$ if β is assumed constant within the wave flume. *E(F)/E(0)* represents energy with wind normalised by energy with no wind. Symbols represent varying wind fan frequencies, with ○=2.5Hz (ca. 5m/s), □=3.3Hz, ◇=4.2Hz and ▽=5Hz. Figure taken from Bole and Hsu (1969).

Elliott (1972) measured wave induced wind pressure and found a phase shift between pressure and surface elevation of ca. 135º during active wave generation. This phase shift did not vary with elevation above the wave crest, and was generally present only when wind velocity at 5m elevation was at least twice the dominant wave phase speed. The pressures measured at low frequencies were an order of magnitude less than those measured by Dobson (1971). However, the statement that perturbation pressure phase shift does not vary with height was generally assumed correct in later studies.

In an attempt to clarify discrepancies between previous experimental results (Dobson, 1971; Elliott, 1972; Shemdin and Hsu, 1967; Snyder, 1974), Snyder et al. (1981) performed new field measurements with an array of wave and wind sensors, which became known as the Bight of Abaco experiment. They also reviewed the instrumentation and data processing techniques used in several previous experiments, and reported that some discrepancies could be eliminated after inter-calibration. Wind input was measured at the same order of magnitude as (Miles, 1957), but exact comparison was found to be difficult, possibly due to

the theory's neglect of many physical processes such as viscosity, dissipation and nonlinear energy transfer between frequencies.

Plant (1982) performed further analysis of the data of Snyder et al. (1981) as well as that of Shemdin and Hsu (1967) and several other studies. He expressed growth rates according to friction velocity and summarised growth rates from all experiments into a consolidated relationship of

$$\beta = \frac{(0.04 \pm 0.02) u_*^2 \omega \cos(\theta)}{c^2} \tag{2.9}$$

where β is the temporal fractional growth rate in units of s^{-1}.

Based on experiments observations of early growth of pure wind-waves made by (Plant and Wright, 1977), he also expressed the view that waves longer than 0.1m grow primarily through nonlinear interactions (e.g. Hasselmann, 1962), because the wave growth was too great even if the waves absorbed 100% of the wind stress. This inference shall be revisited later in this thesis, in conjunction with observations made in the present study. The formulations of Plant (1982) have become a widely recognised benchmark of the magnitude of wind input into waves, but it was noted by Belcher et al. (1994) in Young (1999, p53) that the empirical data used to derive this formula contained a substantial degree of scatter, as can be seen in Figure 2.5.

Contemporary oceanographic modelling draws upon much of the above cited literature. The SWAN oceanographic model draws upon the measurements of both Snyder et al. (1981) and Plant (1982). It provides facility for both the Miles (1957) and Phillips (1957) mechanisms, although exact implementation of each is in accordance with later refinements in both cases (Booij et al., 1999). The Phillips (1957) theory is applied according to Cavaleri and Rizzoli (1981), who drew upon the theoretical enhancements of Phillips (1966, pp123-125) and measurements of Willmarth and Wooldridge (1962) to quantify the directional turbulent wind velocity spectrum. The Miles (1957) theory is applied according to Janssen (1991), who extended the Miles (1957) mechanism to two-dimensional conditions and coupled it with atmospheric boundary layer shear stress modelling as affected by the wind conditions and wave spectrum, particularly the wave age.

The Janssen (1991) application of the theory depended on modelling of turbulent stress using a mixing length model, assuming

$$l = \kappa z, \tag{2.8}$$

where l is the mixing length, κ the Von Kármán constant ≈ 0.4, and z the elevation above the ocean surface. It has been observed (Vanduin and Janssen, 1992) that the turbulence closure method plays a large role in the quantification of wind input. According to Cavaleri et al. (2007), most early wind input theories have relied upon a mixing length turbulence hypothesis, but Belcher et al. (1993) noted that at greater elevations in the atmospheric boundary layer, the disturbances to the mean velocity profile occur more quickly than the time scale of large eddies at those elevations, rendering the mixing length turbulence closure model inappropriate at those elevations. Belcher and Hunt (1993) suggested that the domain of mixing length modelling be truncated, and replaced by a rapid distortion modelling at greater elevations.

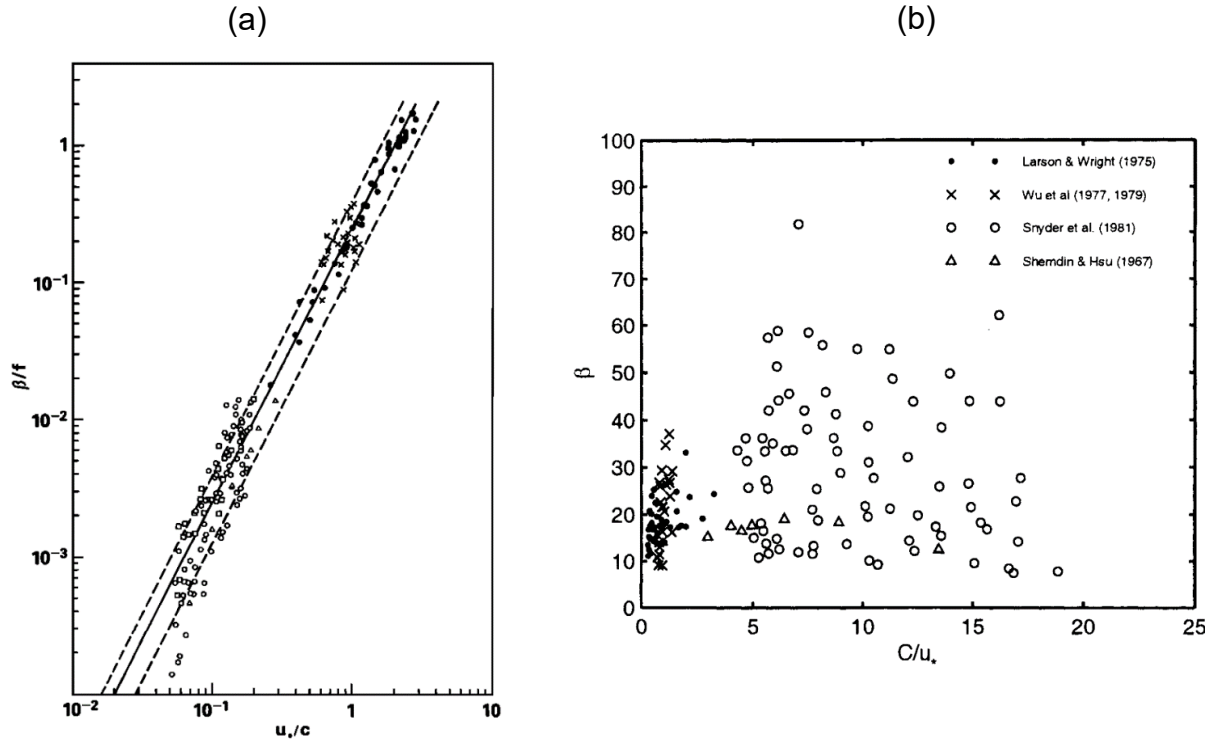

Figure 2.5: (a) β values reported by Plant (1982) combining four earlier experiments, (a) as reported by Plant (1982), and (b) as reproduced by Young (1999, p53). The logarithmic scaling and selection of dimensions in (a) masks the degree of scatter revealed in (b).

These authors also proposed a new model for wind input to waves, related to non-separated sheltering. This mechanism is based on a thickening of the boundary layer on the leeward side of waves, as the near-surface wind works to overcome an adverse pressure gradient. This asymmetrical boundary layer thickness results in velocity field perturbations as experienced by the outer flow which are not in phase with the wave, resulting in a net negative pressure on the forward (leeward) face of the waves. Unlike the theory of Jeffreys

(1925), this mechanism does not depend on separation. However, it stands to reason that this effect must be considered less significant than actual separated sheltering, when wave steepness and wind velocity are sufficiently great as to cause the latter to occur. This non-separated sheltering theory has been mentioned in some subsequent studies, but has not been adopted in ocean modelling packages.

Even more recently than the theoretical work of Belcher and Hunt (1993), observations were made which further revealed the inadequacy of the Miles (1957) mechanism to comprehensively quantify wind input. A long-term field experiment was performed by Donelan et al. (2005) at Lake George, Australia, between 1997 and 2000, making use of newer technologies and sophisticated wave-following equipment, and taking advantage of shallow water conditions which caused waves to be slower and steeper, with wind velocity higher relative to wave celerity, accentuating measurable effects. This experiment became known as AUSWEX (Australian Shallow Water Experiment). It was found in these data by Donelan et al. (2006) that in conditions of strong wind forcing and steep waves, wind separated completely at wave crests, reattaching on the windward face of the following wave. These conditions result in reduced wind input to HF waves on the leeward face of dominant waves, and also reduced wind shear due to the outer flow not being affected by surface roughness for part of the dominant wave phase. Regarding wind separation at wave crests, some studies (e.g. Banner and Melville, 1976; Banner, 1990) concluded this only to occur if the wave is breaking, while other studies (e.g. Veron et al., 2008) observed separation to occur in conditions which 'would normally be considered benign'.

The findings of Donelan et al. (2006) may be considered coherent with the observations of Donelan et al. (2004), performed in a wind-wave flume with wind velocities higher than what had typically been applied in past laboratory conditions. It was observed that wind stress, increasing with wind velocity up to $V_{10} \approx$ 30m/s (extrapolated from laboratory wind velocity), reached saturation beyond that wind velocity beyond which the water surface supported no further wind stress. This was later formulated into an empirical source term in wave modelling software, as a discontinuity in the wind input (Rogers et al., 2012; Zieger et al., 2015). Given that wind stress is widely considered dependent on the HF portion of the spectrum, and given that separation at crests shelters any HF waves on the leeward face of waves from the main wind stream, separation may be considered a possible cause for the wind stress limit observed by Donelan et al. (2004). Wind separation is discussed further in Section 2.2.6 and in Chapters 5 and 6.

In summary, the prevalent theory of wind input (Miles, 1957) was derived based on the simplification of monochromatic waves. Its use in wind-wave modelling is documented in Section 2.2.8 to principally resolve wind input at frequencies individually, without consideration of the effect wave energy at one frequency may have on the wind input at another frequency, other than through a common friction velocity and roughness length which are affected largely by HF waves. Recently, the prevalent theory and source term have been challenged by observations and alternate source terms. Wind input experiments have mostly focused on wave gauge measurements combined with wind pressure variation with respect to the dominant frequency, or the intensity of microwave energy backscattered by HF waves. Experimental observations have exhibited a significant degree of scatter, highlighting the difficulty of accurate water wave forecasting, even at laboratory scales but especially in oceanic conditions.

2.1.2 Dissipation

Wave dissipation is a process whereby kinetic and potential energy in waves is transferred into turbulence, heat and mean currents (Rapp and Melville, 1990) or into feeding waves of longer wavelength, with momentum being conserved. Wave dissipation is possibly the most observed source term in the Kinematic equation, yet the least understood (Young and Babanin, 2006a; Cavaleri et al. 2007). Donelan (2001) stated that 3.5% or less of wind input remains in the wave field, shown in Figure 2.6 to reduce to 0% at fully developed conditions, with the remaining 97 – 100% being consumed and transformed by dissipative processes.

Generally speaking, there are four types of wave dissipation mechanisms accounted for in research or operational wave models. Two of these mechanisms are only applicable in depth-limited conditions, namely bottom friction (including dampening by mud) and depth-induced breaking. These are outside the scope of this thesis.

The third mechanism to be mentioned, being viscous dissipation, may affect waves in deep or shallow water, but is generally considered to be most relevant in short waves with wavelength less than 0.2m (e.g. Caulliez, 2013). It has however been acknowledged that for swell waves of very low steepness, steepness induced breaking disappears, resulting in viscous dissipation again becoming the primary (but extremely weak) sink for such swell waves in deep water, acting over length scales measured in thousands of kilometres (Arduin et al., 2009). The fourth mechanism relates to steepness induced breaking in either deep or shallow water, often called whitecapping dissipation, dependent primarily upon wave steepness and in some cases affected by wind. This chapter discusses the third and fourth

dissipation mechanisms listed above, except for the above-mentioned slow viscous dissipation across thousands of kilometres, due to its lack of relevance to the research topic. More attention is given in this section to breaking rather than viscous dissipation.

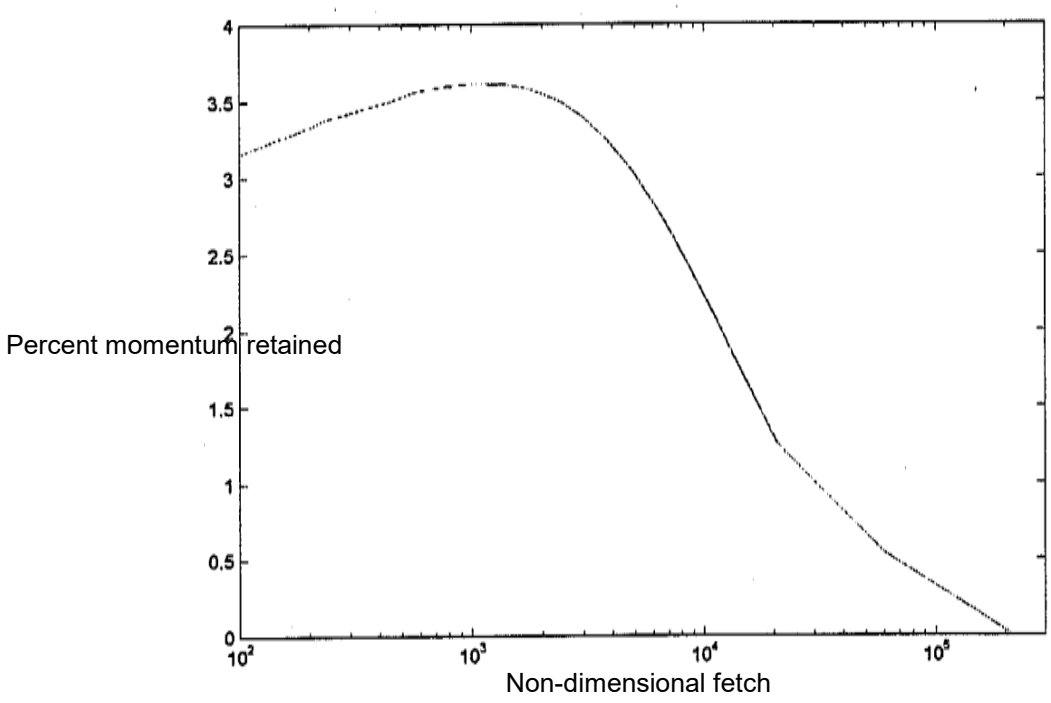

Figure 2.6: Figure copied and re-scaled from Donelan (2001), showing percentage of momentum transferred by wind to the water surface which is retained in the wave field. Where this value reaches zero at non-dimensional fetch of ca. $2x10^5$, the spectrum is hypothesised to be fully developed.

Several alternate definitions have been proposed to describe the physical process of breaking, or to identify the onset of wave breaking. It is well known that for waves of relatively low steepness and low nonlinearity, celerity of a given wave train is substantially greater than the orbital water velocities contained within that wave train. However, because orbital velocities increase proportional to wave height, increase in wave height causes orbital velocities to become larger relative to the celerity, particularly in nonlinear crests. Banner and Phillips (1974) identified the onset of breaking to occur when the horizontal orbital water velocities at the crest become equal to or exceed the wave celerity, which causes a water velocity stagnation point near the crest when viewed in a frame of reference following the wave phase celerity. It was stated that this stagnation point may not necessarily coincide with a discontinuity in the water surface slope, but declared the formation of this singularity to be the point of no return, after which breaking of some degree must occur.

Phillips (1958) described incipient wave breaking differently, that as orbital velocities and accelerations increase with steepness, there reaches a limiting point at which the vertical downward acceleration $a\omega^2$ at the crest reaches g. Upon exceeding this limit, the crest detaches resulting in breaking. In identifying the onset of breaking, Babanin (2011, p13) provided a definition that the point of no return has been reached once the water surface becomes vertical at any point. Bonmarin (1989) also used this definition in identifying plunging breakers, but for spilling breakers used the visible presence of foam. Longuett-Higgins and Smith (1983) in an experimental study identified breaking by observing "jumps" in the temporal rate of change of the ocean surface, using a floating device fabricated specifically for this purpose. Melville (1982) observed the onset of asymmetrical sidebands corresponded with the onset of breaking. Rapp and Melville (1990) documented increasing asymmetry of waves as they approach breaking, which observation should be no surprise to recreational beach goers, but which was argued by Babanin (2011, p46) to be an unreliable identifier for breaking onset due to its rapidly changing nature near the onset of breaking. He instead suggested skewness of waves as a better indicator of breaking onset, being defined as

$$\frac{a_1}{a_2} - 1, \tag{2.10}$$

where a_1 is the peak height above the MWS, and a_2 is the trough depth below the MWS. Babanin (2011, p46) proposed breaking-limited values for skewness of 1.0 for waves travelling in a single direction such as in a flume, and 0.7 for multi-directional surface waves such as is found on the ocean surface.

Beyond the point of no return, breaking typically occurs by water at the crest falling forwards on the face of the wave, either in formation of a jet which encloses a packet of air, or by gradually sliding down the front of the wave. The degree to which the crest separates from the wave is a major factor in how breakers are classified.

Breakers are generally defined as plunging, spilling or microbreaking events. Definitions of plunging and spilling breakers are common enough not to warrant explanation in this document, and descriptions may be found in Nielsen (2009, pp109-110) or Babanin (2011, pp40-41). Microbreakers are described by Tulin and Landrini (2001) as the forming of a bulge forward of the crest, which may propagate with fairly constant form for some time, without visible jets or whitecapping. These breakers, which are affected by surface tension effects, are a source of vorticity in the water and consequently dissipate energy, albeit more gradually than larger breaking events. They usually only occur in waves less than ca. 0.75m

in length, and were observed by Banner and Phillips (1974) to be very widespread in active wave fields.

Babanin (2011, p11) also described the ripping of steep wave crests off the top of waves under extreme wind forcing as a type of breaking of the water surface, but the physics of this process is very different to that of other breaking mechanisms, and use of the word 'breaking' in this thesis will not refer to this wind ripping mechanism unless specifically stated. Wind is also known to affect breaking, aside from the above-mentioned ripping off wave crests under extreme forcing. Babanin et al. (2010) observed wind of strong but not extreme forcing to increase the probability of breaking events, but reduce the severity. It would appear that the wind causes waves to break at a lower steepness than they would have otherwise, but being lower in steepness, possess less energy to instigate strong turbulent dissipation and mixing. At wind velocities above U_{10}=14m/s, dissipation was stated by Babanin and Young (2005) to be a function of wind velocity, although this was not explicitly stated to be resulting from the wind ripping wave crests off.

Liu and Babanin (2004) define four stages of breaking events. The incipient stage is defined as the previously discussed point at which waves reach limiting conditions, or the point no return. The developing stage includes the action of the crest falling down the front of the wave, and is characterised by an increase in width and steepness of the breaking wave front, such that the crest to front steepness is greater during this stage than at the incipient stage. The relaxing stage begins when the wave front slope begins to decrease in steepness. The final stage has arrived when the wave has propagated beyond the area of residual white capping foam still left on the surface.

While breaking is most likely to occur at the spectral peak, it was observed in the previously documented AUSWEX data (Donelan et al., 2005) that breaking at peak frequencies cause dissipation of energy in a broad range of higher frequencies (Babanin and Young, 2005; Young and Babanin, 2006a), which mechanism was referred to as a cumulative effect by these authors. This effect is related to the focus of the present study, and is thus discussed in more detail in Section 2.2.5. These studies also discussed the nonlinearity of dissipation due to a threshold level of energy for a given frequency, below which no breaking dissipation was observed. Babanin et al. (2010) also pointed out that wave breaking has been observed to shift the peak frequency of a spectrum up or down, with the overall shift more often down. However, a mechanism for this was not explained.

While some characteristics of breaking vary at different wavelength scales, Caulliez (2002) stated that shapes of waves at the point of incipient breaking are fairly similar at many length scales, and concluded that the underlying mechanisms are similar at all scales. However, it must be noted that the frequency of dominant waves measured in the experiment for that study was limited to a fairly narrow range of 1.5 to 2.4 Hz, which excludes much of the range of HF waves measured in the present study.

As previously mentioned, waves of short wavelength may also be affected by viscous dissipation, described by Babanin and Young (2005) as increased turbulent viscosity. Teixeira and Belcher (2002) theorised that this is due to distortion of turbulence by the wave Stokes drift, and through this mechanism work is performed and further turbulence is produced at the expense of wave energy. Crapper (1957) formulated a mechanism for waves with strong surface tension, which suggested that the limiting steepness of such tiny waves is close to 0.73, as opposed to the commonly referenced 0.142 steepness limit for gravity waves. From this, it appears that surface tension at short wavelength scales inhibits breaking of waves, allowing waves to become much steeper before breaking.

Caulliez (2013), seemingly contrary to the 2002 study by the same author, observed that dissipative regimes for wind generated HF waves vary greatly depending on the wavelength. In the 2012 experiment, for waves less than ca. 0.1m wavelength, viscous damping and nonlinear transfer of energy to lower frequencies prevented wave steepness developing to the point where breaking could occur. In HF waves of this scale, viscous dissipation was found to occur in the primary waves, and also occurred as a result of parasitic capillaries riding on the forward face of waves. These capillaries were not seen in waves longer than 0.18m, and the observations of breaking events on waves between 0.1m and 0.18m was hypothesised to be a result of parasitic capillaries being too small relative to the wave to dissipate the excess energy provided by wind, thus resulting in steepening to the point of breaking. Breaking observed between wavelength of 0.1 and 0.2m was observed to manifest itself with surface disruptions on the forward face of crests. Waves longer than 0.2m were observed to exhibit plunging type breaking events, involving bulge of the crest, followed by a jet falling forward in front of the wave front, and then splash-up.

In summary, dissipation of HF waves may occur through either breaking or turbulent dissipation, with the nature of dissipation depending on the wave lengths in question. Dissipation of HF waves, which is closely related to suppression, may also be affected by presence of or breaking of relatively longer waves, which cumulative effect is discussed further in Section 2.2.5.

2.1.3 Evolution of waves by instability and nonlinear interactions

There are two widely observed mechanisms by which wave spectra are changed independent both of any direct forcing from wind and of loss via dissipation, through energy moving between frequencies. The first mechanism is the instability of individual wave trains of finite height which transfers energy to surrounding frequencies, known as Benjamin-Feir Instability (Benjamin and Feir, 1967). The second is nonlinear interactions between multiple wave trains (Hasselmann, 1962).

Benjamin-Feir instability

Benjamin and Feir (1967) identified analytically that finite amplitude sinusoidal waves on deep water are unstable, and formulated a mechanism by which energy is shed from a spectral peak and develops unbounded in sideband pairs equally separated in the frequency domain by δ (Rad/s) above and below the peak angular frequency in the range of

$$\omega_P \pm 0 \leq \delta \leq \sqrt{2}\omega_P ka \tag{2.11}$$

where ω_P is the spectrum's peak angular frequency, as illustrated in Figure 2.7. The peak growth of such sidebands was predicted to occur at frequencies $\omega_P ak$ above and below the peak frequency. This theory states that all Stokes wave trains are unstable regardless of how small the steepness ak, but it was acknowledged that low steepness waves are in practice considered stable as their instability is negligible in scale, and suppressed by viscous damping. It was also proposed by these authors that this instability causes initially monochromatic waves to eventually becoming irregular at long distances. The pioneering nature of this work resulted in this instability and associated sidebands being named after these authors. It should be noted that this theory was formulated in the absence of wind forcing.

Several later studies were performed to investigate the behaviour of this instability. Laboratory observations by Lake et al. (1977) observed the instability to lead formation of regular pulses or wave groups, which after reaching a point of close to zero amplitude between pulses, would then re-form into a regular wave train somewhat approaching monochromatic conditions, although with the lower sideband in the reformed wave train becoming stronger than the upper side band. They suggested that over very long distances, the wave train would oscillate between near monochromatic conditions and pulse-like conditions harmonically in a consistent manner, although may eventually experience a downshift of peak phase frequency with the lower sideband eventually becoming stronger than the primary harmonic. Melville (1982) observed that the onset of sideband asymmetry

typically corresponded with the onset of breaking. Bliven et al. (1986) observed that wind forcing applied to the monochromatic paddle waves reduced the evolution of sidebands, and documented, unsurprisingly, that no sidebands were discernible in wind-only cases. They also discussed a downshift in peak frequency, but one may consider any discussion on the downshift of peak frequency to be problematic given that the dominant frequency is bound in monochromatic laboratory experiments to the paddle frequency. Waseda and Tulin (1999), performing both seeded and unseeded experiments, argued that the wind effects on sidebands was more complex than observed by Bliven et al. (1986), with low wind velocity suppressing sidebands, high wind velocity enhancing sidebands, and wind forcing generally altering the location of the sidebands in frequency space.

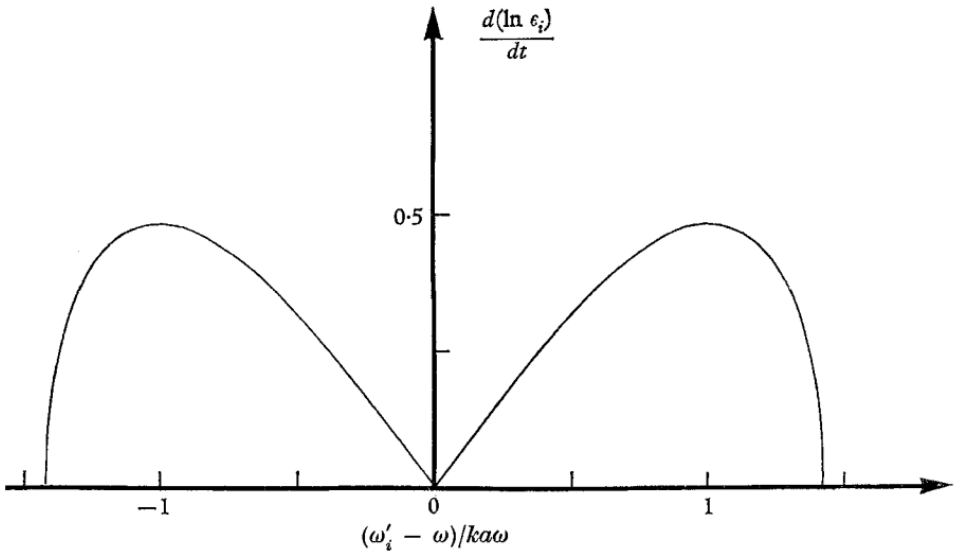

Figure 2.7: Figure from Benjamin and Feir (1967), displaying asymptotic growth in sideband frequencies. Frequency zero in this plot corresponds to the primary or paddle frequency, while label ϵ_i represents the amplitude of sideband modes (m), ω_i represents frequencies within the sideband frequency range and ω represents the primary frequency.

Further review of studies on Benjamin-Feir instability was not considered essential for this thesis, given that the interactions researched in the present study occur between waves of distant frequencies.

Nonlinear interactions between wave numbers

Separate to Benjamin-Feir instability, multiple waves trains of differing wave numbers and directions in a distributed sea spectrum are known experience nonlinear interaction of energy between frequencies. This interaction is generally considered more significant to oceanic wave modelling than Benjamin-Feir instability, and is the basis of one of the three major ocean modelling deep-water source terms.

Prior to 1960, wave-wave interactions were not given substantial attention in wave evolution literature. Longuet-Higgins and Stewart (1960) identified that LF waves perform work against HF wave radiation stress which contributes to the steepening of HF waves on LF wave crests, although in this overall mechanism the HF wave energy is conserved over time. However, Phillips (1960) analytically arrived at a mechanism by which two wave trains of finite wave height travelling at different directions can interact to transfer energy to a 3rd wave train in the resultant combined direction. Such a mechanism has since been referred to as nonlinear triad interaction. He theorised that these interactions are relevant in deep or shallow water, but Hasselmann (1962) later proved that these interactions are only applicable in water of finite depth.

Hasselmann (1962) extended the derivation to 4th order, whereby quadruplets of wave trains in deep water meeting the resonant wave number and direction conditions may experience nonlinear interaction and transfer energy within themselves. The quadruplet may achieve resonance if and only if

$$k_1 + k_2 = k_3 + k_4\,, \qquad \text{and} \qquad \omega_1 + \omega_2 = \omega_3 + \omega_4 \tag{2.12}$$

which resonant condition was also portrayed diagrammatically by Young (1999, p64), as reproduced in Figure 2.8.

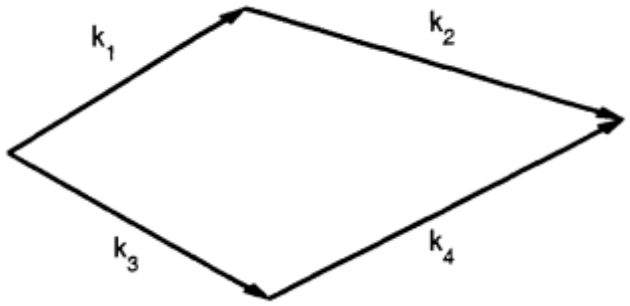

Figure 2.8: Figure from Young (1999, p64), displaying resonant conditions required for nonlinear interaction between wavenumbers according to the theory of Hasselmann (1962).

Within this mechanism, energy and momentum are conserved in the wave field. The main challenge in application of this mechanism to wave modelling has been the computational effort required to calculate the interaction term at each grid point in space and time. Every such iterative calculation must process a large number of wave number combinations to quantify resonant conditions and the outcome of the interaction. Multiple numeric simplifications have been proposed to facilitate practical inclusion in wave models

by reducing computational load. The most prevalent are the Discrete Interaction Approximation (DIA) produced by Hasselmann and Hasselmann (1985), and the Neural Network Interaction Approximation produced by Tolman et al. (2005). An in-depth discussion of these approximations is outside the scope of this thesis, as is commentary on the complete derivation of the Hasselmann (1962) interaction.

A few significant constraints are relevant to this mechanism. The time scales required for Hasselmann (1962) interactions to significantly alter ocean spectra is more often measured in hours rather than seconds. An example was provided by Badulin et al. (2008), who documented a 25% shift in peak frequency for a spectrum taking 256 hours in a wave modelling exercise. Another aspect of the interaction highly relevant to this thesis, as pointed out by Kitaigorodskii (1983) is the dependence of wave trains being local in frequency space. The likelihood and magnitude of interaction between wave numbers reduces quickly with increasing separation in frequency space. Chen and Belcher (2000), based on calculations by Masson (1993), concluded that the interaction is insignificant where wave numbers differ by a factor of ca. 1.6 or more.

One other aspect of nonlinear interactions to be noted is the potential in the theory of Hasselmann (1962) for energy transfer to both longer and shorter wave numbers. While these interactions are considered primarily responsible for evolution of spectral energy from high to low frequencies, some authors have focused on transfer from low to high frequencies. Kitaigorodskii (1983) proposed a theory to explain the equilibrium range of the HF spectral tail, dependent heavily upon nonlinear transfer of energy from lower frequencies to frequencies this range, as opposed to wind input in this range. This is documented further in Section 2.1.4.

In spite of the computational difficulty, and although the physics of this interaction is yet to be fully understood (Young 1999, p64), this mechanism has received unquestioned acceptance by the wave modelling community, and features in contemporary oceanic modelling tools. The key characteristics of this interaction which are relevant to the present study are the large time duration required for this effect to occur, and the necessity for the four wave numbers to be of close proximity in frequency space. It was noted by Cavaleri et al. (2007) that nonlinear triad interactions take effect more rapidly than nonlinear quadruplet (Hasselmann, 1962) interactions, and play a dominant role in nonlinear transfer of energy between frequencies in shallow water. However, triad interactions have no impact in fully dispersive deep-water conditions and are thus outside the focus of this thesis. Quadruplet

nonlinear interactions as applied specifically to suppression of HF waves are discussed further in Section 2.2.7.

2.1.4 Wave spectrum evolution – general shape and HF equilibrium

In this section, the concept of a fully developed wind sea or equilibrium of HF wave energy shall be discussed, as well as the prevalent research concerning the shape of oceanic wind-wave spectra.

Phillips (1958) pioneered the concept of wave fields reaching equilibrium values based on stationary atmospheric conditions, proposing HF wave breaking as the limiting mechanism. Through dimensional analysis, he arrived at the conclusion that energy in the HF tail of the wave spectrum is governed by the approximate relationship

$$S_{\eta\eta}(\omega) \sim \alpha g^2 \omega^{-5} \tag{2.13}$$

for the ω spectrum, and

$$S_{\eta\eta}(\boldsymbol{k}) \sim f(\theta) k^{-4} \tag{2.14}$$

for the directional $\boldsymbol{k}$ spectrum, where α represents in this case an absolute constant value of 7.4×10^{-3}, and $f(\theta)$ is a function dependant on angle of the spectral component propagation relative to the dominant angle of the directional spectrum, with variance density spectra $S_{\eta\eta}(\omega)$ in units of m^2s and $S_{\eta\eta}(k)$ is in units of m^4. Phillips (1985) stated that these relationships generally match observations in frequencies and wave numbers above twice that of the spectral peak.

Stimulated by the work of Phillips (1958), Pierson and Moskowitz (1964) used non-dimensional analysis to derive a theoretical expression for the entire fully developed wind-wave spectrum, defined as

$$\mathrm{S}_{\eta\eta}(\omega) = \frac{\alpha g^2}{\omega^5} e^{-\beta\left(\frac{\omega_0}{\omega}\right)^4}, \tag{2.15}$$

where in this case $\alpha = 8.1 \times 10^{-3}$, $\beta = 0.74$ and $\omega_0 = \frac{g}{U}$ where U is the wind velocity as "reported by weather ships". They suggested that parameters may shift based on fitting to improved future data. This has become known as the Pierson Moskowitz (PM) spectrum. While other empirical spectral shapes such as the JONSWAP spectrum (Hasselmann et al., 1973) were published later which more closely follow observed oceanic conditions, the PM spectrum received much acclaim for resembling practical oceanic spectra while being derived analytically, albeit with some fitting to empirical data. It was used as a springboard

for much later work, and the PM peak frequency still features today in some source terms in SWAN (The-SWAN-Team, 2018, p33).

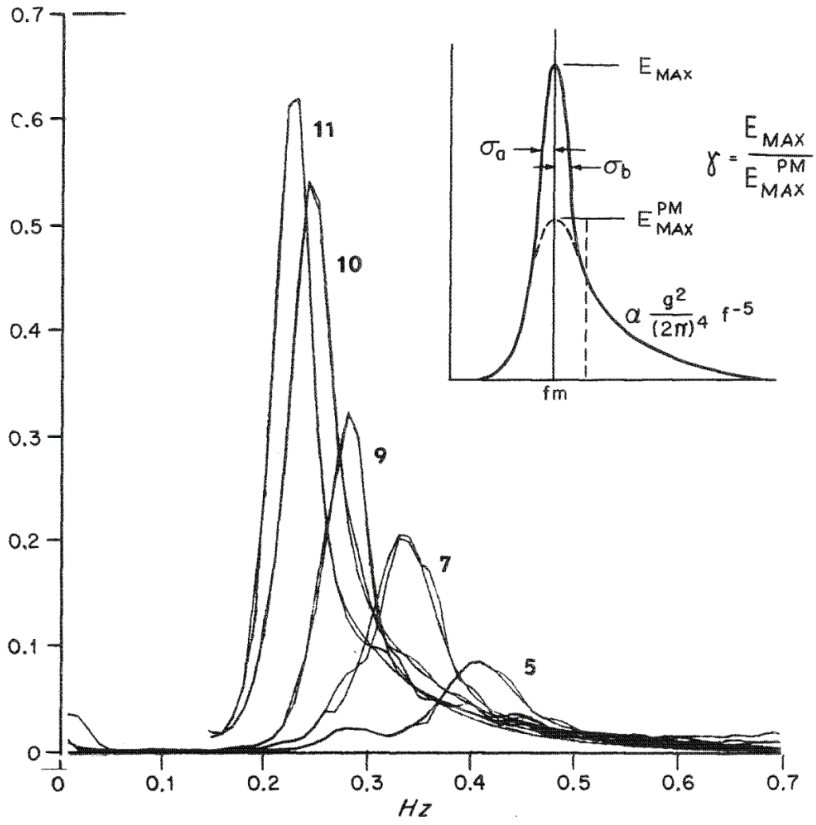

Figure 2.9: JONSWAP fetch limited spectra, with labelled fetches 5: 9.5km, 7: 20km, 9: 37km, 10: 52km, 11: 80km (Hasselmann et al., 1973)

It was mentioned in Section 2.1.1 that theoretical advances of the late 50's and 60's, including that of Pierson and Moskowitz (1964) stimulated several new experimental studies to test and calibrate these new theories. The most prevalent study focused on measuring real oceanic spectral shape was the Joint North Sea Wave Project (JONSWAP), documented by Hasselmann et al. (1973). In this study, fetch-limited wave evolution was measured at several fetches for offshore winds from the coast of Sylt, Germany, up to a maximum fetch of 160km. The wave instruments measured frequencies up to 1Hz. Figure 2.9 displays samples of spectral evolution at various fetches for an offshore wind event in this study, which was considered close to pure fetch-limited conditions without pollution by swell. Hanson and Phillips (1999) pointed out that these spectra exhibited a more enhanced peak than the Pierson and Moskowitz (1964) spectrum, regardless of fetch. A generic spectrum was obtained empirically from these measurements at various fetches, equal to

$$S_{\eta\eta}(f) = \alpha g^2 (2\pi)^{-4} f^{-5} e^{-\frac{5}{4}\left(\frac{f}{f_m}\right)^{-4}} \gamma^{e^{\frac{(f-f_m)^2}{2\sigma^2 f_m^2}}}, \quad (2.16)$$

where α corresponds to the α of equation 2.13, f_m the peak frequency, σ a shape tuning value which varies depending on whether the frequency in question is higher or lower than f_m, and γ another tuning parameter related to peak enhancement. Empirical values for all of these tuning parameters were obtained as functions of dimensionless fetch, but there was substantial scatter in the data, present in Figures 2.6, 2.7 and 2.8 of Hasselmann et al. (1973) (not reproduced here), even when data was plotted on logarithmic axes. This seemingly irreducible scatter suggests that attempts to use these empirical relations to predict wave spectra, even in consistent fetch limited conditions, may experience a high degree of prediction error.

One key conclusion from this study was that growth in most of the lower frequency portion of the wave spectrum was a result of transfer of energy from higher frequencies by wave-wave nonlinear interactions, rather than by direct wind input at the lower frequencies (Hasselmann et al., 1973). In addition, they concluded that only ca. 5% of momentum transferred from the atmosphere to the wave field remains in the wave field, with the remainder being transferred to short waves by nonlinear interactions and then to mean ocean currents by dissipation.

Donelan (2001) also reported that the proportion of received momentum remaining within the wave field decreases with dimensionless fetch, eventually reaching zero, which constitutes the fully developed spectrum. The behaviour of a spectrum being fully developed and not growing much as a result of wind forcing is highly relevant to any oceanic experiments which attempt to measure increase in wave energy as a function of wind forcing, because such renders the relationship between wind forcing and wave growth nonlinear, with nonlinearity dependant on dimensionless fetch. There remains to this day however debate on the definition of a fully developed wind-wave spectrum, and whether the wave spectrum under constant continuous wind forcing ever reaches a point of full development where total energy in every portion of the wind-wave spectrum is stationary (Alves et al, 2003).

There is, however, general consensus on the existence of an equilibrium range in the HF tail of the ocean wave spectrum, although there is some scatter in the magnitude of the observed limit in most experiments. Studies after Phillips (1958) cast doubt on the notion of the equilibrium range being determined primarily by wave breaking. Kitaigorodskii (1983) proposed that energy input into the HF tail of the wave spectrum is due to energy transfer from lower frequencies, in a similar manner to which turbulent energy is transferred from larger to smaller eddies while dissipating.

Phillips (1985) also disputed his own 1958 assumption of wave breaking being the governing mechanism for the equilibrium range, instead arguing that all three processes of dissipation, wind input and nonlinear interactions play a large role in determining the shape and magnitude of the HF tail.

Phillips (1985) pointed out that the so-called constant of proportionality in equation 2.13 decreased with fetch in the field measurements of Hasselmann et al. (1973), and likewise was several-fold larger in laboratory measurements than in field measurements at long fetches. Based on measurements by Toba (1973) and others, he suggested that measurements favoured the revised frequency spectrum relationship of

$$S_{\eta\eta}(\boldsymbol{k}) \sim \frac{u_*}{c} g^2 \omega^{-5}, \tag{2.17}$$

which accounts for wave age or fetch, or expressed another way,

$$S_{\eta\eta}(\boldsymbol{k}) = \alpha u_* g \omega^{-4}, \tag{2.18}$$

where α represents what he calls the Toba constant which appears comparable with the Phillips constant, based on empirical derivations from a laboratory study by Toba (1973) which match this theory. Equation 2.18 was also proposed by Toba (1973). The Toba constant was suggested by Toba (1973) himself to be 0.02, by field studies of Kawai et al. (1977) to be 0.062 and by Forristall (1981) to be 0.11, so recounted by Phillips (1985) after transformation. While the addition of u_* improved universality of the relationship over equation 2.13, there remained nonetheless a dependence on fetch or wave age. Phillips (1985) highlighted the variance in Toba's 'constant', acknowledging that this relation for the shape of the spectral HF tail was still not perfect.

Hara and Belcher (2002) proposed that some of the variance in measurements of wave energy in the equilibrium spectra is caused by sheltering by the lower frequency portion of the spectrum, namely that this portion of the spectrum absorbs part of the wind stress, reducing available wind stress for the HF spectral tail. This sheltering effect is one of the prevalent theories of HF and LF wave interaction, and more detail concerning this mechanism is included in Section 2.2.6.

In summary, the HF tail of the spectrum has generally been observed to exhibit a saturation limit, through mechanisms not fully understood, which limit follows a shape proportional to $u_* \omega^{-n}$ with n being approximately equal to 4 but exhibiting some variation with wave age and location in frequency space. There has also been reported some variation in the range in which there is dependence on u_* and variation in coefficient of

proportionality, or Toba's constant. There are conflicting views as to the mechanism which forces the spectrum to form this shape, with Zakharov and Badulin (2012) commenting that the Phillips spectral tail is at times applied without any certain idea of the mechanism causing it.

This section has documented some general studies on spectral evolution of wind-wave fields, all of which have relevance to the HF tail of the spectrum. The behaviour of the HF spectral tail is central to the present study, particularly variations of energy in the HF tail due to varying LF waves conditions. Literature more focused on this is reviewed in Section 2.2.

2.2 Lower frequency wave effects on high frequency waves

It has been observed in laboratory wind-wave fumes for more than half a century that the presence of paddle waves influences the evolution of high frequency wind-waves, the pioneering study being that of Mitsuyasu (1966). The majority of studies in this topic address the laboratory suppression of HF waves in the presence of following LF waves, but some observations have also been made of LF waves opposing wind doing the opposite, enhancing the development of wind generated HF waves (e.g. Mitsuyasu and Yoshida, 1989). Other studies, such as that of Bliven et al. (1986) and Waseda and Tulin (1999), have observed reduced growth of the wind-wave spectrum as a result of swell, but have not explored this effect in detail.

A few mechanisms have been proposed to explain these effects, but there is no clear consensus (Mitsuyasu and Yoshida, 2005), and the majority of wind-wave theories do not addressed it. Bole & Hsu (1969) explicitly dismissed the significance of nonlinear interaction between paddle waves and wind induced ripples. Donelan et al. (2010) expressed the view that further work is needed to understand the physical mechanism. Mitsuyasu (2015) documented key shortfalls in all three of the prominent theories which are outlined in Sections 2.2.5, 2.2.6 and 2.2.7 of this thesis, and expressed the view that the problem is still fundamentally unsolved.

The lack of an accepted theory is also evident in the minimal consideration given to this effect in oceanic models such as SWAN (Booij et al., 1999). The developers of SWAN were aware of the phenomenon around the time that SWAN was produced (Holthuijsen et al., 2000), and suggested some simplified numerical solutions (Booij et al., 2001), which are outlined in Section 2.2.8. It appears that at that time they considered their solution not ready to incorporate into SWAN without further validation. Most source terms in the current release of SWAN as at late 2018, Cycle III version 41.20A, still do not explicitly account for this effect

(The-SWAN-team, 2018). Only one relatively new source term package, “ST6” (Rogers et al., 2012; Zieger et al., 2015) compensates in part for the observed suppression of HF waves by LF waves, but this source term does not explain the physics behind the interaction, and being relatively new, has yet to be used, tested and refined over an extended period of time.

Observations have widely agreed that the suppression of HF waves is stronger with increased LF wave steepness (e.g. Chen and Belcher, 2000; Mitsuyasu, 1966). Chen and Belcher (2000) expressed this in slightly different terms, being that suppression effects are stronger with lower wave age C_L/u^*.

LF waves in the ocean are widely acknowledged to modulate radar backscatter from the ocean surface, which backscatter is primarily coupled to HF waves, and modulation is partly caused by LF waves physically modulating the intensity of HF waves (e.g. Plant et al., 1983; Smith, 1986; Komen et al., 1989; Hara and Plant, 1994; Keller et al., 1994; Collard et al., 2005; Donelan et al., 2010). Violante-Carvalho et al. (2004) examined Buoy data with multiple distinct swell wave trains present and concluded that LF waves did not influence the development of HF wind-waves. However, direct measurement has mostly clearly taken place in laboratory experiments, as the effect is more discernible in laboratory flumes with monochromatic paddle generated LF waves. Hanson (1997) and Chen & Belcher (2000) stated that suppression is less apparent in the open ocean than in flumes. Mitsuyasu and Yoshida (2005) and Donelan et al. (2010) also documented this, and suggest it is due to typically lower LF wave steepness in oceanic conditions, at least in the case of swell, than what is present in wind-wave flumes. Chen and Belcher (2000) argue suppression is less prevalent in the ocean is due to the lower inverse wave age u^*/C_{LF} in the ocean. In the previously mentioned study of Donelan et al. (2005), suppression was implicitly observed through reduced HF energy immediately after LF wave breaking events, but was not correlated directly with the amount of energy in LF waves. Direct (wav-gauge) field quantification of HF wave suppression as a result of the presence of LF waves (rather than the breaking of LF waves) is yet to be performed with any degree of certainty, so it is still unconfirmed whether or not the magnitude of suppression is significant in the field.

If suppression is found to be quantifiable in the field, it is relevant both to field data collection, and to ocean modelling source terms. Many remote sensing techniques for measuring the wind field are dependent on radar backscatter from the water surface dependent on the wind-wave spectrum (Bliven et al., 1986). And for modelling of wave fields, given that wind stress is considered primarily dependent on HF waves, an improved understanding of HF wave behaviour may improve wind stress calculation and consequently

wave predictions. Given that contemporary wave forecasting is based on the three main source terms of wind input, dissipation and nonlinear interactions, still typically performs with RMS errors in the order of 0.5m (Rogers et al., 2007) even with empirically based parameter tuning, it must be acknowledged that there is room for improvement in state-of-the-art wave forecasting.

The remainder of Section 2.2 documents observations of this effect, then discusses the prevalent theoretical approaches which have been used to explain it, being the theories of enhanced dissipation, modified wind input and direct coupling between wave components, and outlines some shortfalls in each. Finally, in 2.2.8, wave modelling source terms are touched upon in light of HF and LF wave interaction.

2.2.1 Prevalent laboratory studies

Mitsuyasu (1966) performed the pioneering laboratory study which ascertained a strong interaction between HF and LF laboratory waves. He measured the suppression of HF waves due to the presence of paddle waves in a large wind-wave laboratory flume, with total flume length of 70m and breadth of 8m. The effective fetch was far shorter, with reported measurements taken at wind fetch of 5.2m, but the experimenters stated that measurements at increased fetch did not substantially alter findings. The experiment was run with LF paddle waves reaching steady state before adding wind, and also in reverse order with HF wind-waves reaching steady state before LF paddle waves were introduced. The order in which these were added was reported to make no significant difference to the final steady state of the combined system.

The transient duration for HF waves to reach their new equilibrium after introduction of paddle waves appeared in Figure 2.10 to be around 3 – 4 wavelengths of the paddle wave at 5.2m fetch, and this includes the first few paddle waves which had not yet reached maximum height, which ramping of amplitude is unavoidable at the onset of paddle generated laboratory wave trains. The time duration taken for HF waves to reach equilibrium at this fetch when wind was introduced, either in paddle-only or quiescent conditions, is not reported in this article. More precise measurement of this transient time is one key focus of the current study, as discussed in Section 2.3, and reported on in Section 5.3.

One other key finding by Mitsuyasu (1966) was that the HF wave spectrum as impacted by paddle waves not only reduced in amplitude, but sometimes increased in peak frequency of the HF component of the spectrum. In cases of strong suppression, the HF wave spectrum was sometimes seen to be spread across a wider range of frequencies, appearing

shorter and flatter in the frequency domain (Mitsuyasu, 1966). In one case, one HF frequency spectrum plateaued such that there was a marginal double peak, as illustrated in Figure 2.11, but based on their positioning in frequency space, at least one of these twin peaks may have been related to the paddle wave higher harmonics.

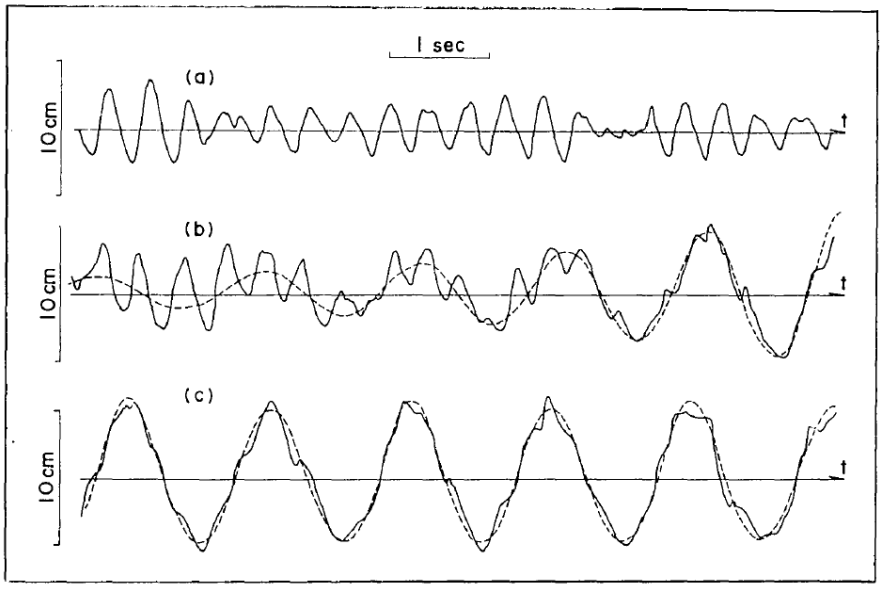

Figure 2.10: Figure from Mitsuyasu (1966), (a) displaying wind-waves with no paddle waves, (b) the transition as paddle waves were added, and (c) the final steady state of combined wind forcing and paddle waves, at fetch=5.2m.

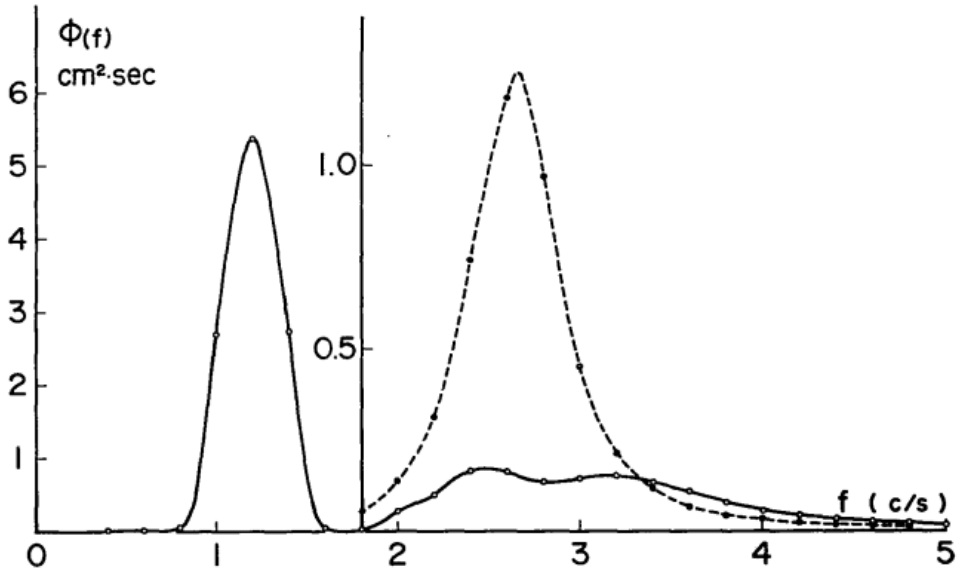

Figure 2.11: Figure from Mitsuyasu (1966), With solid line displaying spectrum with combined wind and paddle waves, and dotted line the corresponding pure wind-wave spectrum. Nb. Two different vertical scales are used side by side in this plot.

Mitsuyasu (1966) also made the observation that suppression of the HF waves was positively correlated with increasing paddle wave height and shorter paddle wave lengths, which shorter paddle waves were consequently nearer in frequency to the HF waves. In combining wave height and wavelength into wave steepness, a positive correlation was usually observed. In some cases, as much as 75% of the HF wave energy was suppressed in the presence of the paddle waves (Mitsuyasu 1966). Mitsuyasu (1966) also documented noticeable enhancement of paddle wave higher harmonics in the presence of wind forcing, as paddle waves became more nonlinear.

It must also be noted that paddle waves of very low steepness (T = 1.4s, H = 0.025m, H/L = 0.008) appeared in Figure 9 of Mitsuyasu (1966) to slightly enhance the HF wave spectrum, rather than suppress it, but this was not explicitly discussed by those authors. This suggests however that the overall effect may be a combination of multiple distinct physical mechanisms, and enhancement of HF waves by following LF waves of low steepness, which has not received attention in literature, was also measured in the present study, as documented in Section 5.5 and 5.6.

Keller & Wright (1975) identified the change in microwave radar backscatter from HF waves when LF waves swept through the illuminated area and suggested that while the LF wave slope plays a part, this is partly also due to the HF wave energy being modulated by the LF waves. Like Mitsuyasu (1966), they observed modulation of HF waves proportional to paddle wave height. One unexpected observation made in this study was that the HF wave portion of the spectrum became almost flat in frequency space at the highest paddle wave amplitude (0.074m), as illustrated in Figure 2.12, and this flattened spectrum had a much higher mean magnitude than spectra with similar u^* and lower paddle wave amplitudes, or even the corresponding pure wind-wave spectrum. This was attributed by the Keller & Wright (1975) to noise, but similar levels of noise were not present in this magnitude in cases with shorter paddle waves, and possibly deserved more attention at the time. It may have been representative of turbulent HF waves being generated as a bi-product paddle wave breaking.

A comparable effect was seen in the laboratory results of Donelan (1987) in conditions of paddle waves following the wind, which showed only a marginal decrease of energy in HF wave spectrum at frequencies situated more than $1 \times f_{paddle}$ above the HF peak of pure wind-waves, and in some cases a slight increase.

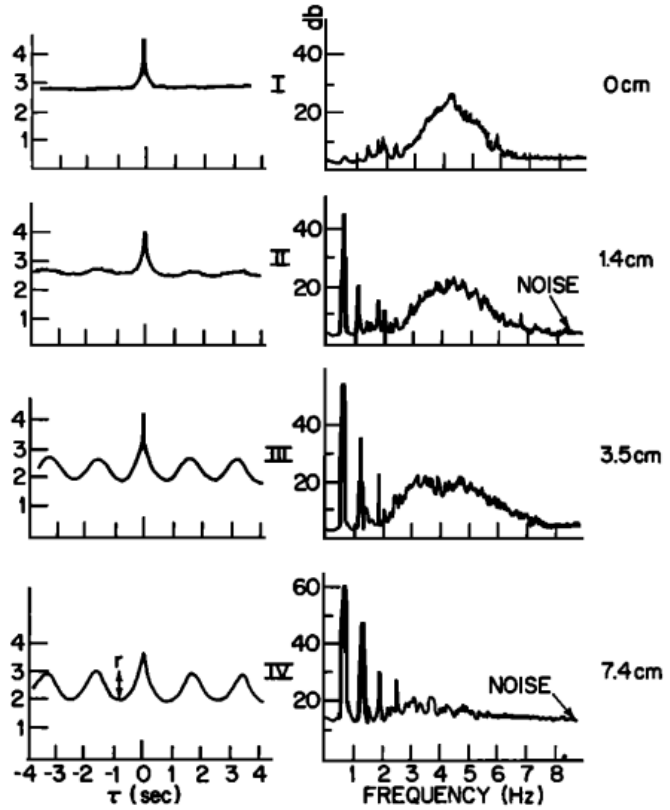

Fig. 2. Autocorrelation functions of the microwave return (left) and wind-wave spectra (right) for various wave amplitudes at $u^* = 16.5$ cm sec^{-1}.

Figure 2.12: Figure from Keller and Wright (1975), in the bottom right pane displaying a flattened HF portion of the spectrum with HF energy higher than for pure wind-waves, in the steepest paddle wave conditions (0.074m amplitude).

Hatori et al. (1981) studied the effect of paddle waves on wind-wave development and also the corresponding growth of the paddle waves. They observed that suppression of the wind-waves and momentum absorbed by the paddle waves both increased with paddle wave steepness, and also expressed this as suppression increasing as the wind-wave peak frequency drew near to the paddle wave frequency. They inferred that the momentum absorbed by paddle waves and suppression of HF waves were related to each other, but did no more to propose a mechanism. Hatori et al. (1981) also observed that the suppression effect and growth of the paddle wave varied along the 14m fetch, both increasing and then decreasing at different fetches. This led them to infer that there are four distinct stages in the development of the combined wave spectrum under the influence of wind. Stage 1 exhibited similar growth of HF waves regardless of the presence of LF paddle waves. Stage 2 exhibited suppression of HF waves, and strong growth of LF waves. Stage 3 exhibited further strong growth of LF waves in near absence of HF waves. In stage 4, after LF wave breaking, they reported that LF waves evolved into low frequency random

waves. To specify four classifications using a 14m fetch may seem excessive, but at least the first three of the stages documented by Hatori et al. (1981) were all observed in the current study, although typically not at the same time. The same research group in Imai et al. (1981) performed more laboratory experiments, with paired wave gauges attempting to track individual waves. The overall conclusion from that study was that the majority of interaction occurs near the crest of the LF wave.

One final observation is mentioned here, being that of Smith (1986), using the data of Plant et al. (1983), that degree of suppression of HF waves measured with 0.021m wavelength radar was found to be dependent on wind velocity, whereas suppression of HF waves measured with a 0.12m wavelength radar did not depend in wind velocity for the range of wind velocities measured. Such may suggest multiple mechanisms exist for varying HF wavelength scales.

2.2.2 Spatial distribution of HF waves

Measurements of the distribution of HF energy along the LF wave phase have exhibited some variation in the location of maximum HF wave intensity. Keller and Wright (1975) reported maximum hydrodynamic MTF on the forward (leeward) face of laboratory paddle waves following wind using microwave backscatter detection, meaning the maximum HF energy was present on the forward face. Reece (1978), using laboratory slope meter measurements of HF wave energy in the range between 5 to 20Hz frequency, also observed HF energy to be strongest on the forward (leeward) face of paddle waves after applying a correction for advection by the LF waves. Donelan et al. (2010) in a laboratory flume using a laser slope instrument, observed HF wave to be strongest near the crest at low wind velocities, with this maximum moving down the forward face of the LF waves with increasing wind velocity.

In contrast, Hwang (2002) observed HF waves to be strongest near the crest of following LF waves, but slightly stronger on the rear face. And Miller et al. (1991), using a laser slope instrument and reporting downwind component of surface slope, produced figures with an overall trend for HF energy to be stronger on the windward (rear) face of LF waves, although there was substantial scatter in the data. The overall trend discussed by Millar et al. (1991) was that HF wave energy was strongest at LF wave crests.

Field observations of the distribution of HF wave energy along the LF wave phase have typically been made in reference to a modulation transfer function (MTF) of radar backscatter measurements. Donelan et al. (2010) explained this to be composed of three

components; a tilt MTF for how LF wave slope affects measurements, a range MTF for variation in range caused by LF waves, and a hydrodynamic MTF related to the actual change in energy of HF waves. Hara and Plant (1994) grouped tilt and range MTF together under the umbrella of geometric effects. The isolation of hydrodynamic effects (altering of HF waves by LF waves) depends upon filtering out of geometric effects from the total MTF.

Smith (1986), when analysing the field data of Plant et al. (1983) recorded on the German NORDSEE platform using radar backscatter methods, observed HF wave energy to be strongest slightly forward (leeward) of the LF wave crest. Keller et al. (1994) measured the MTF from data taken from the same platform in the SAXON-FPN experiment (Plant and Alpers, 1994), and like Smith (1986), concluded both that the hydrodynamic MTF was detectable in this field data due to geometric effects not adequately accounting for the observed modulations, and that HF wave energy was strongest on the forward, leeward face of LF waves. Greco et al. (2004) measured modulation in backscatter energy intensity from HF waves along the phase of field LF waves, but provided little detail regarding the magnitude of modulation.

In summary, the majority of reports have observed HF wave intensity to be strongest on the leeward (forward) face of following LF waves, although this conclusion has not been unanimous. The report of Donelan et al. (2010) suggested the location of maximum HF energy may be partly dependent on the magnitude of wind forcing.

2.2.3 Opposing LF waves

Studies of the interaction between HF waves and LF waves opposing the wind are fewer than those for LF waves following the wind, with the majority of relevant observations seemingly originating from the one research group, although reported in multiple publications (Mitsuyasu and Yoshida, 1989; Mitsuyasu and Yoshida, 1991; Cheng and Mitsuyasu, 1992; Mitsuyasu and Yoshida, 2005). These experiments were performed using distributed wave gauges throughout an effective fetch of ca. 13m. In the results of Mitsuyasu and Yoshida (1991), as shown in Figure 2.13, the HF wave spectrum was observed to increase in peak height and decrease in peak frequency.

However, in the spectra published by Cheng and Mitsuyasu (1992), also for LF waves opposing wind, enhancement of HF waves was less obvious than what was displayed by Mitsuyasu and Yoshida (1991), and much less clear than the magnitude of suppression for LF waves following the wind reported in other studies (e.g. Mitsuyasu, 1966). The spectral peaks of HF waves in Figure 2.14 did not change significantly with opposing LF waves, but

energy increased at HF wave frequencies lower than the peak, as seen in Figure 2.14. Cheng & Mitsuyasu (1992) described this as the HF spectrum becoming wider, and it can be seen that this entails a downshift in average HF frequency. It must be kept in mind that any downshift in average HF wave frequency, though not increasing the energy density, will still increase the magnitude of energy flux passing through any given space.

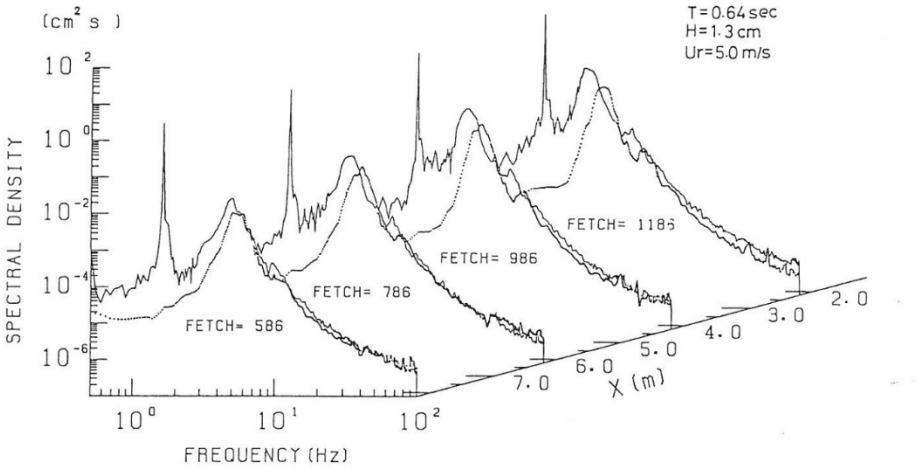

Figure 2.13: Figure from Mitsuyasu and Yoshida (1991), with the solid line representing spectral density with opposing paddle and wind, and dashed line representing pure wind-wave conditions.

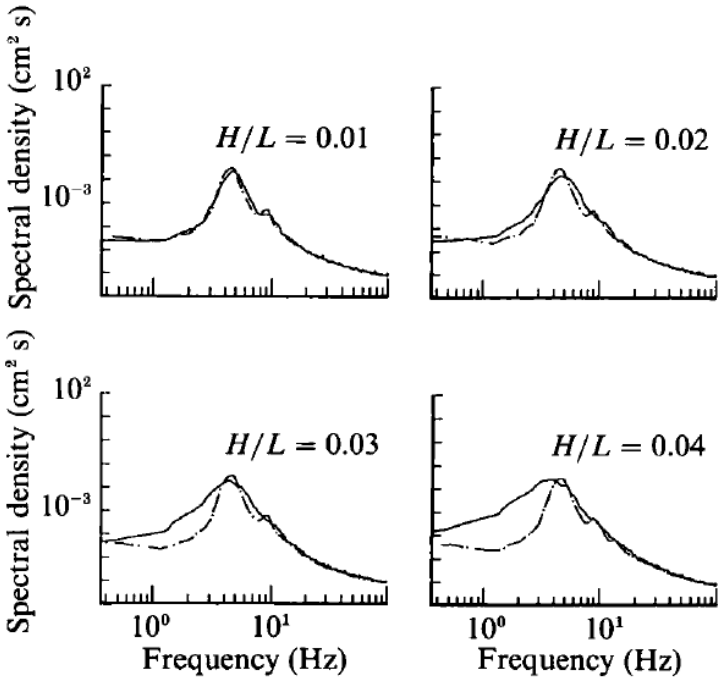

Figure 2.14: Figure from Cheng and Mitsuyasu (1992), with the solid line representing spectral density with paddle waves opposing the wind, and dashed line representing pure wind-wave conditions. Opposing waves of increasing steepness in these spectra exhibited an increased enhancement of HF wave energy over a broad range of frequencies, without increasing height of the spectral peak.

Consistent both in the spectra of Figure 2.13 and Figure 2.14 is the minimal lack of change to the forward, or equilibrium (Phillips, 1958) face of the spectrum, at all frequencies higher than the natural peak frequency of pure wind-waves. This is contrary to some laboratory observations of HF wave energy modulation by following LF waves, which suppress HF energy over a broader range of frequencies above and below the natural HF wave spectral peak, as seen in Figure 2.11, and also seen in measurements in the present study.

According to Figures 8 and 9 in Cheng and Mitsuyasu (1992), it also appears that both enhancement of HF waves with opposing LF waves and suppression with following LF waves, when normalised by the HF wave energy in absence of paddle waves, were stronger for lower wind velocities. This dependence was also stated by Donelan (2010). Mitsuyasu and Yoshida (2005) also observed the enhancement of HF energy to increase with steepness up to H_{LF}/L_{LF} ≈0.033, after which it decreased, as shown in Figure 2.15. Mitsuyasu and Yoshida (2005), after re-analysing data from the earlier experiments, again documented the observation that the spectrum was only marginally affected in the portion of the HF wave spectrum with frequency higher than the HF spectral peak.

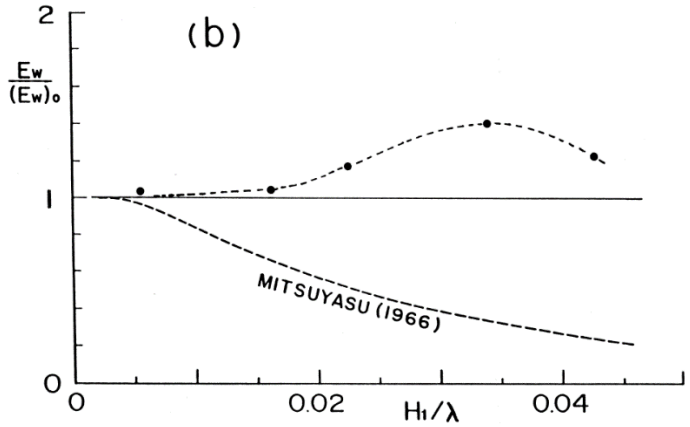

Figure 2.15: Figure from Mitsuyasu and Yoshida (2005), showing suppression ratios greater than one, meaning negative suppression or HF wave enhancement, in experiments with paddle waves opposing wind (dashes with solid circles). The experiments of Mitsuyasu (1966) (dashes only) where paddle waves followed the wind were included for reference.

Some other studies have been performed (e.g. Peirson et al., 2003; Donelan, 1999) with LF paddle waves opposing the wind, but which focused on measuring the attenuation of LF waves by the wind rather than the response of HF waves to opposing paddle waves. Therefore, the science of HF wave response to an opposing LF wave train is seemingly heavily dependent on experiments from the one facility, and more studies should be

performed to cross-validate these observations, and gain a clearer quantification of the mechanisms present when LF waves oppose the wind.

2.2.4 Other observations

Another source of possible generation of HF waves is mentioned here very briefly. Kelvin (1871) identified a mechanism of potential HF wave generation which may or may not be significant. The mechanism was summarised by Lighthill (1962) as follows – under very strong wind forcing, the strong positive pressures in wave troughs and negative pressures on crests can alter the dispersion relation, and can also reduce the stiffness of the water surface, destabilising the water surface to incite “disturbances of small wavelength”. Lighthill (1962) dismissed this mechanism, stating it to be of minor significance to wave evolution. However, an effect of this nature which could potentially generate affect HF waves should nonetheless be acknowledged in the present study.

One more observation should be included at this point, made by Reece (1978) concerning the behaviour of paddle wave harmonics as forced by wind. In some experiments performed in that study, the primary LF wave frequency did not change as acted upon by wind. The first higher harmonic was seen to increase in amplitude in the spectral plot, while the second higher harmonic was recorded to reduce in amplitude to the point of being smothered within the HF wave field. This inconsistent behaviour of harmonics is relevant to observations made in the present study, reported in Section 5.6.

Chapter 2 up to this point has discussed the prevalent observational studies which are relevant to HF and LF wave interaction. The next three sections of this chapter, being 2.2.5 to 2.2.7, discuss theories which have been proposed to explain suppression of HF waves by LF waves. It may be noticed that the three theories are each closely related to a specific and different oceanographic modelling source term. The greatly differing fundamental physics of each theory demonstrates the lack of consensus and understanding regarding the basic nature of the influence of LF waves on HF wave evolution.

2.2.5 Theories of enhanced dissipation

Phillips and Banner (1974) (hereafter denoted PB74 in this section only) acknowledged the rapid nature of HF wave suppression by LF waves, and argued that nonlinear interactions according to theories of the day (Hasselmann 1962) could not account for such an immediate effect. They proposed that the interaction is due to enhanced dissipation of the HF waves at LF wave crests.

PB74 referred to the Longuet-Higgins and Stewart (1960) (hereafter LH&S in this chapter only) mechanism of compression of short high frequency waves on the crest of much long waves, with HF wavelength reducing and amplitude increasing as a result of vertical accelerations altering the dispersion relation. The net effect is steepening of HF waves at LF wave crests. PB74 suggested that this mechanism outlined by LH&S would cause short waves to break preferentially near the crests, with the increased breaking limiting the mean amplitude of the HF waves.

PB74 also suggested that dissipation is enhanced by the interaction of the wind drift with the incipient HF waves. They drew upon observations by Wu (1968) of a thin wind drift layer with high vorticity, of magnitude approximately 3 – 4 % that of the 10m wind velocity. They suggested that this wind drift layer at the crest is faster relative to the HF wave celerity at the crest of LF waves, due to thickening of the drift layer and also due to convergence of HF waves at this location. The augmented wind drift, as termed by PB74 to represent the localised wind drift variation along the phase of the LF waves, was theorised at wave crests to be as much as 6 times the normal wind drift. Because breaking of any wave occurs when water particles near the crest reach a velocity equal to the wave celerity, causing stagnation, this increase in water velocities results in the HF waves at the crest breaking sooner, limiting the maximum amplitude of the HF waves.

Donelan (2001) proposed a slightly different variant of the enhanced dissipation theory, suggesting that HF waves steepening and preferential breaking occurs on the forward face of following LF waves, with reduced steepness on the rear face allowing enhanced growth. He suggested that the enhanced growth on the rear of waves is not as strong as the enhanced dissipation. He did not provide explanation or evidence as to why HF waves are thus modulated, but intuitively one may reason that convergence and divergence of the horizontal component of orbital velocities on the forward and rear face of waves respectively may result in compression and stretching horizontally of the HF waves at these locations.

Donelan (2001) attempted to quantify the observed enhanced dissipation of HF waves by including the mean surface slope (MSS) of the long wave as an additive factor in the dissipation source term. Donelan et al. (2010) again stated the view that suppression of HF waves by LF waves is due to enhanced dissipation, with the LF waves eliminating the peak enhancement of the HF wave spectrum, reducing the latter's peak to the level of a saturated HF tail.

As mentioned in Section 2.1.2 a “Cumulative Effect” of dissipation has been observed (Babanin and Young, 2005; Young and Babanin, 2006a), in that wave dissipation in the HF portion of the spectrum is affected by either the energy or the breaking near the spectral peak. This observation was made through classifying wave time segments to be either at or near the point of incipient breaking, or else having already broken, and observing the reduced spectral energy in the broken segments to be lower throughout the spectrum, not just near the spectral peak. This observation correlates HF wave dissipation with LF wave breaking, rather than simply the presence of LF waves. Babanin (2011, pp264-265) suggested the enhanced dissipation could be a result of some or all of the PB74 & LH&S mechanism of steepening and preferential HF waves breaking on LF wave crests, LF wave breaking events engulfing HF waves, or turbulence generated by LF wave breaking events interacting with HF wave orbital velocities, increasing turbulent dissipation. The former two of these three mechanisms depend on HF wave breaking, while the latter is related to the LF wave presence alone.

Wright (1976) re-examined the formulation of the PB74 mechanism of wind drift augmentation enhancing HF wave breaking, and challenged it quantitatively. Drawing on the measurements of Keller et al. (1974), he observed that HF waves broke at much higher wind velocities than predicted by PB74. Wright (1976) also referred to observations that the suppression effect is less prevalent at higher wind velocities than low wind velocities, and given that the theory depends heavily upon wind driven drift of the water surface, argued that this cast doubt on this theory. Peirson and Garcia (2008) suggest that the wind-speed related discrepancies pointed out by Wright (1976) may be due to a lack of HF wave coupling to the wind in the PB74 mechanism.

Cheng & Mitsuyasu (1992) measured wind drift with opposing paddle waves, and found drift to also be enhanced by opposing paddle waves, not just at the crest but averaged throughout the LF wave phase by as much as ca. 46% of its value for pure wind waves. The relationship in these conditions to LF wave steepness is presented in Figure 2.16. This observation, combined with observations of opposing LF waves enhancing HF waves, contradicts the idea that wind drift causes suppression. For paddle waves following the wind, they did not detect significant enhancement of the average surface drift, which observation (or lack thereof) also contradicts the PB74 theory of augmented wind drift at the crests of LF waves following the wind. Cheng & Mitsuyasu (1992) also followed the formulation of PB74 to calculate an expected augmented wind drift at the crest of paddle

waves following the wind of ca. 1.2x the mean wind drift throughout the phase, far less than the 6x multiple proposed by PB74.

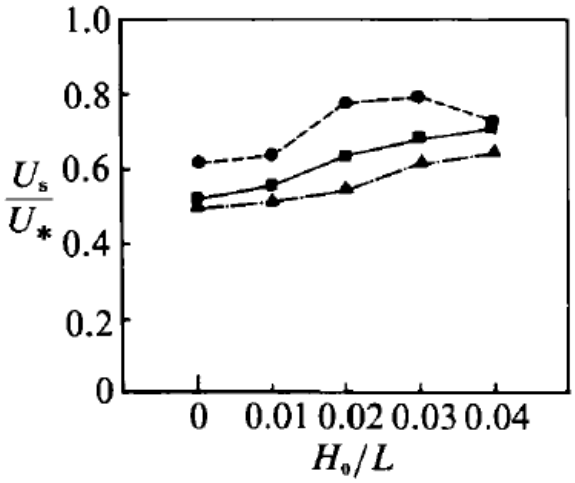

Figure 2.16: Figure from Cheng and Mitsuyasu (1992), with surface drift normalised by wind shear velocity plotted against opposing paddle wave steepness.

Cheng & Mitsuyasu (1992) also noted that the wind drift takes much longer to reach a stationary state than the HF waves. Smith (1986) made a similar observation, but expressed slightly differently, that the duration for wind drift to reach equilibrium was of the same order of magnitude as that for HF waves to reach equilibrium. If it could be proven that suppression takes place at a quicker time scale than typical HF wave evolution or wind drift evolution, this would cast doubt on the PB74 mechanism related to wind drift augmentation. Experimental results from the present study regarding the timescale of suppression onset are reported on in Section 5.3.

Mitsuyasu and Yoshida (2005) argued against the PB74 mechanism involving LH&S straining of HF waves, again because opposing LF waves were observed to enhance wind-wave development, given that the LH&S steepening of HF waves at LF wave crests which leads to their premature breaking and suppression occurs regardless of LF wave direction.

All of the above arguments do not discredit enhanced dissipation overall, but suggest that the mechanisms proposed by PB74 on their own do not adequately to explain all of the key interactions between HF waves and LF waves which cause such strong suppression in laboratories. The proposed suppression of HF waves related to LF breaking events (Babanin, 2011, pp264-265) or “Cumulative effect” may play a part, but if strong suppression can be proven to be present in complete absence of LF wave breaking, then some other major mechanics must also be involved. It is generally acknowledged that breaking dissipation, being always present to some degree in HF waves of low age C/u_*, plays an

important role in the evolution of HF waves and limit of the equilibrium range, but by exactly what physical process is yet to be confirmed, and whether or not enhancement of this dissipation is the dominant cause of HF wave suppression has not been proven.

One other study worth mentioning is that of Longuet-Higgins (1969), who theorised that strong dissipation of HF waves near LF wave crests imparts momentum into the LF waves, enhancing the latter's growth. While this mechanism does not state explicitly or in detail why HF wave breaking is enhanced by LF waves, it does argue that LF waves are capable of absorbing energy from breaking HF waves, which should be kept in mind during theoretical reasoning of HF wave suppression.

2.2.6 Theories of modified wind input

Some authors have hypothesised that HF waves are suppressed through LF waves modulating the wind field above waves. Mitsuyasu (2005) found that the wind shear stress increased marginally due to paddle waves opposing the wind, and attributed the small increase in HF wave energy in the presence of opposing paddle waves to this increased wind shear. However, those marginal changes reported cannot be considered adequate to account for a 75% reduction in HF wave energy when LF waves follow the wind, as observed by Mitsuyasu (1966).

Smith (1986) examined prevalent theories concerning HF and LF wave interactions available at that time, and argued that modified wind input was the only feasible mechanism, based on a model including wind drift, dissipation and wind shear modification, which was calibrated against data from Plant et al. (1983). However, the physical mechanism of how the wind shear modification exists was not explained clearly in this article. Four years later, the same author stated

> "beware of any who claim to have solved this problem: There remain too many ill-known or even unknown aspects of the total interaction of long and short surface [waves] and surface shear layers to hope for a final solution" (Smith, 1990).

Hara and Plant (1994) suggested multiple mechanisms for modulation of HF waves of varying wavelength. They concluded that very short HF waves with wavelength of order 0.02m or less are primarily suppressed by wind stress modulation, or reduced wind stress in troughs, whereas for HF waves of longer wavelength, modulation throughout the longer wave phase occurs by straining effects from LF wave orbital velocities. However, while

straining was concluded to affect longer HF waves, it was not clearly stated to actively suppress the average HF wave energy across the entire LF wave phase.

Kudryavtsev et al. (1997) and Kydryavtsev and Makin (2002) acknowledged that LF waves orbital velocities modify the wind velocity relative to the water surface along the LF wave phase, causing a variation of wind input into HF waves along the LF wave phase. However, these authors recognised that the magnitude of orbital velocities relative to typical wind velocities could not explain on its own the intense reduction of HF wave energy or even the magnitude of variation of HF wave energy along the LF wave phase, particularly at higher wind velocities, where the variation in wind velocity relative to LF wave phase speed is a lower proportion of the wind velocity. They proposed that the relatively small reduction in wind stress leads to a corresponding reduction of HF wave energy, which in turn provides feedback to the wind field to reduce wind stress further. A mutual feedback mechanism then occurs between wind stress and HF wave energy, exhibiting mutual amplification to result in a total reduction of both variables several times stronger than the initial reduction triggered by orbital velocities. Waves providing feedback to wind, or the coupling of waves to wind stress, is universally accepted and features in most theories whether explicitly stated or not (e.g. Jeffreys, 1925; Miles, 1957; Phillips, 1957). However, this feedback effect is generally considered to be always present (Jeffreys, 1925; Miles, 1957) and the idea that such a slight variation in orbital velocities, which are often much lower than 0.1xV_0, could result in a 75% reduction in HF wave energy (Mitsuyasu, 1966) seems fanciful, when naked-eye observations in the wind-wave flume during the current study suggest a 10% reduction in V_0 does not cause a 75% reduction in HF wave energy.

A more explicitly described theory related to modulation of the wind field is that of Chen and Belcher (2000), who focused on direct coupling between LF waves and wind. They segmented wind stress to be a summation of LF-wave-coherent eddies and turbulent stresses, as illustrated diagrammatically in Figure 2.17. Building on the assumption that LF wave coherent wind eddies reduce with elevation, reaching zero at no great height, with total wind stress to be constant with height, they implicitly assumed total wind stress to be constant regardless of the existence of LF waves. They argued that only the turbulent fluctuation component of wind stress is responsible for generation of HF waves, and as the component of wind stress coherent with LF waves increases, there is consequently less turbulent wind stress available near the wind water surface to feed HF waves, resulting in their growth being suppressed.

Such a concept is in harmony with the observations of Townsend (1980), who reported a decrease in ratio of Reynolds Stress to total turbulence intensity due to the presence of flow curvature, such as may be experienced over LF waves within the order of one wavelength. It is also generally understood that turbulent wind eddies coherent with the dominant wave become insignificant above a certain height, which height was observed by Longo and Losada (2012) to be $5 \times H_{rms}$.

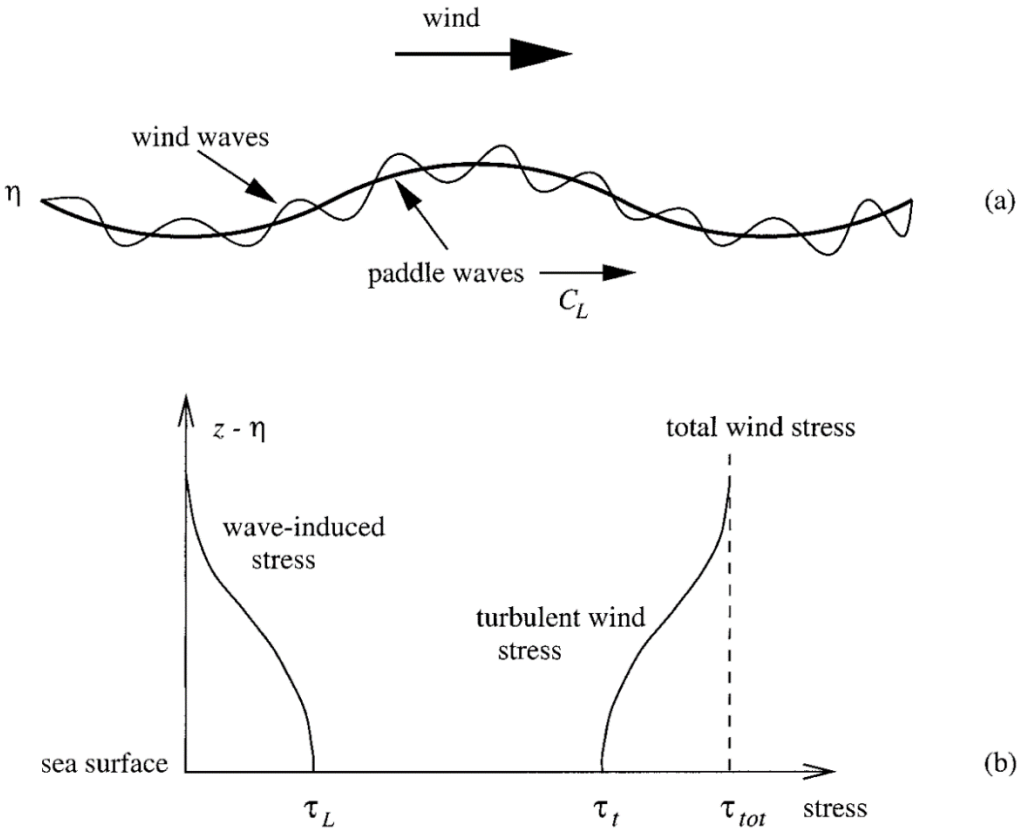

Figure 2.17: Figure from Chen and Belcher (2000) illustrating the decrease in wave coherent (wave-induced) stress with elevation. (a) represents the water surface consisting of LF and HF waves, while (b) depicts the mean wind field, at any point in space.

Wu (1977) also hypothesised that the LF waves concentrate wind input to the LF wave frequency. The Chen & Belcher (2000) theory can be supported to some degree by the laboratory observation of Wu (1977) that aerodynamic roughness length appears to decrease with the presence of LF waves, or rather, that the LF waves cause the water surface to be more aerodynamically smooth as felt by the wind, which would reduce overall momentum transfer. Wu (1977) suggested the possibility that this be due to the number of roughness elements per unit area of surface to decrease, but appeared to dispute this at the end of the article, settling on the hypothesis that roughness is reduced in the presence of LF waves by the suppression of HF waves.

The specific theory of Chen and Belcher (2000) can be challenged on several fronts. Observations of wind input by Donelan (1987) using a wave following pressure sensor suggested that wind input to the HF wave component of the wave spectrum wind-waves did not decrease in the presence of paddle waves. Donelan et al. (1997) observed up to a three-fold increase in wind stress when LF waves were present, although these were opposing the wind direction. The Chen and Belcher (2000) formulation depended on a simplification of very slow growth of LF waves in space, with the same author in Hara and Belcher (2002) clarifying a dependence on stationary and homogeneous conditions. However, in preliminary experiments performed in the UQ wind-wave flume, monochromatic paddle waves have been observed to triple in height within a fetch of less than 14m. The observations of enhancement of HF wave energy by opposing LF waves also contradicts this theory, which does not depend on LF wave orientation.

While some assumptions of the model proposed by Chen and Belcher (2000) appear to be questionable, this does not prove that modified wind input plays no part in suppression. Indeed, the simplified statement by Belcher (2001) indicating that wind stress coherent with and acting on LF waves removes turbulent wind stress available to input into HF waves, was more difficult to challenge, and is consistent with previously documented assertions of Townsend (1980) and Kudryavtsev et al. (1997) to this effect.

Perhaps the most relevant studies related to the role wind input plays in suppression of HF waves by LF waves is that of Donelan et al. (2006), who observed during the AUSWEX experiment (Donelan et al., 2005) that wind separates from the water surface at wave crests, resulting in a large portion of the water surface (the leeward face and trough of LF waves) not being exposed to the main wind stream. In addition to reducing the amount of water surface available to provide drag on the wind, this also reduces wind forcing of HF waves on the leeward face and trough. It stands to reason that wind separation of this nature likely plays some part in HF wave suppression, but whether this is of major or minor in significance is yet to be tested in the present experimental study.

One key aspect of theories related to modified wind input is that they focus upon HF waves being inhibited in their growth to an absence of wind input, and are not based upon a mechanism which destroys waves. The observations of Mitsuyasu (1966) suggest that the suppression of HF waves occurs quickly after the arrival of LF waves, which suggests the possibility that HF waves are actively broken down, rather than merely being inhibited in growth. More careful study of the time taken for HF waves to decay after the onset of LF wave arrival forms part of the present study.

2.2.7 Theories of direct coupling between wave components

Hasselmann (1963) built upon Hasselmann (1962) in its direct application to the evolution of wind-generated wave spectra. This included investigation of the interaction that occurs when a lower frequency wave train travels through a HF wave field. This study presented a decay factor for the LF wave that depends upon the angle between HF and LF wave directions, as well as the relative periods. It must be stressed that in this mechanism, energy was conserved. A loss in energy of one frequency equates to gains in other frequencies.

Masson (1993) applied this theory in reverse to investigate the effect a lower frequency wave train exerts on a HF wave field that it passes through, and found that in some combinations of angle difference and swell wave period, the decay is negative, and the LF wave train absorbs energy at the expense of the HF waves. The time scale was stated to be of the order of 5 minutes for laboratory LF waves to experience a four-fold increase in energy at the expense of HF waves.

Tamura et al. (2009) also suggested that under resonant conditions, LF waves and HF waves can experience nonlinear interaction according to the Hasselmann (1962) mechanism. They performed hindcasting of an event with suspected strong nonlinear interaction within a WAVEWATCH III model, with some alterations to the nonlinear source term as per Tamura et al. (2008), which they believed more accurately reflect the Hasselmann (1962) theory than the DIA. The wind sea in this study exhibited T_p in the order of 5s, with swell T_p between 8 and 10 seconds, exhibiting a ratio of 1.6 to 2.0 between the respective peak periods. Their model calculated strong interaction between HF and LF waves, with the timescale for significant interaction in the order of 1600 wave periods, which is considered shorter than typical Hasselmann (1962) interaction time scales. Nayak et al. (2013) supported the notion that nonlinear interactions were responsible for enhancement of HF waves by opposing LF swell, but this was based on an ocean modelling exercise without offering significant physical explanation for the interaction.

The time scales reported in the above studies cast significant doubt on the applicability of nonlinear interactions to suppression observed in relatively short wind-wave flumes. Badulin (2004) performed modelling with initially bimodal conditions, and suggested that nonlinear interactions may cause dual peaks to merge into a single peak within a duration of only dozens of wave periods. However, as acknowledged by Badulin (2004), even this is far too long to reconcile with the rapidity of suppression observed in laboratory experiments.

Chen and Belcher (2000) highlighted that nonlinear interactions between waves at different frequencies depends on proximity of the respective frequencies, being almost negligible between any two frequencies when the ratio of frequencies exceeds 1.6. Given that suppression affects a broad range of the spectrum extending much further than 1.6 times the paddle frequency, they argued that the Masson (1993) mechanism could not adequately explain suppression, a flaw which was also highlighted by Mitsuyasu (2015).

Another theory involving direct coupling between wave components to be mentioned was put forward by Miller et al. (1991), who argued that longer wave orbital velocities perform work against the radiation stress of the short waves, based on the mechanism of Longuet-Higgins and Stewart (1960). They derived a generalised equation for interaction between LF waves and a broad spectrum of HF waves which are assumed for simplicity not to interact with each other within the HF spectrum. However, Miller et al. (1991) did not explain clearly how the original mechanism, in which average HF energy along the LF wave phase is conserved, results in a permanent transfer of energy to LF waves.

It seems appropriate to include at this point the inferences of Imai et al. (1981), who concluded that the majority of interaction between HF and LF waves occurs near the crest of the LF waves. They suggested that as HF waves approach the LF wave crest, they accelerate due to increased wind forcing. They did not mention increased celerity due to LF wave orbital velocities. Given that LF waves are constantly overtaking HF waves, as HF waves increase in celerity, their duration riding at the top of the LF wave crest is extended, resulting in strong localised growth of the HF waves at the crest. Some excess HF energy is suggested to then be transferred between individual HF waves and to the LF wave, either at the LF wave crest or on its downwind face. Whether this is by HF wave dissipation or some kind of nonlinear wave-wave interaction is not specified. This study did not attempt to provide a complete theory, and does not shed light on any existing theories, but these inferences are documented here as they may play a part in the interaction.

2.2.8 Contemporary wave modelling relevant to HF and LF wave interaction

Currently the two leading ocean wave modelling tools are SWAN, short for Simulating Waves Nearshore (Booij et al., 1999), and WAVEWATCH III (Tolman, 1991; WAVEWATCH III Development Group, 2016). Both of these software tools contain source terms derived from the Wave Action Model (WAM) Cycle 3 (WAMDI Group, 1988) and Cycle 4 (Komen et al., 1994), which form the basis of commonly applied physics, although both models also feature optional alternative source terms. In this chapter, physics from the SWAN model relevant to interaction between HF and LF waves is examined, acknowledging that the

physics in SWAN and WAVEWATCH III is largely similar, as most prevalent source terms exist in both. Wind input and dissipation source terms are focused on, due to theories involving these source terms being more realistically likely to have relevance to suppression.

As discussed by Booij et al. (1999), the SWAN model accounts for both the mechanisms of Phillips (1957) and of Miles (1957), although exact implementation of both of these mechanisms is according to modified versions in later studies. The Phillips mechanism is formulated according to Cavaleri and Rizzoli (1981), with a filter according to Tolman (1992) which prevents growth in frequencies lower than the Pierson and Moskowitz (1964) frequency. In formulating the mechanism for exponential growth as first proposed by Miles (1957), two options are provided. One option is based on the WAM-3 model (Hasselmann et al., 1988), based on the model of Komen et al. (1984) who called on the growth rate results of Snyder et al. (1981), and the wind stress coefficients of (Wu, 1982). The other option is based on the WAM-4 model (Komen et al., 1994), including the work of Janssen (1991) to determine drag coefficient dynamically based on the wave field, using the numerical procedure of Mastenbroek et al. (1993).

In the years after SWAN was first introduced (Booij et al., 1999), the developers, Holthuijsen et al. (2000), acknowledged that their model lacks consideration of the effects of swell on wave growth, both of suppression with a following swell, and enhancement with opposing swell. They assumed that this effect is caused by an increase in whitecapping, and by surface straining near the swell crests. The SWAN white capping source term as summarised by Booij et al. (2001) calculated dissipation proportional to mean wave steepness, according to

$$S_{wc}(\sigma,\theta) = -C_{wc}\tilde{s}^4\frac{\tilde{\sigma}}{\tilde{k}}kE(\omega,\theta) \tag{2.16}$$

where $\tilde{s}$ is mean steepness of the entire spectrum, C_{wc} is an empirically obtained coefficient equal to 2.36×10^{-5}, $\tilde{\sigma}$ and $\tilde{k}$ are mean frequency and mean wave number respectively for the whole spectrum. However, because swell waves are less steep than wind-waves, the presence of swell reduces the mean steepness of the spectrum, which decreases white capping and consequently increases development of the wind-wave spectrum regardless of swell direction, contrary to observations. Holthuijsen et al. (2000) proposed a modification of the white capping dissipation term in SWAN to calculate white capping dissipation to be proportional to the mean steepness in the wind-wave part of the spectrum only, introducing $\tilde{s}_{hf}(\sigma)$ in the place of $\tilde{s}$. Holthuijsen et al. (2000) also suggested

an empirical straining function be added to further suppress HF waves, to account for increased white capping dissipation caused by straining of the surface at the wave crests.

The final modified whitecapping formulation as documented in Booij et al. (2001) is

$$S_{wc}(\omega,\theta) = -f(\beta)C_{wc}\tilde{s}_{HF}{}^{4}\frac{\tilde{\sigma}_{HF}}{\tilde{k}_{HF}}kE(\omega,\theta) \tag{2.17}$$

where $S_{wc}(\omega,\theta)$ is the white capping dissipation source term,

$$f(\beta) = (\beta-1)^2 + 1 \quad or \quad 1 \tag{2.18}$$

whichever is greater, and

$$\beta = \frac{\tilde{S}_{HF}}{\tilde{S}} \tag{2.19}$$

where $\tilde{s}_{HF}$, $\tilde{\sigma}_{HF}$ and $\tilde{k}_{HF}$ are the high frequency values, determined for each wave component (ω,θ) as the mean across all frequencies exceeding ω. $f(\beta)$ is the straining function, determined for each wave component, which further suppresses HF waves, but does not differentiate swell direction. The straining function is a numeric factor which increases whitecapping in almost all frequencies, with a maximum at the highest frequencies, gradually reducing to

$$\beta = \frac{\tilde{S}_{HF}}{\tilde{S}} = 1 \tag{2.20}$$

at the lowest frequency, equating to no alteration to the original source term. The extent to which this represents the physics of HF wave suppression by LF waves is that any energy in lower frequency waves, with lower steepness than any waves higher in frequencies, will increase whitecapping dissipation in all higher frequencies.

Booij et al. (2001) further suggested a couple of corrections to the WAM wind input formulation, based on statements by Mitsuyasu and Yoshida (1989) that HF wind-waves are more exposed to the wind near crests of the swell than in troughs. Booij et al. (2001) suggested that when combined with longer residence time at crests with opposing swell, and shorter residence time at crests for following swell, this would enhance growth of wind-waves. They consequently experimented with two changes to the exponential wind input in WAM-III (WAMDI group 1988), which as previously mentioned, is also used in SWAN. The first change was to replace the friction velocity with an apparent friction velocity, taking into account wind velocity minus a fraction of swell orbital velocity at each wave frequency. The

second change was to scale the wind input with the ratio of the orbital velocity over the phase speed of the wave at that frequency.

The original WAM-III term for wind input, as expressed by Booij et al. (2001), is

$$S_{wind} = 0.25\frac{\rho_{air}}{\rho_{water}}\left[\frac{28U_*}{C_{phase}}\cos(\theta - \theta_{wind}) - 1\right]\omega E(\omega,\theta), \tag{2.21}$$

where U_* is calculated by

$$U_*^2 = C_D U_{10}^2, \tag{2.22}$$

in WAM Cycle 3 formulation where C_D is obtained empirically from measurements, or through a more complex set of equations if using the WAM Cycle 4 formulation (see The-SWAN-Team, 2018). If using the WAM Cycle 4 formulation, drag coefficient does depend on the wave field, which in turn is used for calculation of wind input at all frequencies. It should be noted that by this process, energy in some wave frequencies could be considered to be coupled to wind input in other wave frequencies, but not in a manner which would actively reduce wind input to the HF portion of the spectrum only.

The modified expression for exponential growth dependent on the wave field, suggested by Booij et al. (2001), was

$$S_{wind} = 0.25\frac{\rho_{air}}{\rho_{water}}\left(1 + \alpha\frac{\widetilde{\omega}_{LF}\sqrt{m_{LF}}}{C_{phase}}\right)\left[\frac{28U'_*}{C_{phase}}\cos(\theta - \theta_{wind}) - 1\right]\omega E(\omega,\theta) \tag{2.23}$$

where $\widetilde{\omega}_{LF}$ is the mean of the frequencies lower than ω, and m_{LF} is the variance of those frequencies. The differences, as outlined above, are the factor

$$\left(1 + \alpha\frac{\widetilde{\omega}_{LF}\sqrt{m_{LF}}}{C_{phase}}\right), \tag{2.24}$$

and the new apparent wind velocity, U'_*.

The combination of the white capping dissipation and wind input modifications were reported by Booij et al. (2001) to enable SWAN to achieve a better match to measurements of Donelan (1987), Mitsuyasu and Yoshida (1989) and JONSWAP (Hasselmann et al., 1973). However, it was acknowledged that this modification must be validated by comparison against more experimental data before it is implemented in the official version of SWAN. While physics has evolved slightly in the current WAM-based implementation of SWAN, version 41.20A in 2018, it does not include this wind input correction, nor does it include the suggested white capping alterations (The-SWAN-team, 2018). Although these modifications reduced the incorrect enhancement of the wind-wave spectrum by swell, and

had a suppressing effect of the wind-wave field overall, they did not provide a physics-based explanation for suppression or enhancement of wind-wave spectral development. Rather, they proposed removal of an existing coupling that was causing LF waves to enhance HF waves, and added a convenient numerical term to increase dissipation due to the presence of any lower-steepness energy in lower frequencies.

The previously mentioned “ST6” source term package (Rogers et al., 2012; Zieger et al., 2015), is one of the alternatives to the WAM-based source terms, featuring in both SWAN and WAVEWATCH III and containing alternatives for both wind input and dissipation source terms. It was developed based on the Lake George experiments of Donelan et al. (2005), and the subsequent studies of Babanin and Young (2005), Young and Babanin (2006a), Young and Babanin (2006b) and Donelan et al. (2006), which were discussed in Sections 2.1.1 and 2.2.5. Wind input in this source term package accounts for airflow separation at wave crests at strong wind velocities, and the closely related nonlinearity encountered in extreme wind velocities, when wind shear stress reaches a limiting maximum. The wave breaking source term has been designed as a two-phase equation featuring a cumulative term, whereby dissipation at LF results in energy loss throughout the spectrum. A threshold value has also been applied to dissipation, whereby if energy in a given frequency is below the threshold, zero breaking dissipation occurs. Very slow non-breaking viscous dissipation is also accounted for, which was noted in Section 2.1.2 to be the only deep-water dissipation source available for swell waves of low steepness. The “ST6” equations are excluded from this thesis for brevity, but are found in Rogers et al., (2012) and Zieger et al., (2015). This empirically-based source term package’s accounting for wind separation, as well as the cumulative effect, do account in part for HF wave suppression by LF waves. However, this source term package has not yet been trialled and tested for as long as the WAM-based source terms, and to the writer’s knowledge does not feature in operational ocean forecast modelling. Some recent testing by Violante-Carvalho et al. (2017) found it to return results comparable in accuracy to the WAM-based source terms.

In summary, the most prevalently used source terms in state-of-the-art oceanic modelling contain no allowance for inter-frequency interaction apart from:

a) the wind stress term, which is constant across entire wave spectrum at each grid point in 2D space and time, and
b) the NL4 nonlinear interaction term, which operates on far longer timescales than what is present in laboratory conditions and which is ineffective for wave components not local in the frequency domain.

The new observation-based source term “ST6” should in part account in part for HF wave suppression by LF waves, but is largely empirically-based, has not yet been proven to be universally more accurate than WAM-based source terms, and does not extensively explain how HF waves are suppressed by LF waves.

2.3 Summary, research questions and plan

In this literature review, it has been established that the suppression of HF waves in the presence of LF waves is clearly visible and measurable in laboratory wind-wave flumes. This effect has not been as conclusively measured in field conditions, likely due to the lower LF wave steepness when compared to laboratory LF wave steepness, and also due to the lack of direct control over ocean conditions making it difficult to obtain measurements of HF wave growth both with strong LF waves, and with absolutely no LF waves, for comparison. While the presence of a hydrodynamic modulation transfer function (MTF) has long been acknowledged in the ocean, the quantification of this relies heavily on data processing methods to filter out the multiple geometric MTF effects, and this has also resulted in difficulty pinpointing occurrences of strong suppression in field conditions. Theories have been proposed to explain suppression of HF waves by LF waves based on all three major mechanisms of deep-water wave evolution, being wind input, dissipation and transfer of energy between frequencies by nonlinear interactions.

The first theory or school of thought was that of HF wave dissipation being enhanced at the crests of LF waves, which was first discussed by Phillips and Banner (1974). One suggested cause for enhanced dissipation involved Longuet-Higgins and Stewart (1960) steepening of HF waves at LF wave crests (Phillips and Banner, 1974; Babanin, 2011, pp264-265), which is challenged by observations of enhanced HF wave energy with opposing LF waves (Cheng and Mitsuyasu, 1992). Another suggested cause is augmented wind drift at LF wave crests leading to earlier breaking at crests (Phillips and Banner, 1974), which was challenged quantitatively by comparison against measurements, indicating this effect was too small in magnitude (Wright, 1976; Cheng and Mitsuyasu, 1992), and by observations that opposing LF waves also enhanced wind drift, which should indicate LF waves also suppress HF waves, which is contrary to observation. Two other proposed mechanisms are the engulfing of HF waves by LF wave breakers, and increased turbulent dissipation of HF waves by LF-breaker-induced turbulence (Babanin, 2011, pp264-265). Both of these latter mechanisms would be expected to suppress HF waves regardless of LF wave direction, which is contrary to observations of Cheng and Mitsuyasu (1992) and Mitsuyasu and Yoshida (2005). They also both depend on LF wave breaking, which limits

their range of applicability. The above counter arguments to each proposed mechanism do not prohibit dissipation playing a major part in suppression, but suggest that further investigation and explanation is needed.

Another prevalent school of thought is that of wind input to the HF waves being altered by the LF waves, or wind input being preferentially absorbed by the latter, with the most developed theory being that of Chen and Belcher (2000). However, like most suppression theories mentioned in this thesis, the Chen and Belcher (2000) mechanism fails to explain how HF waves are enhanced by opposing LF waves, given that the wind field effects outlined in Section 2.2.6 should be present regardless of LF wave orientation. Some of the implicit mathematical assumptions of this theory involving wind stress being constant with or without LF waves, and the assumption of stationary conditions, may also be easily questioned. It seems logical that the observation by Donelan et al. (2006) of complete wind separation at LF wave crests reducing wind stress, could contribute to HF wave suppression, with part of the water surface in the separated zone, leeward of LF wave crests and in the trough, being sheltered from wind input. However, for this to be the primary suppression mechanism one would expect negligible suppression where no wind separation occurs, transitioning suddenly to strong suppression after the separation threshold is reached. This would be manifest in a strong discontinuity in the relationship of HF wave suppression versus LF wave steepness and wind velocity. No such nonlinearity of suppression has been documented in literature. In addition, this effect is constrained to act on a time scale comparable to the time taken for a HF wave field to evolve, which time scale might be longer than that of suppression. Separation and modified wind input likely contributes to the overall mechanics of suppression, but to exactly what degree, whether major or minor, is yet to be tested.

The other school of thought explaining suppression of HF waves by LF waves is that of direct coupling and transfer of energy from HF waves to LF waves by nonlinear interactions, as suggested by Miller et al. (1991) and Masson (1993). These theories in their current form do not come close to explaining the strength and rapidity of the interaction as observed by Mitsuyasu (1966) and in several other experimental studies.

No theory exists which comprehensively and unquestionably explains the cause for HF wave suppression by LF waves. Given the fact that theories exist which involve fundamentally different physics, without a general consensus of which source term is most significant, and given that wave modelling source terms in production use do not account for this interaction in any way, it must be clear even to the most casual observer that suppression of HF waves by LF waves is far from satisfactorily understood. The question

as to which of the three source terms is most responsible for suppression of HF waves has yet to be conclusively answered. Of the proposed theories, all have components which may be challenged. The aim of the present study is to gain further insight towards explaining the underlying physics of the mechanism. The primary methodology used for this research is laboratory experimentation, supplemented by a field experiment. Five issues in particular are considered.

1. Suppression by destruction or inhibited growth

One basic point not agreed upon or even frequently discussed is that of whether LF waves actively destroy HF waves, or whether they only suppress the growth of HF waves. Proving that LF waves actively destroy HF waves would favour enhanced dissipation as a mechanism, and cast doubt on mechanisms which rely on LF waves only preventing HF waves from evolving, (e.g. Chen and Belcher, 2000). To address this, a laboratory experiment was designed to obtain clear high-resolution data on the temporal transition from wind-only (WO) conditions to wind + paddle (W+P) conditions. In the present study, identical transition sequences were repeated 186 times and averaged to provide a smooth LF wave signal and measure of average HF wave intensity at very granular and fine time scales after the onset of paddle waves. This was compared against the duration required for pure wind-waves to evolve from a quiescent state. Mitsuyasu (1966) provided some observations of this, but at only one relatively short fetch, for one time series and without comparison against the growth duration of pure wind-waves. If a careful study of transition times indicates HF waves are suppressed far quicker than they evolve, this would support HF waves being actively erased by LF waves to be the dominant mechanism, as opposed to inhibited wind input into HF waves. Observations of rapid suppression onset would also further disqualify theories involving nonlinear interactions transferring energy directly from HF waves to LF waves, a mechanism which theoretically occurs more slowly than either wind input or dissipation.

2. Suppression by LF wave breakers

As previously discussed, two of the suggested mechanisms involving enhanced dissipation depend on breaking of LF waves rather than the presence only of LF waves, these mechanisms being the engulfing of HF waves by LF wave breakers, and increased LF-breaker-induced turbulence (see Babanin, 2011, pp264-265). One shortfall of many past studies on this topic is the minimal documentation of paddle wave breaking during experiments. While sonic instrumentation was not deployed in the current experiment,

paddle wave breaking probability was quantified through the analysis of wave gauge data. If suppression effects are strong in the complete absence of paddle wave breaking, this must prove that suppression at least does not depend on LF wave breaking. Alternately, if a strong correlation with LF wave breaking could be identified, this would support the mechanisms dependent on LF wave breaking. Such correlation should appear as a discontinuity or nonlinearity in the measured dependence of suppression versus LF wave breaking, which was examined in the current study.

3. Suppression by wind separation

It was previously acknowledged that wind separation at crests, observed previously to decrease wind shear stress, likely plays a part in HF wave suppression by LF waves, but it remains to be tested whether this is primary or secondary in nature. If suppression is negligible in the absence of probable wind separation, and steadily increases once wind separation commences, this would indicate separation plays a major part in suppression. Measurements of suppression were consequently compared against a wave steepness – wind velocity factor slightly modified from that used by Donelan et al. (2006), and an attempt was made to identify the presence of a discontinuity in this relationship.

4. Suppression by non-linear interaction

Theories dependent upon nonlinear interactions to induce suppression have already been severely challenged in this thesis. Hasselmann (1962) type interactions typically depend on a continuous flow of energy through the frequency spectrum, rather than energy jumping across portions of the spectrum. If cases could be found in which HF waves were substantially suppressed but which remain far isolated from paddle waves in frequency space, with portions of the spectrum containing minimal energy in between, this isolation between HF and LF wave energy would further discredit theories dependent on these nonlinear interactions.

Laboratory methodology for questions 1, 2, 3 & 4

Many past laboratory experiments focused on the interaction between HF and LF waves have deployed sophisticated equipment at single or limited fetches, and with limited wind or paddle conditions. Such instruments have included laser slope gauges and radar backscatter devices, each of which have their advantages. In the present study, in order to search for the above-mentioned discontinuities in suppression versus wind separation and suppression versus LF wave breaking probability, it was decided to measure suppression with a broader range of wind velocities, paddle wave conditions and fetches than has been

published in most past studies. It was necessary to ensure at least some experiments were performed with and without both LF wave breaking and wind separation, to examine trends in these relationships (to address Topics 2 and 3 listed above), and it was hoped also that cases could be found in which LF energy was isolated in the frequency domain from HF wind energy (Topic 4 listed above). It was also hoped that accurate measurement of HF and LF wave energy throughout the flume in a broad variety of conditions may facilitate other useful but unexpected insights and comparisons.

To achieve this, the experimental study was performed in a laboratory wind-wave flume with a broad array of precisely synchronised wave gauges, enabling examination of wave conditions in all parts of the flume concurrently. In the major laboratory experiment in the present study, twenty-four resistance type wave gauges were deployed throughout the flume's fetch. This approach is not dissimilar to that of Mitsuyasu and Yoshida (2005), but in the present experiment paddle waves follow the wind, which conditions are more frequently encountered in ocean wind-wave fields. Twin wave gauge arrangements were installed at many fetches in an attempt to track individual HF waves and determine celerity for some wave components, in a similar physical arrangement to Imai et al. (1981). The installation of closely spaced wave gauge pairs also made possible monitoring of reflection from the absorbing beach using the method of Baldock & Simmons (1999).

While observations of the spatial distribution of HF energy along the LF waves have been carried out previously, this analysis was also included in the current research, with a goal of both confirming past observations, and obtaining a higher resolution picture of the distribution than has previously been obtained. As previously documented, attempts to perform the challenging task of tracking individual waves between pairs of wave gauges are relatively few (e.g. Imai et al., 1981), and this was also attempted in the present study.

5. Suppression in the field

Another gap in the literature is in direct field measurements focused on this interaction between HF and LF waves, as discussed in Section 2.3. While the significance of suppression in laboratory wind-wave flumes with monochromatic LF waves is beyond doubt, the question remains as to how significant these effects are in the field. Some past field experiments (e.g. Plant et al., 1983; Smith, 1986; Keller et al., 1994) related to HF and LF wave interaction have been carried out using radar backscatter methods to measure HF wave intensity rather than the actual HF wave time series, while others examined buoy data (e.g. Violante-Carvalho et al., 2004) which severely truncates the range of HF frequencies

measurable. In an attempt to identify suppression in nature, a field experiment was performed in a fetch-limited coastal lake, using a point wave gauge to measure HF and LF waves, synchronised with wind anemometers and other instruments. Some of the aspects of this experiment (e.g. measurement of water velocities) are not reported on in depth in this thesis, but the measurements relevant to HF and LF wave interaction, including comparison of HF wave energy and growth as a function of varying pre-existing LF wave conditions, has been documented and discussed.

Summary

The HF portion of the spectrum is widely accepted to govern wind stress, which influences the growth of wind-waves throughout the entire spectrum. Given that HF and LF wave interaction is not adequately explained by any known mechanism, and knowing that wind-wave interaction remains a topic with much room for improved understanding, gaining greater understanding of LF and HF wave interaction through the present research was hoped to be fruitful not only for improved prediction of HF wave energy and wind stress, but also for improved understanding of wind-wave physics generally.

3 Setup of laboratory experiment

This chapter details the setup of laboratory experimentation in the present study, with the setup of field experimentation detailed in Chapter 4. There were two primary batches of laboratory experiments performed in the study, the first one taking place in winter 2015 and the latter in winter 2016. These two batches of experimental cases shall be referred to as LAB2015 and LAB2016 respectively from here on.

Much of the physical configuration was unchanged through these two batches, with any variation between the two batches noted specifically within this chapter. These two main batches do not include the numerous test cases performed as part of the design and testing of the flume physical and instrumentation setup, and for planning of experimental cases. It shall be apparent upon reading this chapter that LAB2016 was performed with some refinements over LAB2015, due to application of lessons learnt during earlier experimentation. For example, the mean water level in the flume was allowed to fluctuate within a range of ca. 25mm in LAB2015, but was rigidly controlled within ca. 3 mm in LAB2016. The results of both datasets were considered of value in identifying the presence of suppression, but analysis included in this thesis has focused on LAB2016.

3.1 Physical set up

3.1.1 Locality and Time

The University of Queensland is located in Brisbane Australia at latitude -27.499° and longitude 153.015°. The Advanced Engineering Building which houses the Civil Engineering Hydraulics Lab is stationed is built within 500m horizontally of the Brisbane River, at an elevation not more than 20m above sea level. The Civil Engineering Hydraulics lab sits in the basement level of this building, and this fact, combined with the large volumes of stored water in the lab, helped dampen air and water temperature fluctuations during experiments. Both LAB2015 and LAB2016 were carried out during Brisbane's cooler months, with the large batch of LAB2015 commencing 18th May and running for ca. 1 month, and the large batch of LAB2016 commencing mid-June and running for ca. 2 months. These durations do not include experimental setup. Water temperature in the flume was measured frequently during LAB2016, and found to be consistently within the range of ca. 18 to 20 °C. Air temperature was typically 0 – 2 °C higher than the temperature of the water.

3.1.2 Wind-wave flume

The University of Queensland hydraulics laboratory houses three 24m long water wave flumes, one of which has an internal breadth of 0.8m and internal height of 1.0m. Walls of the flume were constructed with glass throughout the test section, which may be treated as a hydraulically smooth surface. The bed was constructed from compressed fibre sheeting coated with a waterproof membrane, which was visually estimated to have a roughness height in the order of k_s of 0.01mm, based on the k_s value for rubber published by White (2011, p371). In order to reduce impact on flume water velocities by the end effects (see Nielsen and You, 1996), rubber matting with roughness height of ca 20mm was installed throughout and extending beyond the test section of the flume. The layouts for LAB2015 and LAB2016 are illustrated in Figure 3.1 (a) and (b).

(a) LAB2015 arrangement

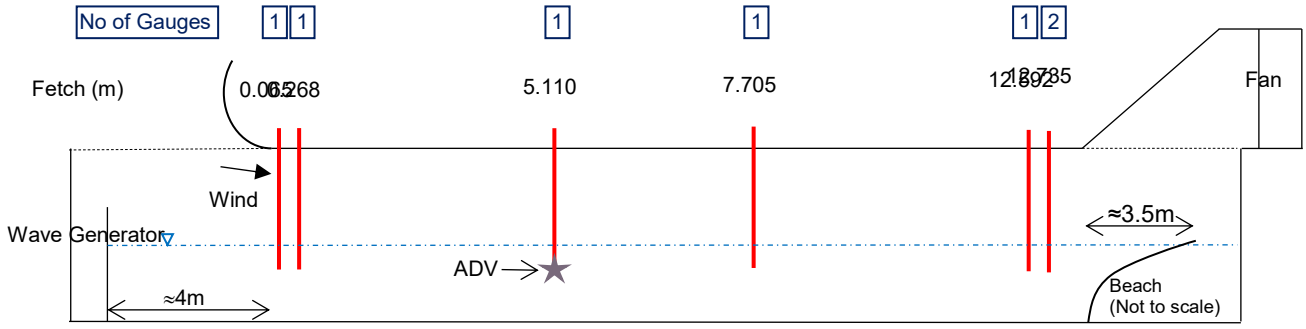

(b) LAB2016 arrangement

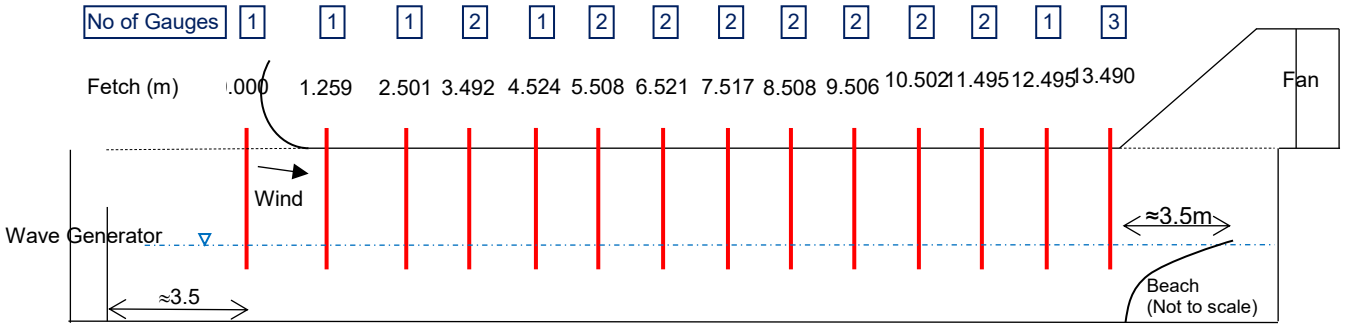

Figure 3.1: Wind wave flume arrangements for LAB2015 and LAB2016. Red vertical bars represent wave gauge stations, with fetch (m) and number of gauges (1, 2 or 3) printed above each station. In LAB2015 an ADV was deployed as illustrated. Measurements from this ADV are not documented in this thesis, but this ADV instrument in this flume was used by Olfateh et al. (2017), although with slightly different positioning.

Throughout most experiments, paddle waves were observed to be uniform without significant cross-tank variation for the majority of cases. In a minority of cases with steep

paddle waves and moderate to strong wind, breaking paddle wave crests were observed to not be perfectly perpendicular to the direction of propagation. In cases with paddle wave periods less than 0.8s and with moderate to large H_{pad}, paddle waves were observed to resonate with the width of the flume, causing cross-tank instability. Once instigated, this instability was reinforced by the paddle, and grew continuously and violently until cross-tank wave crests approached the ceiling of the flume, requiring the experiment be stopped. Once this instability was observed early during LAB2015, cases of short T_{pad} were excluded from later experiments, and from results.

3.1.3 Wave generation

A DHI rigid flat piston-type wave generator with frontal area filling the entire flume cross-section was situated at the upwind end of the flume, with a maximum stroke of 1.5m and maximum velocity of 0.8m/s. This generator was capable of producing Pierson-Moskowitz or JONSWAP spectra, solitary waves, monochromatic waves of frequency up to 2Hz, user defined spectra and user defined time series'. The wave generator also possesses optional active absorption capability, which uses wave probes fixed to the face of the paddle to modify the generator signal in order to reduce reflection back into the flume of waves incident to the face of the generator (which likely originated as reflection from the beach at the opposite end of the flume. It is impossible with current technology to absorb all incoming waves with such a system, and the effectiveness of the generator's active absorption capacity is difficult to quantify in isolation, given the continuous presence of reflection at the opposite end of the flume and minor dissipation along the flume. It was determined to run experiments documented in this thesis with active wave absorption enabled, to minimise build-up of reflected waves as much as possible.

In both LAB2015 and 2016, a distance of 3.5m or more extended between the wave generator and the wind inlet, allowing paddle waves to fully develop before being first measured and acted upon by wind. In light of the assertion by Shemdin and Hsu (1967) that a development length of 3 times the water depth was required prior to wind forcing, this distance, being 8 or more times the water depth, was considered more than adequate to allow waves to develop.

3.1.4 Wind fan

A 7.5kW 1m diameter axial flow turbine fan was installed at the outlet of the wind-wave tank (downstream, downwind end) as shown in Figure 3.3, with a variable frequency control system and a maximum fan frequency of 50Hz. At full capacity with a water depth of approximately 0.43m and a wind depth of 0.58m, this fan was capable of generating

maximum wind velocities in the order of 15-17m/s, depending on the length of the experimental volume, and quantity of equipment deployment in the wind stream. Many past laboratory studies of wind-wave interaction have been carried out at wind velocities less than this (e.g. Buckley and Veron, 2010; Kato and Tsuruya 1978; Plant and Wright, 1977; Wu, 1968). Some past experiments have been carried out with comparable maximum wind velocity (e.g. Duncan et al., 1974), and some at wind velocities up to 20m/s (e.g. Mitsuyasu, 1966), however the maximum wind velocity available in the present study was considered at least adequate to not be less than the majority of past studies. Setting the fan at maximum power in the present study was observed to be strong enough to generate substantial spray and possibly some ripping off of wave crests (Babanin, 2011, p11), and no stronger wind was desired for this study of HF wave and LF wave interaction.

Figure 3.3: Photograph of the wind fan at the downwind end of the flume.

The fan was positioned at the downwind end of the flume to minimise fan induced turbulence in the experimental control volume. This is consistent with some past experiments (e.g. Banner and Melville, 1976; Miller et al., 1991; Donelan et al., 2010), although many (e.g. Mitsuyasu, 1966; Keller and Wright, 1975; Wu, 1977; Hatori et al., 1981; Imai et al., 1981; Mitsuyasu and Yoshida, 2005) positioned the wind fan at an upwind location, and some (e.g. Donelan et al., 1987) used a closed recirculating wind tunnel. A closed wind tunnel was not feasible in the present experiment due to physical constraints, and this limited any wind measurement techniques requiring wind seeding or excessive smoke generation.

3.1.5 Wind containment

Prior to the experiments reported in this thesis, this flume was open on top with no wind containment. Conversion into a closed wind tunnel was performed by laying clear acrylic sheeting across the top of the flume, the transparency of which facilitated lighting and visibility of the experimental volume. These sheets were 12mm thick, and were reinforced with steel equal angles to ensure rigidity and reduce vibration. A longitudinal foam gasket was installed between the acrylic sheeting and the top of each of the flume walls. The sheets as supplied by the manufacturer had smooth clean edges, and when multiple uncut sheets were butted up to each other end-to-end, no visible air gap existed and this was considered adequate to prevent significant inflow. Where any joins in the acrylic were not smooth, due to modifications made for instrumentation, foam gaskets were installed to fill the joins. This acrylic covered the length of the measurement volume, which was ca. 13m, varying slightly between LAB2015 and LAB2016. At the inlet and exit points of wind flow, sheet metal contraction and expansion shrouds were installed, in an attempt to streamline the flow and remove sharp edges, minimising unnatural turbulence within the control volume.

Most wind-wave laboratory experiments in past studies have of necessity been designed with a change in wind direction to some degree immediately upwind of the fetch, to direct the airflow down to the water surface (e.g. Mitsuyasu, 1966; Mitsuyasu and Yoshida, 2005; Shemdin and Hsu, 1967). There are a few exceptions, for example Caulliez and Guerin (2012), but such experiments often had limited capability to generate paddle waves. The curved inlet in the present study acted somewhat like a pipe bend with the shearing of wind resulting in large vortex cells, the presence of which was verified using smoke seeding as shown in Figure 3.4.

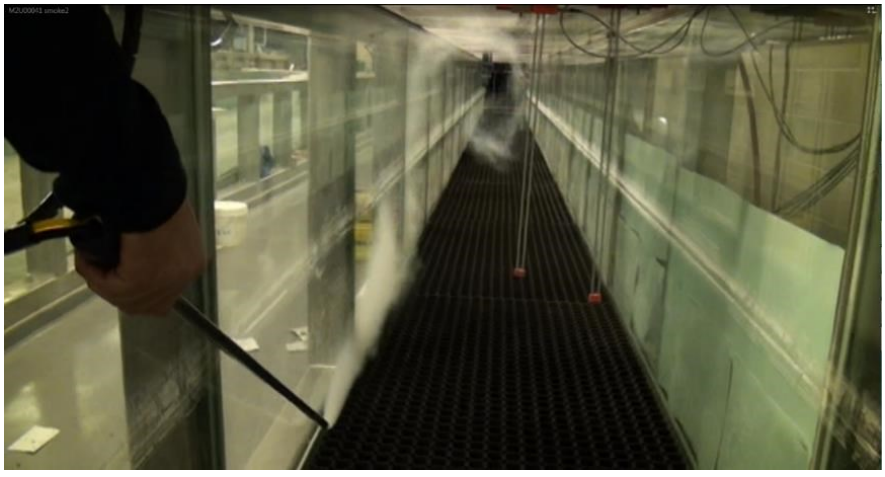

Figure 3.4: Smoke visualisation of secondary circulation cells, with smoke stream generated at the inlet. While no water was present when this photograph was taken, the effect was observed both with and without water.

The inlet bend was also believed to be responsible for wind velocity profiles measured near the inlet which did not increase with elevation above the mean water surface logarithmically as expected, but instead decreased with elevation as illustrated in Figure 3.5 (a). The profile taken at the downwind end of the flume in Figure 3.5 (b), being closer to what was expected, demonstrated that at increasing fetches this inlet effect had at least been partially overcome, but the boundary layer was not assumed to have fully developed anywhere within the experimental volume, given the length of the test section was only ca. 16-24 times the wind hydraulic diameter. This, combined with the strong wind circulation cells, resulted in a lack of confidence to obtain reliable friction velocity readings through the conventional method of measuring vertical velocity profiles.

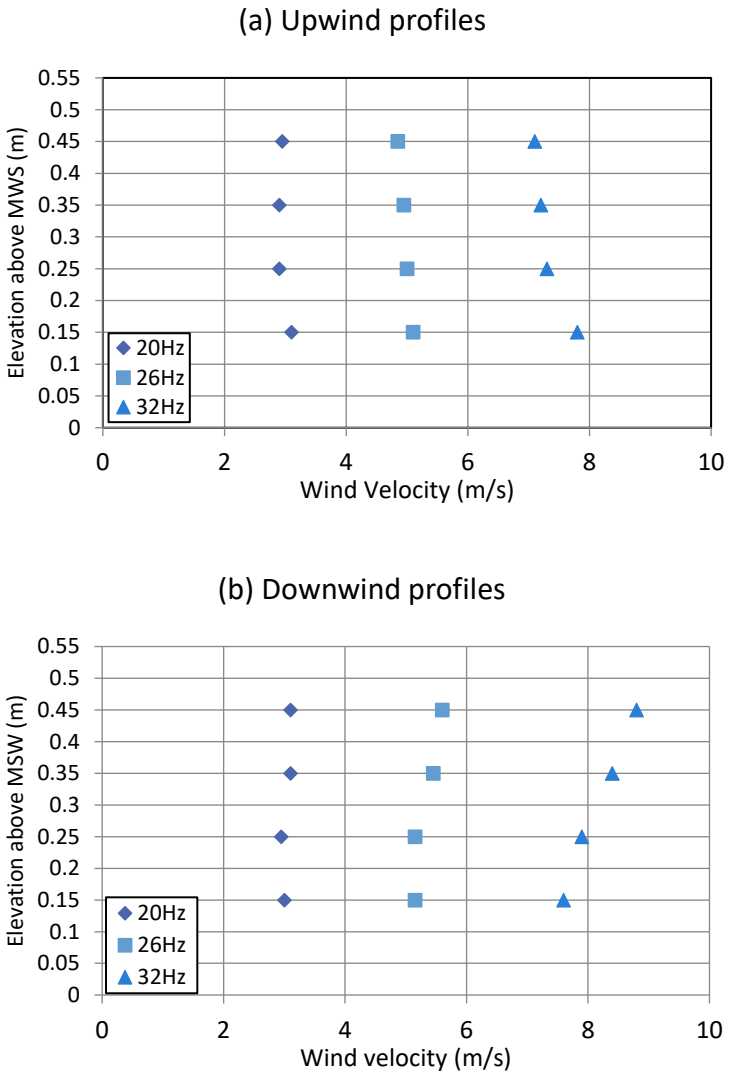

Figure 3.5: Wind velocity profiles measured (a) within ca. 2m of the inlet, and (b) within ca. 2m of the toe of the beach, prior to LAB2015, with 0.45m water depth. Elevation zero in these plots represents the mean water surface (MWS), with the flume ceiling at ca. 0.55m above the MWS.

No honeycomb or grid was installed at the wind inlet for the bulk of experiments in LAB2015 and LAB2016, nor was a roughened transition plate installed. This decision was in contrast to some experiments performed in the past (e.g. Hatori et al., 1981; Shemdin and Hsu, 1967; Bole and Hsu, 1969; Thais and Magnaudet, 1996; Young and Sobey, 1985), in which either or both of transition plate and grid has been installed. However other laboratory wind-wave experiments (e.g. Banner and Melville, 1976; Miller et al., 1991) in which the wind fan was positioned at the downwind end to avoid fan induced turbulence in the experimental volume, have been conducted in which no mention is made of either grid or transition plate.

(a)

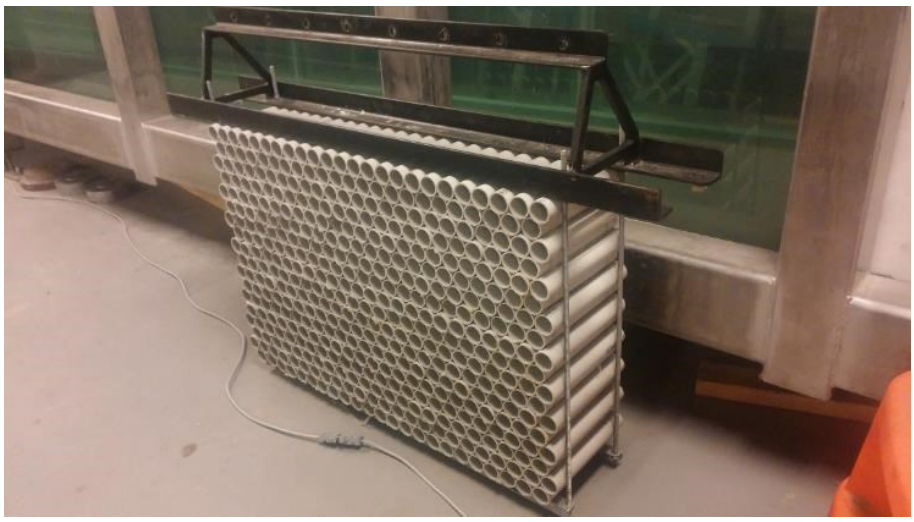

(b)

Figure 3.6: (a) First design of the wind inlet honeycomb prior to testing, and (b) Second honeycomb design during testing in the flume.

While not adopted for most experiments, two inlet honeycombs were tested during the present study, in an attempt to generate more uniform wind inflow without compromising other aspects of the experiment. Photographs of the two trialled inlet honeycombs are

shown in Figure 3.6 (a) and (b). Each honeycomb was suspended from the ceiling of the flume immediately adjacent to and downwind of the curved inlet. The first honeycomb was constructed of hundreds of lengths of PVC pipe glued together, each of length ca. 0.2m and diameter ca. 0.03m, with a gap of ca. 0.1m between the bottom of the honeycomb and the MWS. This was found to substantially limit the maximum wind velocity achievable in the flume. In addition, it caused the flow to be significantly channelled preferentially into the gap between the base of the honeycomb and the water surface, due to the lower resistance at that point in the cross section. It was feared that this discontinuity of the inlet wind velocity profile was not an adequate reflection of natural conditions, and this honeycomb was consequently abandoned. The second honeycomb was constructed with sheet metal welded together in a coarse rectangular grid, of cell size ca. 0.17m and length ca. 0.2m in the direction of wind flow. The second honeycomb was designed so that its vertical members penetrated the water surface in order to remove the wind flow discontinuity observed when trialling the first honeycomb. The second honeycomb was tested and found to reduce wind velocity marginally, but otherwise had no discernible effect on wave evolution. This metal honeycomb however did introduce operational nuisance, as the weight of the honeycomb and supporting framework restricted manhandling, and its presence prohibited easy access to the inside of the drained flume when mats required adjusting or wave gauges required spirit-level checking. Given that the fan was located downwind which reduced fan-induced turbulence in the experimental volume, and because of the operational nuisance of the honeycomb, the decision was made to run experiments without this honeycomb.

The focus of the present study was measurement of wave conditions rather than detailed wind profile investigations. It is possible that large wind eddies could affect the momentum transferred to the water, thus affecting the wave field measured in the present study. However, such pollution of wave growth by minor variations in the shape of the wind profile caused by inlet effects was expected to be secondary in nature and not sufficient to significantly distort the growth of LF or HF waves in the flume, and measurements were observed to be at least qualitatively comparable with past studies (e.g. Mitsuyasu, 1966).

3.1.6 Wind freeboard

When working in a wind tunnel, any changes in the wind flow cross section inevitably affect the wind field. In the present laboratory study, it was expected that the wave crests and troughs, combined with the ceiling of the tunnel, must cause some constriction and expansion of the flow, with velocity and pressure perturbations at wave crests and troughs

not purely representative of perturbations over hypothetically identical forced waves in the ocean. This is an almost inevitable difference between laboratory and field wind-wave experiments.

Zavadsky and Shemer (2012) performed wind-wave measurements in a tank with mean water depth of 0.2m and wind freeboard of 0.3m. Phillips & Banner (1974) used a water depth of ca. 0.4m and wind freeboard of 0.2m. Wu (1977) ran an experiment with wind freeboard of only 0.31m and water depth of 1.24m. Plant and Wright (1977) used a wind-wave flume with water depth of 0.3m and wind freeboard of 0.3m. Buckley and Veron (2010) adopted a mean water depth of 0.71m and wind freeboard of 0.54m. Olfateh (2014) performed measurements in the Miami ASIST flume with approximately 0.4m water depth and 0.6m wind freeboard. The present study was performed in a wind-wave flume with total available height of 1.0m. Given that H_{LF} was observed to approach 0.15m in some conditions, with L_{pad} ranging up to ca. 4.8m in cases with the longest period in LAB2016, it must be acknowledged that the flume ceiling may have altered the wind pressures experienced by the water surface, at least in cases of taller and longer paddle waves. However, the general shape of wind velocity and pressure perturbations along the longer wave phase, namely increased velocity and decreased pressure at wave crests, was not expected to change qualitatively as a result of ceiling effects. Exact quantification of paddle wave behaviour was not the focus of the present study, but rather the behaviour of HF waves of lesser height and length, and the wind perturbation of these HF waves was expected to experience negligible direct impact by ceiling effects. It was determined that for most cases, a water depth of between 0.4 and 0.45m, and freeboard of 0.55 to 0.6m would minimise ceiling effects as much as was practicable in the present facilities. This was not be inferior to most past studies, and was close to double the freeboard of some previous experiments.

3.1.7 Wave absorption at the downwind end of flume

Ouellet & Datta (1986) reported that in hydraulics laboratories worldwide there is a wide variety of shapes, slopes, permeability and surface texture of wave-absorbing beaches. For wave absorption in the present study, a curved beach was designed and constructed from perforated sheet metal, with a total surface length of 3.5m measured along the chord, and a maximum segment depth of 0.15m at the mid-point. Such a curved beach was preferable over a straight beach in order to minimise the length of the beach, maximising the available fetch in front of the beach, and minimise the reflection of waves of all frequencies. The beach was angled so that its slope reduced to near zero slightly above the mean water

surface, at a height of ca. 0.45m above the floor of the flume. The beach exhibited a maximum slope of ca. 20° at the toe.

The design approach used in the present study was based somewhat on trial and error, initially mimicking an operational design used by DHI in the Netherlands (Fuchs, 2014), a photograph of which is shown in Figure 3.7. The first iteration of the UQ absorber used sheet metal with 9mm diameter holes, cross bars sitting on top of the sheet constructed from 20mm equal angle, centres of ca. 0.1m, to increase turbulent dampening and partially retard run-down. The sheet procured had an open area ratio of 40%, which followed the visually estimated open area ratio of the DHI design, rather than comments by Cho and Kim (2008) which suggested less permeable plates would perform better.

Figure 3.7: Photograph provided in personal communication from Fuchs (2014) of wave absorbing beaches used by DHI.

Initial testing of this design was performed with wave heights of 0.06 and 0.12m, and periods of 1.0 and 2.0s. Measurement of K_r was obtained using two methods. The first method involved generating single wave group pulses of short duration, and measuring the incident and reflected wave height in the time domain with wave gauges. The second method was performed in the frequency domain according to the procedure outlined by Baldock & Simmons (1999), with wave gauges positioned ca. 0.13m apart. K_r values were well below 0.1 for 1s waves, but around 0.3 to 0.5 for 2s waves, which was far from acceptable. Minimal breaking was visually observed, so it was determined that a less permeable design was required to force waves to break, in agreement with the observations of Cho & Kim (2008).

In order to reduce permeability, a second sheet of perforated mesh was screwed on top of the first sheet, with hole size of 3mm and open area of 30%. Theoretically this could be

approximated to possess a combined open area of $40\% \times 30\% = 12\%$, but hole alignment along with warping of the steel during galvanising resulted in some air gap between the two sheets, and a practical open area was likely slightly higher. In order to further reduce the effective permeability, thin geotextile was installed between the plates. In the final design, shown in Figure 3.8, equal angle cross bar spacing was increased close to the mean water surface, in an attempt to reduce reflection of some HF waves caused by the cross bars. Open cell acoustic foam with cell size of ca. 1.0mm and thickness 30mm was placed on the beach to further reduce turbulence generated by the cross bars, and in the swash zone a small strip of some coarse grid mesh (hole size of ca. 25mm) was added to further dampen reflected HF waves. A gap of ca. 1m was present behind the beach, with half of this filled from floor to above the MWS level with the same coarse grid plastic mesh mentioned above, and a layer of the acoustic foam was attached to the end wall behind this mesh, also extending from floor to above the MWS. This final design allowed for some large waves to overtop the beach and be dampened in multiple stages.

Figure 3.8: UQ wave absorbing beach during testing.

In order to obtain optimal absorption, a range of water levels was trialled with short and long paddle waves, and it was found that the absorbing beach performed best at depths of 0.415 to 0.44m, with minimum reflection at ca. 0.425m depth. It was determined that all experimental runs would be performed near this depth.

This final configuration produced K_r values averaging ca. 0.06 or less for free waves of up to 2s period, as analysed using the method of Baldock and Simmonds (1999). Past wind-wave flume studies (e.g. Waseda and Tulin, 1999) have acknowledged that some reflection is inevitable, although they often allowed the reflected waves to settle to an equilibrium state before measurement commenced, to ensure steady-state conditions. Miller et al. (1991) observed K_r of ca. 0.1 for paddle waves and less than 0.05 for paddle wave harmonics. Shemdin and Hsu (1967) reported reflection to be less than 10% for waves ranging from 0.6 to 1.2 Hz. In many prominent experiments on this topic (e.g. Mitsuyasu, 1966), magnitude of reflection is not documented. Bole and Hsu (1969) noted an envelope of 20% from lines of best fit along the flume, which they attributed to standing wave patterns caused by reflection. The measured K_r of 0.06 or less in the present study, in conjunction with the active absorption at the paddle, was considered comparable with or slightly better than similar past studies.

3.2 Instrumentation

This section provides details of instrumentation which was installed in the UQ wind-wave flume and used during LAB2015 and LAB2016.

3.2.1 Instrument synchronisation

The DHI system which generated paddle waves also recorded water surface elevations, and these two signals were consequently synchronised in time. The system was also capable of generating a sync pulse that would generate 5 Volts of EMF between two wires from the exact commencement of each run, being 0 Volts prior to the run commencing. This pulse was fed to other instruments (e.g. wind data logger, ADV) to enable synchronisation of all measurement systems, and even fed to LED lighting which enabled synchronisation with video data.

3.2.2 Water surface elevation

Past experiments related to interaction of HF and LF waves have used any of point wave gauges, laser slope meters or radar backscatter instruments. Wave gauges fixed in place are unable to directly measure $\eta(x)$. However, unlike radar backscatter methods, they have the advantage of measuring exact water surface elevation at each point in time, and are similar qualitatively to wave rider buoys. They are also simpler and cheaper than other methods, enabling a greater number of measurement locations. For these reasons, wave gauges were selected as the primary measurement device in the present study, being DHI type 201 resistance gauges with 2 prongs. Each gauge provided an analogue signal to the

DHI data acquisition system, which digitised this signal at 40Hz and applied a quadratic calibration formula to output water surface elevation as a function of time. Wave gauges were regularly calibrated during batches of experiments according to the DHI recommended procedure, which involved physically positioning gauges at their design location, as well as 0.1m above and below, sampling at each point to obtain a three-point calibration curve.

Wave gauges were attached to the ends of 10mm dia. brass rods, which rods were inserted through holes in the acrylic ceiling of the flume. At each gauge hole, the acrylic was thickened locally to provide extra support. In spite of this, some wave gauges were observed to deflect in LAB2015 during very strong wind and wave combinations. For LAB2016, in order to reduce deflection caused by the small amount of play in the holes, the tops of the brass rods (protruding 0.15 to 0.40m above the flume ceiling) were restrained during measurement by tensioned elastic octopus straps extending between pairs of brass rods, visible in part in Figure 3.9 (b), which prevented any play in the holes. Even with this mitigation, the base of the wave gauges was still observed to deflect by the order of 10mm under near maximum wind velocity with large waves, due to flex in the brass rods and in the wave gauges themselves. It was determined that any phase sensitive calculations between adjacent wave gauges must be treated with some caution.

The number and position of wave gauges in LAB2015 and LAB2016 has been illustrated in Figure 3.1 (a) and (b) respectively. In Figure 3.1 (a) for LAB2015, where two wave gauges are indicated at the one fetch, these were positioned at exactly the same fetch, separated laterally by ca. 0.4m with each gauge utilising an individual brass holding rod. This arrangement provided means to detect cross-tank instability. Waves measured during LAB2015 were observed to be predominantly two dimensional in nature, apart from the previously mentioned cross-tank instability. Consequently, the positioning of multiple gauges at exactly the same fetch was abandoned during LAB2016, in favour of increasing the number of fetches measured with single gauges, similar to the approach of Mitsuyasu and Yoshida (2005), with cases being designed specifically to ensure avoidance of the previously documented cross-tank instability. In Figure 3.1 (b) for LAB2016, annotation of two gauges at the one location involved the second gauge being positioned 0.055m downwind, directly in line with the first gauge, and attached to the same brass holder rod. The fetch of each second gauge was thus 0.055m greater than what is marked in Figure 3.1 (b). A photograph of this arrangement is included in Figure 3.9 (a). Three gauges were installed on the single most downwind holder, one being 0.067m in front and another being 0.055m behind the middle gauge, with the fetch annotated in Figure 3.1 (b) representing

fetch of the middle gauge. Deployment of some closely spaced gauges facilitated measurement of wave number, celerity and K_r for waves of some frequencies, the latter using the method of Baldock & Simmons (1999). It also enabled the attempt to track individual HF waves between the two gauges. The wave gauge pairs were fixed at the desired spacing top and bottom, resulting in a constant displacement between the two gauges at all times, in spite of any overall deflection of the gauge system.

(a)

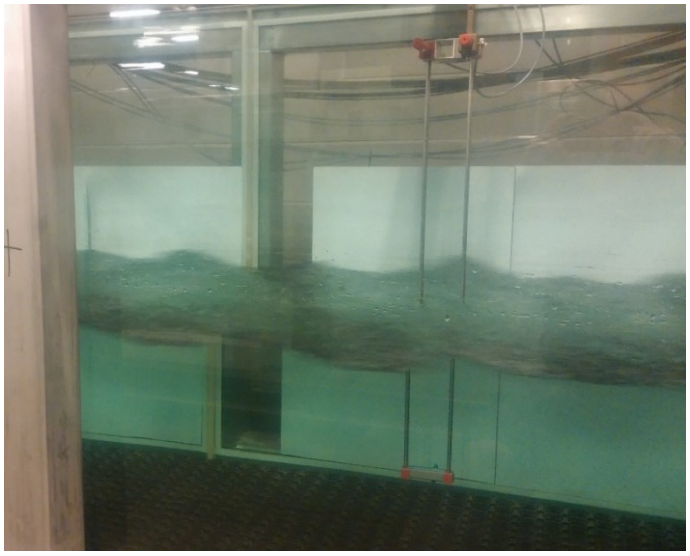

(b)

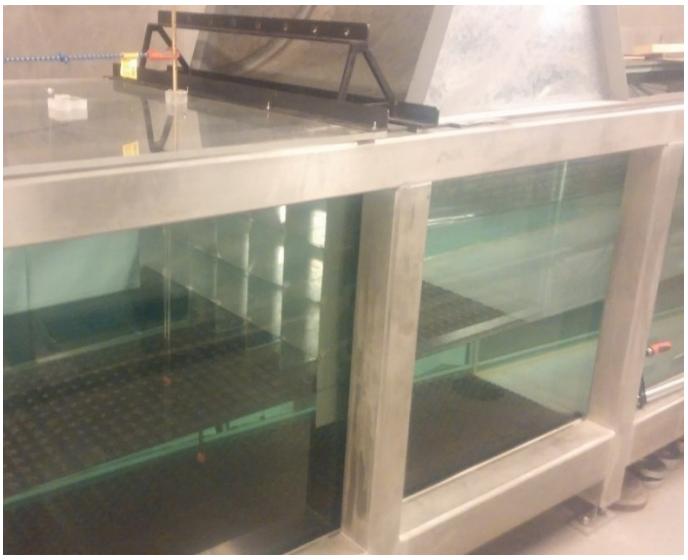

Figure 3.9: DHI resistive wave gauges deployed in flume, (a) in a paired arrangement in LAB2016. (b) Octopus straps were used to tension the wave gauge holders in LAB2016 to reduce deflection. Note, wind honeycomb shown in (b) was not used during measurements documented in Chapter 5.

The minimum gauge spacing of 0.055m was determined after testing several possible spacings, and visually selecting the closest spacing at which ripples generated by passing

paddle waves did not appear to reach the adjacent gauge. This is comparable with experiments by Caulliez (2002) who adopted spacing of 0.050m for a similar dual wave gauge arrangement in a laboratory.

Each DHI system was capable of recording 8 wave gauges, but could also record an additional 8 analogue inputs. Because 24 wave gauges were used during LAB2016, this required recording water surface elevation on one of the two adjacent wave flume systems, synchronising between each DHI system by means of the sync-pulse wire from the primary system being fed to one of the available inputs on each of the other systems. Coordination of recording wave gauges on other active operational systems was not a trivial task. Data collected independently on each of the three DHI systems was compiled during post-processing.

3.2.3 Wind velocity and pressure

Wind velocity was measured by means of a pitot tube, which for most experimental runs was positioned at ca. 0.2m above MWS as a measure of ambient wind velocity, at fetch=12.15m. During LAB2015, the pressure difference between static and dynamic tappings was measured with a high precision air water manometer, with sensitivity of 0.2mm water head, which is roughly equivalent to sensitivity of 0.2m/s velocity at 15m/s mean wind velocity. The manometer reading fluctuated during experiments, and RMS values were obtained by the labour-intensive process of video recording the manometer for durations of ca. 60 – 120s and manually sampling the video still frame images every 2s. In LAB2016, the pressure difference between static and dynamic tappings was acquired digitally.

Wind pressure variation along the flume fetch was measured by means of static pressure tappings in the ceiling of the flume, at fetch increments of 2 – 3 metres. During LAB2015, this pressure drop between first and last tappings was measured with an air water manometer inclined at 18° above horizontal to increase resolution, with effective sensitivity of 0.3mm water head. RMS averaging was not required, due to lower degree of instrument fluctuation.

In LAB2016 for both wind velocity and tapping pressure, pressures were measured using Honeywell DCXL01DS differential pressure transducers, with calibrations performed approximately each week throughout LAB2016. One input to each pressure transducer measured the laboratory ambient pressure, outside of the wind tunnel, and this included the two pitot tube pressure tappings. The signal was logged on a dataTaker DT80 Series 2 data logger at 1Hz sampling frequency. Synchronisation with wave gauge data was achieved

using the electronic synchronisation pulse emitted from the DHI wavemaker system. In LAB2016, fluctuations in all tubes were dampened by means of constricting clamps. For the majority of LAB2016, this wind velocity was only obtainable as a time-averaged value due to an instrument malfunction. However, ceiling pressures sampled effectively at 1s frequency were also converted to their time-averaged value during post-processing.

Given the significant number of wave gauges and associated cabling present in the wind flow, particularly during LAB2016, the drag and associated pressure drop caused by this equipment could not be deemed insignificant, even though shear stress on the water surface was expected to produce the majority of drag. However, the shear stress calculation outlined in Section 3.4.4 taken from Donelan et al. (2004) did not require estimation of drag from any of the instruments, sidewalls and ceiling in order to calculate the shear stress acting on the water surface.

3.2.4 Video recording

During LAB2015, no systematic video recording took place, but recording was ad-hoc in nature. During LAB2016, four GoPro video cameras were installed at fixed locations along the flume, simultaneously capturing the entire fetch for the first ca. 11min of each run, which included approximately 3 minutes of duration with paddle and wind combined. Even though each GoPro was started manually by hand at a different time for each run (the difference being the time taken to walk between them), these video recordings could be synchronised with wave gauge data by means of multiple LEDs within the field of view of each connected to the DHI synchronisation pulse, which all lit up simultaneously at the commencement of the run. However, such synchronisation was not automated, and only deemed necessary to perform ad hoc when required during analysis. So far this has not been required to generate the results included within this thesis.

3.3 Laboratory experimental conditions

3.3.1 LAB2015

The main batch of experiments in LAB2015 consisted of 416 test cases, each case lasting 9 minutes, not including flume settling time between runs. This settling time ranged from 4 minutes for cases with low wind velocity, up to ca. 10 minutes for cases with maximum wind velocity. It was found that water surface elevation flat-lined far sooner than water velocities monitored by means of the ADV, which as discussed previously was installed in this batch of experiments. The settling time was governed by the water currents.

Each case was run first with paddle waves only for 3 minutes, after which wind was introduced for the remaining 6 minutes. In spite of inevitable reflection from both ends of the flume, the HF wave spectrum was found to approach equilibrium relatively soon during this 6-minute time period, which allowed for spectral averaging of water surface elevation. LF wave amplitude typically did not vary by more than ca. 10% at the one location during the ensembles which commenced 60s after the onset of wind.

Table 3.1 lists the experimental parameters used in LAB2015. Wind velocity is expressed in terms of wind fan frequency, which was the controlled variable for each experiment. Wind velocity varied slightly between cases with the same wind fan frequency, and values in this table are typical averaged values, not to be considered precise for all cases of the specified fan frequency. Each and every combination of the parameters in Table 3.1 was intended to be performed, however it was found that waves of greater wave height and shorter period became unstable, breaking instantly or else resonating to produce the previously documented cross-tank oscillations. These steeper cases were excluded from the remaining experimental plan once these behaviours were observed, and excluded from results. All paddle waves in this batch of experiments were designed as monochromatic waves.

Table 3.1: Experimental conditions in LAB2015.

Fan frequency (Hz)	Approx. wind V (m/s)	Paddle wave H (m)	Paddle wave T (s)
5	2.1	0	0.5333
10	4.0	0.01	0.7111
15	5.8	0.02	1.0667
20	7.5	0.03	1.6
25	9.3	0.04	2.1333
30	10.9	0.06	3.2
35	12.6	0.08	
40	14.3	0.10	
45	15.8		
50	17.2		

3.3.2 LAB2016

The aims of LAB2016 were to obtain cleaner and clearer frequency spectra for HF and LF wave combinations, and to more closely examine the rapidity of suppression onset as paddle waves enter existing pure wind-wave conditions. To achieve the former of these

aims, It was determined to run experiments for longer, allowing longer durations of spectral ensemble averaging, but running less wind-paddle combinations. The primary group of experiments in LAB2016 consisted of 64 experiments combining each combination of the variables listed in Table 3.2, excluding the combination of H_{pad}=0.1m and T_{pad}=0.838, which was deemed to be too steep to propagate without breaking almost immediately after leaving the paddle. It must again be noted that wind velocities documented in Table 3.2 are typical values only, and not representative or even a true average of all cases of the specified fan frequency, because actual velocities varied between cases. The fetch was ca. 1m longer in LAB2016 than in LAB2015, with a wind cross section much more congested by the presence of instrumentation, and these two factors are thought to be responsible for the reduced wind velocities in LAB2016 compared with LAB2015.

In reverse order to that of LAB2015, each experiment in the above mentioned 64 experiments in LAB2016 commenced with quiescent conditions, after which wind-only (WO) forcing was applied without any paddle waves present for 8 minutes. At this point, paddle waves were introduced and the combined wind + paddle (W+P) forcing was run for 26 minutes until the 34-minute mark of the experiment. At that point, the wind fan was stopped and paddle-only conditions remained for a further 5 minutes until the 39-minute mark, with HF waves observed to have vanished by the 37-minute mark. From that point, recording of water surface elevation continued during and beyond the settling of the paddle waves, until the completion of the run at the 43-minute mark.

Table 3.2: Primary experimental conditions in LAB2016. The combination of conditions run 186 times to examine transitions is marked with *.

Fan frequency (Hz)	Approx. wind V (m/s)	Paddle wave H (m)	Paddle wave T (s)
20	5.7	0	0.838
30	8.7	0.01	1.257*
40*	11.4*	0.025	1.886
50	14.5	0.05	2.514
		0.1*	

It was mentioned previously that examining the transition from pure wind-only (WO) conditions to wind + paddle (W+P) forcing was one focus of LAB2016. Separation of HF and LF waves is difficult in this scenario, due to the inability to apply a Fourier transform to transient time series'. Wavelet based methods are often utilised in in transient systems (e.g.

Donelan et al., 1996), but such are subject to significant scatter when examining one transition only, and do not provide means to ascribe energy to HF or LF components as clearly as Fourier analysis can. In order to overcome this challenge, and as previously mentioned, the transition sequence from WO conditions to W+P conditions was repeated 186 times for H_{pad}=0.1m T_{pad}=1.257s and V_0=11.4m/s, a combination known to exhibit strong suppression of HF waves based on observations in earlier experiments. Through careful timing and synchronisation of each transition, it was possible to average the η time series for all transitions to obtain a clean signal for the transient paddle wave train relevant to all transition sequences, after which the HF component could be obtained by subtracting the paddle signal from the total η signal within each transition sequence.

3.4 Data processing

A variety of common methods was used to analyse wave gauge data, including Fast Fourier transformation of the η time series, discrete integration of energy in spectral bins to obtain total wave energy in the spectrum, and zero-crossing analysis to detect individual waves. Methods of this nature which are common and universally adopted are not explained in this section. Less common analyses performed in the present study are explained in this section. It must be noted that except where otherwise stated, spectral plots throughout this thesis were obtained by ensemble averaging of multiple overlapping individual spectra. In LAB2015, ca. 5 minutes was used to average the W+P η spectra, and a similar duration for WO η spectra. In LAB2016, ca. 24 minutes of data was used to average W+P conditions, while spectra of pure wind-waves were generated using either ca. 7 minutes of wind-only conditions at the commencement of each experimental run, or else by averaging several of these ca. 7 minute segments for multiple separate experimental cases with the same wind velocity and almost identical water depth to obtain a smoother spectrum.

3.4.1 Alignment of frequency bins

In both LAB2015 and LAB2016, paddle wave frequencies were chosen to be located exactly at FFT frequency harmonics, to enable paddle wave energy, to be isolated easily. This also enabled direct correlation of the magnitude of spectral energy in the paddle wave bins to be correlated with wave amplitude by multiplying by a constant, equal to $2/N_{fft}$, where N_{fft} represents the number of sample points within a Fourier Transform window. Unfortunately, an error in programming the wave maker in LAB2016 resulted in the actual intended frequencies not matching the design values. To compensate for this, data was re-sampled using cubic splines, resulting in an effective sampling frequency not precisely equal

to 40Hz, but rather a calculated value between ca. 39 and 41 Hz which depended on the paddle frequency in question. This resampling enabled the paddle frequency to be positioned precisely in a single bin. Because the η signal produced by the DHI system was clean and free of non-physical spikes, this cubic spline was found to accurately replicate the original surface elevation, with any slight variation not significantly affecting the frequencies being focused on in the present study, which typically did not exceed ca. 6-8Hz.

3.4.2 Separation of HF, LF and seiching wave components

In analysing η time series records, it was necessary to separate the measured signal into HF and LF components, in both frequency and time domains. Reviewing of the definitions of LF and HF waves recorded in the front pages of this thesis may be helpful prior to reading this section. The frequency domain separation was required in order to quantify the energy for each component across the entire spectrum. Time series separation was required to enable zero-crossing analysis to be performed for both HF and LF waves.

The action of wind shear stress on the water surface inevitably leads to a gradient in the MWS elevation along the flume, and upon switching the wind on or off, seiching oscillations with amplitude of order 0.02m and period of ca. 22s were present for ca. 120-180s as the MWS adjusted to a new steady gradient (this new gradient being zero when the new wind velocity was zero). Given that such seiching motion is outside of the scope of the present study, and any MWS offset may pollute analysis involving zero-crossing detection, it was deemed necessary to filter out these seiching oscillations before any subsequent signal processing could take place. As a result, in all plots of laboratory data in this thesis, η spectra time series' are plotted with a high pass filter having been applied to remove energy below ca. 0.2 Hz. This filtering involved performing a Fourier transform of the water surface time series, setting energy in bins with $0 < f < 0.2$ Hz to zero, then performing an inverse Fourier transform to reconstruct the time series without seiching. This was found to effectively remove MWS offset and any wave oscillations with frequency lower than 0.2 Hz.

It was desired for the entire bound wave, including fundamental and higher harmonics, to all be attributed to LF waves. This was complicated by the expectation for some HF energy (not bound to the paddle waves) to also be present in paddle harmonic frequencies. A few methods were trialled to separate LF and HF wave components in the laboratory data. The first attempt shall be referred to as Separation Method 1, and is described as follows. The paddle wave frequency and higher harmonics up to 6 times the fundamental frequency were all assumed to be comprised partially of HF energy (random wind-waves) and partially of LF energy (bound to paddle waves), with all other frequencies being attributed to HF

waves. For the fundamental and harmonic frequencies, the HF component of energy was set to be an average of the two adjacent bins, with the LF component of energy comprising the remainder of the energy, as illustrated in Figure 3.10. The LF and HF η time series were constructed by inverse Fourier transforming the respective LF and HF spectra. It can be seen that this method relied on an assumption that HF energy in each harmonic bin was an average of adjacent bins. Upon visual inspection of the time series with HF and paddle wave components, Separation Method 1 appeared to be accurate in most cases from LAB2015 and LAB2016.

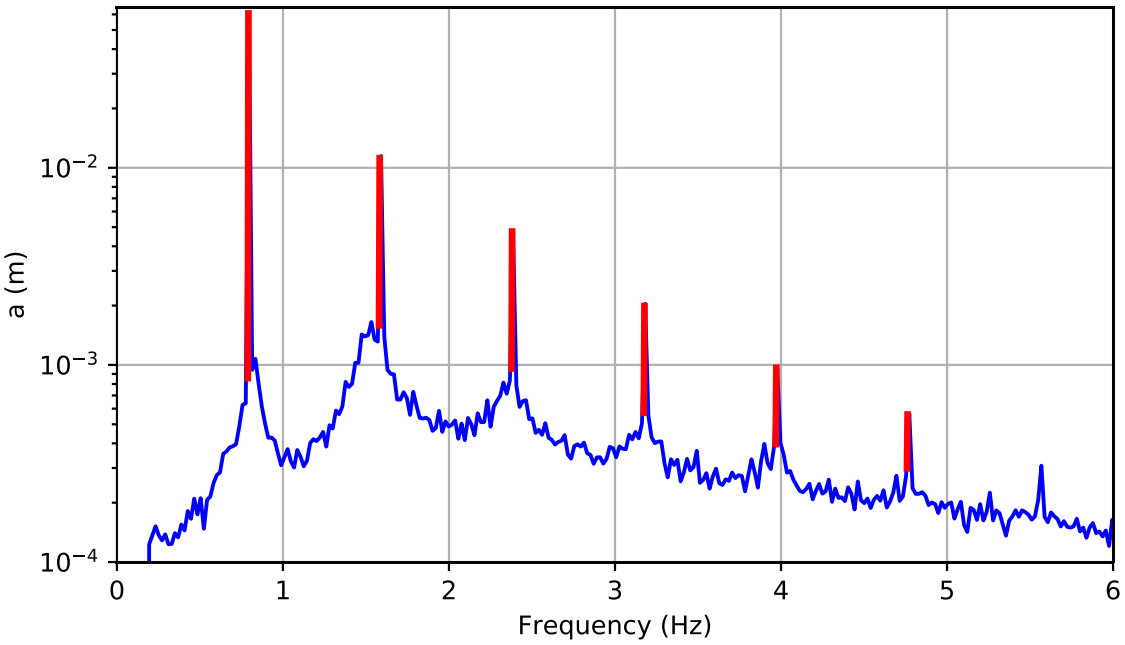

Figure 3.10: Separation Method 1 in a typical spectrum. The component of energy attributed to LF waves is marked red. The remainder of energy in these paddle harmonic bins, and energy in all other bins, was deemed to be HF, or random wind-waves.

However, when performing some analysis using Separation Method 1 for cases with low paddle wave steepness, it was discovered that energy in the bins of higher harmonics may grow significantly, without this added energy being bound to the paddle wave, which observations are documented in Section 5.6, and which effect has not received adequate coverage in literature. When Separation Method 1 was applied in these conditions, the LF wave time series appeared rippled as seen Figure 3.11, and examination of video records confirmed that these ripples did not travel at the paddle wave celerity. These waves must then be classified as HF (random wind-waves) rather than LF (bound to the paddle waves), but determining how to proportion the energy in the bin between HF and LF components required careful consideration.

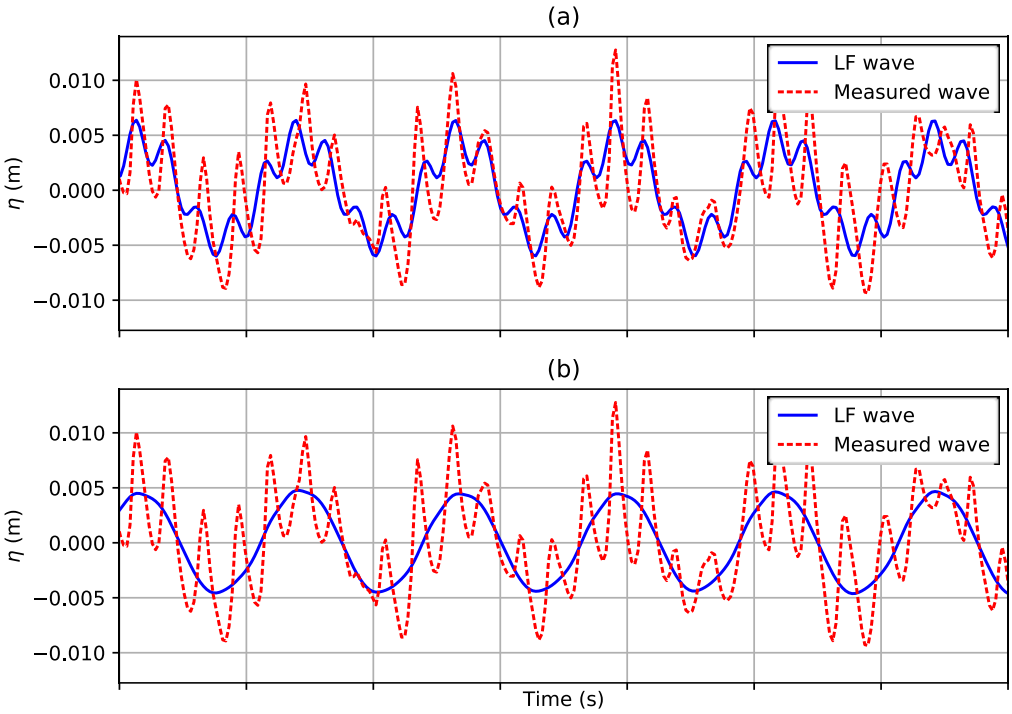

Figure 3.11: Short segment of time series for H_{pad}=0.01m, T_{pad}=1.25s, and V_0=5.7m/s, separated (a) using Separation Method 1, and (b) using Separation Method 6, the latter being the final separation method selected for most laboratory data analysis in this thesis (see text).

It must be noted that Separation Method 1 includes an assumption that Benjamin-Feir instability or similar mechanisms do not significantly contribute to the energy in the two adjacent frequencies, with energy in these adjacent frequencies completely attributed to HF wind-waves. However, this was challenged by observations low T_{pad}, where the peak frequency of $\eta_{HF_{wo}}$ was not far removed from f_{pad}, an example being illustrated in Figure 3.12 (b). It was revealed that the assumption of energy in frequencies adjacent to paddle harmonics being entirely unbound to the paddle wave was inaccurate in some cases, with energy humps forming in the spectrum in frequencies near f_{pad} and its harmonics, as seen in Figures 3.10 and 3.12 (b). Using Separation Method 1, and examining the separated results in time series, there was a tendency for HF wave peaks to coincide with paddle wave peaks, an example being displayed in Figure 3.13 (a), indicating that some paddle wave energy was being incorrectly attributed to HF energy, and that these humps were in fact bound to the paddle wave.

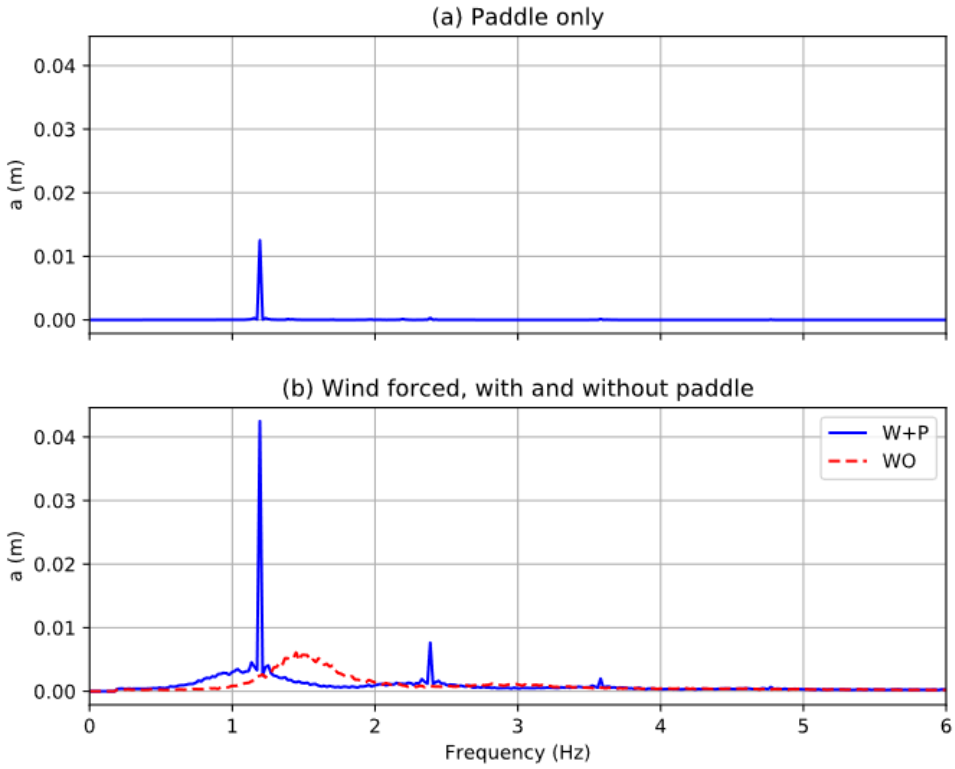

Figure 3.12: Spectra from case with T_{pad}= 0.838s, H_{pad}= 0.025m, f_{fan}= 50Hz, and fetch = 12.5m. Humps in the W+P spectrum were observed near f_{pad} and its harmonics.

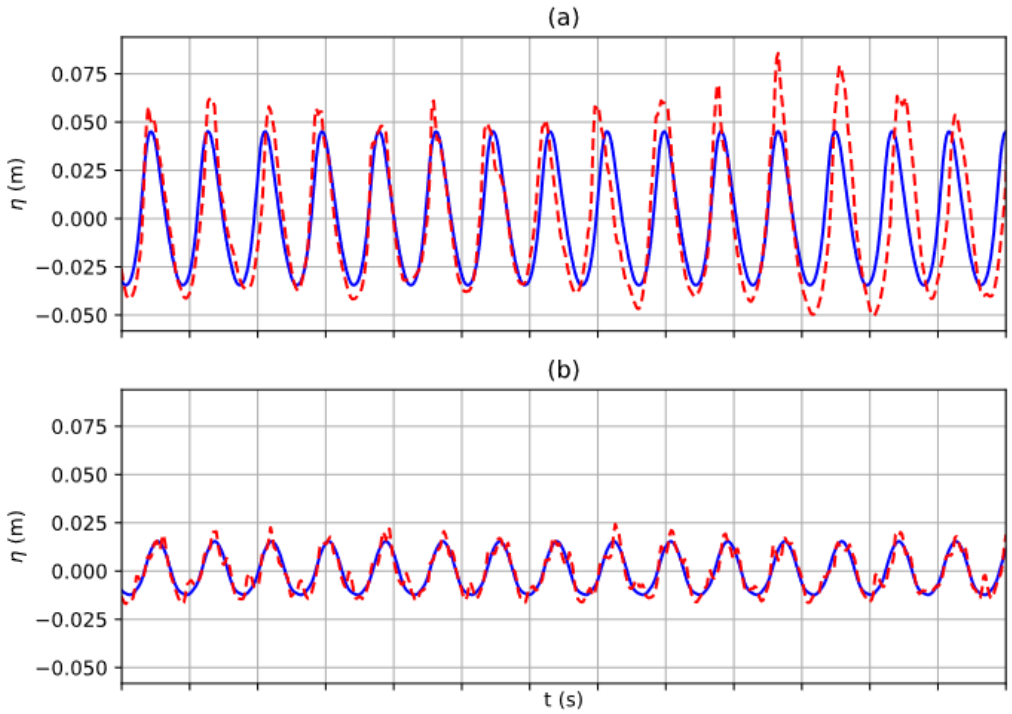

Figure 3.13: Example time segment with similar conditions to Figure 3.12 at two fetches, (a) at fetch=12.5m, and (b) at fetch=1.26m. X-axis ticks correspond to 1s intervals. The dashed red line represents the total wave signal, while the blue line is the LF wave component obtained by Separation Method 1.

This also tended to occur in cases with strong fractional increase in paddle wave H due to wind forcing, usually at largest fetches. This wind input to frequencies in the humps, as opposed to input focused entirely into the paddle frequencies, is related to the formation of group patterns and slight irregularity in the paddle wave periods, as seen in Figure 3.13 (a). While the dominant wave attracted an influx of energy, the energy did not necessarily target the individual frequency bin of the dominant wave cleanly. This is not believed to be caused by the active wave absorption system, because the irregularity of paddle wave periods was not present at the smaller fetch in 3.13 (b). The danger in failing to account for phase irregularity is that misalignment of the separated LF wave signal with the dominant physical wave results in the difference being attributed incorrectly to HF energy, over-stating actual HF energy in the presence of paddle waves ($E_{HF_{w+p}}$), thus overstating the suppression ratio and under-stating the suppression effect. It was concluded that part of the humps in the combined wind-wave spectra, which include sidebands, should be classified as paddle wave component, but the decision of how to divide these humps remained unresolved.

An attempt was made to separate HF and paddle waves (including harmonics) by phase averaging in the time domain, and this was known as Separation Method 2. It exhibits similarities to the phase averaging method used by Miller (1991). The paddle wave was first extracted by phase averaging, and then the HF wave was obtained by subtracting the paddle wave signal from the total wave signal. During phase averaging, the time series was up-sampled so that the timestep was an exact fraction of the paddle wave period, to ensure that all points in the time series were at discrete and replicable locations along the paddle wave phase. After phase averaging, the time series was down-sampled to return to the original timestep. This method effectively attributed the averaged paddle wave signal to the LF component, but was found to also possess similar flaws to Separation Method 1. For low steepness waves, the phase averaged paddle wave signal surprisingly possessed ripples comparable in magnitude to those of Separation Method 1, even when averaged over ca. 24 minutes. For cases with low T_{pad} (i.e. high steepness) and strong growth, the paddle wave envelope of Separation Method 2 was almost identical that obtained by Separation Method 1 which is displayed in Figure 3.13. It was deemed to be a marginal at best improvement over Separation Method 1.

It was determined that the most accurate while still imperfect separation of LF and HF waves must be a more complex solution, and was developed iteratively with substantial trial and error. The final method of dividing the η spectrum into LF and HF components, which shall be referred to as Separation Method 6, is illustrated in Figure 3.14. All energy lower

than 1.333 times the fundamental paddle frequency was attributed to LF energy, including energy in the fundamental harmonic. All energy equal to or higher than this frequency was completely attributed to HF wave energy, except for that in paddle harmonic frequencies. The second harmonic was completely attributed to harmonic energy. Within the 3rd to 8th harmonic frequencies, the amplitude of each was compared to the respective amplitude of PO free waves with identical paddle forcing. In most cases these harmonics contained more energy due to the wind, and in these cases the LF portion was set to be equal to that of the free wave spectrum. In less common cases where the free wave energy was higher at the specific harmonic than that with W+P forcing, the HF energy in adjacent frequencies was averaged to obtain the value of HF energy in the harmonic bin. The remainder of energy within the harmonic bin in question was attributed to LF energy. When separating energy within the one bin into LF and HF components, the phase of both HF and LF components were both set to equal to the actual phase in the bin, with only amplitude being changed. In this manner no LF wave distortion was introduced, and energy was conserved so the total energy in the W+P spectrum was equal to the sum of energies in the LF and HF components, not including the previously discussed removal of energy in frequencies less than 0.2Hz.

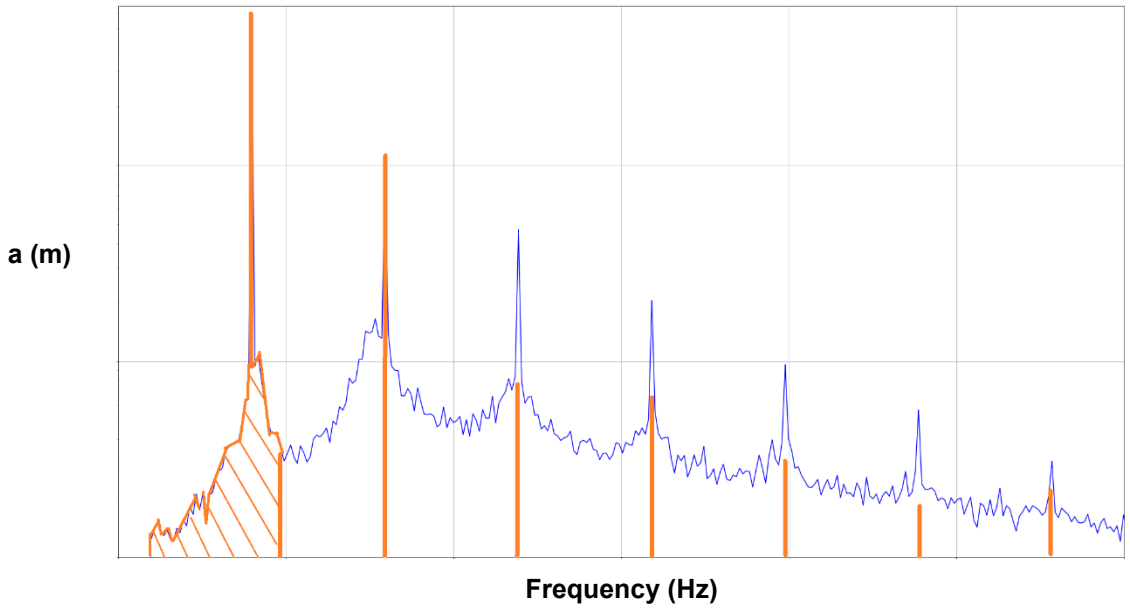

Figure 3.14: Separation Method 6 for a typical W+P (wind + paddle) spectrum, with the LF portion of the spectrum indicated by brown tracing / hatching. The height of brown bars in higher harmonics varies, and is not to scale in this figure. See text for full description.

This method, while far from perfect, was found to remove the paddle wave ripple effect visible in Figure 3.11 (a) for cases with low paddle wave steepness, and increased the correct allocation of the dominant wave energy to the LF component, as seen by comparing

Figure 3.15 (a), which was generated using Separation Method 6, against the less effective Separation Method 1 used in Figure 3.13 (a). One disadvantage of Separation method 6 is its dependence on requiring measurements of the free wave spectrum in the absence of wind for identical paddle forcing conditions, to determine the distribution of energy in the 3rd to 8th harmonic frequencies. However, in the present study, all combined W+P cases were also performed immediately before or afterwards with no wind, so a reference free-wave η spectrum was always available. While not perfect, Separation Method 6 was generally adopted for separation of HF and LF waves in laboratory data in the present study.

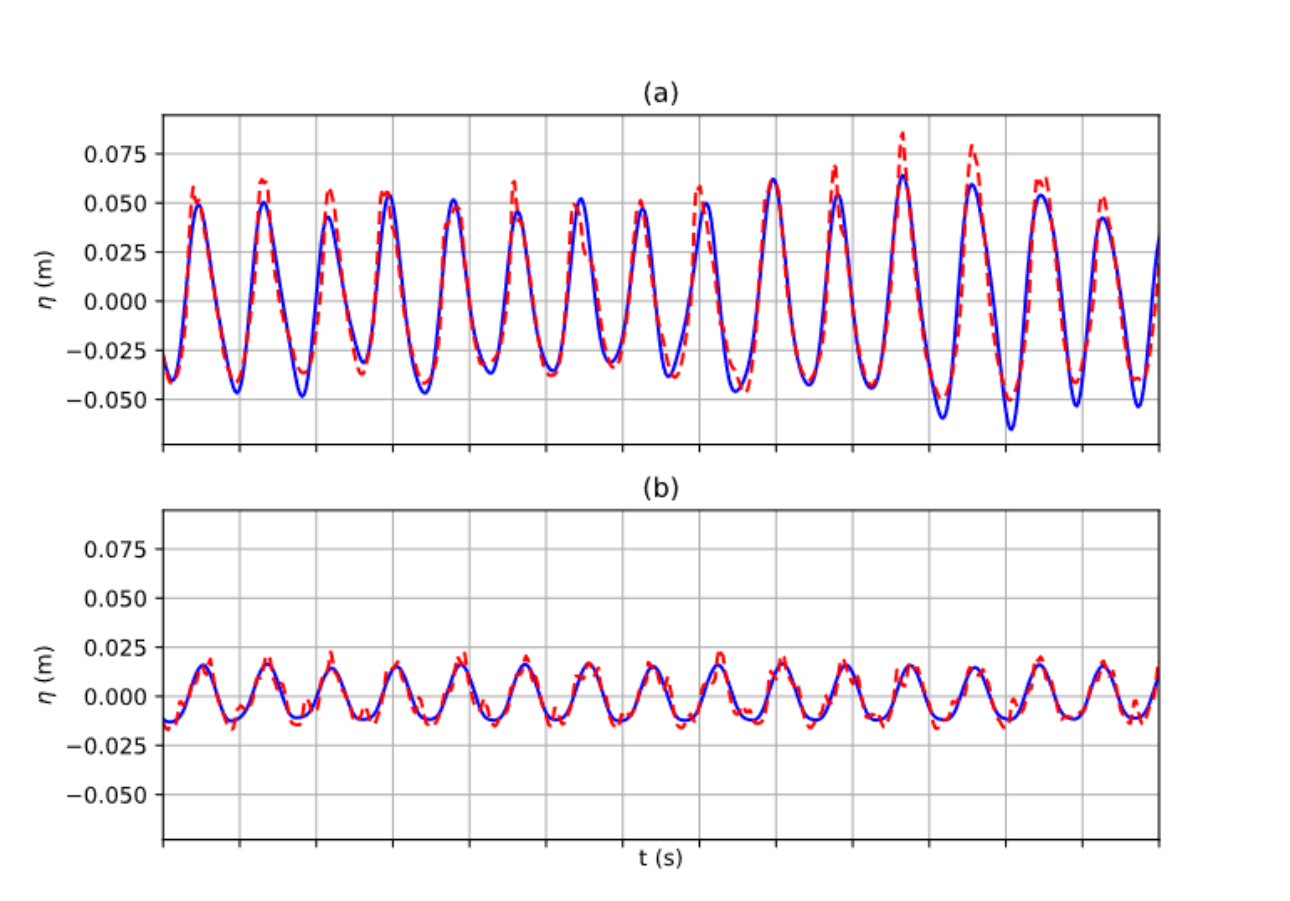

Figure 3.15: Separation Method 6 applied to the same wave records as Figure 3.13.

3.4.3 Identification of LF wave breaking

A wide variety of methods have been used historically to detect wave breaking, including visual observation of foam, acoustic measurement of surface turbulent noise, and a variety of methods which analyse the wave gauge signal (see Babanin, 2011, pp49-117 for a general review). Longuett-Higgins and Smith (1983) tracked instantaneous surface slope and 'jumps' in the surface in order to detect breakers. Other criterion have been applied to wave gauge data to impose limiting wave characteristics beyond which breaking is expected

(see Babanin, 2011, pp42-47 for a summary). The earliest of these is the well-known Stokes (1847) limit of

$$\frac{H}{L} = \frac{1}{7} = 0.143, \tag{3.1}$$

which is a theoretical upper bound limit not typically reached by wind-driven waves at the onset of breaking, and not of practical use to accurately determine breaking in time series data. This relationship is often expressed as

$$a_{downwards} = a\omega^2 = \gamma g, \tag{3.2}$$

where the limiting value for γ theoretically is 0.5 but in practice rarely exceeds 0.4, and is often lower (Snyder et al., 1983; Longuet-Higgins, 1985; Liu, 1993; Babanin, 2011). Ramberg and Griffin (1987) suggested a more practical value for the limiting steepness in Equation 3.1 is 0.11 rather than 0.143, and expressed this in the convenient form of

$$H = 0.021gT^2. \tag{3.3}$$

This is almost identical to the results of Ochi and Tsai (1983), who obtained

$$H = 0.020gT^2. \tag{3.4}$$

by averaging the measured acceleration of several breaking events. The limiting value of 1.0 for skewness has also been widely used (see Equation 2.10), as has asymmetry, although the latter was advised against by Babanin (2011). In order to apply Equation 3.2 to random wave fields, Liu (1993) developed a method involving a Continuous Wavelet Transform using the Mortlet wavelet to obtain a local value for ω, which was tested by Liu and Babanin (2004). While promising for quantifying probability of wave breaking in random seas, the distinctly bimodal conditions of a paddle wave being combined with HF wind-waves are substantially different in nature to the sea states for which this method was developed. In addition, this method focuses on the portion of the spectrum with frequencies higher than 1.35 or 1.5 times the peak frequency, and when examining LF waves, much of this portion has been filtered out.

All of the above methods involve limiting values of wave parameters, which are typically associated with the incipient stage of wave breaking, and may at times not detect waves which are already in the later stages of breaking events. In addition, it must also be recalled that the presence of strong wind is known to increase the probability of wave breaking (Babanin et al., 2010), as is the condition of shallow or intermediate water depth (Liu and Babanin, 2004).

Another possible method for detection of wave breaking is the tracking of wave height in an array of distributed wave gauges. A distinct decrease in either wave height or wave growth downstream should indicate the presence of significant dissipation at the point observed.

In the present study, in order to obtain a measure of the likelihood of LF wave breaking either occurring or having recently occurred, it was decided to apply Equation 3.3 / 3.4 to the separated η_{LF} time series, rearranged to the form of

$$K_b = \frac{H}{gT^2}, \tag{3.5}$$

Where K_b in this instance represents the constant 0.021 from Equation 3.3, or 0.020 from Equation 3.4, and is representative of steepness. K_b was evaluated at every fetch, using average LF wave height at that fetch. Figure 3.15 displays the value of K_b as a function of fetch for a few selected cases which exhibited some of the highest K_b values. The decay in LF wave steepness after the onset of breaking is evidence of breaking events persisting for a substantial distance after inception.

Because of this, it was decided that for each case and fetch, an appropriate measure for the likelihood of a breaking event having occurred upwind would be the maximum K_b value anywhere upwind of the fetch in question. K_b on its own, without considering upwind fetches, was considered an appropriate measure for detecting the onset of breaking, but this was secondary in importance to the parameter which takes into account upwind onset of breaking. Some scatter is inevitably present in the maximum K_b value reached prior to breaking, hence the decision to keep these breaking variables as continuous measures, rather than a to binary classification of broken vs non-broken. No large-scale consistent decay of LF waves is visible in this figure for cases where K_b never reached 0.15 or more at any stage. Therefore, a lower bound limit of 0.15 was considered adequate to indicate that strong breaking events were most probably not occurring.

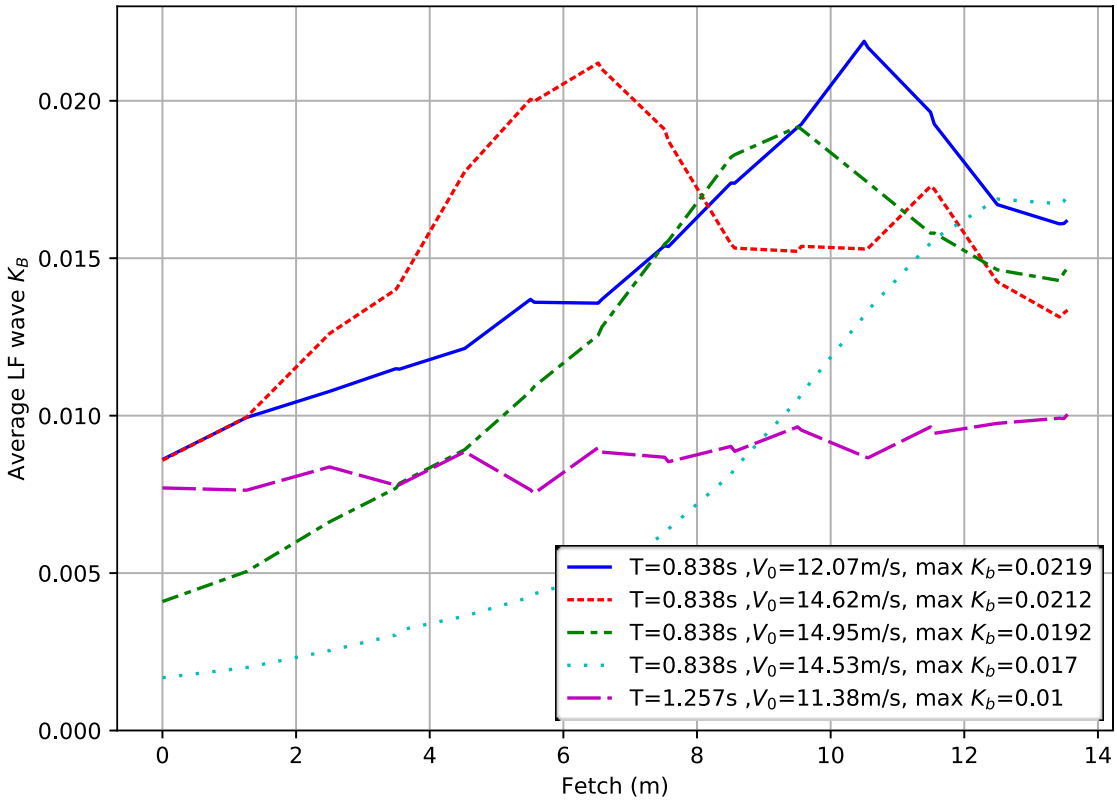

Figure 3.15: K_b measured along the flume for some of the steepest cases. K_b is according to Equation 3.5.

The breaking-detection parameters used in this thesis were thus:

1. Average value of LF wave $\frac{H}{gT^2}$, and
2. Value of LF wave $\frac{H}{gT^2}$ relative to the maximum of all upwind gauges (meaning LF wave likely already broken).

Most recordings in LAB2016 exhibited a K_B value below 0.02, although a small subset of measurements were shown to exceed this.

3.4.4 Calculation of wind shear velocity

Shear velocity was obtained in a manner similar to Donelan et al. (2004), who made use of pressure tappings in the ceiling of a wind-wave flume for measurement of wind shear at high laboratory wind velocities up to 30m/s, in conditions where airborne spray rendered pitot tube wind measurement impractical. Donelan et al. (2004) examined a control volume of water in the flume depicted in Figure 3.16, and derived the relation

$$\tau = \rho_w g s h + \frac{\Delta P}{L} h + \frac{\Delta S_{xx}}{L} h - \tau_b, \tag{3.6}$$

where τ is the average wind shear stress in Pascals acting along the water surface between cross sections A_1 and A_2 (See Figure 3.16), L is the distance between sections A_1 and A_2, s is the gradient of the water surface, $(H_2 - H_1)/L$, h is the average depth $(h_1 + h_2)/2$, $\Delta P = P_2 - P_1$ the wind pressure difference, expected to be negative, $\Delta S_{xx} = S_{xx2} - S_{xx1}$ is the change in radiation stress, and τ_b is the water shear stress acting at the bed. In the present experiment, no instrument was installed to measure water stress near the bed, so this term was ignored, based on observations by Donelan et al. (2004) that τ_b was of order magnitude less than 2% of the total stress. Loss of momentum due to water leaving the wind-wave flume via airborne wind particles was also ignored in the present study, being estimated by Donelan et al. (2004) to have a magnitude of 1.5% or less of the total shear stress.

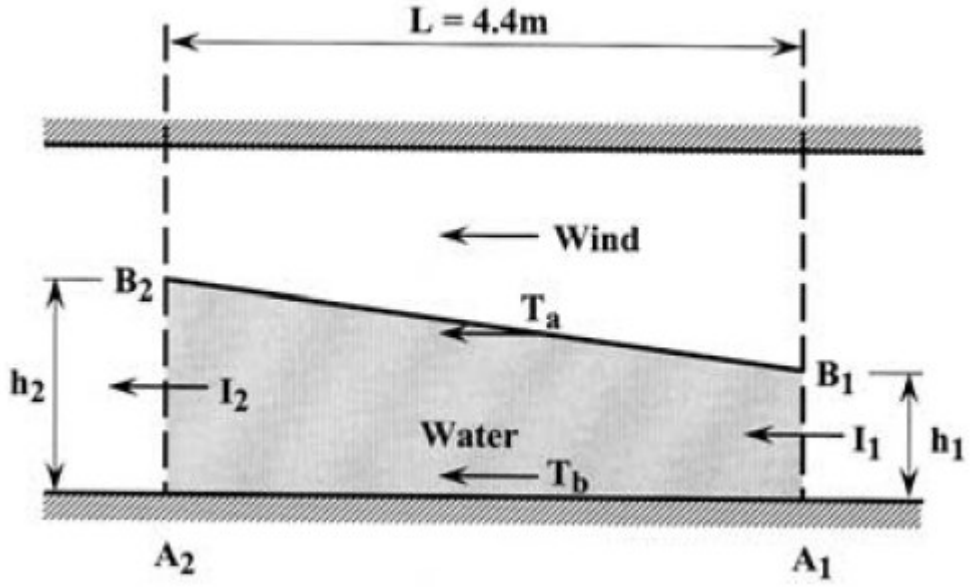

Figure 3.16: Figure from Donelan et al. (2004) of control volume within the wind-wave flume, used to derive the expression of wind shear stress acting at the water surface. See text for description.

For low wind velocities, shear velocity is strongly affected by any imperfection or inaccuracy in wind pressure measurements, because these measurements of ΔP are very small. Based on observations, the instrumentation was not considered sufficiently accurate to measure shear stress for wind fan frequency of 20Hz or lower, so V^* measurements for this fan frequency were ignored. In addition, due to scatter in V^* measured between individual ceiling pressure tappings, the shear velocity was averaged across the whole fetch, using the first and last tapping, at fetches 2.349m and12.349m respectively.

3.5 Summary

This chapter has summarised the methodology employed in designing, building and operating the required laboratory experiments for the present study. The facilities built were mostly consistent with past wind-wave laboratory experiments. However, the large range of wind and wave conditions and fetches measured, including the repeat of transitions from WO to W+P conditions, provided means to obtain some novel insights and evaluate the questions posed in Section 2.3. Examination of laboratory wave gauge data from LAB2016 provided the majority of analysis and insights reported on in this thesis.

4 Setup of field experiment

A field experiment was carried out during March 2016 at Lake Cootharaba, in Queensland Australia, which experiment is termed COOTHA in this thesis. One primary aim of this fetch limited experiment was to measure water velocities underneath growing forced wind-waves, to investigate vertical transfer of horizontal momentum through the water column, which research has not been documented in this thesis. A second aspect of this experiment was an attempt to detect HF wave suppression by LF waves in the field, using a point wave gauge. This section outlines the experimental setup and procedure. Some of the instruments do not play a major part in the data analysed in this thesis, but their deployment is included to provide an accurate account of the experimental setup.

4.1 Locality and time

Lake Cootharaba is located in the Sunshine Coast region in Queensland, Australia. It is separated from the ocean in line-of-sight direction by a line of small hills, with an average separation between lake and ocean of ca. 2km. At its SSW point it feeds into the Noosa River, and is connected to the ocean via ca. 19km of tidal river passages. The lake is known to experience strong winds during the months of December to March, predominantly from a south-easterly direction. While measuring ca. 9.5km through its longest dimension running SSW – NNE, and ca. 4.5km across it's shorter dimension WNW – ESE, it is relatively shallow, averaging a depth of 1-2m throughout the lake. Slight periodic fluctuations in the MWS elevation were present, consisting of a small tidal component with amplitude of the order of 0.05 to 0.1m, as well as a seiche component with amplitude in the order of 0.01m, the latter caused by wind shear stress. The bed is mostly soft mud, but some parts are firm with rock or sand. An instrument mast was deployed at ca. latitude -26.241° and longitude 153.025°, in the north-western part of the lake, on a flat section of the bed in an area with rock and sand. This location maintained a distance from the NW shoreline in the order of 400m, and an average fetch of 3 – 4km, depending on the wind direction. The depth at the primary measurement site was ca. 1.55m, but was observed to be ca. 2m across much of the fetch near the middle of the lake.

In addition to the primary measurement site, star pickets were installed at three other locations through the fetch, with self-logging pressure transducers installed on each star picket at ca. 0.6m depth, which enabled approximate measurement of the long wave amplitude at multiple stages in the fetch. To each star picket was attached a stilling well,

which provided a mean water surface elevation with wind-waves damped out to assist with calibration. Measurement locations are described in Figure 4.1, and Table 4.1.

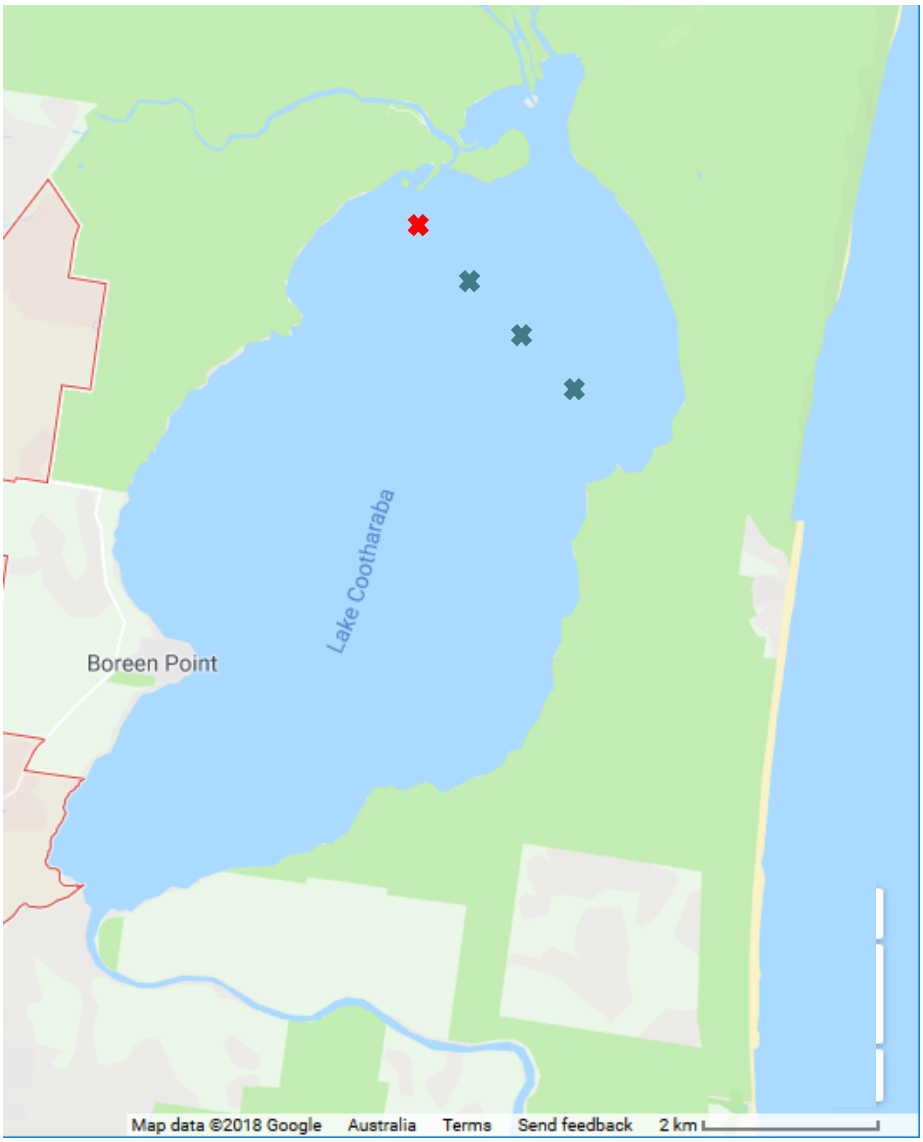

Figure 4.1: Map of Lake Cootharaba measurement sites. Red cross (A) marks the location of the instrument tower, while blue crosses (B, C, D) mark locations of pressure transducers fastened to star pickets. Map data © 2018 Google Australia.

Table 4.1: Instrument deployment locations

Location	Structure	Measurements
A	Instrument mast	Wind velocity, temperature, water surface elevation, water velocity, water pressure
B	Star picket	Water pressure
C	Star picket	Water pressure
D	Star picket	Water pressure

Measurements documented in this thesis were recorded over a period of approximately 6 days, from 13th to 19th March 2016. On the first day, from ca. 0830hrs 13/03/2016 to ca. 1200hrs 14/03/2016, a data logging issue resulted in the logger not capturing every ca. 2nd sample point, meaning on this day the effective sampling frequency was ca. 7-10Hz instead of the designed 20Hz. Given that the goal of analysing HF waves in the range up to 4-5Hz, this low sample frequency was considered inadequate. Because of this, data recorded during that period was not included in results in Chapter 5, except in the overview of Figure 5.37.

4.2 Instrument mast

The mast deployed was of ca. 5.1m maximum height, measured from the lake bed to the measurement volume of the highest anemometer, with the supporting structure being constructed of 80mm OD aluminium tube extending ca. 4.59m above the lake bed. A photograph is displayed in Figure 4.2. The mast was seated upon a base unit from which protruded three thick tubes, or horizontal legs, two of which extended ca. 3m from the mast centreline, and the third extending ca. 2.4m from the mast centreline. The weight and spread of this base unit were sufficient to prevent any sliding or overturning of the mast during strong wind and wave conditions. In order to stiffen the aluminium mast against wind and wave induced vibration, three tensioned guy wires were connected between the outer extents of each base leg and a point near the top of the mast. This eliminated deflection greater than the order of a few millimetres when testing by cyclic hand forcing. The assembled mast was floated with drums attached to the ends of the three legs, and towed behind a boat to the measurement site where the mast was lowered from its floats.

4.3 Water surface elevation measurement

The primary instrument used for water surface elevation was a two-pronged wave gauge, which was custom built by the writer for this experiment. The prongs consisted of tensioned stainless-steel cable of ca. 4mm thickness, separated by ca. 30mm and insulated at top and bottom from the metal support frame. Insulated copper wires were attached to the top ends of the prongs, which fed an analogue voltage signal to the data logger. The staff was positioned facing the oncoming waves, on the south-east face of the mast, so that wave crests travelling in the dominant direction did not pass any portion of the tower prior to being measured by the wave gauge.

This staff was tested in the fresh water UQ laboratory wave flume prior to deployment, and compared against one of the DHI wave gauges described in Section 3.2.2, in the laboratory wave flume with waves present. Given that the salinity of lake Cootharaba was measured to be ca. ¼ that of sea water, known to exhibit a very different conductance range to the fresh water in the laboratory, it was necessary to calibrate the instrument in the field.

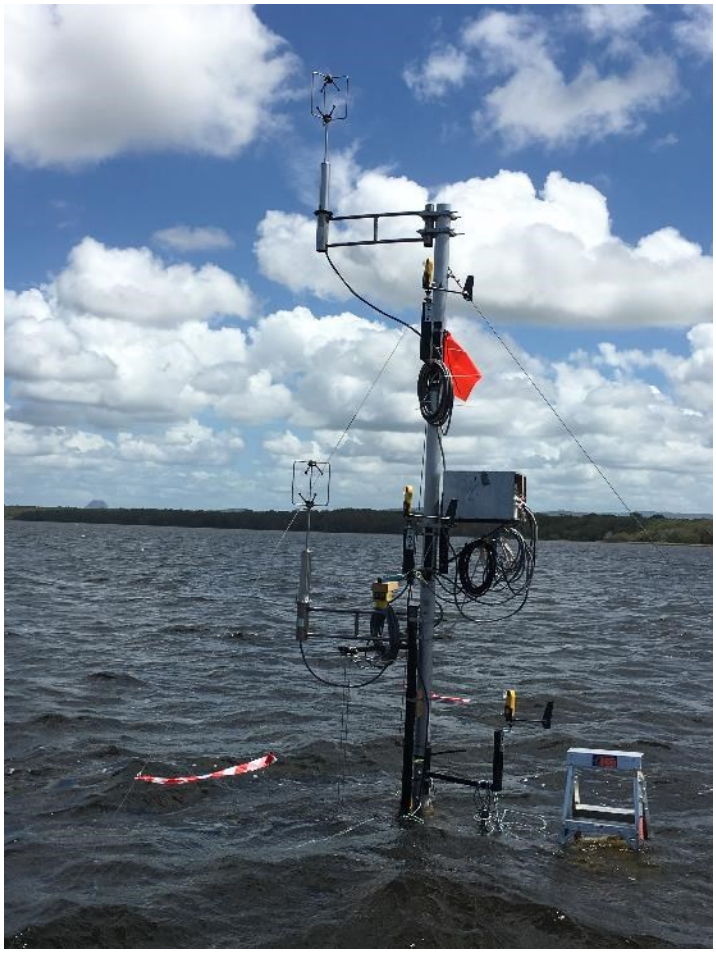

Figure 4.2: Instrument tower.

This wave staff was fixed in place such that adjustment was difficult, and because of this it was only calibrated once during the experiment by means of offsetting the wave gauge above and below the neutral position, and correlating these measured offsets with the voltages measured. A stilling well fastened to the wave gauge enabled the MWS elevation relative to the wave gauge to be captured accurately.

A UDM was also installed at ca. 1.03m above the mean water surface, which output an analogue voltage dependent upon calibration. Unfortunately, due to an instrument error, this instrument only provided a reliable signal for small waves, and could thus not be relied upon primarily for water surface elevation measurement in the experiment. It was thus only used to perform sense checks on the wave gauge signal, comparing the two instruments

during times of relative calm when the signal was clean. During these calm periods, there was insufficient tidal variation to confidently use this instrument to calibrate the wave gauge. It must be noted that any UDM distributed footprint on the water surface is significant relative to the wavelength of at least the smaller HF waves, which must result in under-representation of actual wave heights due to some averaging taking place across the footprint. Because of this, the UDM technology was considered to be inferior to point wave gauges for measurement of HF waves.

4.4 Wind measurement

Wind was primarily measured by means of two Gill Windmaster Pro sonic anemometers, which measured 3D turbulent wind velocity with sampling frequency of 20Hz. These were mounted onto brackets which provided a horizontal separation of ca. 0.6m from the mast. They were positioned at elevations of ca. 3.65m and 1.56m relative to the MWS, and were located crosswind to the pole, to reduce impact on the measurements from the mast. These provided 3D turbulent velocity measurement, which digital signal was fed into the data logger and logged synchronously with other instruments. This was the same wind measurement and logging equipment as was used by Shabani et al. (2014) and Shabani et al. (2016), although deployed at a different location, using a different support structure and positioned at different elevations.

In addition to the sonic anemometers, three self-logging Kestrel 5500 weather stations were deployed at elevations 2.52m, 1.5m and 0.5m above the MWS, which measured mean wind velocity and mean wind direction. These were not considered as precise as the two sonic anemometers, and only sampled at frequencies of one to ten seconds in this experiment, but they did provide the capability for sense checking the Gill Windmaster Pro measurements, and also provided measurements of temperature and relative humidity.

4.5 Water velocity measurement

Water velocities were measured during COOTHA, but analysis of these measurements is not included in this thesis. Deployment of this instrumentation is nonetheless documented for completeness. To support water velocity equipment, a metal frame was stationed on the lake bed immediately adjacent to the instrument mast at a distance of ca. 1m. This stand consisted of a weighted flat base, the top of which sat ca. 55mm above the lake bed, a stiffened 20mm vertical SHS steel bar extending vertically to a height of 0.945m above the lake bed, and a 20mm SHS steel cross bar with its upper face at height 0.585m above the lake bed.

Water velocities were measured using a Sontek YSI Field Acoustic Doppler Velocimeter (ADV). This ADV consisted of a long cylindrical canister connected to a small measurement head via an umbilical cable. The head was stationed at the top of the vertical bar at ca. 0.65m water depth below the MWS, facing upwards to measure point velocities 180mm above the head. The large canister at the other end of the umbilical cable was strapped to the base of the mast, with its axis vertical. This canister also provided real-time measurement of salinity, water temperature and pressure, which was digitally output from the system in sync with the three-component water velocity, and fed into the data logger.

In addition to the ADV, a self-logging Nortek Aquadopp Acoustic Doppler Current Profiler (ADCP) was deployed on the stand. For some periods of the experiment it was positioned on top of the base, while at other times it was strapped to the cross bar at elevation 0.585m above the lake bed. Its head extended beyond the end of the bar, and was thus horizontally separated from the ADV head by ca. 1m. This profiler was able to provide a measure of velocities throughout the water column and provided an indication of depth, but was not considered as accurate as the ADV, and neither of these instruments are discussed further in this thesis.

4.6 Data logging

A Campbell Scientific CR1000 data logger was used to capture, synchronise and timestamp measurements from the ADV, wave gauge, sonic anemometers and UDM. This logger possessed out of the box capability for excitation and recording of electrical resistance instruments on one of its ports, and was thus equipped to excite and measure the resistance (or conductance) of the wave gauge described in Section 4.3. The logger was set to sample at 20Hz, although at this sample frequency, with the large number of instruments deployed, it was found to be at borderline capacity to write data to the SD card. As previously discussed, on one day of recording the logger malfunctioned and was only able to sample at 7 - 10Hz, and during other runs it occasionally missed data points. However, because its timestamping was observed to be reliable even when data points were missed, single missing data points at 20Hz sampling frequency were not fatal to the usability of the data.

4.7 Spike detection and removal

It is well documented that data from sonic anemometers can exhibit unphysical spiking (Shabani et al., 2014; Szhwartz, 2008, p97), and such require detection and cleaning before anemometer data can be used to determine wind stress. Schwartz (2008) observed that

spikes occur in multiple channels for the one instrument simultaneously, and Shabani et al. (2014) similarly observed them to occur in multiple instruments connected to the one data logger simultaneously, the latter attributing them to be caused at least partially by rain events. As previously documented, the present study was performed using the same sonic anemometry and logging equipment as was used by Shabani et al. (2014), and unsurprisingly exhibited simultaneous multi-instrument spikes or defects. However, these were more obvious in wave gauge and UDM time series data, and observed less in the anemometer time series. Significant rain was only present on one of the deployment days (17th March), so it seems most likely that momentary interference in the data logger was responsible for the majority of the spikes, rather than rain. Schwartz 2008 documented spikes to only affect single isolated data points, but in the present study defects often affected up to three adjacent data points. An example spike only affecting one data point is shown in Figure 4.3.

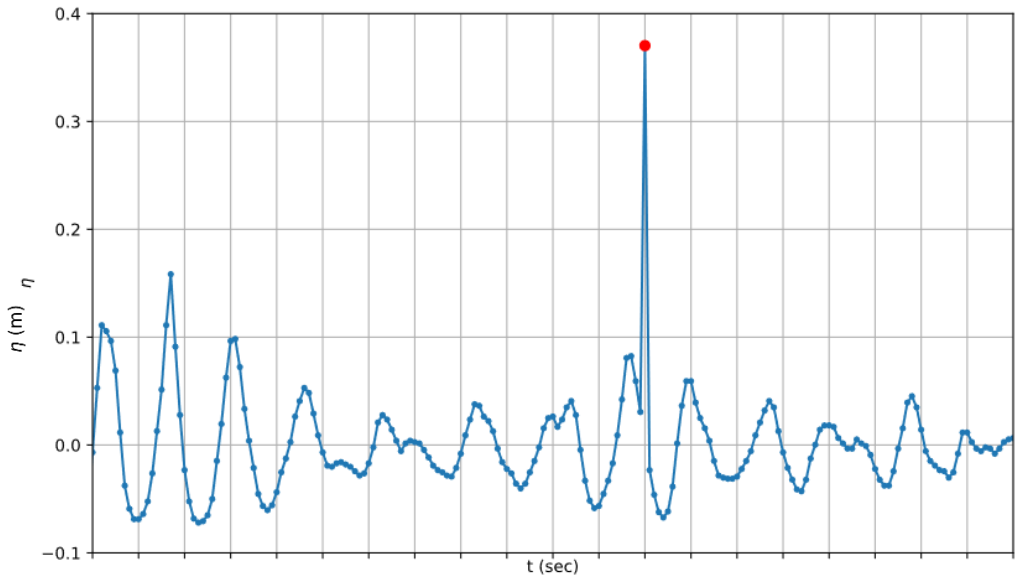

Figure 4.3: An example spike in the wave gauge record, highlighted by the solid red circle. Each tick on the X-axis represents ca. 1 second.

A spike detection algorithm comparable to that of Shabani et al. (2014) was developed, which was further custom-modified and calibrated to the present dataset. The critical requirement for the present study was removal of spikes in the wave gauge signal, as opposed to the study of Shabani et al. (2014) which was a study in wind stress. While these spikes were rarely observed in the wind data, rainy periods were excluded from most analysis, and this was expected to remove the effect of spikes in the wind data. For processing the wave gauge data, the customised spike detection algorithm is described as follows.

The absolute η value (with MWS set to zero) was compared to the standard deviation of η during a rolling window of the previous 6000 sample points, $\sigma_{\eta.rolling}$, which window was typically ca. 5 minutes when the data logger functioned correctly. The instantaneous value of $\delta\eta/\delta t$ was also compared against its standard deviation during the same rolling window, $\sigma_{\frac{\delta\eta}{\delta t}.rolling}$. Trigger values for η of +7× $\sigma_{\eta.rolling}$ and -4× $\sigma_{\eta.rolling}$ were selected, along with trigger values of ±5× $\sigma_{\frac{\delta\eta}{\delta t}.rolling}$ for $\delta\eta/\delta t$. The data point was registered as a spike if any one of the positive or negative η or $\delta\eta/\delta t$ trigger values was reached or exceeded.

As previously mentioned, it was observed that the anomalies could cover multiple data points, although rarely more than 2. Once a spike was triggered at one data point, the trigger values for absolute η for detecting spikes in the subsequent points were reduced to +5× $\sigma_{\eta.rolling}$ and -3× $\sigma_{\eta.rolling}$ times the standard deviation, and slope trigger was reduced to ±4× $\sigma_{\frac{\delta\eta}{\delta t}.rolling}$, because the likelihood of the next few points exhibiting non-physical spiking was observed to be much higher than that for most other data points. After triggering a spike, once a subsequent data point was encountered which did not register as a spike, the trigger thresholds were reset to the original values from that point on, until the next spike was detected.

Upon passing the slope detection function over the dataset, spikes were removed, with the algorithm being run again several times. The reason for this repetition was that some spikes were sufficiently large as to affect the rolling standard deviations of η and $\delta\eta/\delta t$, so for each successive run where some spikes were removed, the standard deviation was smaller than the prior run, resulting in lower η and $\delta\eta/\delta t$ trigger threshold values, capturing more spikes which were not detected in the previous slope detection pass. After running the function 5 times, it was found that no more spikes were being detected in any of the datasets, with the rolling standard deviations reaching stationary values. The above-described constants used as limiting multiples of $\sigma_{rolling}$ for both η and $\delta\eta/\delta t$ were calibrated through a manual trial and checking process which minimised false positives, and upon applying these values, no further spikes were visibly detected by the naked eye within the dataset.

After all spikes were removed, the missing values were interpolated using a linear spline. The linear spline (as opposed to a cubic spline) was considered safer to prevent creation of artificial peaks or troughs in the record, and was consistent with the interpolation used by Shabani et al. (2014).

4.8 Other data quality assurance

After performing interpolation to replace spikes, or data points missing due to temporarily lower sampling frequency, a rule was applied being that any ensemble averaged spectrum failed quality requirements and was discarded if more than 10% of wave gauge data points had been interpolated. In addition, within each ensembled spectrum (typically comprised of an average of 10 individual spectra), if any individual spectrum contained more than three consecutive interpolated data points in any part of the time series from which it was derived, this spectrum was excluded from the ensemble. Any ensemble averaged spectrum was discarded if more than ¼ of the individual contained spectra had been excluded due to the three consecutive interpolated point limit. In addition to the above automated quality assurance, the entire dataset was manually examined for anomalies. Such anomalies include durations where recording was paused, during replacement of batteries, downloading of data from the logger SD card, or other maintenance on the tower. These times were typically known, and easy to filter out. Other anomalies present may have included occasional pollution from the wake of power boats, which frequently used the lake during the experimental period, but these latter occurrences were known to be rare and were not detected by the manual examination of wave gauge time series data.

It was known that substantial rainfall occurred in the area on 17th March. There was no active rainfall detection on the tower, but this was partially mitigated by the sonic temperature measured by the Gill anemometers, which recorded temperature on some but not all days. These time series were examined visually, with sudden drops in temperature or periods of low temperature classified as being periods of likely rainfall. The drops in temperature correlated reasonably well with the known periods of rainfall. Unless explicitly stated, plots in this thesis were produced using data where it is believed no rainfall was occurring at the tower.

4.9 Anemometer tilt correction and wind shear calculation

It is prudent for clarity to mention that within this section, the velocity components u, v, and w, along with all superscripts etc, are in reference to the wind. It is well known that evaluation of wind stress by correlation of horizontal and vertical turbulent fluctuating velocities ($\overline{u'w'}$) may be polluted by any degree of tilt of the anemometer coordinate system relative to the mean wind direction and plane (Shabani, 2013), and consequently data used for this purpose is typically rotated so that the data u coordinate coincides precisely with the mean wind direction. In the present experiment, data from the Gill Windmaster Pro

anemometers was rotated according to the Double Rotation method outlined in detail by Shabani (2013, p119), which sets $\bar{v}$ and $\overline{w}$ to zero over a selected time period, and which method has received widespread usage. In the present experiment, the averaging duration was varied to match the length of time being examined. After applying this method within a specific time period, the resulting w data series was assumed to represent the fluctuating component of vertical velocity, w'. The fluctuating component of velocity in the dominant wind direction, u', was obtained by taking the rotated u dataset and subtracting its mean, $\bar{u}$. Shear stress was then obtained by

$$\rho_a \overline{u'w'} \tag{4.1}$$

After applying this method, stress measurements at the top sonic anemometer were observed to be 23% greater on average than at the bottom sonic anemometer, after removing records with less than 3m/s average velocity at the bottom anemometer. This variation between top and bottom anemometer stress is greater than observations by Shabani et al. (2014) displayed in Figure 14 of this paper, in which the variation appeared to range from ca. 2% to 25% depending on location of that instrument relative to the shoreline, but averaging ca. 11%. However, the surface in that study was sand and nearshore swash and breaking waves, which surface was different in nature to the water surface in the present study. Shabani et al. (2014) also excluded time periods with very low wind velocity, which were known to exhibit a greater degree of variation. The calculated shear velocity is plotted against mean wind velocity for the top anemometer in Figure 4.4, exhibiting the expected dependence of shear velocity on average wind velocity, suggesting the V^* obtained in the present study was fit for the purpose of examining HF and LF wave interaction.

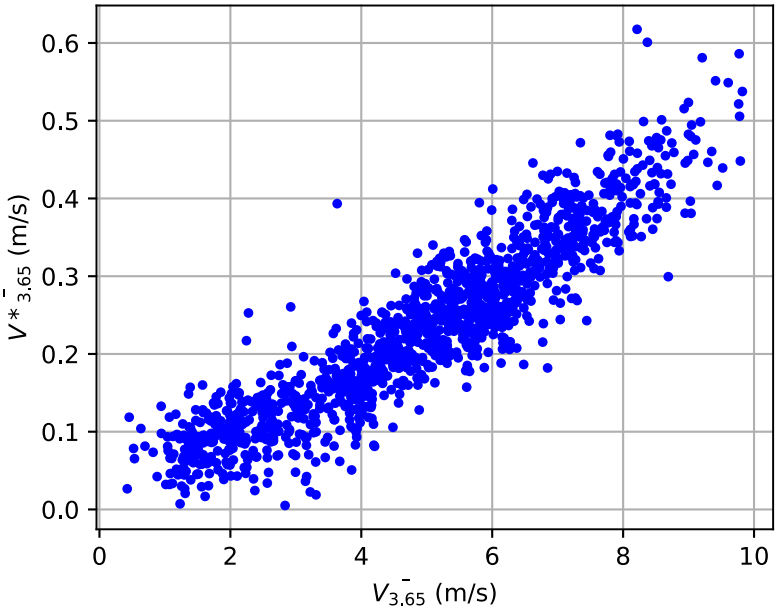

Figure 4.4: COOTHA $V^*_{3.65}$ vs $\overline{V_{3.65}}$, for 4-minute averaging periods.

4.10 Separation of field HF and LF waves

Separation of HF and LF waves was inherently more difficult in field data with frequency distributed LF waves than in wave flume data, where LF waves were monochromatic and controlled. Mitsuyasu (1977) used a differentiating circuit to separate HF and LF waves with apparently great effectiveness, but details regarding the mathematics used were not provided in this publication. Hanson (1997) developed an algorithm to partition HF and LF waves, but such relied upon measurements of wave direction.

In the present study, relatively simple methods were adopted. Initially a HF maximum frequency was determined to be 4Hz, with the HF lower limit (also the LF upper limit) equal to $1.5f_p$, and the LF lower limit set as $0.5f_p$. All energy below the LF lower limit (i.e. tides and seiching) was ignored, as was all energy above 4Hz. This dependence of cut-off frequencies on the spectral peak had the advantage of scalability with wave spectra at varying stages of evolution. However, use of this method on COOTHA data was found to cause distortion of two types. The first type of distortion occurred in a minority of cases with extremely LF wave conditions. In these conditions, energy in frequencies typically associated with HF energy (e.g. 2-3Hz) was sometimes greater than the energy in frequencies typically associated with LF energy (e.g. 0.5-1.0Hz), fluctuating substantially between the higher and lower frequencies from one chunk to the next adjacent chunk. The second type of pollution occurred due to slight shifting of the spectral peak resulting at times

in a large change in HF energy due to the relatively large width of frequency bins. This is demonstrated in the example spectrum displayed in Figure 4.5. In this spectrum, energy in the bin immediately adjacent to f_p (at higher frequency) was almost as great as that in f_p. If energy at frequency $f_p + \delta f$ were slightly greater, the spectral peak would have shifted by δf, resulting in the cut-off frequency between LF and HF energy being consequently higher. The energy in the bin marked with a red X, currently attributed to HF energy would have been attributed to LF energy if the spectral peak had shifted in this way. This would have caused a reduction in calculated HF energy of 29% in this instance, caused by the slight shift in f_p which is not related at all physically to HF energy.

A greater duration of ensemble averaging could have smoothed the spectra reducing the susceptibility for scatter in HF energy, but this was not desirable as HF energy was anticipated to change at timescales shorter than the ca. 5 minutes of ensemble required to adequately smooth the spectrum. It was determined that cut-off frequencies should remain constant, sacrificing scalability to avoid the above illustrated susceptibility for irrelevant scatter in HF energy values. The LF lower limit was fixed at 0.33Hz, the LF upper limit / HF lower limit was fixed at 1.5Hz, and the upper limit of HF energy remained fixed at 4Hz. One weakness of this method was that did not enable attribution of the higher harmonics of LF waves correctly to LF energy. It was hoped that in spite of this, trends of HF wave energy (E_{HF}) dependence on LF wave energy (E_{LF}) could still be observed in the data.

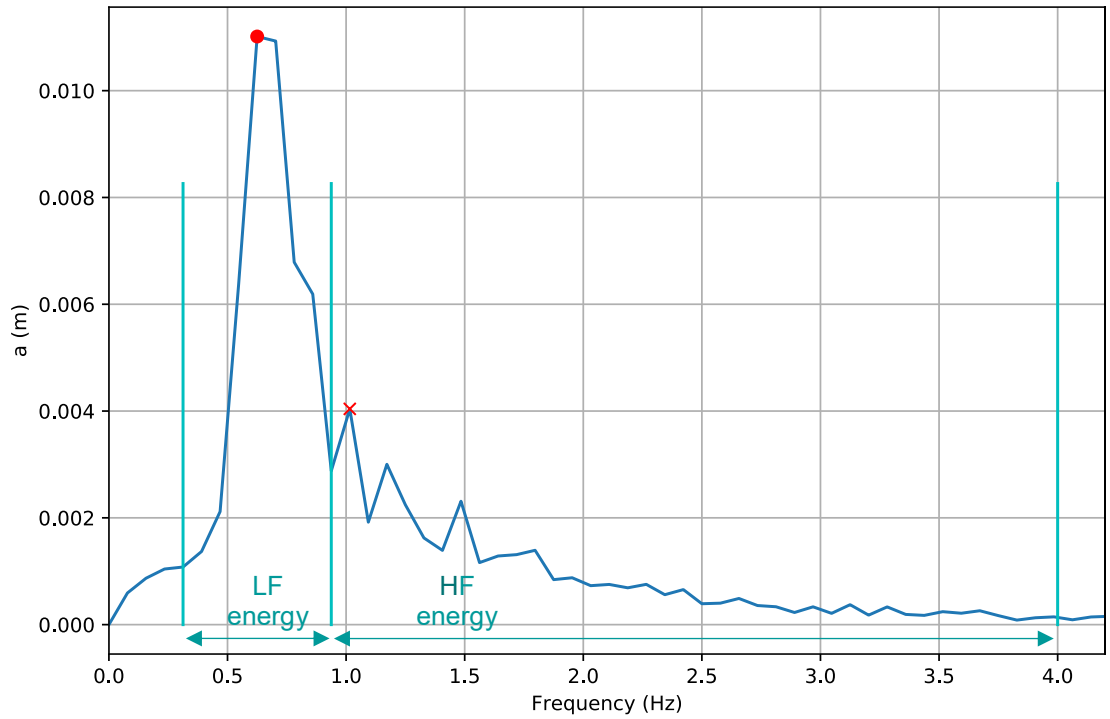

Figure 4.5: Separation of example spectrum from COOTHA, with cut-off frequencies dependent on f_p. Spectral peak is highlighted with a red solid circle, at 0.625Hz. Cut-off frequencies for LF and HF waves are marked with vertical cyan lines. See text for details concerning the red X.

4.11 Summary

This chapter has summarised the COOTHA field experimental procedure performed in March 2016. The goal of the experiment was not limited to the study of suppression of HF waves by LF waves, but was able to capture more than 100 hours of synchronised wind and wave gauge data for analysis to examine HF wave dependency on LF waves. Studies of HF wave suppression by field LF waves have typically referred to swell as the LF waves, which are known to exhibit very small steepness. Few if any past studies describing suppression in the field have explicitly discussed the effect that dominant wind-waves in the lower frequency portion of a wind sea may have on HF wind-waves on the forward face of the spectrum. The COOTHA experiment focused solely on LF waves of this nature, because swell did not exist in the coastal lake. It was an attempt to identify the suppression of HF waves by LF waves still classed as wind-sea, but less distant in frequency space, and greater in steepness, than swell waves.

5 Experimental results and analysis

This chapter outlines observations made and analysis of data obtained during the experiments performed in this study. It may be recalled that the five principle research questions discussed in Section 2.3 were;

1. Is suppression caused by destruction or inhibited growth of HF waves,
2. Is suppression a result of LF wave breaking,
3. Is suppression caused by wind separation at LF wave crests,
4. Is suppression due to Hasselmann (1962) nonlinear interactions, and
5. Is suppression significant in field conditions.

The content of this chapter is not organised strictly according to these questions, but rather organised by the nature of the observations, some of which were unexpected but relevant and novel. Research Question 4 was addressed by some comments included in Section 5.1, as well as in Section 5.7. Section 5.2 briefly notes some anecdotal observations of reducing HF energy versus fetch, being of relevance to suppression generally. Research Question 1 is addressed primarily in the observations of temporal transition from WO to W+P forcing in Section 5.3, and also in the distribution of HF energy throughout the LF wave phase in Section 5.4. Research Questions 2 and 3 are addressed as part of the examination of general suppression trends documented in Section 5.5, with the wind separation of Research Question 3 also discussed in Section 5.7. Section 5.6 documents observed enhancement of HF waves and 5.7 documents observed nonlinearity of LF wave growth, and both of which observations were unexpected, but which have relevance to suppression and to wind-wave theory generally. Research Question 5 is addressed in Section 5.8.

5.1 Typical HF suppressed conditions

To commence, it is appropriate to demonstrate the manner in which suppression was typically evident in laboratory data in the present study, in both time and frequency domains. In the time domain, suppression was identified by comparing wave conditions under constant wind fan forcing, with and without paddle waves. Linear wave theory states that multiple wave trains of different frequencies should not interact when superimposed. In practice, given that no waves of finite steepness are purely linear, it is generally assumed that permanent distortion of each wave train is usually minimal. However, what was observed, as shown in the example time series of Figure 5.1, was that the height of the wind-generated HF waves under W+P conditions ($H_{HF_{w+p}}$) displayed in (c) and (d) of this figure

was much smaller than the height of wind-generated HF waves in WO conditions ($H_{HF_{WO}}$) in (a), indicating that HF waves were suppressed by the LF waves.

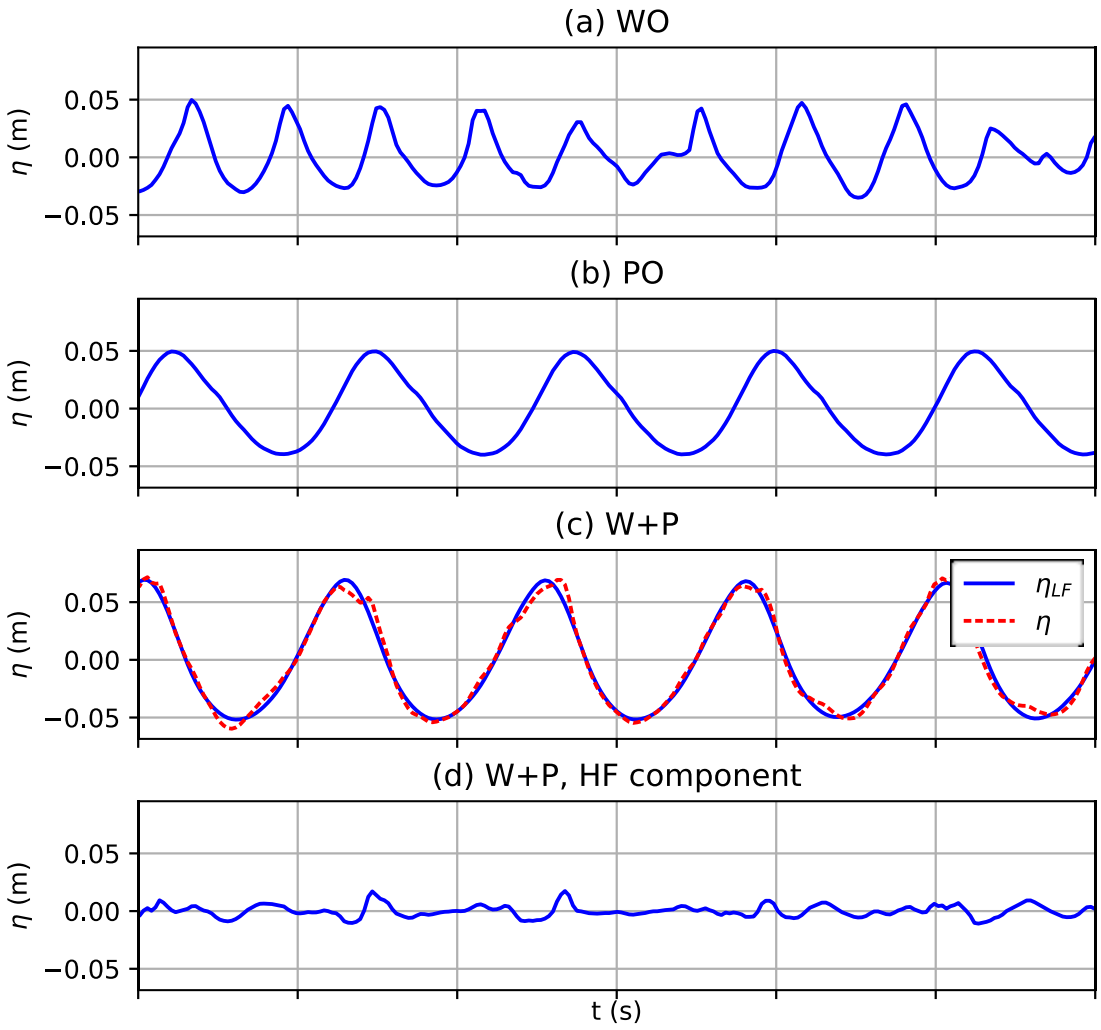

Figure 5.1: Comparison of η time series at fetch=10.56m for one case in LAB2016, displaying (a) WO conditions with f_{fan} =40Hz, V_0 =11.4m/s, V^* =0.97m/s, (b) PO conditions with T_{pad}=1.26s and H_{pad}=0.1m, (c) W+P with the measured waves plotted in dashed red and the filtered LF component, $\eta_{LF_{w+p}}$ plotted in blue, and (d) the filtered HF component, $\eta_{HF_{w+p}}$ for W+P conditions. Time axis ticks are at 1s intervals.

In the spectral domain, suppression of HF waves is manifest in a reduction of energy at frequencies which would have contained energy under identical wind conditions in the absence of paddle waves, as shown in Figure 5.2. In some but not all experimental conditions, including those of Figure 5.1 and 5.2, significant growth of η_{LF} due to wind forcing was visible in both time and frequency domains.

Of note in these spectra is the absence of energy in the W+P spectrum near ca. 1Hz, being greater in frequency than the fundamental paddle wave frequency but lesser in

frequency than almost the entire wind-only spectrum. This has relevance to Research Question 4. Theories involving suppression dependent upon Hasselmann (1962) type interaction, which interaction is typically associated with continuous flow (in frequency space) of energy from higher to lower frequencies, with the interaction effect reducing to almost zero between frequencies separated by more than a factor of 1.6. It appears impossible for energy to be continuously flowing in frequency space through the part of the spectrum near ca. 1Hz, because there is no energy in those frequencies. This observation also challenges the inference by Plant (1982) based on observations by Plant and Wright (1977) that waves longer than 0.1m grow primarily due to nonlinear interactions, although with the reservation that this inference was based on pure WO wave data, without paddle forcing.

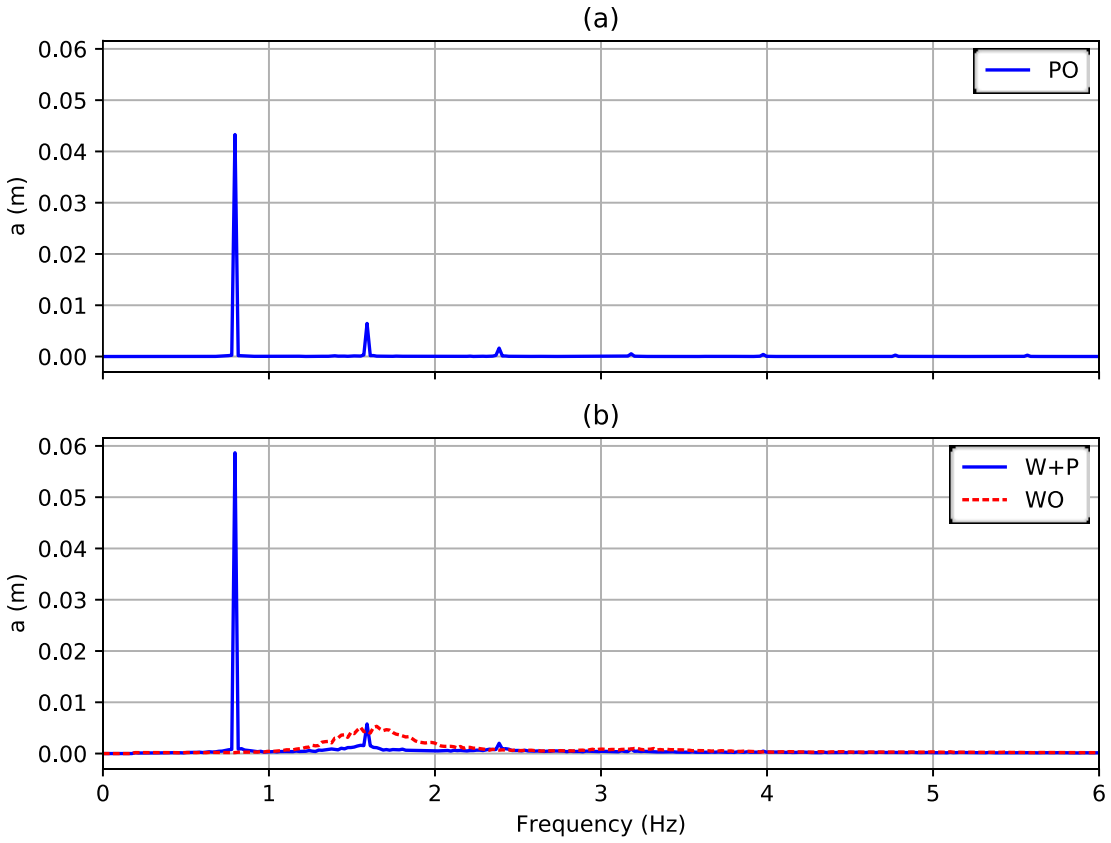

Figure 5.2: Amplitude Spectra of similar conditions to Figure 5.1, fetch=10.56m, V_0=11.4m/s, V^*=0.97m/s, T_{pad}=1.26s, H_{pad}=0.1m.

Through spectral filtering of frequencies using Separation Method 6, documented in Section 3.4.2 of this report, it was found that $E_{HF_{w+p}}$ was ca. 0.11 times the magnitude of $E_{HF_{wo}}$ with an identical wind fan frequency, in the conditions shown in Figures 5.1 and 5.2.

This shall be referred to as having a suppression ratio ($E_{HF_{w+p}}/E_{HF_{wo}}$) of 0.11. Section 5.5 in particular documents the dependence of the suppression ratio on a variety of parameters.

5.2 HF wave energy ($E_{HF_{w+p}}$) saturation and decay along the flume

This brief section highlights the observation that in some conditions $\eta_{HF_{w+p}}$ appeared to reach a fully developed or saturated state beyond which negligible growth took place down the flume, and in a few cases $E_{HF_{W+P}}$ significantly decreased downwind. This decay was documented in cases with a broad range of V_0, and usually but not always with steeper paddle waves. A photographic example is shown in Figure 5.3 (a) and (b), where $E_{HF_{w+p}}$ was clearly much lower at the downwind fetch than at mid-fetch. In these conditions, $E_{HF_{w+p}}$ reached a maximum around mid-tank, never developing far beyond ripple-like conditions, and as such may have been affected strongly by viscous dissipation (Caulliez, 2013) to cause the energy to reduce to the level observed in Figure 5.3 (b). However, decay versus fetch also measured in cases with stronger HF waves.

One such example from LAB2016 in which decay was visible in spectral data, where $\eta_{HF_{w+p}}$ reached a more developed state than in Figure 5.3 is seen in Figure 5.4, at ca. 5.5 to 6.5m fetch, and also at ca. 10.5 to 12.5m. While suppression was significant, with a suppression ratio at the most downwind fetch of 0.32, it was not the strongest suppression case. The conditions in Figures 5.1 and 5.2 exhibited a suppression ratio of ca. one-third of this. Given that suppression is known to correlate with LF wave steepness (Hatori et al., 1981), if H_{LF} had increased significantly downwind, as was observed in many cases, this could have provided a possible explanation, with increasing H_{LF}/L_{LF} resulting in a stronger suppressive force downwind, causing a decrease in $E_{HF_{w+p}}$. However, H_{LF} was not observed to increase significantly prior to the observed HF wave decay in Figure 5.4. This is further evidence of the complex nature of HF wave suppression, and may also indicate a dependence of the suppression mechanics on $E_{HF_{w+p}}$ itself. It may also add weight to theories of enhanced dissipation, rather than suppression by HF waves being inhibited in growth, because if modified wind input according to Chen and Belcher (2000) were the only mechanism, HF waves would logically be expected to plateau in growth but not to substantially decay.

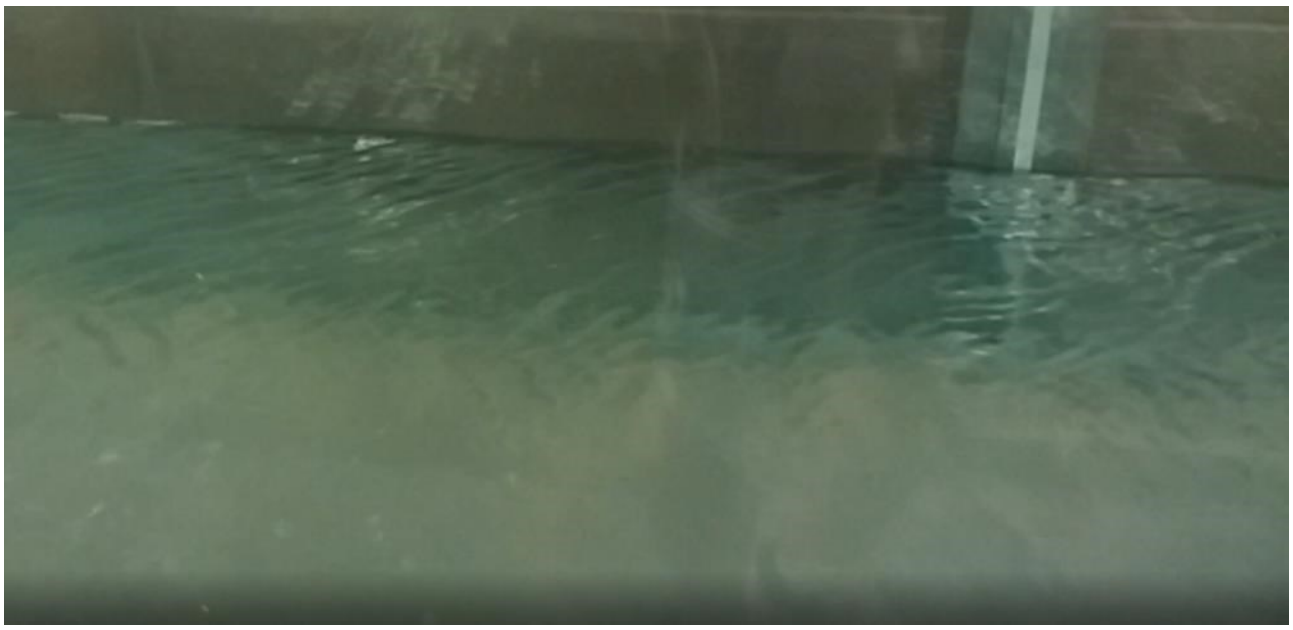

Figure 5.3 (a): Water surface at ca. 5m fetch, f_{fan}=25Hz, T_{pad}=2s, H_{pad}=0.1m.

Figure 5.3 (b): Water surface at ca. 9m fetch, f_{fan}=25Hz, T_{pad}=2s, H_{pad}=0.1m.

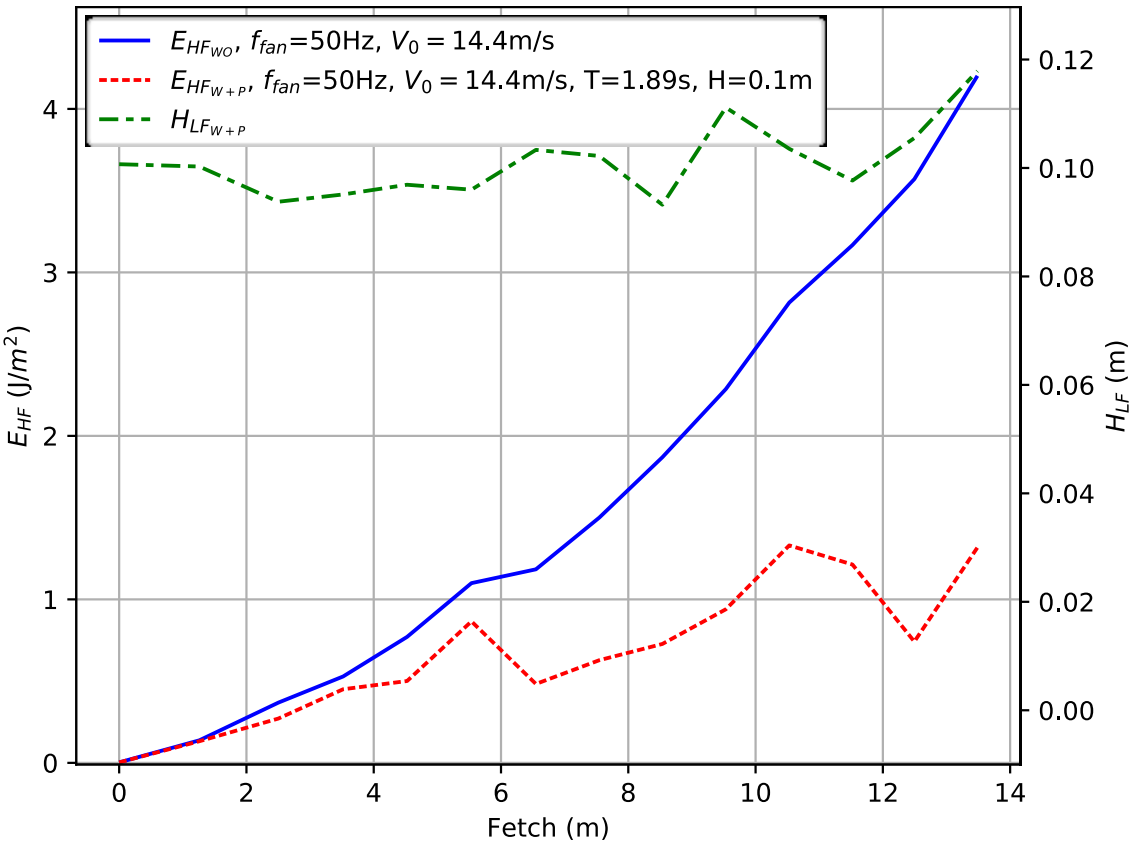

Figure 5.4: E_{HF} under wind forcing as a function of fetch, with and without paddle waves, after filtering out LF waves by Separation Method 6. H_{LF} was averaged in time series using peak to trough measurements on η_{LF}. E_{HF} was obtained by summing the energy throughout the η_{HF} spectrum.

5.3 Wind-only (WO) waves transitioning to wind + paddle (W+P) waves

When HF waves were allowed to reach equilibrium in WO conditions, and then paddle waves introduced, it was observed by Mitsuyasu (1966) (see Figure 2.10 of this thesis) that the HF waves reached their new suppressed equilibrium relatively quickly. This was also generally observed in the present study. This section contains an in-depth analysis of this time scale, and performs a comparison against the evolution time scale of HF waves with no paddle.

As documented in Section 3.3.2, the transition from WO to W+P conditions was repeated 186 times in LAB2016. The conditions selected were H_{pad}=0.1m, T_{pad}=1.26s and wind V_0=11.4m/s, which conditions, based on observations in LAB2015 and in earlier LAB2016 experiments, to exhibit strong suppression. These are the conditions which were presented in Figures 5.1 and 5.2 at a fetch of 10.56m.

The first portion of each repeated transition sequence time series' consisted of WO conditions for at least 60s, which was observed to be adequate to allow $\eta_{HF_{wo}}$ to reach a state close to equilibrium. The paddle was then started without varying the wind fan, and these W+P conditions continued for 60s to allow $\eta_{HF_{w+p}}$ to reach a state close to equilibrium. An example η time series is plotted in Figure 5.5 (a), zoomed in on the time at which paddle waves first arrive at the gauge, in this case at a fetch of 10.56m. After halting the paddle, 60 seconds of WO forcing was allowed before restarting the paddle for the subsequent transition. It was observed that 60s was adequate WO duration to enable HF waves to recover completely from prior suppression, and to allow residual reflected paddle wave energy to be negligible, as demonstrated in Figure 5.5 (b) by the minimal paddle wave energy present prior to the LF wave arrival, i.e. minimum paddle wave energy present at t < 11s in this figure. The allowance of 60s for HF waves to reach equilibrium can be verified in Figure 5.6 by the rapid recovery of H_{HF} near ca. 80s, and in Figure 5.7 by the time taken for $\eta_{HF_{wo}}$ and $H_{HF_{wo}}$ time series' to approach equilibrium from a quiescent state, which was of the order of 30s or less at this fetch.

The transition sequences were performed in segments or batches of 60 minutes, with ca. 240s of WO duration at the commencement of the segment to further ensure HF waves reached equilibrium before commencing the repeated transitions. Between 60-minute batches, the flume water level was topped up to account for water lost as spray from the flume, ensuring that depth did not vary by more than 5mm, and typically only around 1-2mm.

The timing of each transition sequence was carefully synchronised, so that each transition could be compared at exact times after onset of the paddle wave signal. The paddle was programmed with a specific repeated time series, to ensure phase consistency between each transition sequence. Because of this phase consistency, it was possible to average all 186 time series', which effectively filtered out wind generated HF waves due to their being random in nature. The LF paddle wave signal, being consistent between each time series and not random in nature, remained cleanly after averaging, as seen in Figure 5.5 (b). The lack of LF waves prior to t≈11s in this plot was evidence that 60s settling time between each transition was adequate to allow E_{LF} to dissipate. The η_{HF} signal for each transition time series was obtained by subtracting the η_{LF} signal (already extracted by averaging all time series) from the total η signal for each respective time series. Each individual data point on the σ_{HF} curve in Figure 5.5 (c) represented the standard deviation of 186 η data points, each data point being the measurement of η_{HF} at that precise time after the paddle was started within one of the 186 transition sequences. This standard deviation

is proportional to $\sqrt{E_{HF_{w+p}}}$, and is representative of HF wave intensity. While variance may be more commonly used to describe wave spectra, and being proportional to $E_{HF_{w+p}}$ to the first power it corresponds better with wave energy, but variance is in units of length squared, having the disadvantage that that it cannot be displayed on the same axis as η or H, which are in units of length to the first power. Therefore, standard deviation, being also in units of length to the first power, is at times used as a proxy for HF wave intensity in this thesis.

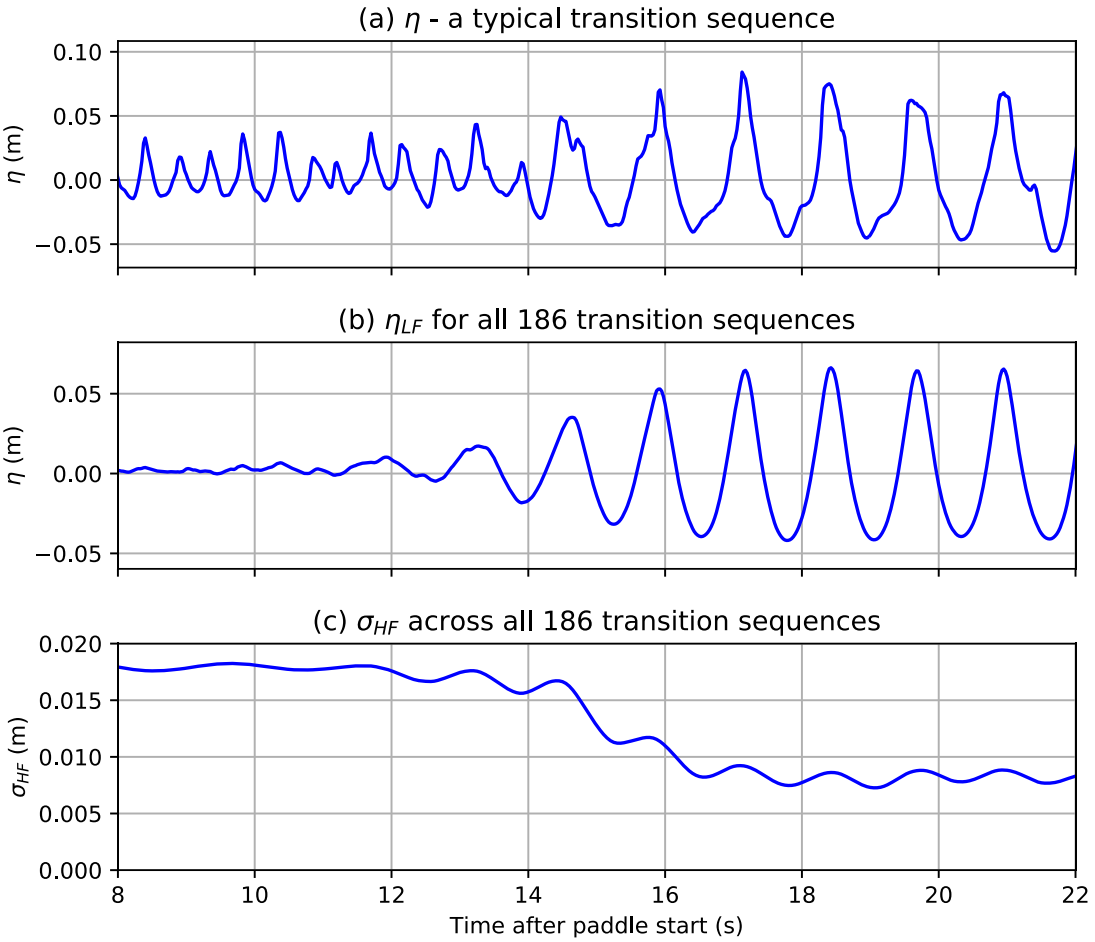

Figure 5.5: Transition time series as paddle waves arrive at fetch=10.56m, (a) for one randomly selected transition time series, (b) η_{LF} obtained by averaging across all 186 transition time series', which effectively filters out HF waves, and (c) σ_{HF}, which represents HF wave intensity. Time series in (c) was smoothed over one paddle wavelength. T_{pad}=1.257s, H_{pad}=0.1m, V_0=11.4m/s, V^*=0.97m/s.

The gradual ramping up of η_{LF} amplitude in each transition, visible in Figure 5.5 (b), is largely unavoidable at the smooth commencement of paddle waves groups, familiar to all who perform wave flume experiments. A similar ramping up of the paddle signal was present in the experiments of Mitsuyasu (1966), as reproduced in Figure 2.10 of this thesis. This ramp was accounted for in the programming of the paddle, although had it not been explicitly

programmed, it would have been present regardless. These paddle waves have an approximate wavelength of 2.1m, meaning that approximately 5 paddle wavelengths are present in the fetch at the point when paddle waves first arrive at 10.56m fetch in Figure 5.5. However, the paddle waves at commencement also take ca. 5 wavelengths to reach its full wave height, as seen in Figure 5.5(b). Therefore, as the start of the paddle wave train arrives at a 10.56m fetch, the paddle waves at zero fetch have only just reached full height.

As seen in Figure 5.5 (c), by the arrival of the first full sized wave, $\sigma_{HF_{w+p}}$ appears to have already approached near to the new suppressed asymptotic equilibrium. The larger σ_{HF} at LF wave crests in Figure 5.5 (c) could be interpreted to indicate that $E_{HF_{w+p}}$ is greater at LF wave crests than in LF wave troughs, but such an interpretation based on from this plot is unreliable, both because the numerical smoothing of the signal in Figure 5.5 (c) reduced resolution, and also because synchronisation between successive paddle waves was likely not perfect. Any slight misalignment of the paddle wave phase between each transition time series' will slightly reduce the represented H_{LF}, but more importantly will attribute some η_{LF} incorrectly as η_{HF}. Misalignment between successive waves and transition sequences may have been due to the active wave absorption at the paddle, resulting in the paddle wave time series being slightly indeterminant. It may also be caused by instability in the η_{LF} train itself, where slight irregularity occurs between successive waves, an example of which is displayed in Figure 3.13.

Further work was performed during post-processing to detect and quantify lag between each of the 186 time series' by means of cross correlation and splines, and each transition was then shifted in phase by the measured time lag. Figure 5.5 was produced from data which had already had this lag correction done. This was found to reduce but not eliminate the sinusoidal pattern in Figure 5.5 (c), which periodic variation would otherwise have appeared larger in Figure 5.5 (c) had this shifting not been performed.

The correlation of HF wave standard deviation with paddle wave phase evident in Figure 5.5 may possibly be a consequence of HF waves being stronger near the crest, but is almost certainly due at least partially to the above described interference. Any such pollution inevitably overestimates $E_{HF_{w+p}}$, and were it possible to perfectly separate HF and LF waves, the suppressed σ_{HF} would be shown in Figure 5.5 (c) after ca. 11s to be even less, corresponding with a lower suppression ration and representing stronger suppression. Examination of the distribution of $E_{HF_{w+p}}$ along the LF wave is addressed more specifically in Section 5.4, using Separation Method 6, which was more effective in mitigating slight

phase variations than the phase-averaging separation method used for transition time series.

Another method of analysis performed on the temporal transition from WO to W+P conditions was the examination of how H_{LF} of individual HF waves responded during the transition. After acquiring the η_{HF} signal, HF waves were individually detected and quantified by performing zero-crossing analysis on the residual HF wave time series from each individual time series. A sharp drop in the average height of individual HF waves was clearly evident in Figure 5.6, with onset at ca. 13s correlating well with the onset of reduced σ_{HF} displayed in Figure 5.5 (c). It was observed in Figure 5.6 that while the majority of decay occurred rapidly, gradual decay continued to take place for ca. 25s after arrival of paddle waves at that fetch. The approximate locations of rapid initial decay and gradual secondary decay are annotated on each of Figures 5.6, 5.9 and 5.10. The 2-stage nature of decay is discussed further in Chapter 6.

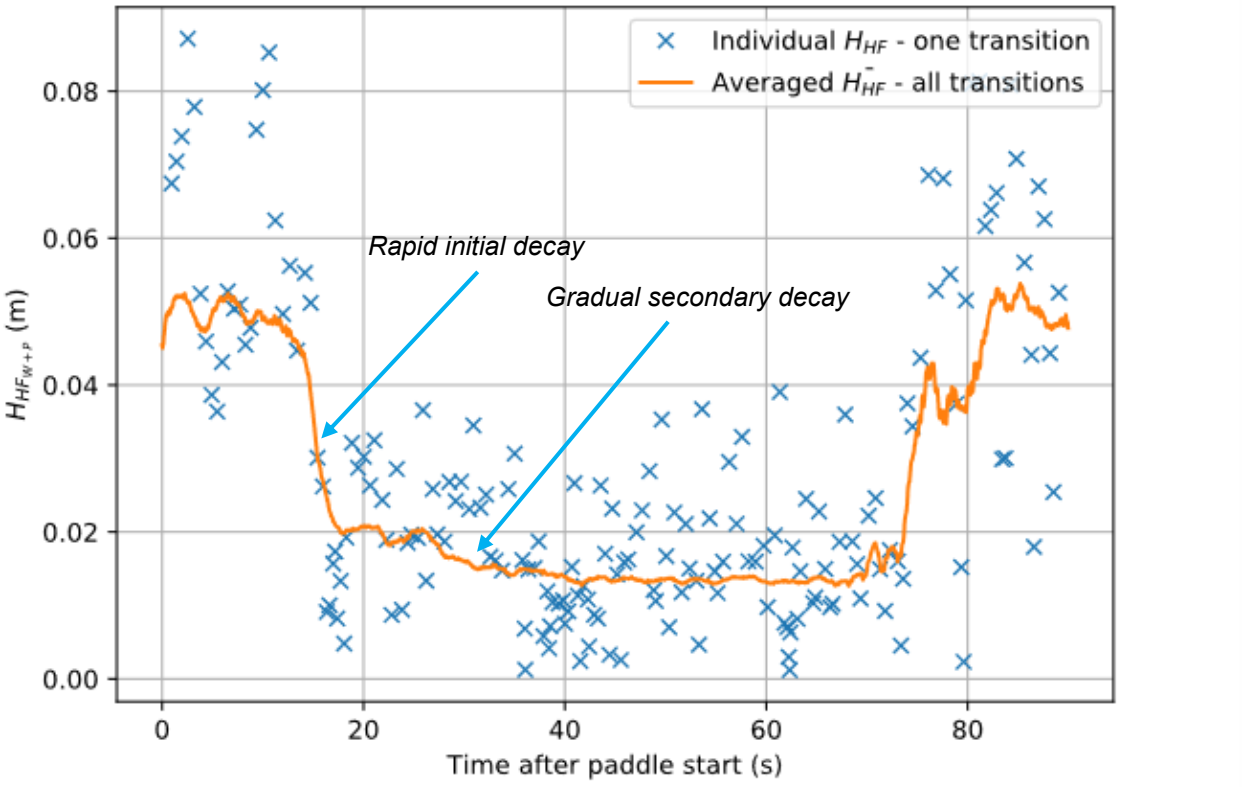

Figure 5.6: Height of individual HF waves (blue crosses) for one randomly selected transition. The brown line represents the average of these across all 186 transitions, smoothed using a rectangular window of length≈ T_{pad} . T_{pad} =1.257s, H_{pad} =0.1m, V_0=11.4m/s, V^*=0.97m/s.

At this point it is appropriate to examine the evolution time of WO HF waves. This was performed by examining the $\eta_{HF_{wo}}$ time series as the wind fan was started from previously quiescent conditions, a situation which occurred at the commencement of many experimental runs, selecting those runs with identical wind fan frequency (40Hz) to that used for the transition sequences.

Figure 5.7 displays a typical experimental start up time series at 10.56m fetch. The wind fan as controlled by its variable speed drive consistently took ca. 12s to spin up to 40Hz, as shown in this plot. After the wind fan reached full speed at ca. 12 seconds, it took a further ca. 14 seconds for the wave heights at this fetch to reach their equilibrium value.

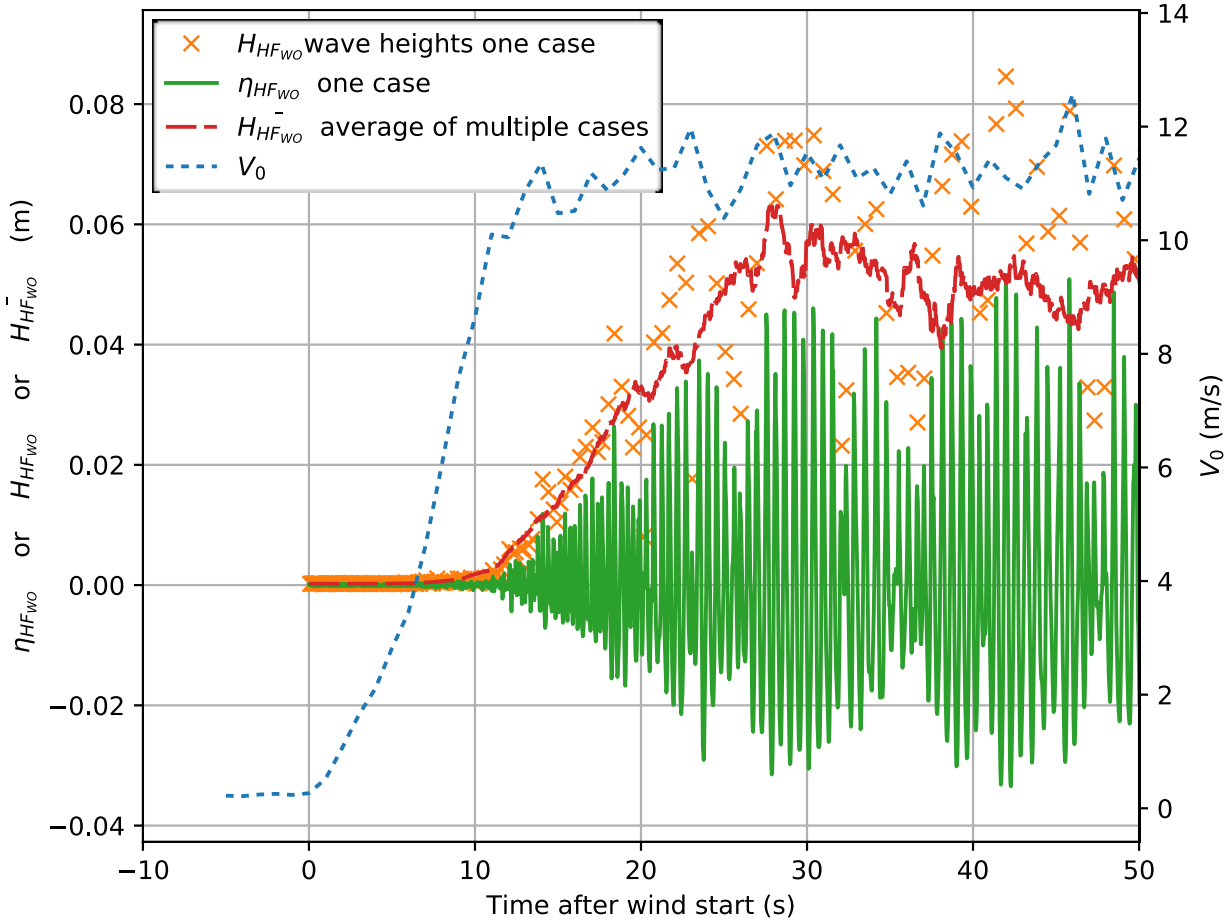

Figure 5.7: Typical wind-only start-up of experimental run (f_{fan}=40Hz, fetch=10.56m). Time zero on this axis is the wind inception time, as opposed to the experiment start time (wind was turned on manually for each run, typically around 3s after wave measurement commenced). The $\overline{H_{HF_{wo}}}$ series was averaged over a window of 1.0s and across 14 cases which all had a fan frequency of 40Hz.

At first glance this $H_{HF_{wo}}$ evolution time appears substantially longer than the time taken by the onset of paddle waves to suppress HF waves to their new equilibrium. Although most reduction in $E_{HF_{w+p}}$ was shown in Figures 5.5 (c) and 5.6 to occur within a few LF wave periods after the arrival of LF waves, it must be noted that by the time paddle waves arrived at a fetch of 10.56m, they had already occupied at least part of the upwind fetch for some time. This could have potentially been influencing the gradual evolution of HF waves in parts of the fetch prior to the LF waves arriving at fetch=10.56m. Paddle waves travelled much quicker than HF waves, especially in the smallest fetches where HF wave periods were close to zero, so any accumulated effect of reducing growth of HF waves should arrive gradually after the LF waves.

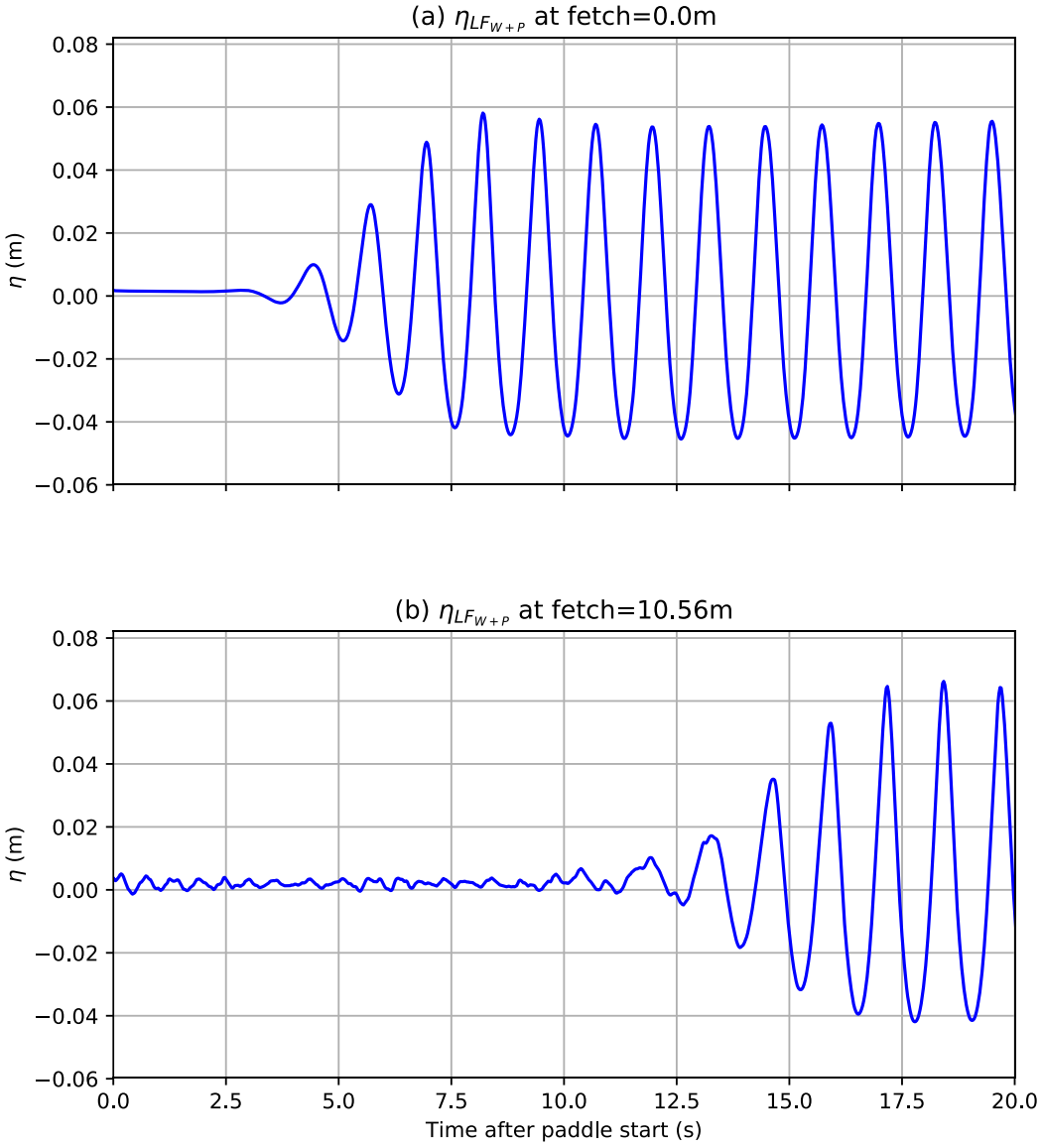

Figure 5.8: η_{LF} time series at two fetches, obtained by averaging across all 186 transition time series'. T_{pad}=1.257s, H_{pad}=0.1m, V_0=11.4m/s, V^*=0.97m/s.

It can be seen in Figure 5.8 that the paddle waves first began to be visible at zero fetch at ca. 3 seconds, while they began to be visible at ca. 11 seconds at 10.56m fetch, indicating that it took 8 seconds for the paddle wave group to reach a fetch of 10.56m, therefore the paddle wave front moved at a group velocity of 1.32m/s. This corresponds reasonably well with the theoretical group velocity of 1.48m/s for waves with T=1.26s in 0.42m water depth. Thus, there are paddle waves of at least some wave height present in at least some part of the upwind fetch for 8 seconds prior to the point at which they arrive at a fetch of 10.56m in the plots of Figures 5.5 and 5.6.

Figure 5.9 compares the duration for HF waves to develop against the duration for HF waves to reach their suppressed equilibrium, in both cases beginning at the time which the driver of change (wind or paddle) first began to exert any possible influence. In Figure 5.9 (a), time zero is the moment that wind begins to move through the flume from zero velocity, although it takes a further ca. 12 seconds for wind to reach full velocity. In Figure 5.9 (b), time zero represents the moment that paddle waves are experienced at the beginning of the flume (as opposed to 10.56m fetch, the location of the wave gauge being examined). The plot may almost be viewed as a race between the time scales of HF wave evolution (a) and suppression (b), in which suppression wins convincingly, at least with respect to the rapid initial decay. Not only did the rapid stage of suppression finish at ca. 15s, compared with ca. 26s for evolution, the maximum rate of change was observed to be ca. 3 times greater for suppression than evolution, evaluated using the gradient lines superimposed on Figure 5.9 (a) and (b).

It is obvious that on face value, this is not an apples-to-apples comparison, given that time scale for wave decay is being compared against time scale for wave growth, and these are two qualitatively different mechanisms. However, the comparison is consistent when testing the hypothesis that HF waves could be suppressed solely by a reduction of wind input, which must occur gradually, accumulating throughout the entire fetch upwind of the fetch being examined, on a time scale comparable to wave build-up from quiescent conditions. It is clear that the majority of suppression occurs much quicker than this. Possibly the strongest evidence of the rapidity of suppression is found by comparing the time at which H_{LF} reaches its maximum, at ca. 14s in Figure 5.10, against the time taken for rapid initial suppression to finish, being ca. 15s in Figure 5.10. This form of comparison may suggest a true suppression time scale of the order of one LF wave period, rather than three or four periods.

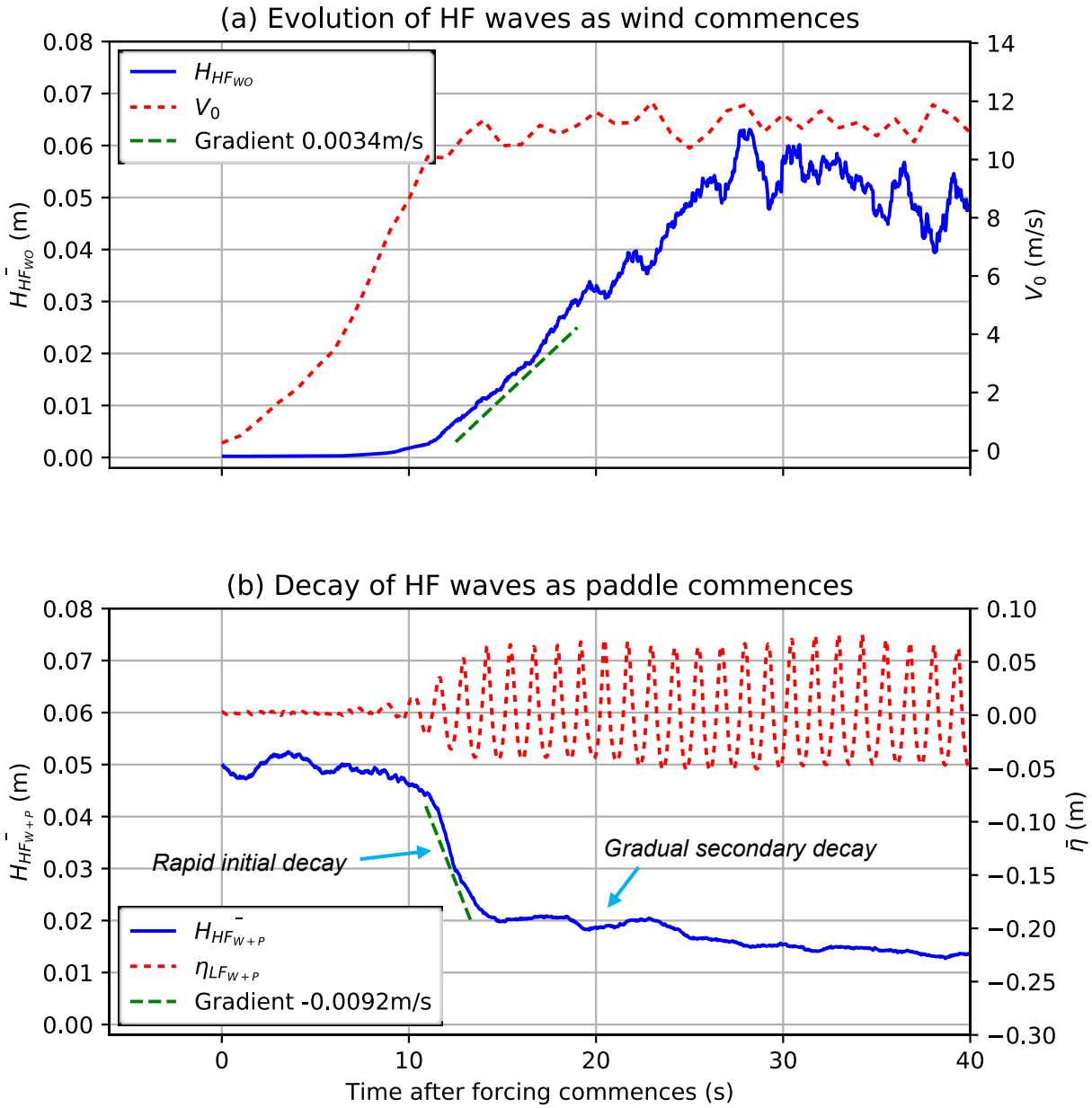

Figure 5.9: (a) Evolution of $H_{HF_{wo}}$ during regular runs at f_{fan}=40Hz, and (b) decay of $H_{HF_{w+p}}$ as paddle waves arrived fetch=10.56m. Paddle waves in (b) were of T_{pad}=1.26s and H_{pad}=0.1m. Time zero in (a) and (b) represents when the forcing mechanism first begins in any small degree, in (a) when the wind fan commencing to spin from stationary, and in (b) the moment at which the start of the paddle wave train arrives at fetch=0m, which is ca. 8s earlier than fetch=10.56m. green dashed lines in (a) and (b) are approximate fits to the H_{HF} gradient, with gradients as marked.

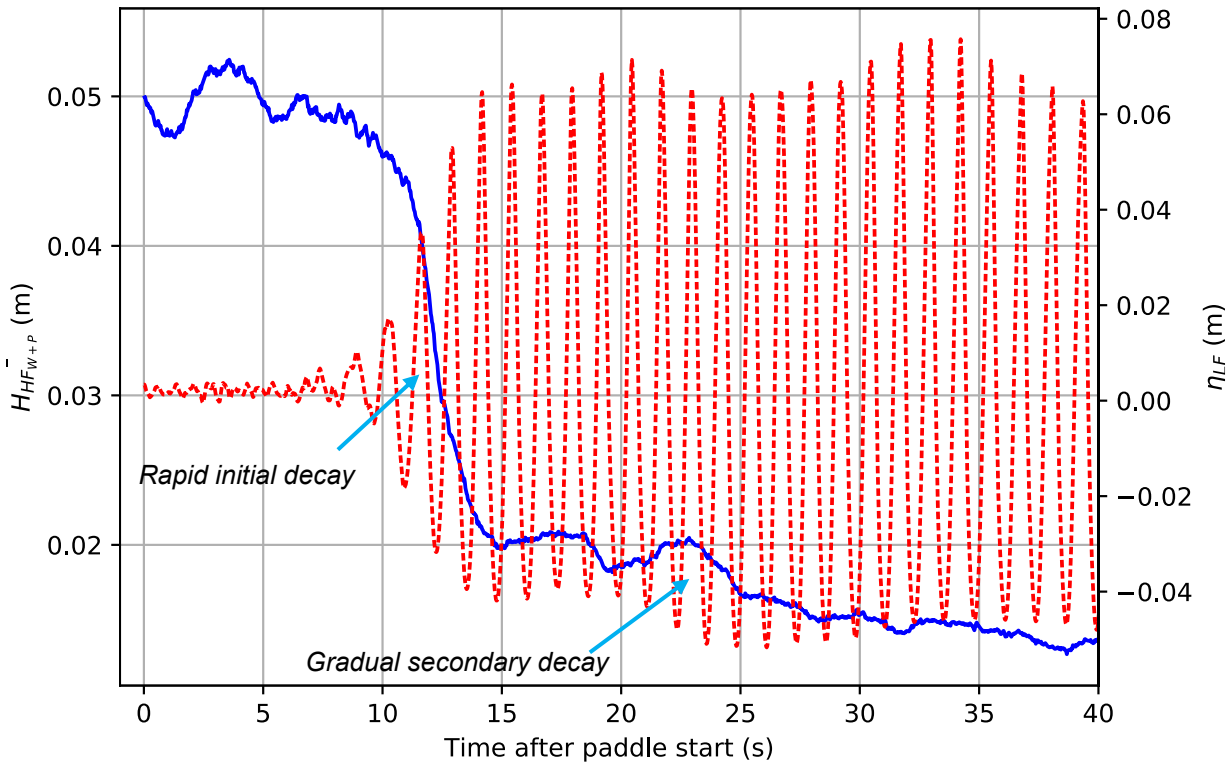

Figure 5.10: $H_{HF_{w+p}}$ averaged across all 186 transition sequences (blue) and η_{LF}, with same conditions and fetch as Figure 5.9, with a stretched vertical axis, highlighting the initial and ongoing changes.

All of this points to a mechanism by which HF waves are primarily erased by the presence of paddle waves. It must be recalled, however, that ca. 20% of suppression was seen in Figures 5.6, 5.9 (b) and 5.10 to occur gradually over a time period comparable with the typical build-up time for wind-waves, suggesting reduced wind input contributes to the observed suppression, although secondary in magnitude to the enhanced dissipation of LF waves.

5.4 HF wave energy distribution along the monochromatic LF wave

The majority of studies which measured $E_{HF_{w+p}}$ distribution along the LF wave phase have indicated $E_{HF_{w+p}}$ to be higher on the forward leeward face than the rear windward face (e.g. Keller and Wright, 1975; Reece, 1978; Smith, 1986; Donelan et al., 2010), but a few have observed contrary observations (Miller et al.,1991; Hwang, 2002). In this section, HF wave distribution is examined by means of measuring the standard deviations of HF wave time series, as well as by the attempted tracking of individual HF waves.

The case and fetch selected for initial observation was one of strong suppression and also a strong decrease of $E_{HF_{w+p}}$ versus fetch, being the conditions in Figure 5.4 at fetch=11.50m. The standard deviation of $E_{HF_{w+p}}$ was obtained by examining the HF wave time series throughout ca. 24 minutes of recording, after the paddle wave signal (including harmonics) had been filtered out, dividing the LF wave phase into 24 bins, and obtaining RMS values of $\eta_{HF_{w+p}}$ within each bin. It must be noted that standard deviation is indicative of HF wave height, independent of HF wave period or HF wavelength. One key difference between this calculation of standard deviation and the calculation method used on transition time series' to obtain Figure 5.5 is the method of separating HF and LF waves. HF and LF waves in transition time series were separated in a manner similar to phase averaging, which is more prone to attribute some LF wave energy to the HF component when paddle wave forms are unstable. However, Separation Method 6 (see Section 3.4.2) partially accounts for such instability, reducing the overestimation of HF waves.

In detection of the LF wave phase, the phase start point could be set as either the LF wave crest (positive $\delta\eta/\delta t$ becomes negative) or the LF wave upward zero-crossing (negative η becomes positive). The precise calculation of phase relative to the crest was considered of critical importance in this exercise, as a small shift in crest position may result in misallocation of HF wave maxima to the forward or rear face of the crest. Therefore, it was determined that the LF wave crest be used as the fixed reference point, with phase bins being determined relative to the average LF crest position. In the figures presented in this section, the horizontal axis was shifted by π Radians to position the crest in the middle of the plots. This enabled easier comparison of front and rear face of the wave crests, but was not representative of the phase start location used during calculations.

At the fetch and conditions observed initially, the $\sigma_{HF_{w+p}}$ is clearly seen in Figure 5.11 to be strongest on the forward leeward side of the crest, with HF waves reducing in intensity

both as they pass over the crest (in reverse direction relative to the crest), and high on the rear (windward) face. In spot checks of other wind, wave and gauge conditions, this trend was apparent in some but not all cases, revealing significant scatter. In order to determine if the trend of reduced $\sigma_{HF_{w+p}}$ at the LF wave crest and on the rear windward face was representative of the entire dataset, $\sigma_{HF_{w+p}}$ in each bin normalised by the mean $\sigma_{HF_{w+p}}$ across the whole phase was examined for all cases and fetches greater than 2.5m. Fetches less than 2.5m were excluded to avoid very small $\sigma_{HF_{w+p}}$ values which were observed to exhibit excessive scatter. The aggregation of results across all QA-passed cases and gauges with suppression ratio less than 0.8 (i.e. with substantial suppression present), shown in Figure 5.12, was reasonably consistent with the trend seen in Figure 5.11, revealing a smooth distribution with maximum $\sigma_{HF_{w+p}}$ in the two bins immediately forward of the LF wave crests, decreasing both on crests and windward of crests. The combined minimum for all cases was seen to be located more centrally in the trough than what was observed in Figure 5.11, where the minimum was halfway up the windward rear face.

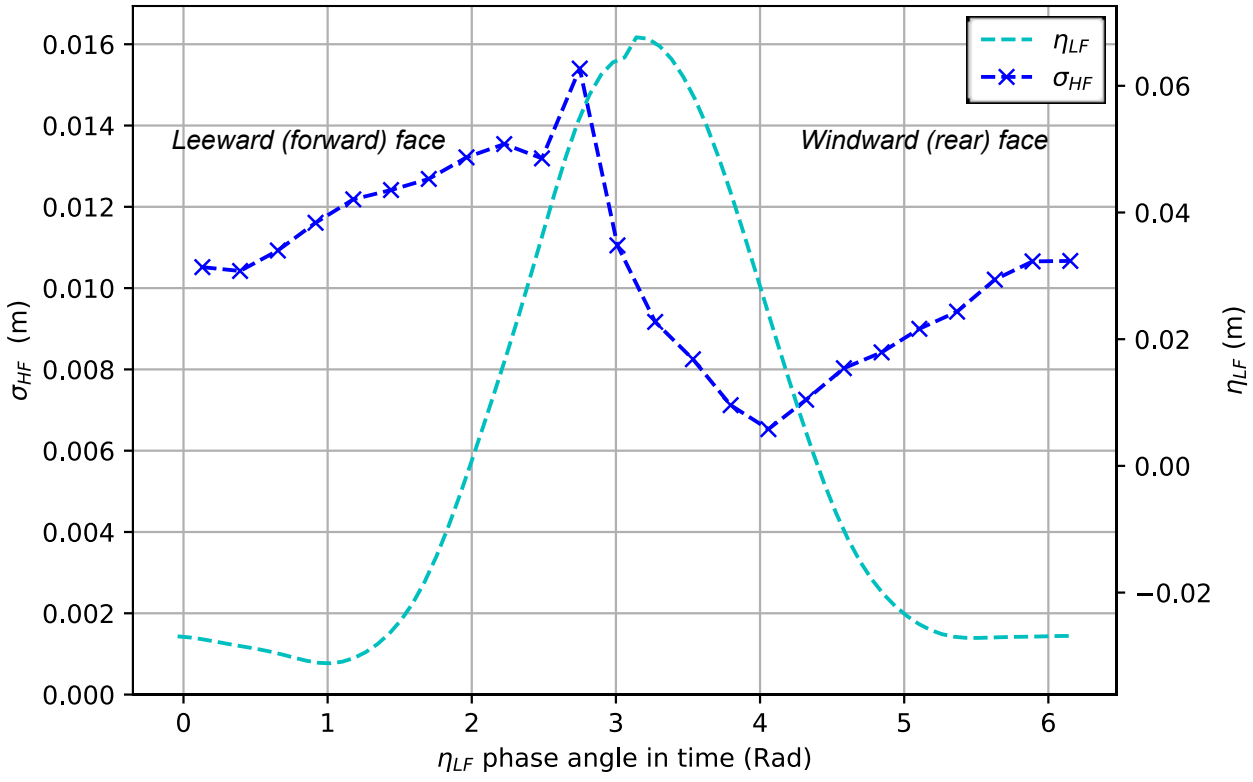

Figure 5.11: Distribution of σ_{HF} along the LF wave phase for one case, averaged over ca. 24 minutes of recording. T_{pad}-1.89s, $H_{pad} = 0.1m, V_0$=14.4m/s and fetch=11.50m. $\sigma_{HF_{w+p}}$ is relative to the vertical axis, not to η_{LF}.

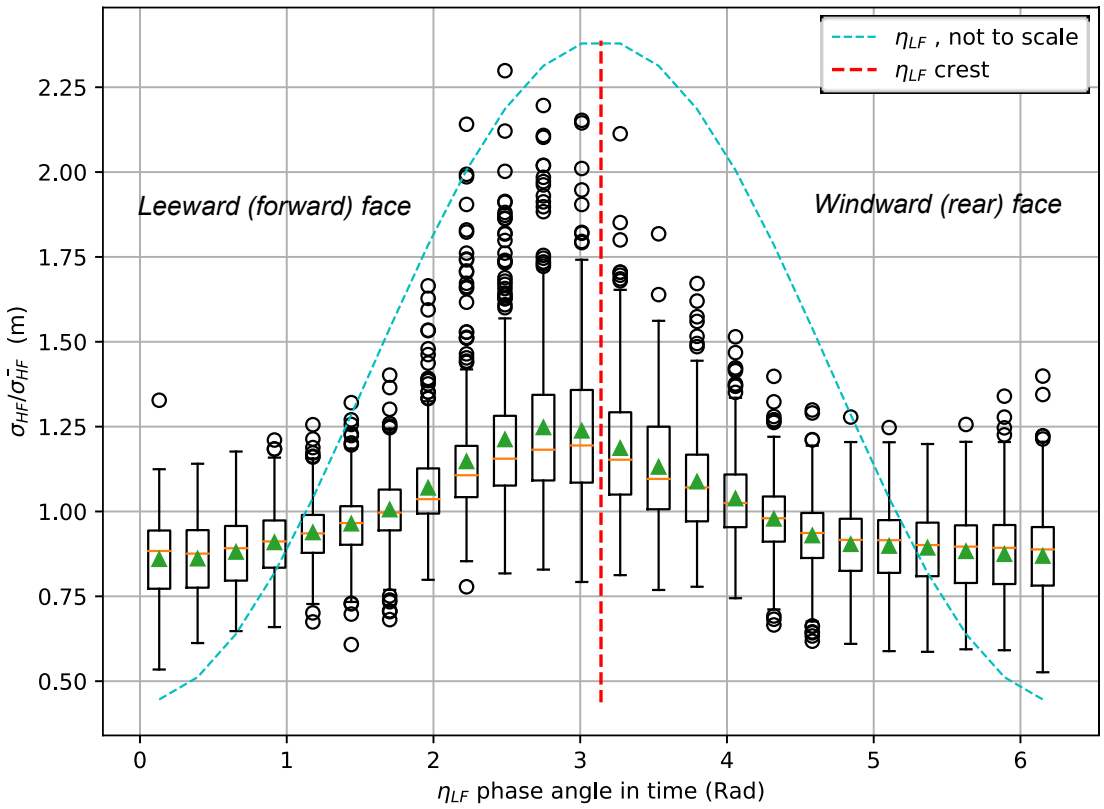

Figure 5.12: Distribution of σ_{HF} normalised by $\overline{\sigma_{HF}}$ throughout the entire LF wave phase, for all QA-passed cases & gauges with suppression ratio less than 0.8, i.e. significant suppression. Each data point within each boxplot distribution is the normalised σ_{HF} for a given time series – gauge - phase bin combination. Each boxplot intermediate horizontal line (brown) represents median, while green triangle represents mean, and box ranges from 25th to 75th percentiles of data points. Boxplot whiskers are located at extremities of data points within 1.5 x IQR (the inter-quartile range), with any data points exceeding this range represented by open circles. A simple sinusoid is plotted to represent the LF wave for all included cases. The average of all green triangles in this figure is equal to 1 by definition.

This analysis was performed again, but for cases and gauges with suppression ratios greater than 0.8, indicating weak, zero or negative suppression. As displayed in Figure 5.13, the pattern was qualitatively similar, with the $\sigma_{HF_{w+p}}$ maximum moving further forward of the LF wave crest. There was also a reduced variability along the phase, with the maximum and minimum $\sigma_{HF_{w+p}}$ being ca. ±0.05 times the average, as opposed to ca. +0.2 and -0.15 times the average in the strong suppression conditions shown in Figure 5.12. This difference in variability between the two figures suggests that the bulk of suppression may act on only part of the LF wave phase, causing an increase in variability along the phase. It

also suggests that even when the net suppression at a wave gauge is not significant, the forces which cause suppression may still be present, but neutralised by other factors in the complex dynamics involved.

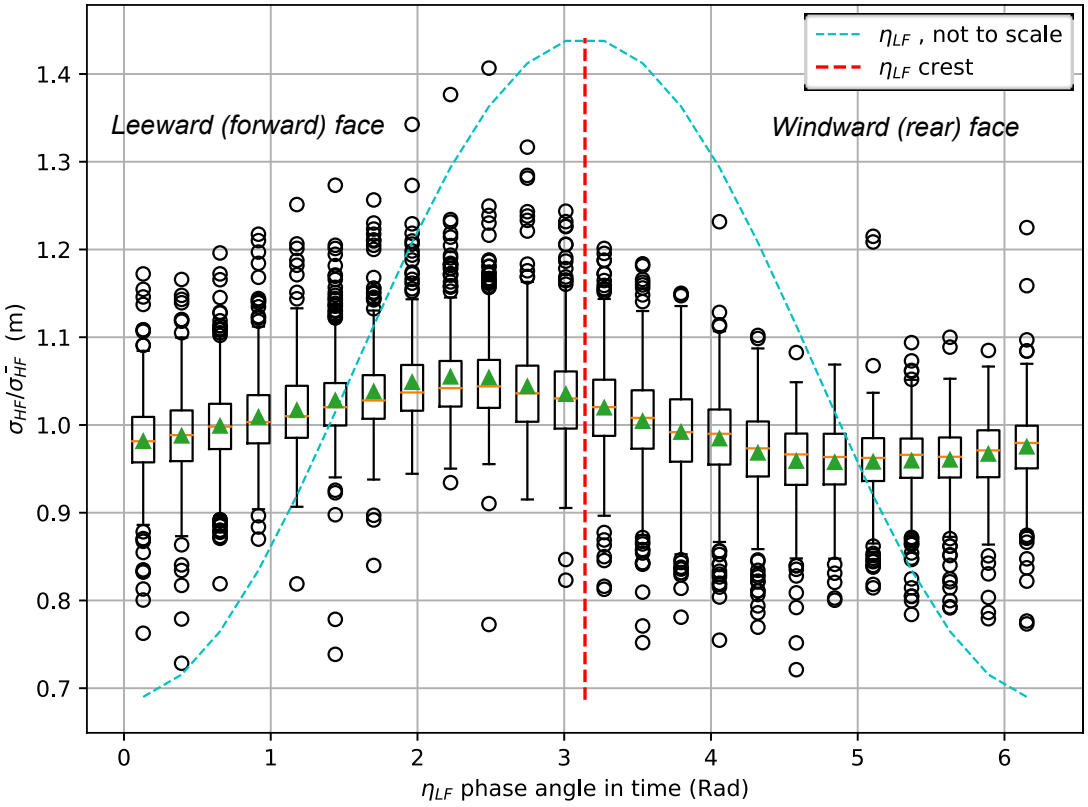

Figure 5.13: Distribution of $\sigma_{HF_{w+p}}$ normalised by $\overline{\sigma_{HF_{w+p}}}$, identical to Figure 5.12 except here for all QA-passed cases and gauges with suppression ratio greater than 0.8, i.e. minimal, zero or negative suppression. Refer to Figure 5.12 caption for a definition of plot features. Nb. vertical scale is different here to that of Figure 5.12.

In order to more directly measure suppression as a function of paddle wave phase, an attempt was made to track growth and decay of individual waves between adjacent wave gauges separated by 0.055m in the downwind-upwind direction. Individual waves were detected peak to peak, and changes in wave height compared between the two gauges. These data were expected to have a high degree of scatter, due to the known evolution of individual HF waves within wave groups, and due to HF waves of different wavelength overtaking each other changing the visible shape of the water surface even in the space of 0.055m. Unfortunately, the magnitude of scatter in results of this analysis was too great for identification of any clear trends in $\Delta E_{HF_{w+p}}$ throughout the η_{LF} phase, as is apparent in

Figure 5.14. The only clear trend visible in this graph is a mean $\Delta E_{HF_{w+p}}$ less than zero, implying that HF energy was reducing at this location in these conditions, which was expected based on the decay visible in Figure 5.4 at fetch=11.50m. It was determined that this particular analysis method was not effective in these circumstances. However, the spread of $\sigma_{HF_{w+p}}$ along the phase in Figures 5.11 to 5.13 display a clear pattern of reduced HF wave intensity on the windward face of waves, which does not contradict the majority of past observations (e.g. Keller and Wright, 1975; Reece, 1978; Smith, 1986; Donelan et al., 2010). Knowing that LF waves overtake HF waves, it is apparent in these figures that HF energy is being destroyed both on wave crests and immediately windward, surprisingly the location on the LF wave phase which is most exposed to wind forcing, and least likely to experience any suppression by reduced wind input. This provides further evidence to the argument that reduced wind input is not the main mechanism of suppression.

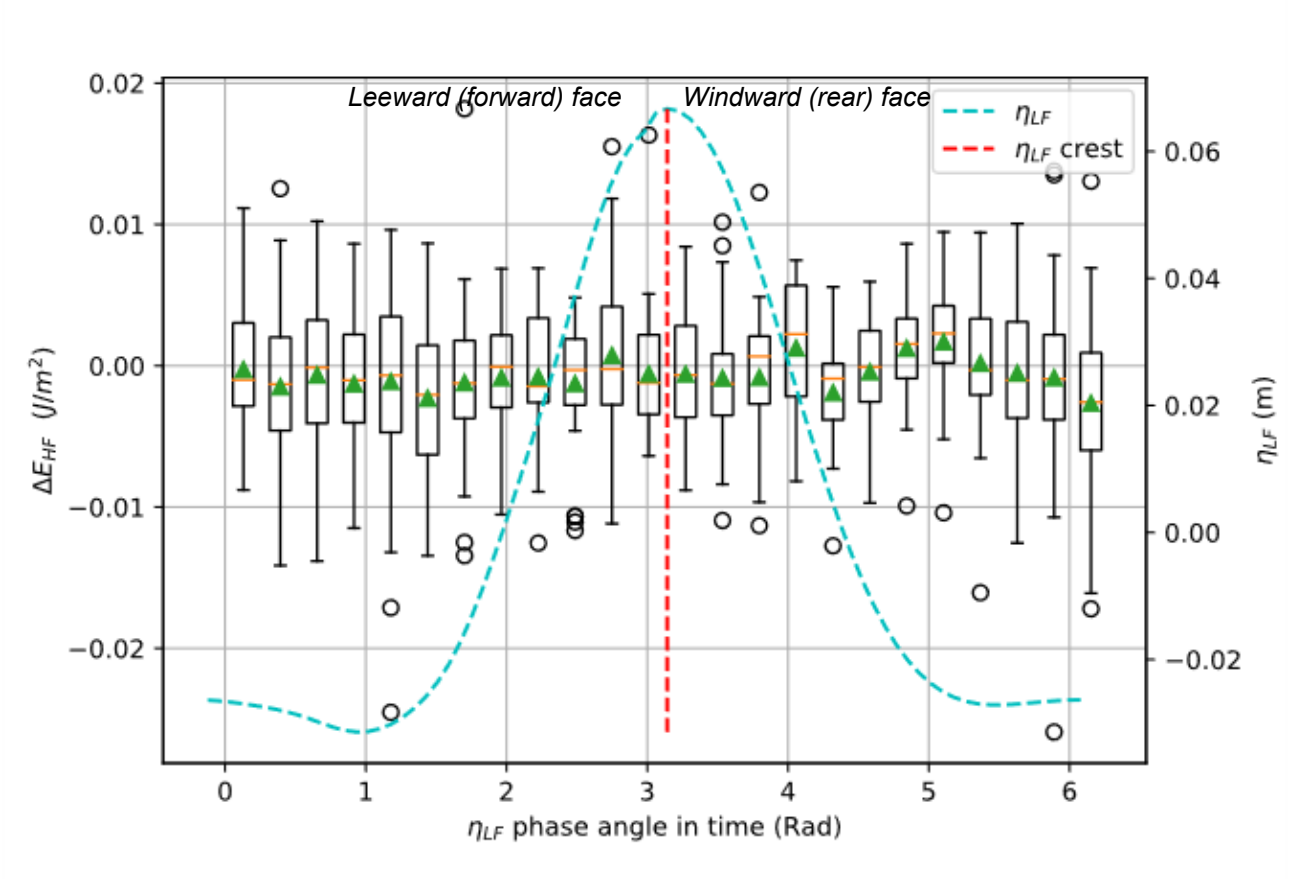

Figure 5.14: Decay of $E_{HF_{w+p}}$ between consecutive wave gauges separated by 0.055m, versus η_{LF} phase, for the same case and gauge as in Figure 5.11. $\Delta E_{HF_{w+p}}$ has been adjusted to filter out Longuet-Higgins & Stewart (1960) increase or decrease of $E_{HF_{w+p}}$ between the gauges. Boxplot median, mean, IQR etc for $\Delta E_{HF_{w+p}}$ are all as per boxplots of σ_{HF} in Figures 5.12 and 5.13. Unlike Figures 5.12 and 5.13, green triangles in this figure are not required to average 1.0 by definition. No clear trend has been observed in this plot.

5.5 General suppression trends

In this section, some general trends are documented regarding the response of suppression ratio to varied wind and LF wave parameters. Cases in which $E_{HF_{w+p}}$ was enhanced rather than suppressed by LF waves are explored in more detail in Section 5.6.

Contrary to comments by Donelan et al. (2010), suppression was not observed to be stronger for lower wind velocities in LAB2016. The suppression ratio as displayed in Figure 5.15 in fact decreased slightly with wind velocity up to ca. 11.4m/s, above which the $E_{HF_{w+p}}/E_{HF_{wo}}$ began to increase marginally. There was a greater degree of scatter with the lowest fan frequency, but this is to be expected with the numerator and denominator of the suppression ratio term (E/E_0) both decreasing. Measurements with strong HF wave enhancement (as opposed to suppression) were mostly taken at lower wind velocities. Had suppression been observed to be more pronounced with lower wind velocity, this may have worked in a minor way against enhanced dissipation theories, with turbulence and white-capping typically observed more in cases with higher wind velocity. However, this observed trend on its own does not conclusively either prove or disprove any theory.

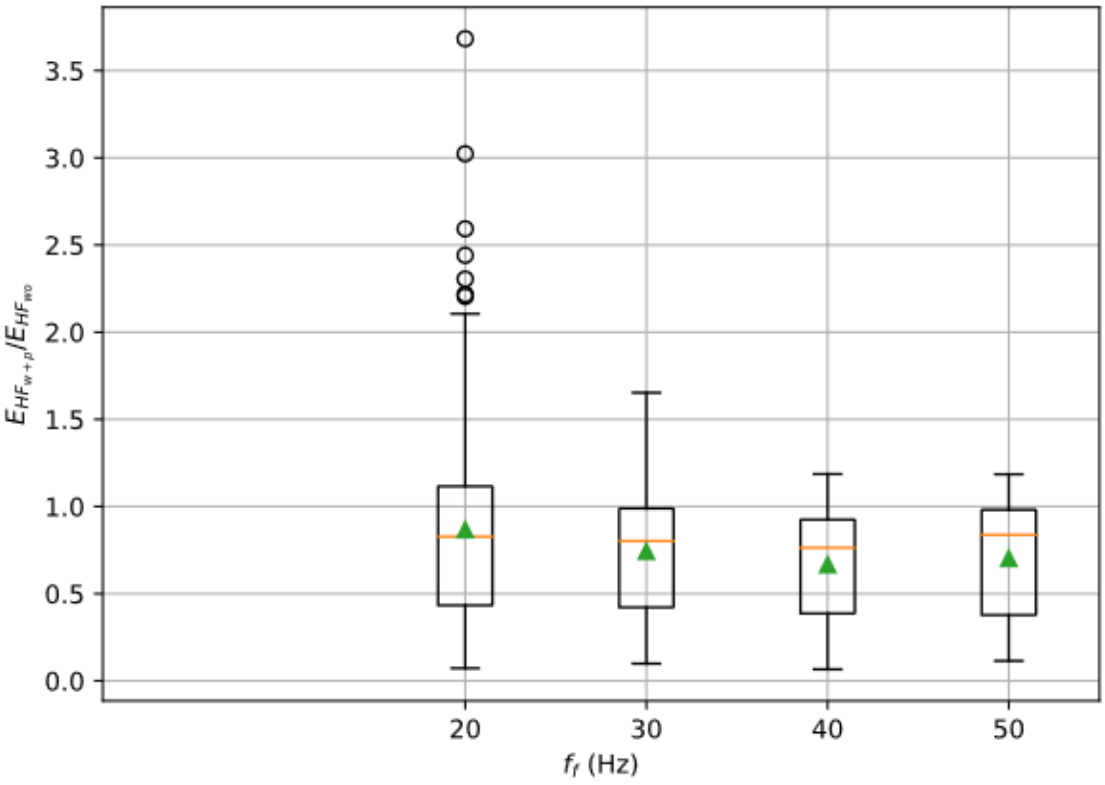

Figure 5.15: LAB2016 suppression ratio versus wind fan frequency for all QA-passed cases and gauges. f_f =20Hz corresponded to V_0 ≈5.7m/s, f_f =30Hz to V_0 ≈8.7m/s, f_f=40Hz to V_0≈11.4m/s, f_f=50Hz to V_0≈14.5m/s.

A clearer trend was apparent when examining suppression ratio versus paddle wave steepness, plotted in Figure 5.16. The steepness was calculated using linear wave theory for waves of intermediate depth to determine wavelength, with paddle wave height including higher harmonics measured in the frequency domain after filtering out $E_{HF_{w+p}}$. The suppression ratio clearly decreases with increasing steepness, which is consistent with expectations and with past studies (e.g. Mitsuyasu, 1966; Chen and Belcher, 2000). The majority of observations of negative suppression were made with relatively lower η_{LF} steepness, with scatter also apparently greater in lower η_{LF} steepness cases. It has previously been documented that Separation Method 6 is not perfect, with inevitably some $E_{LF_{w+p}}$ being attributed incorrectly to $E_{HF_{w+p}}$, and this may contribute to some data points exhibiting mild HF wave enhancement which would otherwise have exhibited positive suppression if Separation Method 6 were perfect. However, as detailed in Section 5.6, this could not be responsible for the substantial $E_{HF_{w+p}}$ enhancement observed in some cases.

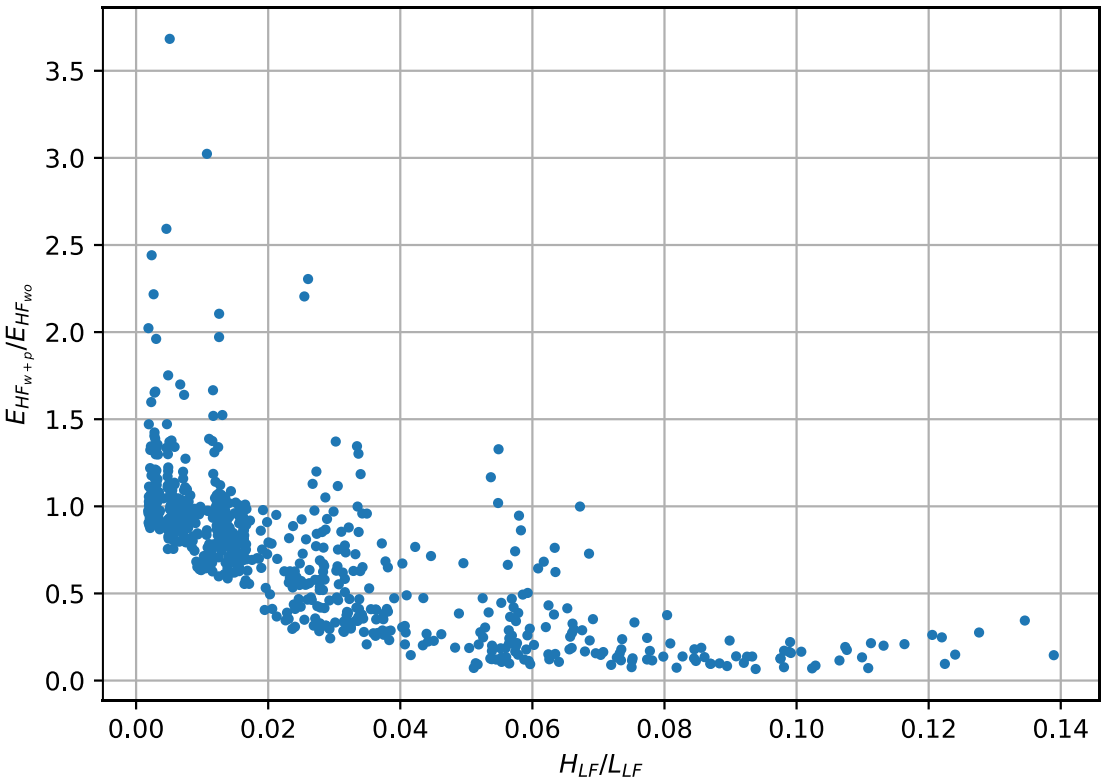

Figure 5.16: Suppression ratio vs LF wave steepness for all LAB2016 QA-passed gauges and fetches.

Suppression ratio was also observed to decrease with increasing fetch, as displayed in Figure 5.17, with cases of HF wave enhancement also occurring far more prevalently at

lower fetches, and also a higher degree of scatter at lower fetches. Greater suppression at increasing fetches likely results from $E_{HF_{w+p}}$ reaching or drawing nearer to a suppressed (or saturated) limit at greater fetches, which was never experienced by $E_{HF_{wo}}$ within the relatively short laboratory fetch. The reduced scatter at higher fetches is likely at least partly due to the suppression ratio denominator, $E_{HF_{wo}}$, increasing with fetch in all cases, dampening out scatter and keeping suppression ratios down. Increased LF wave steepness at greater fetches, caused by LF waves growing, also likely contributes to the overall trend for stronger suppression with greater fetches. It appears unlikely that the trend of reduced suppression ratio in laboratory conditions continues indefinitely as fetch approaches oceanic scales, given that suppression is less noticeable in field conditions (Chen and Belcher, 2000).

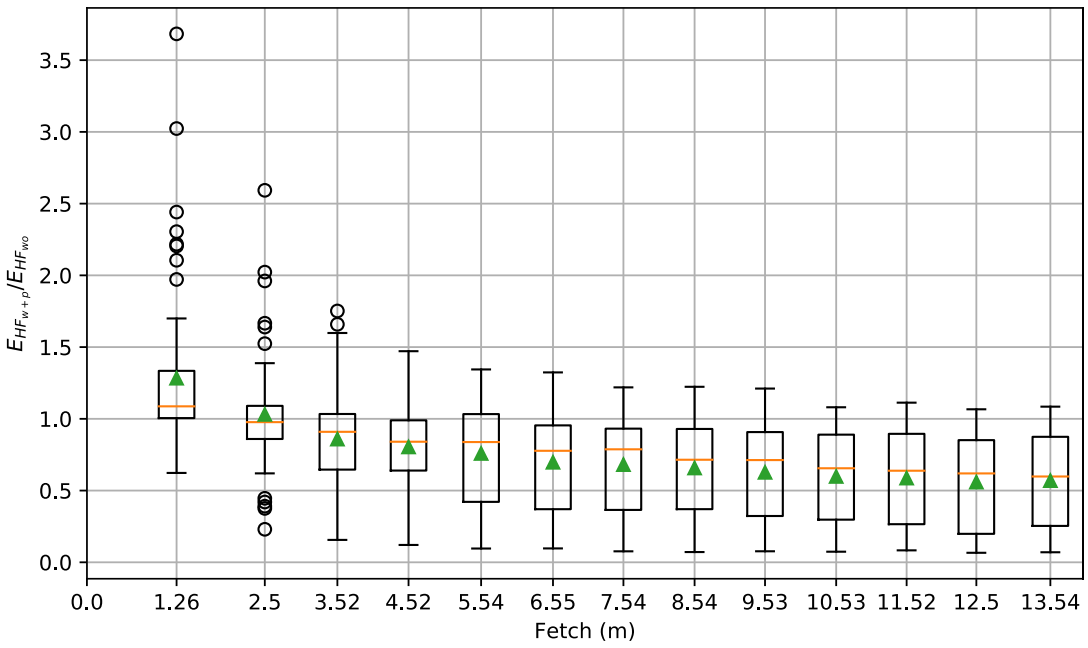

Figure 5.17: Suppression ratio vs fetch for all QA-passed LAB2016 cases and gauges.

One observation goal in LAB2016 was to measure the response of suppression to LF wave breaking. Given that the LF breaking probability score $K_b = H_{LF}/(gT_{LF}^2)$ (as defined in Equation 3.5, Section 3.4.3) was derived from a calculation of steepness, it was no surprise that the relationship of suppression ratio to K_b, plotted in Figures 5.18 and Figure 5.19, almost exactly matched the dependency on steepness displayed in Figure 5.16. Figure 5.19 differs from Figure 5.18 in that it displays the maximum of K_b at any point upwind of the fetch in question, allowing for flow on effects of LF breaking events downstream of where the

breaking started. The observation of any discontinuity in these plots, if present, would support LF wave breaking to be a strong contributor to suppression, particularly if it correlated with a K_b score of ca. 0.2-0.21, being the breaking threshold proposed by Ochi and Tsai (1983) and Ramberg and Griffin (1987). In both Figure 5.18 and 5.19, there was no definite change in suppression ratio above any particular K_b, either local (Figure 5.18) or upwind (Figure 5.19), although more consistently lower suppression ratios were observed above K_b≈0.01. Almost all data points above K_b≈0.01 were for the higher wind velocity cases. It was observed visually in the experiment that for the highest wind fan setting, f_f=50Hz, there was frequently white foam near the crests of LF waves, even though these cases rarely approached a K_B value of 0.02. This may be a manifestation of strong wind ripping off the tops of crests (Babanin, 2011, p11), or wind forcing early breaking of LF waves, but with low severity (Babanin et al., 2010). While the presence of strong suppression at lower values of K_b, including some around ca. 0.002, even with relatively low wind velocity, proves that suppression does not depend entirely on LF wave breaking, these breaking events may still contribute. The degree to which they contribute was not clearly observable in these results, suggesting that LF wave breaking, if it does contribute, may not be quantitatively dominant.

Suppression as dependent on likelihood of separation was examined using a combined wind-steepness variable similar to that used by Donelan et al. (2006) on field measurements, but the Donelan et al. (2006) term of wind velocity at an elevation of $\lambda/2$ was replaced in the present experiment with V_0 in the flume, being the mean wind velocity at ca. 0.2m above the MWS, at 12.15m fetch. The value for wave celerity was calculated based on linear wave theory for waves of intermediate depth. The final wind-steepness term adopted for LF waves in this thesis was

$$a_{LF}k_{LF}\left(\frac{V_0}{C_{LF}}-1\right)^2, \tag{5.1}$$

with C_{LF} representing the LF wave phase celerity. Examination of suppression ratio versus this term, displayed in Figure 5.20, revealed no clear discontinuity. The concentration of data points with very low values of wind-steepness suggests that this variable, developed for field conditions, was not ideally suited for the conditions in the laboratory experiments of the present study. This relationship does not prove a dependence on wind separation at LF wave crests, and the observations in Figure 5.20 displaying very low values of both wind steepness and suppression ratio, suggests that suppression does not depend on wind separation. However, it still may contribute, and this is discussed further in Section 5.7.

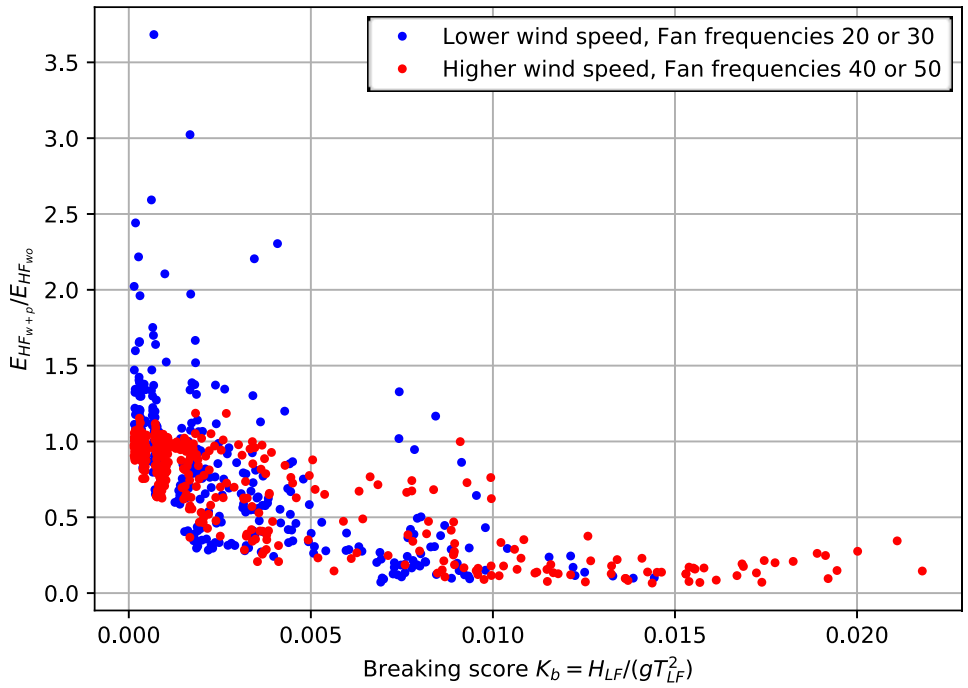

Figure 5.18: Suppression ratio vs local LF wave breaking score K_b, for all QA-passed LAB2016 cases and gauges. Refer also to Figure 3.15, in which most strong LF breaking events are seen to have occurred only after K_b had reached as high as ca. 0.2.

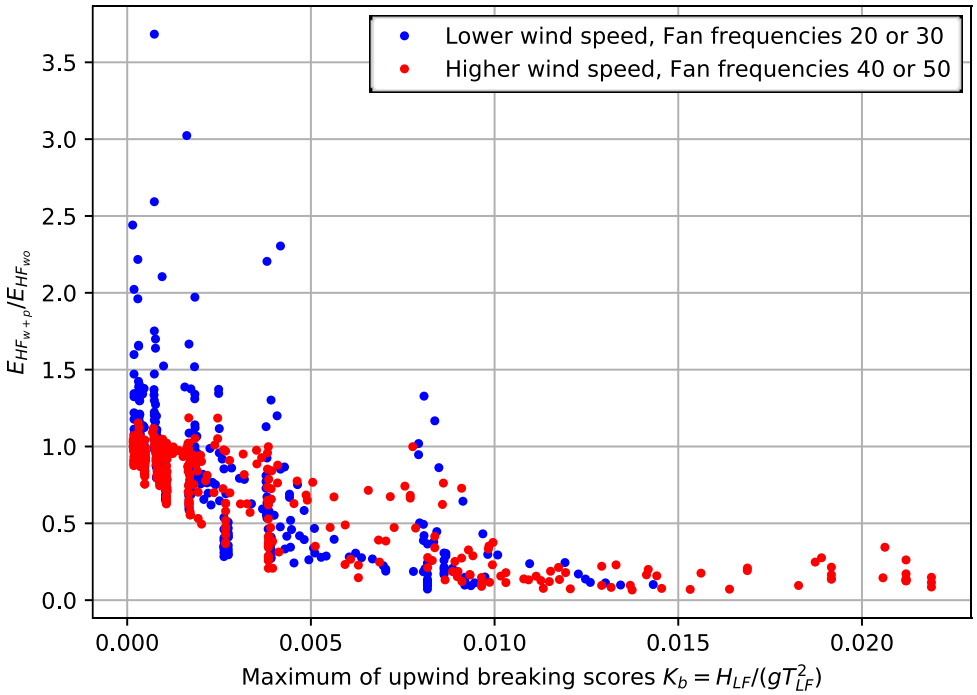

Figure 5.19: Suppression ratio vs maximum upwind LF wave breaking score K_b for each wave gauge holder, for all QA-passed LAB2016 cases and gauges. Refer also to Figure

3.15, in which most strong LF breaking events are seen to have occurred only after K_b had reached as high as ca. 0.2.

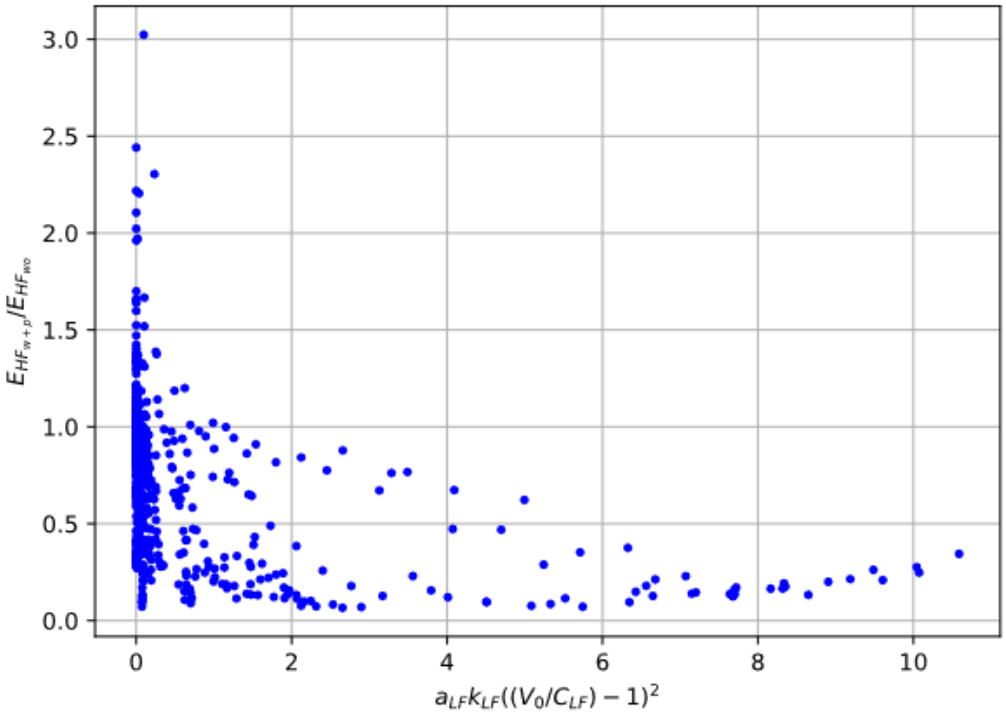

Figure 5.20: Suppression ratio versus wind-steepness, modified from the wind-steepness term used by Donelan et al. (2006), for all QA-passed LAB2016 cases and gauges.

5.6 HF wave and harmonic spike enhancement

It was observed in some cases, typically with low paddle wave steepness, small fetch and lower wind velocities, that the presence of paddle waves resulted in observations of $E_{HF_{w+p}}$ up to ca. 3-4 times greater than $E_{HF_{wo}}$. This may be described as LF wave enhancement rather than suppression of HF waves, and an example spectrum is provided in Figure 5.21 (b). The enhancement in this figure exhibited a marginally increased height of the $\eta_{HF_{w+p}}$ spectrum, a downshift in average frequency of the $\eta_{HF_{w+p}}$ spectrum, increased breadth in frequency space of the $\eta_{HF_{w+p}}$ spectrum, and the formation of energy spikes in bins which correspond to LF wave harmonics frequencies. The downshift in average frequency strictly speaking does not affect the suppression ratio, which depends on wave energy density $E_{HF_{w+p}}$, measured in (J/m²), but does increase the flux of HF energy through any given point.

On face value, it is clear that paddle waves are enhancing the growth of HF waves in conditions of low LF wave steepness, although it is less obvious which of the three main

modelling source term physical processes is responsible. In the condition displayed in Figure 5.21, it was clear that η_{LF} was not preferentially absorbing wind energy at the expense of η_{HF}, as was theorised by Miller et al. (1991) and Masson (1993) to be a cause of suppression, nor did it appear that the reverse could be true, because neither E_{HF} nor E_{LF} was reduced as a result of the interaction in W+P conditions.

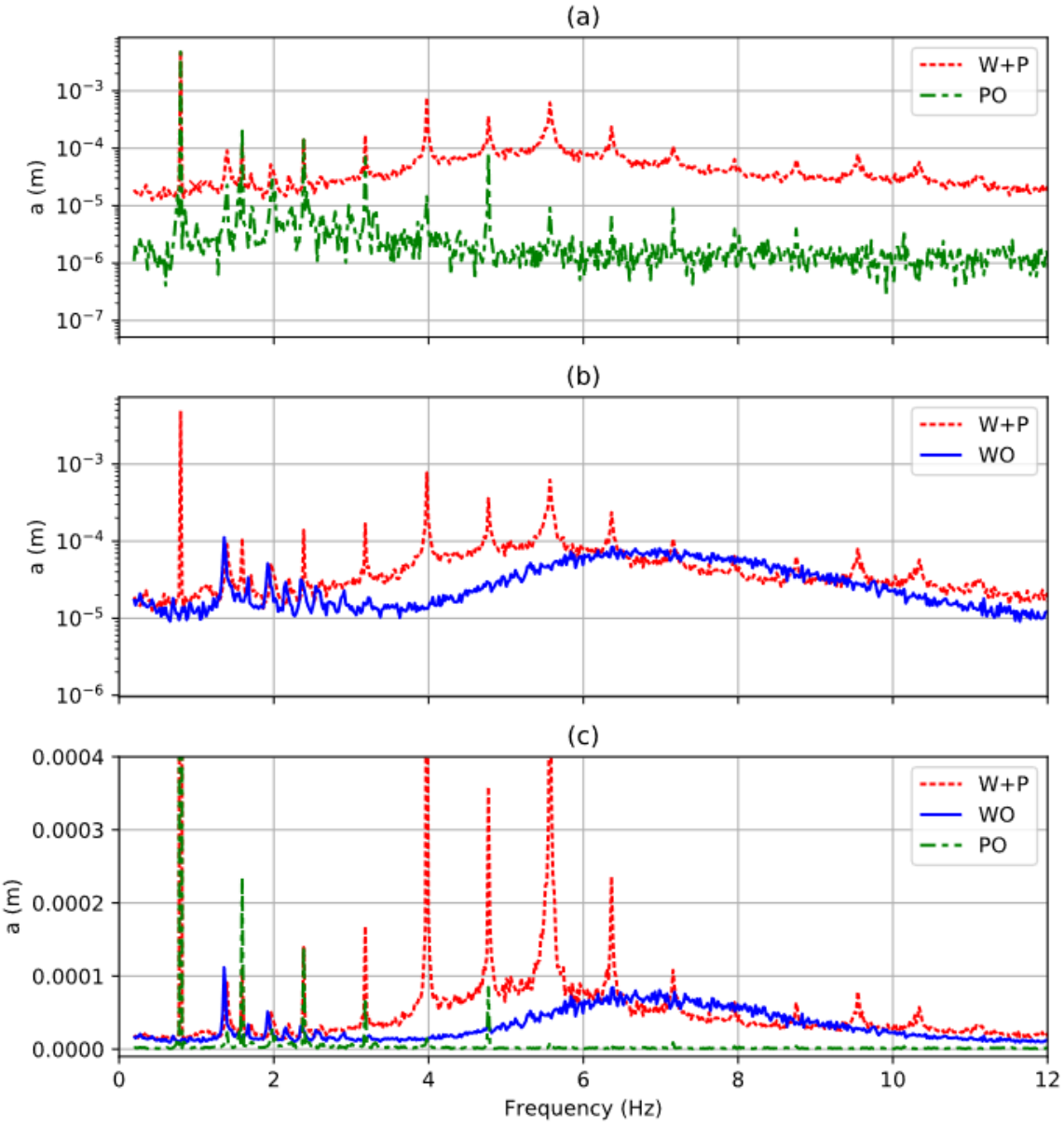

Figure 5.21: Spectra for H_{pad} =0.01m, T_{pad} =1.25s, V_0 =5.7m/s, fetch=1.259m, suppression ratio ≈3.7. (c) combines data from (a) and (b) on a linear axis. Amplitudes of fundamental, 5th and 7th harmonic frequencies in PO and W+P conditions are significantly truncated in (c), to enable a magnified view of the rest of the spectra.

It can be seen in Figure 5.21 (b) and (c) that much of the energy increase was related to spikes within the harmonic frequencies, sometimes approximately an order of magnitude

greater than what was present in surrounding frequencies, and typically multiple orders of magnitude greater than the energy in these frequencies in PO conditions. The spikes seen at higher harmonic frequencies of the paddle wave were initially surprising given that the paddle fundamental frequency only grew marginally, and the 2nd and 3rd harmonics grew less than some of the higher harmonics, such as the 5th harmonic at ca. 4Hz. There are some similarities between this observation and the comments by Reece (1978) who generated spectra with a laser slope sensor, and observed that the fundamental paddle wave did not change but first and second harmonic did, with increase of wind velocity.

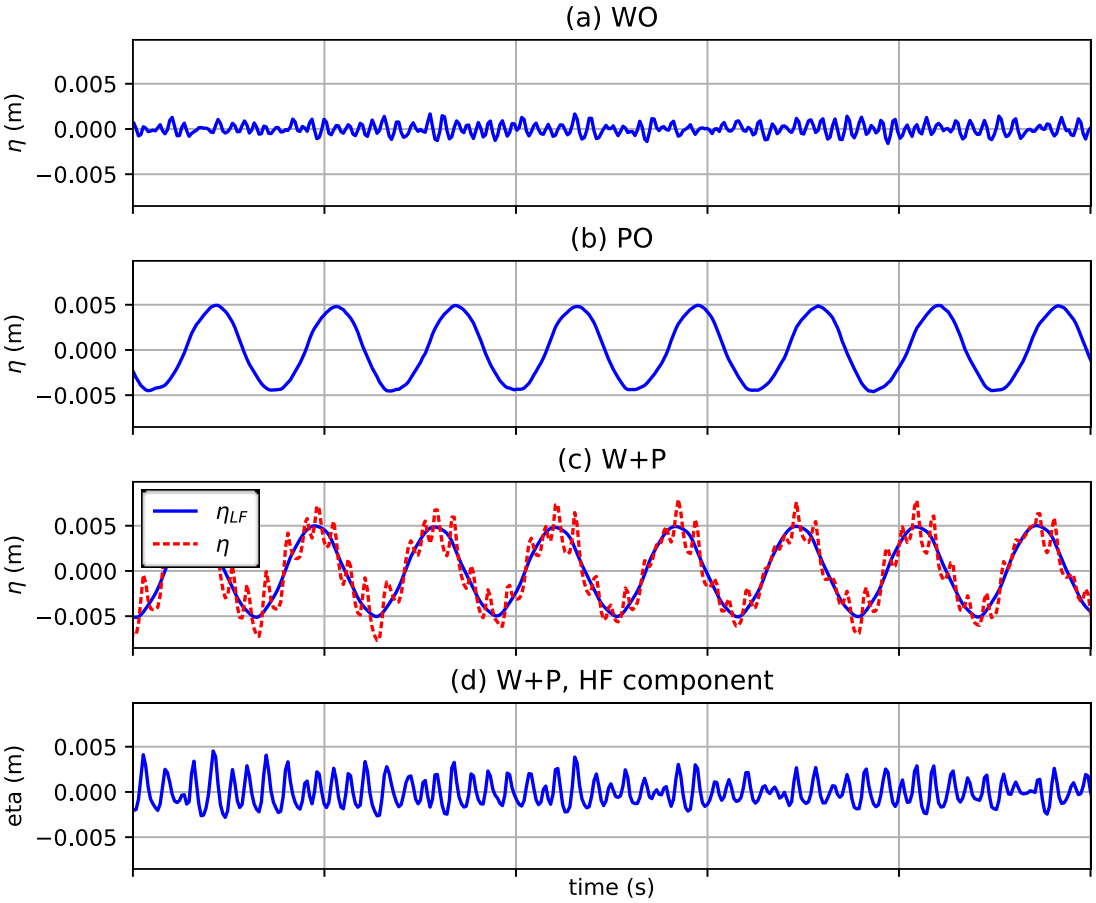

Figure 5.22: Time series plot of conditions from Figure 5.21. Increase in HF energy is apparent when comparing the $\eta_{HF_{(w+p)}}$ time series of (d) against the $\eta_{HF_{wo}}$ time series in (a).

The energy in these higher harmonics was initially expected to be represented in the time domain by a sharpening of the crests and shallowing of the troughs of the paddle waves, with these spikes propagating at the phase celerity of the fundamental harmonic. However, the additional energy was not observed to be bound to the LF wave, but instead added substantial undulations to the overall wave shape, as can be seen in Figure 5.22 (c). When

this analysis was performed using Separation Method 1 (see Section 3.4.2 and Figure 3.11), which attributed these spikes to the LF wave, the resulting LF wave shape became distorted, which was one reason why further effort was expended to develop Separation Method 6. Examination of video data from this experiment, a still-frame of which is displayed in Figure 5.23, confirmed the existence of significant HF waves which were not bound to the paddle wave, but rather were overtaken by paddle waves. It was clear then that these spikes in harmonic frequencies should not be attributed to LF wave higher harmonics, but to random HF waves instead.

Figure 5.23: Still frame from GoPro video of W+P conditions in Figures 5.21 and 5.22, stretched vertically to enable LF waves to be visible, with red star marking the location of the gauge used for measurements in that figure. Fish eye removal was attempted but unfortunately caused substantial horizontal truncation of the photo, reducing visibility of the LF wave. Pale blue squares mark LF wave peaks, while darker blue squares mark LF wave troughs. Steel pillars were at ca. 900mm vertical spacings, with ca. 850mm of glass between the top and bottom horizontal steel chords of the flume.

With this in mind, the discrepancy in growth of the fundamental, 2nd and 3rd harmonics compared against growth of higher harmonics is not surprising, given the understanding that the 2nd and possibly the 3rd harmonics were likely genuine bound harmonics, and higher

harmonics were random HF waves and not true bound harmonics, being a different type of wave altogether. The question remains, however, as to why the frequencies corresponding to higher harmonics gained energy far more rapidly than surrounding frequencies, when such energy was clearly not bound to the paddle wave.

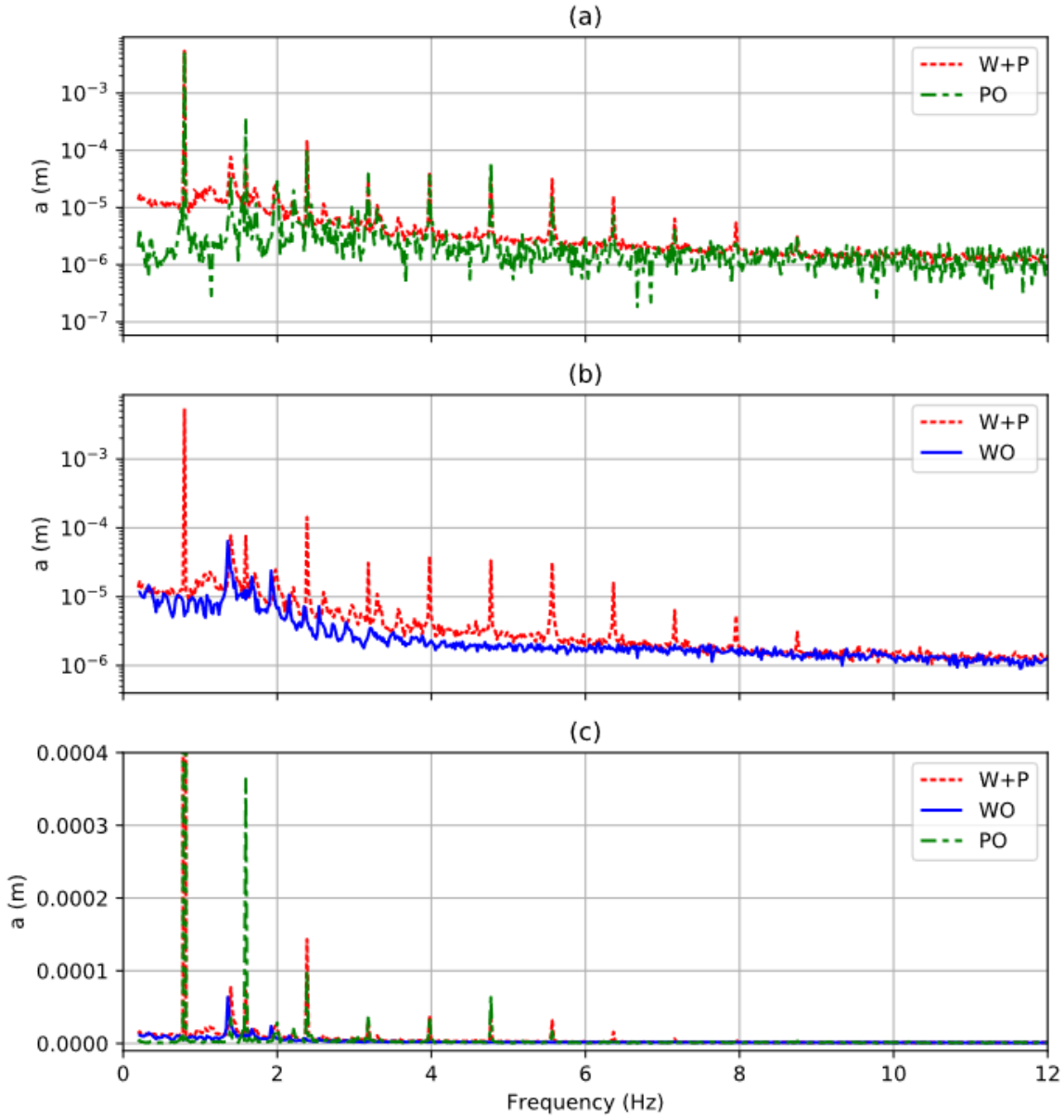

Figure 5.24: Identical spectra to those in Figure 5.21, but at fetch=0m (Figure 5.21 was at fetch=1.259m).

At first glance, one could conclude that this energy increase corresponding with paddle wave harmonics may either be caused by poor data analysis, or else coupled directly to a vibration caused by the wave paddle's active absorption system. However, an examination of the same spectra at zero fetch, displayed in Figure 5.24, did not exhibit the spike enhancement, ruling out the above two possible forms of pollution. The wave gauge data

thus indicates that the barely significant harmonics of these 0.01m tall paddle waves with T=1.26s provides a seeding mechanism for amplified HF wave growth focused within these frequencies, predominantly at early fetches. Such a large growth of waves relative to almost negligible seeding suggests a strong instability mechanism. It was observed in Figure 5.25 that E_{HF} spike enhancement occurred earlier for the spikes which were at higher frequencies, which is consistent with the general growth of the η_{HF} spectrum.

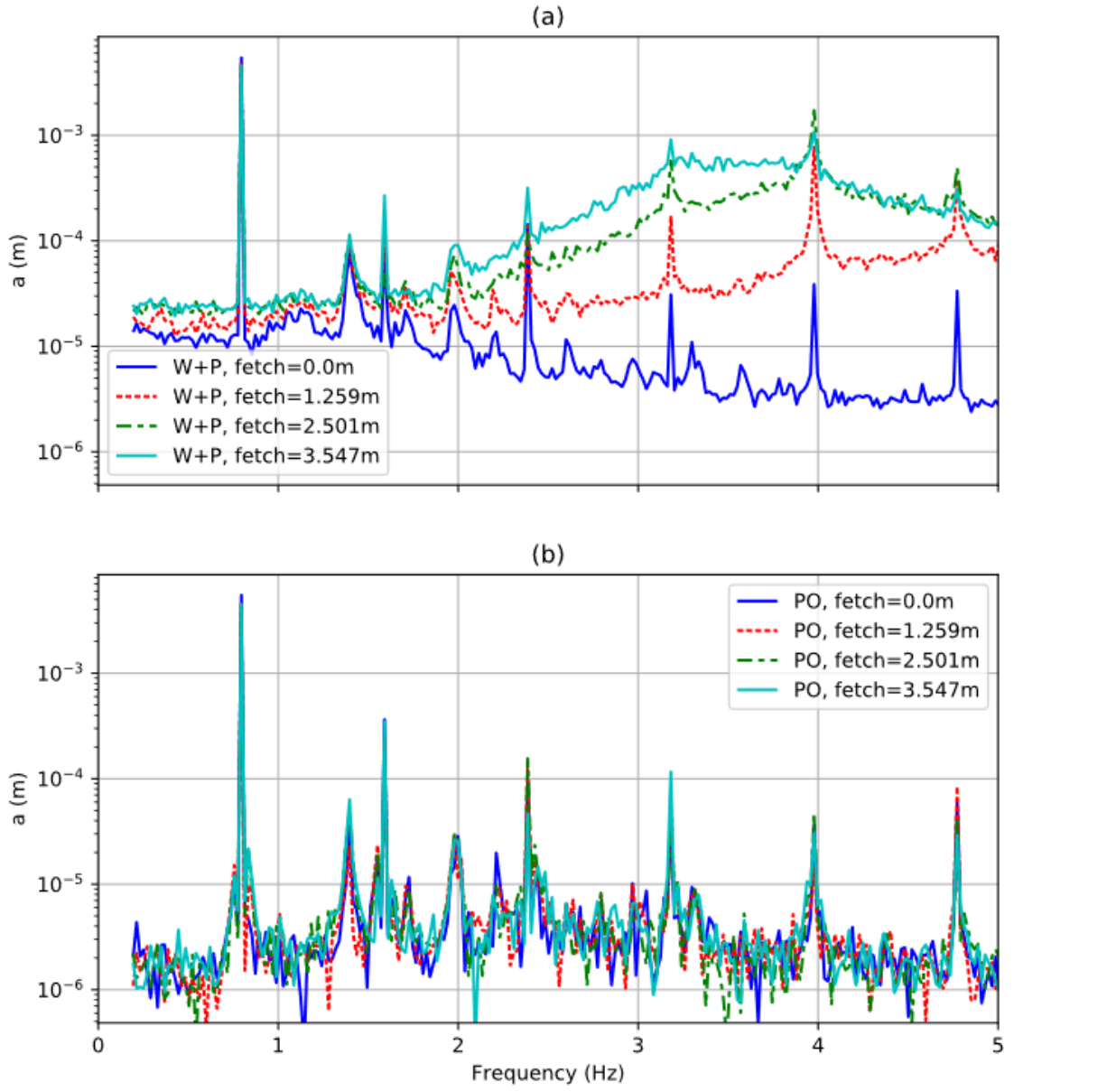

Figure 5.25: (a) Evolution of W+P spectra at short fetches, and (b) corresponding PO spectra demonstrating minimal change in harmonic frequencies in the absence of wind.

In order to identify how this harmonic spike enhancement depended on fetch, the evolution of energy in single specific harmonic bins was examined along the flume in Figure 5.26. In Figures 5.26 – 5.29, $NF_p \pm F_p/2$ is an average of the energy in the pair of

frequencies exactly mid-span (in frequency) between the harmonic in question and its two neighbouring harmonic frequencies, and is used as a proxy for HF energy in the vicinity of but not within the harmonic bin in question. $NF_p \pm dF$ is an average of the energy in bins immediately above and below the harmonic frequency, and is included to provide a rough indication of the spike or sideband width. An example of substantial width variation is displayed in Figure 5.21, in which the 7th harmonic for W+P conditions is much wider than the 4th, 5th or 6th.

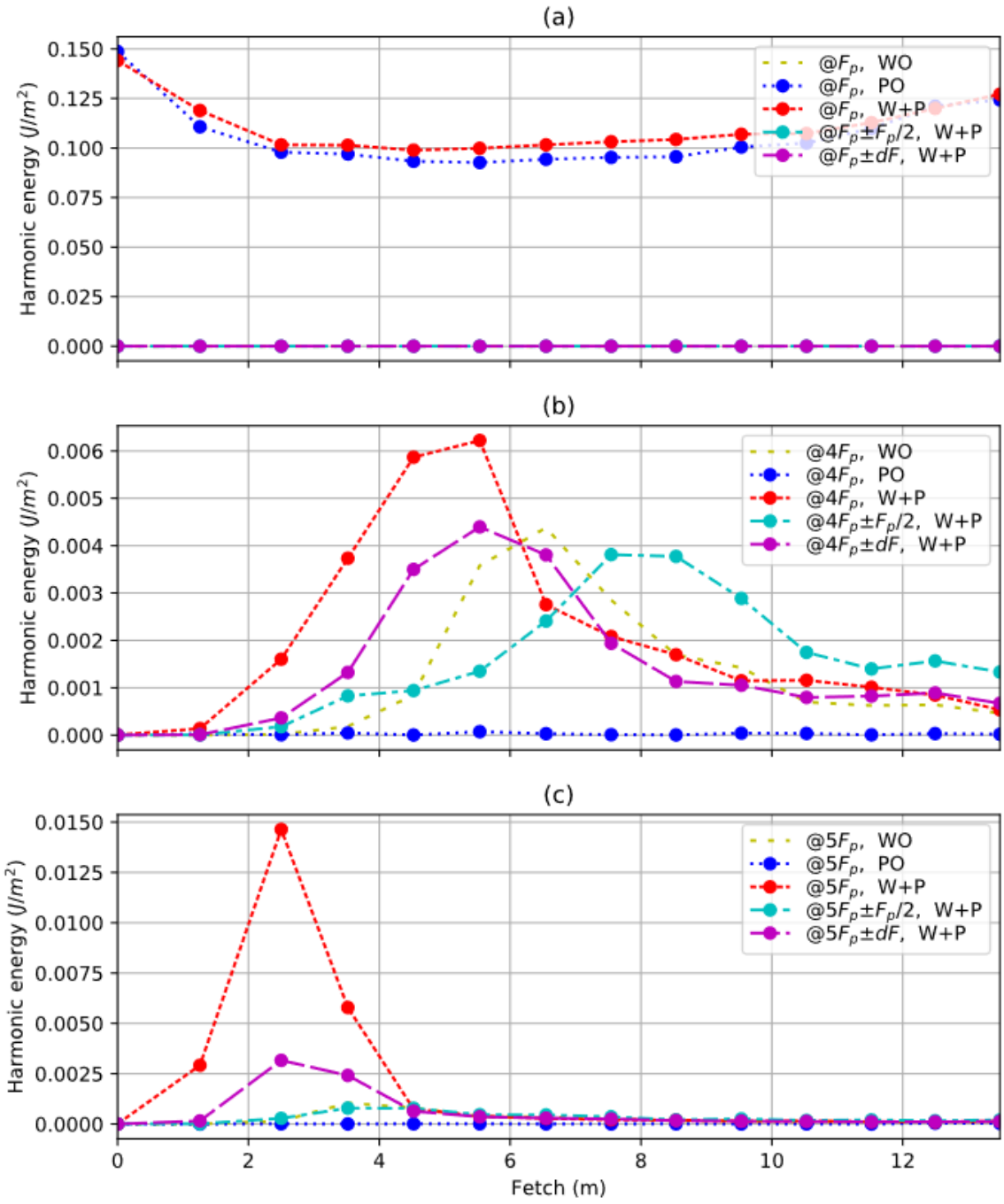

Figure 5.26: Evolution of Fundamental, 4th and 5th harmonics, with V_0 =5.7m/s, H_{pad}=0.01m, and T_{pad}=1.26s. See text for further explanation.

Figure 5.26 reveals that while the fundamental frequency did not grow substantially in these conditions with relatively low wind velocity (a), the energy in higher harmonics was enhanced, before being absorbed back into the HF wave field. The 5th harmonic both peaked earlier (in fetch) and was absorbed by the HF wave field earlier than the 4th harmonic.

The absorption of the higher order harmonic spikes back into the $\eta_{HF_{w+p}}$ spectrum sooner than lower order harmonic spikes is likely due to the surrounding HF wave energy engulfing the harmonic frequency sooner. The enhancement of spikes, also following this trend, suggests that the harmonic spike enhancement is also related to the HF energy in the surrounding spectral frequencies. Enhancement of the harmonic spikes appears to occur somewhere on the rear face of the η_{HF} spectrum, and decay or re-absorption of the harmonic spike occurs on the forward face.

The dependence of this energy enhancement in harmonic frequencies on H_{pad} is examined in Figure 5.27, in which only the 5th harmonic was selected for comparison with three different values of H_{pad}, all with T_{pad}=1.26s. In this figure, (a) is of identical conditions as what was in Figure 5.26 (c). Normally, one would expect energy in the 5th harmonic of steeper waves to be greater than that in low-steepness waves, both due to the overall wave height being greater, and also due to the increased nonlinearity resulting from the greater finite wave height. However, in this comparison, the energy in the 5th harmonic was far greater in 0.01m waves than what was present in 0.025m and 0.05m waves. This indicates firstly that the energy in the 5th harmonic in Figure 5.27 (a) around 1-4m fetch were being enhanced by an unknown mechanism, and secondly that this enhancement effect was limited to waves of relatively low steepness, given that negligible enhancement was present for the cases of 0.025m and 0.05m waves.

A similar comparison was performed keeping wave height constant and varying paddle wave length, the results of which are displayed in Figure 5.28. In this figure, plot (b) corresponds to the same conditions and harmonic as in Figure 5.26 (c) and 5.27 (a). The increased steepness in Figure 5.28 (a) appeared to result in minimal enhancement of energy in the 5th harmonic frequency, and what little enhancement was observed occurred at even smaller fetch, whereas the lowest paddle wave steepness observed in Figure 5.28 (c) was found to both increase the enhancement effect, and cause it to occur later. The trends inferred by the writer from Figures 5.27 and 5.28 are that reduced paddle wave steepness results in both greater enhancement of HF energy in harmonic frequencies, and also later enhancement. How this occurs as H_{LF}/L_{LF} approaches zero is not clear at the present time,

particularly given that the H_{LF}/L_{LF} values encountered in this experiment are typically considered to be near zero already.

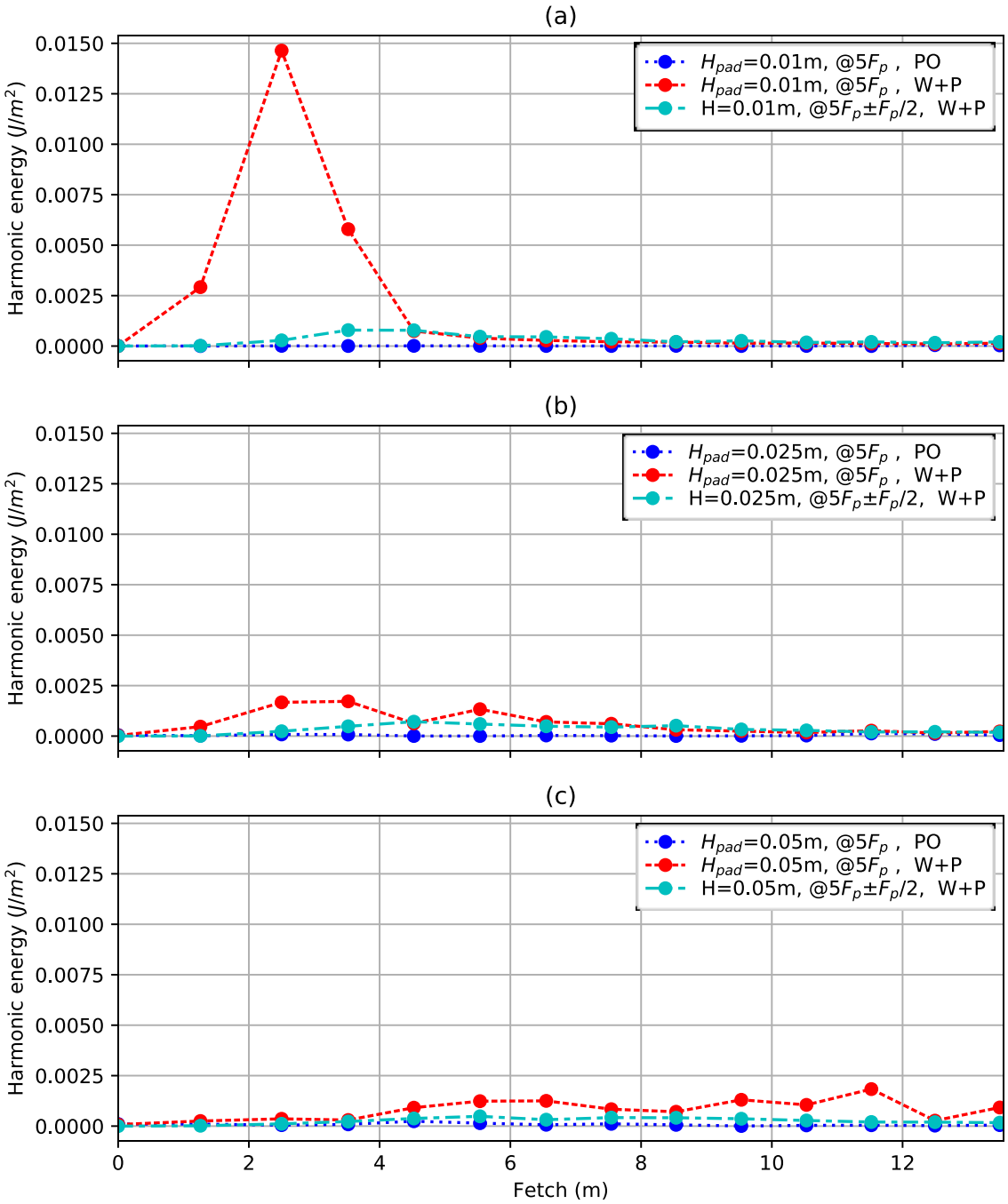

Figure 5.27: Evolution of 5th harmonic with varying paddle wave height, all with T_{pad}=1.26s. See text for further explanation.

While this enhancement of HF energy was most prevalent at lower wind velocities (see also Figure 5.15), it was also observed at relatively high wind velocities, as seen in Figure 5.29. Higher wind velocities correlated with reduced enhancement of HF energy in the harmonic frequencies, and also appeared to cause the enhancement to occur earlier,

somewhat similar to the effect of increased LF wave steepness. It appears that while HF wave enhancement in harmonic frequencies is dependent on some HF wave energy in the surrounding frequencies, it nonetheless was reduced in the presence of excessively strong HF energy in these surrounding frequencies. To the writer's knowledge, there is currently no explanation in literature for any of this behaviour.

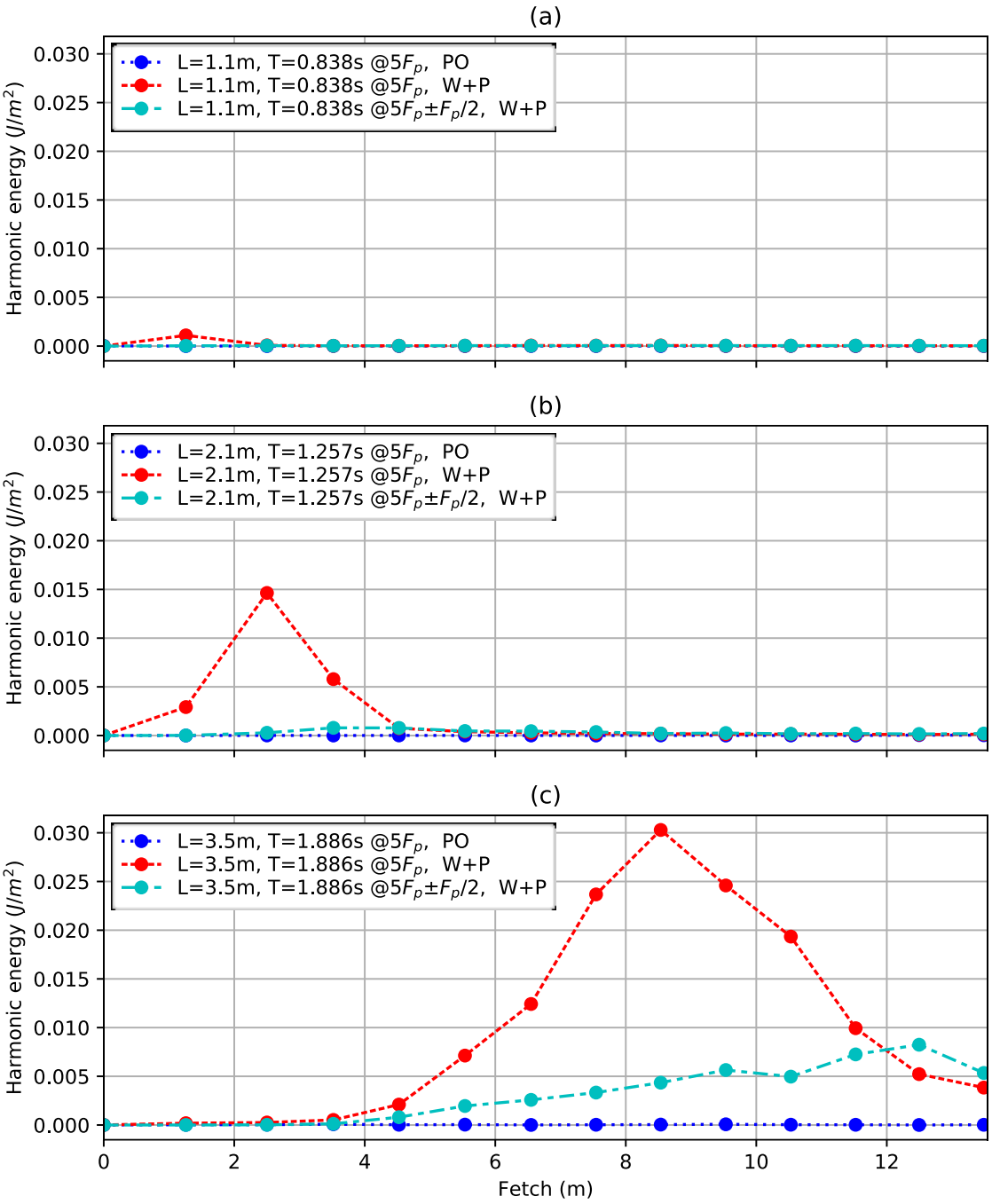

Figure 5.28: Evolution of 5th harmonic with varying paddle wave length and period, all three plots with paddle H_{pad} =0.01m and wind V_0 =5.7m/s. See text for further explanation.

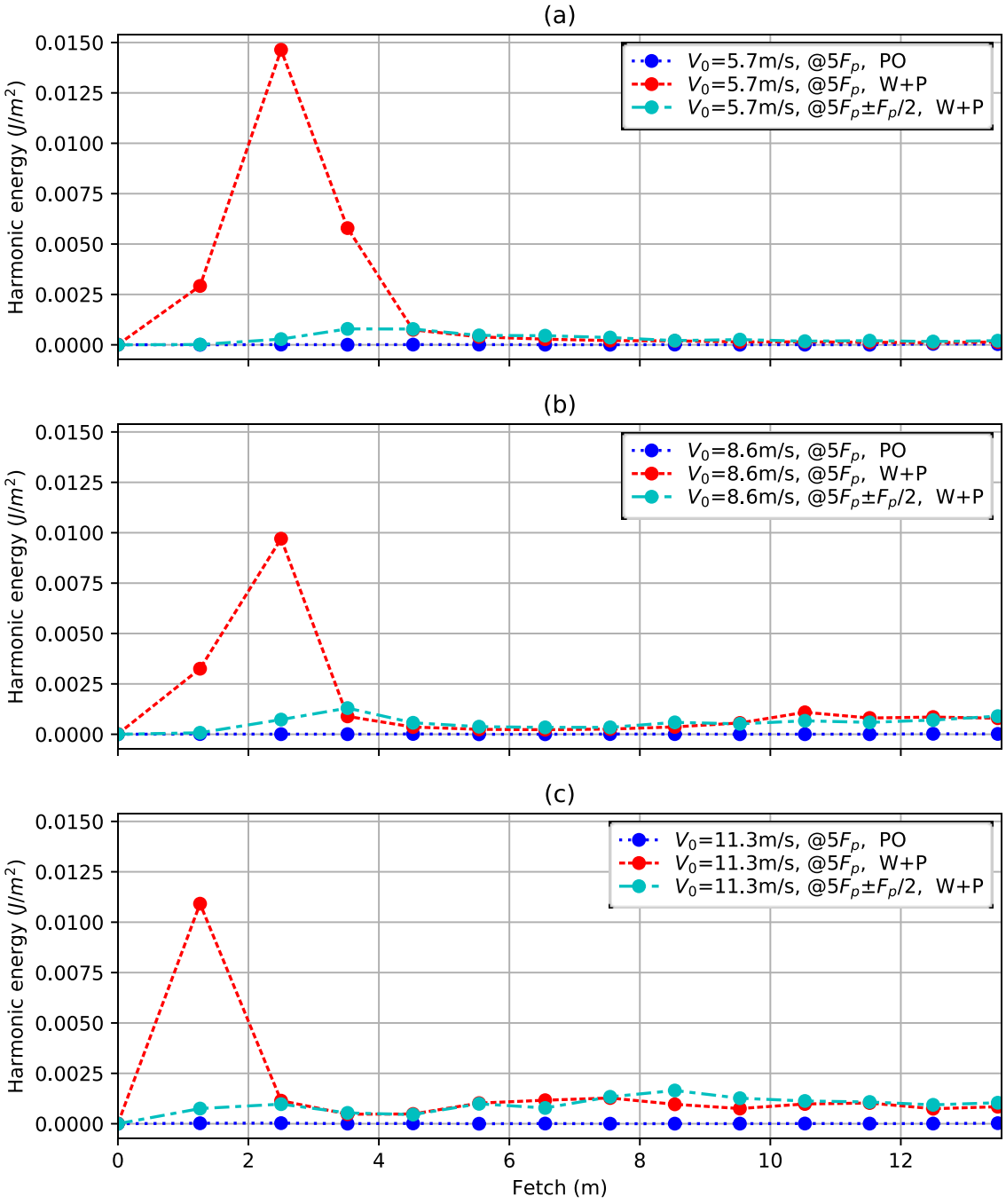

Figure 5.29: Evolution of 5th harmonic with varying wind velocity, all three plots with H_{pad}=0.01m, T_{pad}=1.26s.

A partly unrelated observation is now documented. In Figures 5.21, 5.24 and 5.25, the presence of scattered HF energy between ca. 1.3Hz and 3.0Hz, and in particular a spike at ca. 1.37Hz, was all unexpected. Further attempts were made to determine if this were caused by pollution by experimental factors. There was found to be a consistent spike around 1.37 Hz for all fetches, as shown in Figure 5.30. Given that the wave flume is 0.8m wide, and the natural wavelength for an airy wave of period $(1/1.37)$s in 0.42m depth is

0.83m, it appears likely that this effect was related to cross-tank resonance. Very strong manifestations of cross-tank resonance have in this tank have already been documented in Section 3.1.2, when paddle waves near these frequencies caused the water surface to become unstable laterally, with cross-tank waves growing violently to almost overtop side walls (which extend ca. 0.57m above the MWS) before the paddle was switched off. The resonance visible in Figures 5.21, 5.24 and 5.25 is likely a related phenomenon, although smaller in magnitude, and self-stabilising.

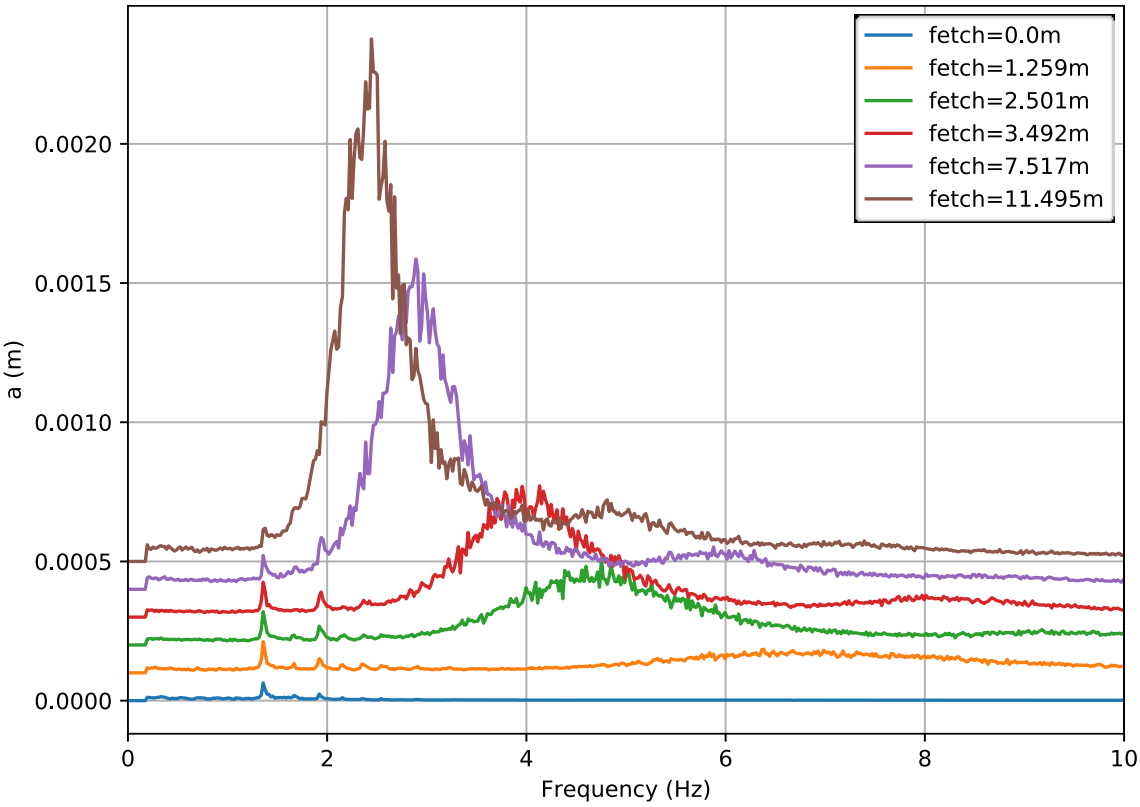

Figure 5.30: Pure wind-wave spectra at various fetches at 20Hz fan frequency. Subsequent fetches separated vertically by 0.0001m amplitude for ease of viewing.

5.7 Paddle wave behaviour

Most results in this chapter up to this point have discussed the evolution of HF waves. In this section, the behaviour of paddle (LF) waves is discussed, along with the distribution of wind input between LF and HF waves. It was usually observed that increase in LF wave energy due to wind forcing was much larger than the HF wave energy lost due to

suppression by LF waves, as seen in Figure 5.31, where loss of HF energy is plotted versus gain in LF wave energy on equally scaled axes. This does not prove or disprove any of the suppression theories, but suggests that if E_{HF} were being transferred to E_{LF} via nonlinear interactions, it was not the major source of energy input to LF waves, with the major source of energy almost certainly being direct wind input to the LF waves. Given that the minimum theoretical wavelength of paddle waves in Figure 5.31 was 1.08m, calculated using linear wave theory, this also contradicts the inference of Plant (1982) based on observations by Plant and Wright (1977), that waves longer than 0.1m grow primarily by nonlinear interactions rather than by direct coupling to wind forcing.

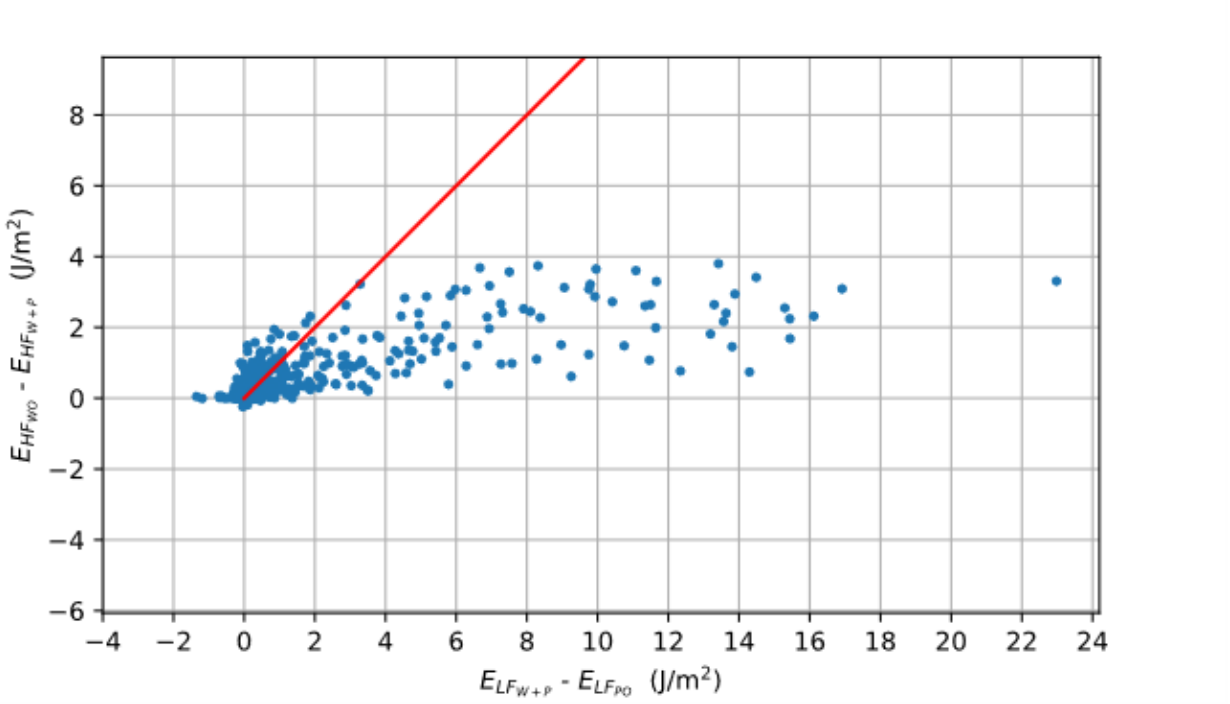

Figure 5.31: Y-axis displays HF energy with no paddle waves minus HF energy with paddle waves (i.e., suppressed HF energy). X-axis displays LF wave energy with wind minus LF wave energy with no wind. Each point is one case-gauge combination. Red line represents a 1:1 gradient.

In Figure 5.31, case-gauge data points with negative suppression, or HF wave enhancement, are those with the blue solid circle below zero on the vertical axis. While the suppression ratio was seen in Figures 5.15 to 5.20 to often be substantially greater than zero, it is clear from Figure 5.31 that negative suppression was only present in cases with very low E_{HF}, e.g. at low fetch and/or low wind velocity.

While examining individual cases in the dataset, it was observed that in some conditions the wind input to paddle waves exhibited a discontinuity or nonlinearity, for which the analogy of a person surfing at a beach may be used. Surfers at a beach either catch or fail

to catch the passing wave. In like manner, paddle waves in the UQ wind-wave flume either caught or failed to catch the wind energy, depending primarily on steepness and wind velocity. In cases in which the paddle wave failed to catch the wind energy, HF waves formed which would have altered the air pressures over the water surface and consequently absorbed momentum from the wind, in effect stealing such wind input from the paddle waves. Such instability supports the Jeffreys (1925) idea of wind input being dependent on wave steepness squared.

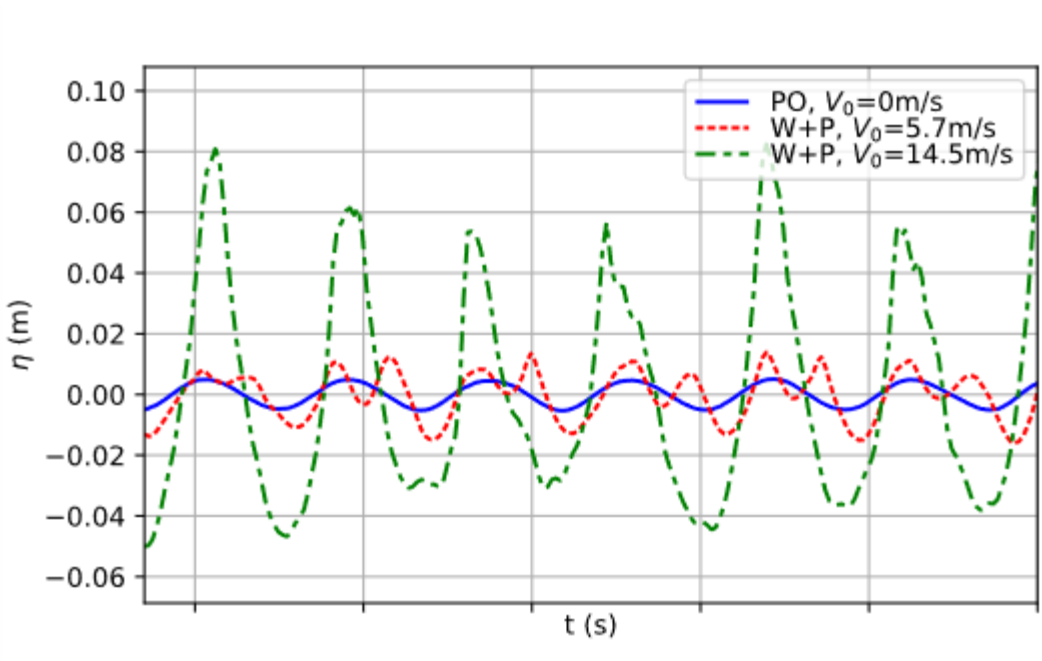

Figure 5.32: Sample of η time series (HF and LF combined) at fetch=13.49m, with T_{pad}=0.84s, H_{pad}=0.01m, $H_{LF_{PO}}/L_{LF_{PO}}$=0.01, C_{pad}=1.08m/s. X-axis ticks are spaced at 1s intervals.

A notable example of this was seen in comparison of paddle waves with H=0.01m and T=0.838s, under wind forcing of ca. 5.7m/s against the same paddle wave conditions with wind velocity of ca. 14.5m/s. Sample time series of typical wave conditions for such cases are plotted in Figure 5.32. For wind velocity of 14.5m/s, almost all of the energy gained by the spectrum is in the LF waves. However, at lower wind velocity this is not the case, but instead the growth occurs at higher frequencies, suggesting a windspeed dependence on wind input to HF waves of low steepness. In Figure 5.33, produced for conditions with $H_{LF_{PO}}/L_{LF_{PO}}$=0.025, steeper LF waves were observed to catch the wind regardless of V_0, while for LF waves with even lower steepness than was present in Figure 5.32, it was revealed in Figure 5.34 that LF waves were unable to catch the wind at any V_0 applied in this experiment, at least within the 13.5m fetch available. It is clear, therefore, that the paddle waves' catching of wind input depends on a combination both wind velocity and wave

steepness. The failure of LF waves to catch the wind is only present with H_{pad}/L_{pad} in the order of 0.01, which is on the low end of the scale of paddle wave steepness applied in laboratory experiments, and this is likely the reason why this nonlinearity of wind input has not been reported previously. However, $H/L \approx 0.01$ is not uncommon in ocean swell waves.

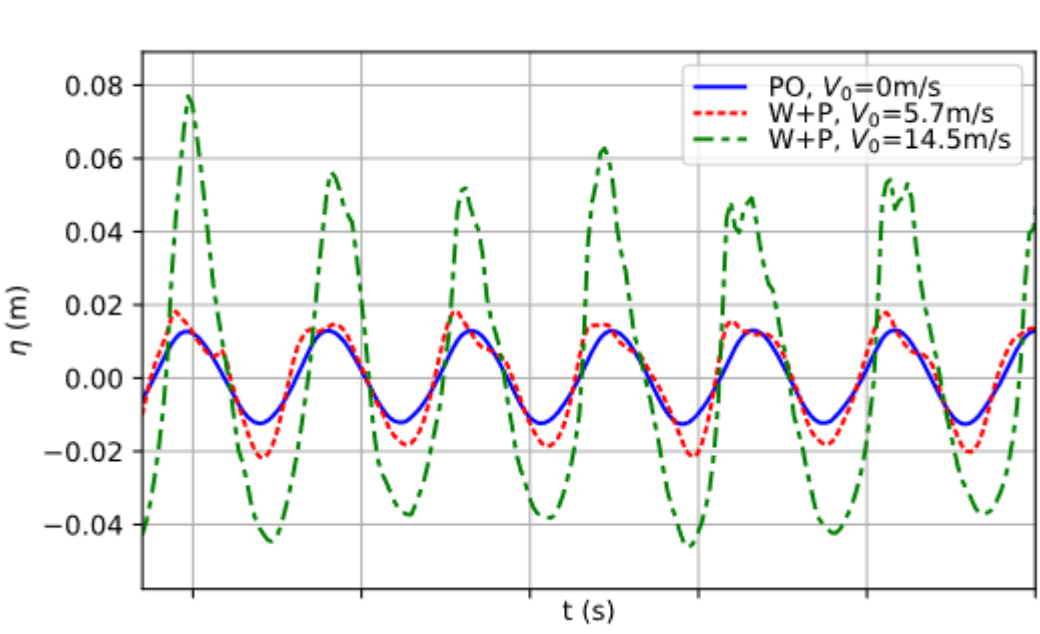

Figure 5.33: Similar to Figure 5.32, but with T_{pad} =0.84s, H_{pad} =0.025m, $H_{LF_{PO}}/L_{LF_{PO}}$=0.025 and C_{pad}=1.08m/s.

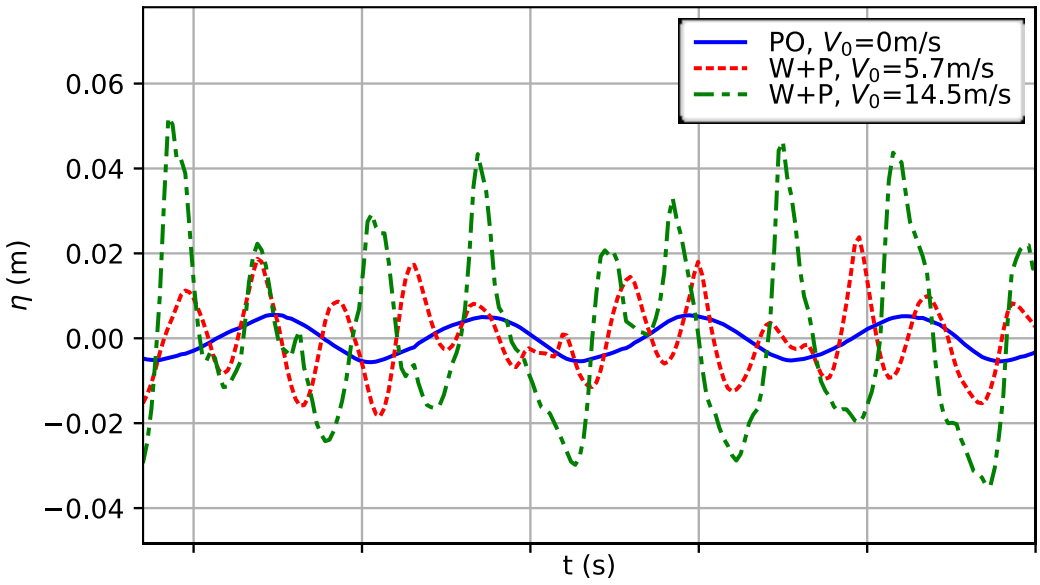

Figure 5.34: Similar to Figure 5.32, but with T_{pad} =1.26s, H_{pad} =0.01m, $H_{LF_{PO}}/L_{LF_{PO}}$=0.005 and C_{pad}=2.1m/s.

The capture of wind input, being dependent on both V_0 and H_{LF}/L_{LF}, may be related to wind separation at LF wave crests causing sheltering of HF waves, as is discussed in Chapter 6, although traditional studies would suggest these LF waves are much too steep (e.g. Belcher and Hunt, 1993). In the conditions of Figure 5.32 the HF waves at V_0=5.7m/s occur quite regularly at almost precisely twice the frequency of the paddle wave, which is not surprising given the peak of the HF portion of the spectrum for these conditions, plotted in Figure 5.35 (b), is at almost exactly twice the paddle wave fundamental frequency.

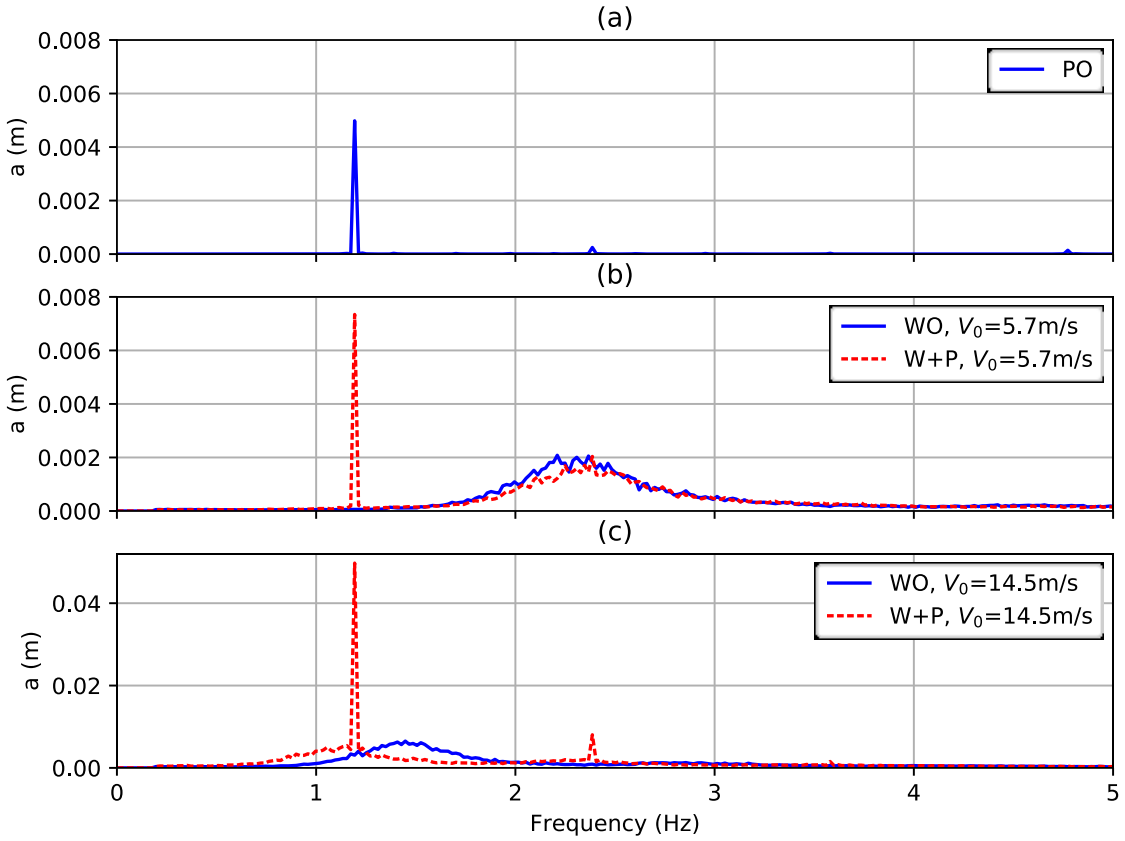

Figure 5.35: Wave spectra at fetch=13.49m, with at fetch=13.49m, with T_{pad}=0.84s, H_{pad}=0.01m, $H_{LF_{PO}}/L_{LF_{PO}}$=0.01 and C_{pad}=1.08m/s, which conditions are identical to 5.32. Nb. Plots (a) and (b) are scaled differently to axis (c) in the vertical dimension.

Also of note in Figure 5.35 (c) is a ca. 10 fold increase in paddle wave amplitude with V_0=14.5m/s, compared with PO conditions. Such fractional increase of paddle waves over the relatively short fetch of ca. 13m has not commonly been documented in literature. The reason such a multiple as large as 10 was present is largely due to the small denominator in this circumstance, namely the small initial $H_{LF_{w+p}}$ of ca. 0.01m.

The discontinuous or varying nature of the distribution of wind input between HF and LF waves can also be identified by examining the LF and HF wave energy evolution down the flume. The evolution of E_{HF} and E_{LF} versus fetch for one set of initial wave conditions in the flume is plotted in Figure 5.36. For the lower fan frequency, HF waves appeared to catch wind input at the expense of LF waves, but for higher wind velocities the paddle waves managed to reach a height or steepness adequate to catch the wind and grow, after which they began suppressing the HF waves, in some cases reducing $E_{HF_{w+p}}$ to a final state much less than what was present upwind.

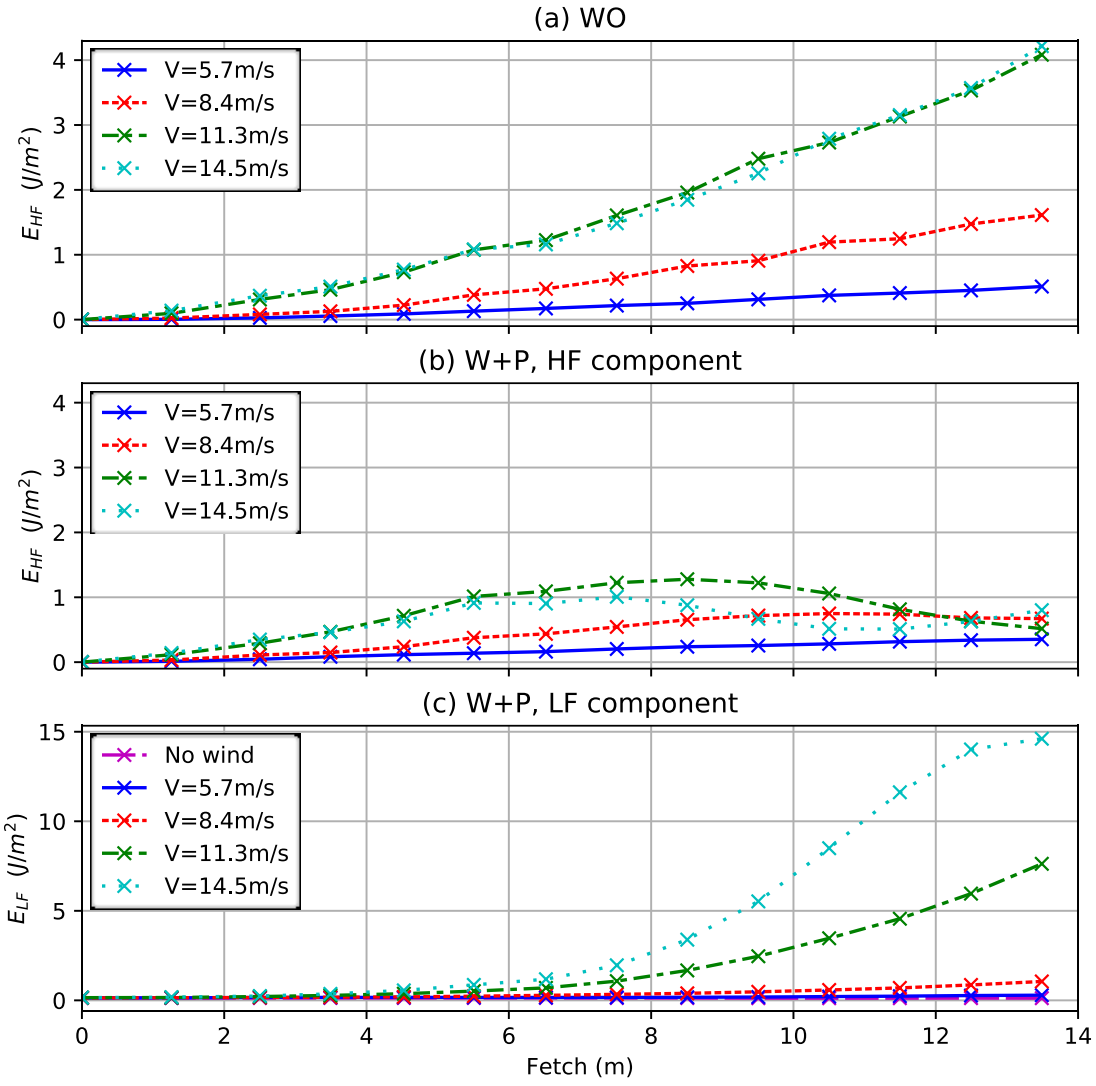

Figure 5.36: Evolution of wave energy vs fetch, for paddle waves with initial H=0.01m and T=0.838s, at all wind velocities in LAB2016.

In Figure 5.36 (a), it was also observed that increasing V_0 from 11.3m/s to 14.5m/s resulted in no significant increase in $E_{HF_{WO}}$, indicating that the WO wave field had reached a limiting value of V^* or V_0 beyond which no more growth could occur, either by the surface reaching a τ_w limit (Donelan et al., 2004) above which it could support no more shear stress, or because of dissipation and nonlinear interactions negating the effect of wind input. This observation is consistent with observations by Wu (1968), who stated that wind-wave momentum transfer did not increase above 12m/s in laboratory conditions. This must not be confused with the concept of fully saturated conditions (e.g. Donelan, 2001), where for a given wind velocity, a wind-wave spectrum reaches a stationary state of full development. It appears that the introduction of paddle waves enabled a greater degree of energy absorption by the wave field, as the (LF) paddle waves in Figure 5.36 (c) absorbed far more energy than was absorbed by the younger (lower C/u^*) WO waves, and did not appear to reach a limiting V_0 in this experiment.

5.8 Suppression in field conditions

This section documents the analysis of field data recorded in Lake Cootharaba during March 2016, and the search within this dataset for evidence of HF wave suppression in the field. In this experiment, E_{LF} consisted of wind-waves near the peak of the spectrum, rather than swell or paddle waves, neither of which were present in the lake.

The 6 days of field experimental recording was divided into data chunks (as they shall be referred to hereafter) representing periods of x minutes duration, where x was trialled at 2, 4, 8 and 20 minutes. Selection of these time durations was a balance of ensuring periods were long enough to capture sufficiently smooth ensemble averaged spectra, yet short enough to capture changes in E_{HF} due to varying conditions, knowing from laboratory experiments that HF waves could increase or decrease in intensity rapidly. Each data chunk was further divided into two halves, so that magnitudes of HF and LF energy in the first half could be compared with magnitudes in the second half, but in most figures in this section the values for measurements displayed are averages of the first and second half of the data chunk, unless otherwise stated. The data chunk length of 4 minutes was adopted for most analysis, which consisted of ensembles of 120s duration, with rectangular Fourier windows of 256 sample points, or 12.8s duration, all of which provided ensembled spectra of passable smoothness. Dividing the entire dataset into chunks in this manner and examining data chunks individually potentially loses some potential for insights gained by sequential

positioning of data chunks. However, this is largely mitigated by the sequential comparison internally within each chunk, between first half and second half.

As displayed in the overview of experimental conditions in Figure 5.37, for the majority of the experimental duration the mean wind velocity did not drop below 4-5m/s, resulting in limited samples of conditions with very low E_{LF} present, for comparison against data with substantial E_{LF}. After heavy rain on 17th March, significantly reduced wind allowed measurement of a duration with minimal E_{LF} to compare the remainder of the dataset against. However, the wind velocities in this calm period were limited in range to less than ca. 3m/s averaged over 20 minutes, resulting in no measurements with strong wind and very low E_{LF}.

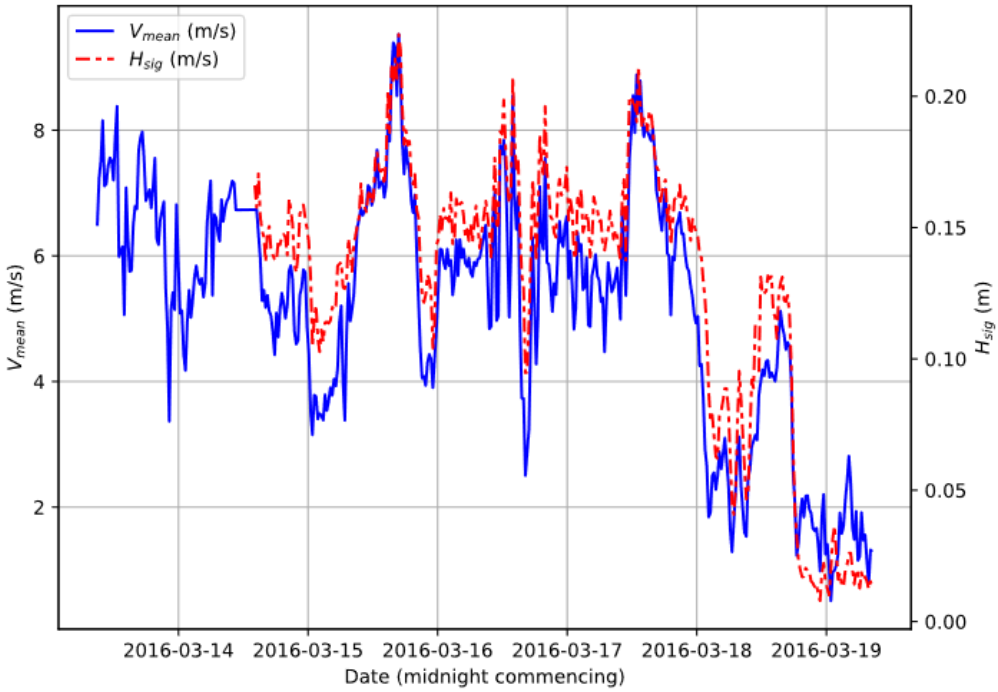

Figure 5.37: Overview of wind and wave conditions throughout the entire 6-day period, averaged across 20-minute periods. Unlike most plots in this section, the only QA applied to data in this figure is removal of wave gauge data on the first day, due to documented calibration discrepancy on this day. The flat line around midday on 14th March was due to a few hours delay during which no recording took place.

It should be noted that an attempt was made to infer LF wave mean direction by averaging the wind velocity during the preceding 10 to 20 minutes of each data chunk, but with limited success. The inferred direction did not appear to correlate well with wave data, was considered of low accuracy and consequently was not included in most analysis.

The variables considered potentially most influential to ΔE_{HF} at any point in time, being quantified as the change of E_{HF} between the first and second half of a data chunk, were

existing E_{HF}, existing E_{LF} and wind input. All three of these influential variables were parameterised as their average values across the entire chunk. For wind input, $V_{3.65}$ was used, being the absolute velocity measured by the top anemometer at 3.65m elevation above the MWS. This averaging across entire chunks is represented in Figures 5.38 and 5.39 by the bar accents on figure labels. As can be seen in Figure 5.38, these variables are all positively correlated together. The correlation in (c) is likely caused by both variables depending strongly on wind velocity, as seen in (a) and (b). A distinct cluster of data points is visible in this figure, most noticeably in pane (c) with near-zero E_{LF}, and E_{HF} reaching as high as ca. 0.08J/m². This small cluster is examined more closely later in this section.

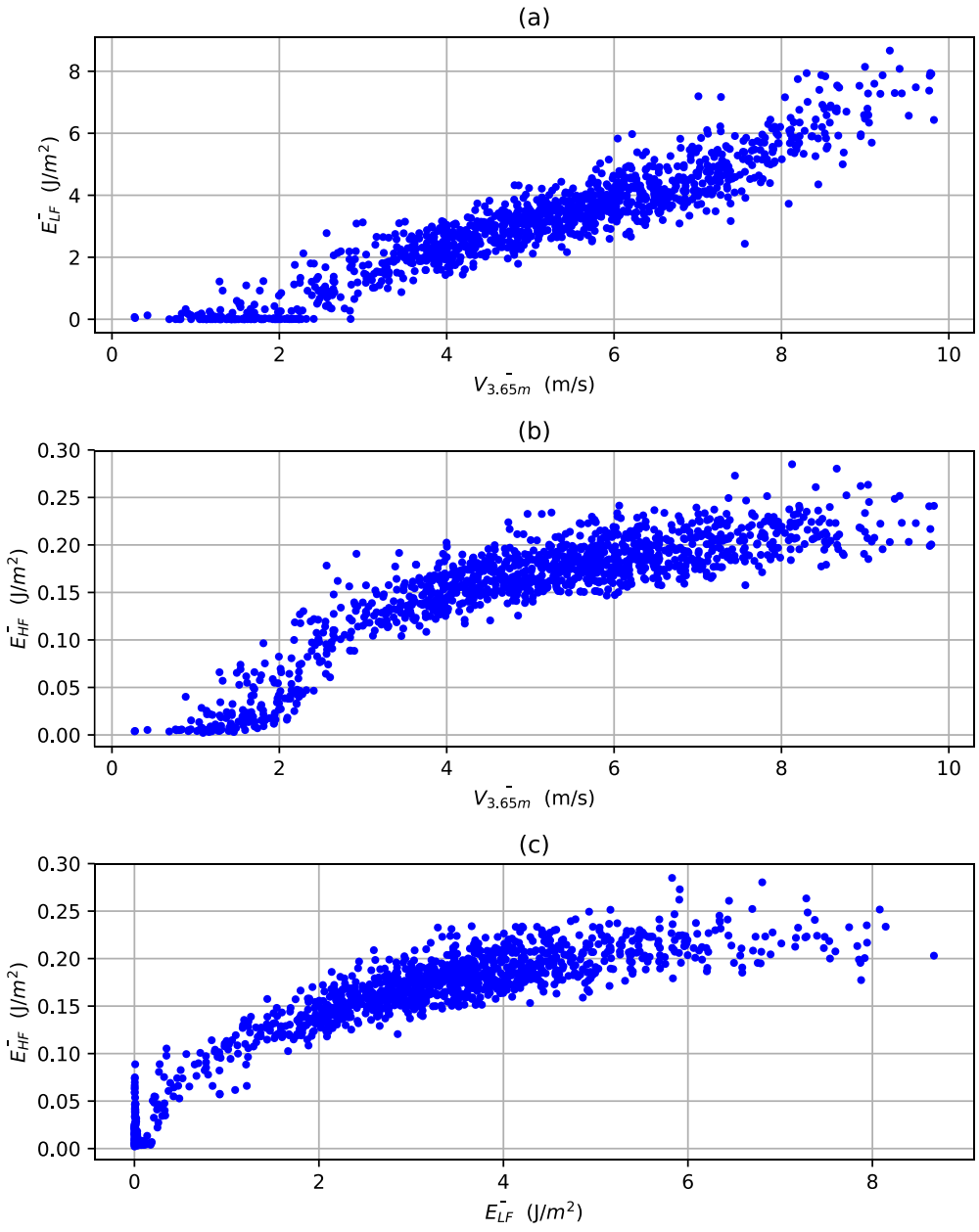

Figure 5.38: Relationships between the three dominant absolute variables, on post-QA dataset, with each variable averaged across chunks of 4-minutes duration.

The strong correlation between variables introduced difficulty in isolating the effect of any individual variable on the target variable, ΔE_{HF}. This is evident in Figure 5.39, in which $\Delta E_{HF}/\overline{E_{HF}}$ the fractional change in HF energy during the data chunk divided by the mean within the chunk, was plotted against each of the three influential variables in isolation. $\Delta E_{HF}/\overline{E_{HF}}$ within each chunk, represented by the blue filled circles in Figure 5.39 exhibit substantial scatter, and no significant gradient could be visibly detected.

In an attempt to isolate the effects of each individual variable, a simple multivariate linear regression was performed on the variables displayed in Figure 5.39, with $\Delta E_{HF}/\overline{E_{HF}}$ as the target and $\overline{V_{3.65}}$, $\overline{E_{HF}}$ and $\overline{E_{LF}}$ as predictors. Because each data point was already an average of a 4-minute period of measurement, it was deemed appropriate not to exclude outliers, apart from those already excluded during data QA. The red trend lines in Figure 5.39 were generated using the output coefficients of this multivariate regression, with trend line average set to equal the average of the dataset. These trendlines are not constrained by definition to follow a line of best fit when plotted in 2D in this manner, and clearly in Figure 5.39 (a) and (c) they do not.

The coefficients output by the regression model, for the most part, qualitatively match what was expected. The positive coefficient for $\Delta E_{hf}/\overline{E_{hf}}$ versus wind $\bar{V}$ was as expected, given that stronger wind was expected to produce an increase in E_{HF} through the chunk, and the low p-value for this coefficient indicated this relationship was not random. The almost flat trendline and high p-value for $\Delta E_{hf}/\overline{E_{hf}}$ versus $\overline{E_{hf}}$ was less expected, because it was anticipated that lower average E_{HF} allowed for potentially greater growth of HF energy in the chunk without being restricted by a Phillips (1958) like saturation limit. The negative coefficient for $\Delta E_{hf}/\overline{E_{hf}}$ versus $\overline{E_{LF}}$ supported a hypothesis that increasing E_{LF} energy results in a decrease of E_{HF} through the chunk, or that HF waves were suppressed by LF waves. The p-value of 0.06 for this coefficient was borderline upon indicating that this relation was not random.

These results must, however, be treated with caution. The root mean squared error of the multivariate regression fit was relatively high at 0.18, which was no surprise given the substantial scatter visible in Figure 5.39. The regression model exhibited an R^2 score of 0.005, being negligibly more accurate than a model with zero coefficients for each variable (which would rend an R^2 score of zero). This indicated that this regression was useless for prediction, and of very limited dependability for drawing inferences on the relationships derived.

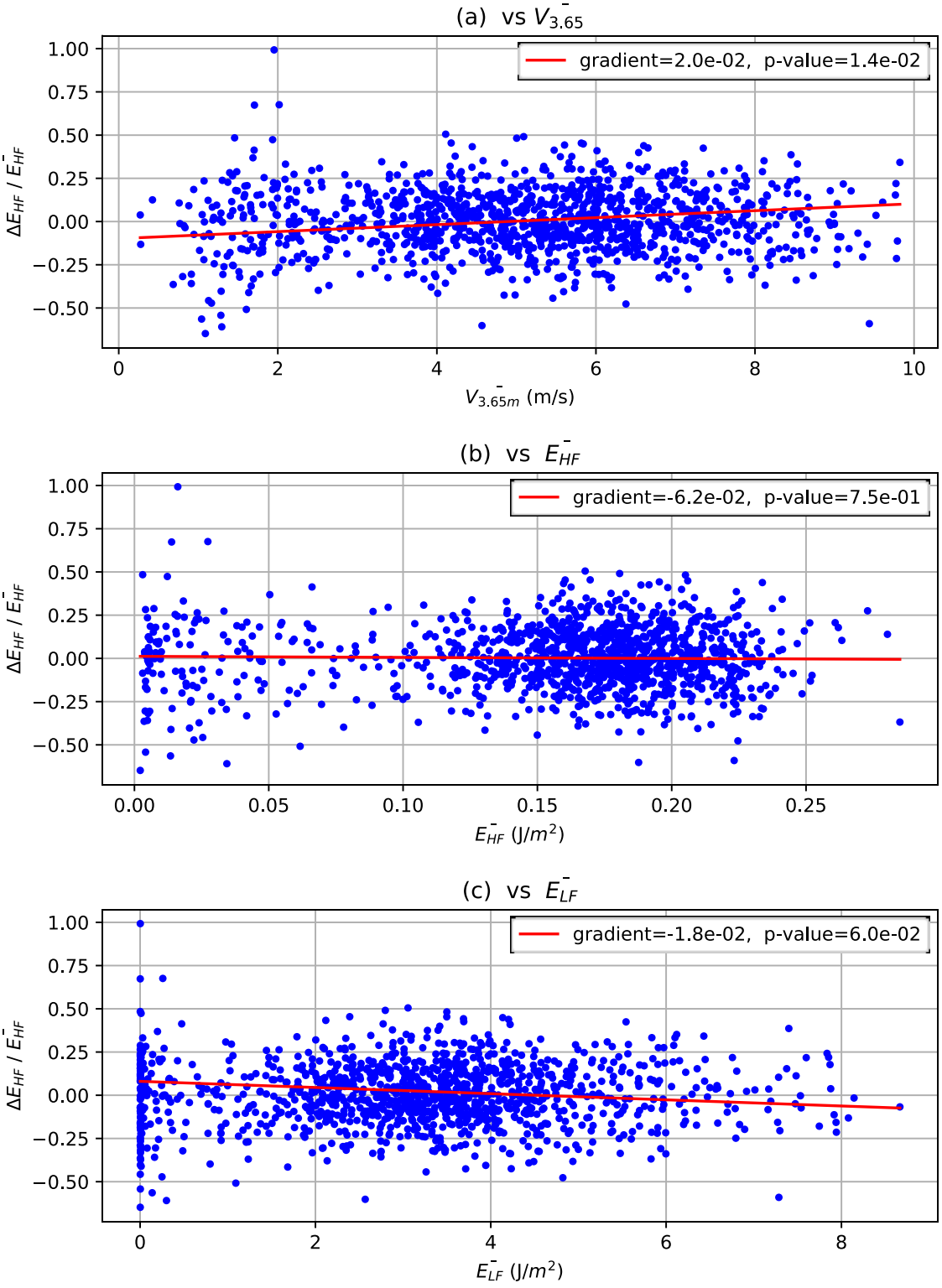

Figure 5.39: Vertical axis for all three plots represents fractional change in HF energy between first and second half of data chunk, with fraction denominator being HF energy throughout the entire chunk. Each data chunk was of 4 minutes duration. Horizontal axes represent (a) average wind velocity at the top sonic anemometer throughout the entire chunk, (b) average HF energy throughout the chunk, and (c) average LF energy throughout the chunk. Nb. Horizontal scale differs between each plot. Red trend lines were produced using coefficients from a multivariate regression. See text for description of regression model.

Because of these shortfalls, the model cannot be argued to prove the presence of suppression in the measured field conditions. The low degree of fit to the data suggested it cannot be used to prove anything. However, there were some points suggesting some inferences from this model may be qualitatively correct. The correlation of $\Delta E_{HF}/\overline{E_{HF}}$ with $\overline{V_{3.65}}$ was in agreement with expectations, with a p-value less than 0.05. The dependence of $\Delta E_{HF}/\overline{E_{HF}}$ on $\overline{E_{LF}}$ exhibited a p-value of 0.06, low enough to suggest the possibility of but not prove a dependence existed. While the two variables $\overline{V_{3.65}}$ and $\overline{E_{LF}}$ were positively correlated with each other, their effects on $\Delta E_{HF}/\overline{E_{HF}}$ were opposite, suggesting that their correlation to each other did not necessarily invalidate their calculated relationship to the target variable, $\Delta E_{hf}/\overline{E_{hf}}$. This opposing effect was a definite contributor to the trend lines in Figure 5.39 (a) and (c) not following the dataset, with the effect of one variable on $\Delta E_{HF}/\overline{E_{HF}}$ being neutralised by the other. The other definite contributor was substantial scatter, which is an inevitable aspect of all wind-wave experiments in field conditions. The scatter in Figure 5.39 is comparable to or less than that in Figures 2.6, 2.7 and 2.8 of Hasselmann et al. (1973), which were already mentioned (but not reproduced) in Section 2.1.1 of this thesis, the relationships of which were used to obtain empirical parameters for the well-known JONSWAP spectrum. However, because of the scatter in the present dataset, and specifically the very poor R^2 value of the regression fit, the results of this basic fit did not prove the occurrence of suppression in the field, and if anything, supported a hypothesis that HF wave suppression was insignificant or extremely weak during the conditions measured.

It was then attempted to perform comparisons of carefully selected clusters of the dataset. In Figure 5.38 (c), the cluster of data chunks with near-zero LF energy and HF energy ranging from 0–0.08J/m² was initially surprising, and after inspection it was found that this cluster represented the time period around the 18th March very calm wind following a rain event, where negligible LF energy was present. Five data points were sampled from this small cluster with HF energy approaching 0.08J/m², and compared against a sample of five data points in the large main cluster in Figure 5.38 (c), chosen with almost identical HF energy to the first five data points, and LF energy typical of the main cluster near that value of HF energy. In Figure 5.40, the 5 spectra from the small cluster are plotted in blue, with the 5 spectra in the main cluster plotted in red. In this comparison, the slope of the HF face of the spectrum appeared slightly higher in the small cluster with negligible LF energy (blue), which may have indicated that HF energy was being suppressed in the conditions within the main cluster (red). However, the average wind velocity was also slightly higher in the small

cluster (marked in blue), with $V_{3.65}$ equal to ca. 2.2m/s for spectra in the blue cluster, and ca. 2.0m/s for spectra in the red cluster, suggesting the marginally increased slope of the blue spectra may have resulted from a different wind velocity. In a similar comparison performed on the dataset prior to QA removal of some data points, with five different data points selected from each cluster, the averaged wind velocity happened to be almost identical, and the forward faces of spectra between the two clusters also aligned almost identically. It was determined that this comparison of two distinct clusters failed to detect any conclusive evidence of HF wave suppression by LF waves in the conditions sampled.

The lack of detected suppression in this comparison could very well be related to the low wind velocity, keeping in mind that suppression was weaker or even negative in the laboratory experiment for low-wind cases. It could also be due to this comparison not accounting for strength of wind forcing immediately prior to the data chunks from which these spectra were obtained. Given that the experiment was performed in a coastal lake with no true swell, the experiment only had the potential to measure suppression internally within a relatively young wind-wave field, with LF waves consisting of wind-waves near the spectral peak, limiting the scope of observation. Regardless what the reasons were, and without being able to conclude whether or not this implies suppression never occurs in field conditions, this comparison is evidence of the difficulty of conclusively measuring field suppression, as has been discovered by others (e.g. Violante-Carvalho et al., 2004), and suggests that the magnitude of suppression in the field, at least in the range of conditions measured, may not be substantial.

In summary, none of the comparisons or data fitting performed were able to detect conclusive evidence of suppression. The failure to detect suppression may have suggested this effect to be of limited quantitative significance in the field conditions measured, however, the range of conditions encountered during COOTHA was limited.

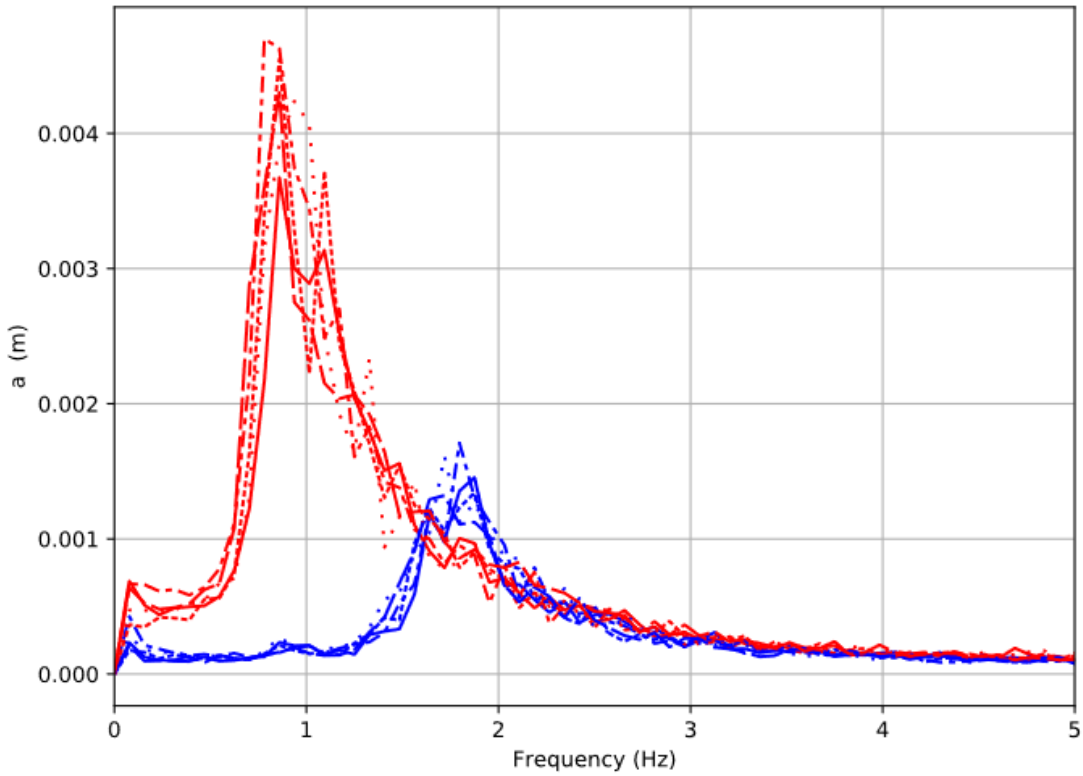

Figure 5.40: Comparison of five sample spectra from the small cluster with near-zero E_{LF} and measurable E_{HF} (blue), against sample spectra of near identical E_{HF} with E_{LF} values typical of the main cluster of the dataset (red).

6 Discussion

As previously stated, this thesis sought to determine which of the prominent theories was most involved in HF wave suppression by LF waves.

In the laboratory experiments within the present study, the increase in LF wave energy with wind was often several times greater than the suppressed HF wave energy (see Figure 5.31). This difference in energy scales makes it difficult to quantitatively correlate HF wave suppression with LF wave growth. In addition, the observation of cases with strong suppression, as well as zero energy (or close to it) portions of the spectrum between LF and HF peaks, demonstrates that a continuous flow of energy through the spectrum (Masson, 1993) is impossible in many suppressed conditions. These observations cast strong doubt on any theories by which HF energy is transferred to LF waves by some form of nonlinear interaction. The timescale required for this type of interaction, which depends on Hasselmann (1962) interactions, is much different to timescales observed in the current study and in prior studies (e.g. Mitsuyasu, 1966). These arguments combined are sufficient to justify discarding this mechanism in its proposed form.

The examination of WO to W+P repeated transitions proved conclusively that HF waves are suppressed by paddle waves much more quickly than they evolve in WO conditions. While one could argue that HF waves of capillary wavelength < 0.05m may dissipate quickly if wind forcing were suddenly switched off, it must be acknowledged that the wind-waves examined in Section 5.3 had already attained a T_p of ca. 0.63s, with a theoretical wavelength of 0.6m for waves at the WO HF peak frequency. Such well-developed waves cannot be expected to lose ca. 90% of their energy within the space of 1 - 5 seconds, decaying in both height and period, purely due to a sudden reduction of wind forcing, even if the wind forcing hypothetically was 100% eliminated. Observations by Donelan and Plant (2009) also found that a sudden removal of wind forcing does not result in immediate destruction of HF wind-waves, but rather a gradual ramping down of HF energy. Given that wind velocity in the repeated transitions was still greater than 10m/s, a complete elimination of wind forcing while the wind was still blowing seems unreasonable. These observations indicate that proposed mechanisms involving modified wind input cannot be solely responsible for suppression of HF waves, suggesting instead that active destruction, i.e. enhanced dissipation, plays a major part.

The approximate breakdown of how much suppression is caused by HF wave decay versus modified wind input, at least in the conditions examined in Section 5.3, is revealed in

Figures 5.6, 5.9 and 5.10. In these figures, ca. 80% of the total E_{HF} decay is shown to occur almost instantly, with ca. 20% of suppression setting in gradually over a duration of ca. 25 seconds. This 25 second duration is of the same time scale as the observed build-up of HF waves from quiescent conditions in WO conditions. One may draw a quick and rough conclusion that ca. 80% of suppression is caused by rapid active decay of HF waves, with 20% caused by reduced wind input acting on a longer time scale, at least in the initial stages as LF waves first arrive in a WO wave field.

The occurrence of HF wave suppression did not appear to depend heavily on wind separation, although Figure 5.20 was not entirely conclusive. How much the wind input component of suppression (ca. 20%) is related to a Townsend (1980) type reduction in turbulent wind shear stress caused by curvature of the streamlines, or by Donelan et al. (2006) wind separation, is thus difficult to determine conclusively based on experimental results. However, the nonlinearity of energy input to HF and LF waves examined in Section 5.7 suggests that wind separation was likely involved in the dynamics, and at relatively low LF wave steepness.

Based on observations, it seems clear however that enhanced dissipation of HF waves is the dominant cause of HF wave suppression by LF waves. Some theories surrounding this enhanced dissipation depend on LF wave breaking events, but this dependence was not clearly detected in the data. Numerous observations were made, however, of strong suppression in cases where LF waves were not near a steepness likely to induce breaking, and in multiple cases where LF wave breaking was not visibly detected (e.g. Figure 5.3). While the present study did not prove whether or not LF breaking events contribute to suppression, it did prove that LF wave breaking is not essential, suggesting it plays a secondary role if any.

It was observed that strong suppression occurs at LF wave crests and high on the windward face of LF waves, which locations are exposed to the highest wind velocities, and least likely to be affected by sheltering. Belcher and Hunt (1993) stated that for a hill with H/L=0.2 (admittedly steeper than LF waves), wind velocity may be increased by a factor of ca. 0.5 near the crest. Based on the observation of suppression at the locations of strong wind forcing, the writer proposes that suppression by enhanced dissipation is strongly coupled to the wind itself. Babanin (2011, p11) described the ripping of steep wave crests off the top of waves by extreme wind forcing, and Babanin et al. (2010) observed wind of strong but not extreme forcing to increase the probability of breaking events, although tending to reduce the severity. Phillips and Banner (1974) proposed augmented wind drift

increases the horizontal orbital velocities of HF waves at LF wave crests, but observations by Cheng and Mitsuyasu (1992) cast doubt on the magnitude or even presence of this effect in wind-wave flume conditions.

Based on the observed location of suppression along the LF wave phase, and the positive correlation with suppression on wind velocity, the writer proposes that HF wave enhanced dissipation is coupled to the wind. HF waves, which are typically steep in nature and already experiencing some dissipation simultaneous to wind input, are caused to break preferentially through one more of the above mechanisms by the sudden increase in wind velocity, at and windward of the LF wave crest, to a wind velocity which these HF waves of very low C/u^* are not sufficiently developed to be able to withstand. This behaviour should occur regardless of LF waves following or opposing the wind, which may be challenged by the observations of Mitsuyasu and Yoshida (1991) and Cheng and Mitsuyasu (1992), in which opposing LF waves enhanced HF waves. However, it must be noted that the spectra displaying enhanced HF energy with opposing LF waves, displayed in Figure 2.13 of this thesis (Mitsuyasu and Yoshida, 1991; Cheng and Mitsuyasu, 1992) were produced from data recorded at V_0=5.0m/s. This relatively low wind velocity may not have been adequately strong to overwhelm the HF waves into breaking suddenly and severely. In the present study, HF waves were actually observed in multiple cases to be enhanced in cases of V_0 comparable to that used by Mitsuyasu and Yoshida (1991) and Cheng and Mitsuyasu (1992), as seen in Figure 5.15, and in Section 5.6. It is possible that the orientation of LF waves relative to the wind direction was less responsible for the enhancement of HF waves observed by Mitsuyasu and Yoshida (1991) and Cheng and Mitsuyasu (1992) than V_0 and H_{LF}/L_{LF}, and that the universality of HF wave enhancement with opposing LF waves may be questioned. It may also be possible that the LF waves in those studies, propagating against the 5.0m/s wind with C_p≈1.48m/s (calculated using linear theory), further reduced the wind velocity present at the water surface marginally, although it must be noted that the orbital velocities at LF wave crests would have also marginally increased the wind velocity experienced by the water surface at crests. The effect of opposing LF waves on HF waves should be explored in the future with a broader range of wind and wave conditions, and fetches.

Typical suppressed conditions, following on from the above proposed mechanism of enhanced dissipation, appears related to excess wind forcing on and windward of the LF wave crest, and a deficit of wind forcing in the LF wave trough. The deficit of wind forcing in troughs is related to the above-mentioned wind input component of suppression,

discovered in the WO to W+P experimentation. While enhanced dissipation constituted ca. 80% of suppression and the wind input component constituted 20% in the WO to W+P experiment, this distribution may not be universal. After significantly suppressed W+P conditions have reached equilibrium, the types of HF waves being suppressed are much smaller in scale of both H_{HF} and T_{HF}, and may be susceptible to different suppression mechanisms. Past studies have observed differing behaviour for capillary scale ripples as for choppy gravity wind-waves (Smith, 1986), so it may be possible that a modified wind stress mechanism is more relevant to capillary waves, and enhanced dissipation is more relevant to choppy gravity-scale HF waves which were present in the WO to W+P transitions prior to arrival of LF waves. Therefore, it is possible that in steady-state conditions, reduced wind input prevents the HF waves from developing, and contributes more than 20% to the overall suppression effect. However, based on the location of suppression in steady-state conditions in Figures 5.11 to 5.13, it seems certain that enhanced dissipation is still relevant, at least to some degree, to suppression of the smaller steady-state HF waves.

In cases of low initial paddle wave steepness, the absorption of wind input observed in LAB2016 could be crudely likened to a race between LF paddle waves and HF waves. HF waves were observed in some cases to develop to a scale enabling them to absorb the major share of wind input, modifying the wind field to be coherent with the HF waves and preventing paddle waves from ever developing. However, in cases with identical paddle signal but higher wind velocity, the paddle waves 'got their noses in front', reaching a steepness adequate to cause the wind field to be coherent with the LF wave, and absorbed wind input, beyond which they grew rapidly and then strongly suppressed HF wave development. It was also observed that HF waves at times gained energy more rapidly than LF waves early in the fetch, then decayed after the LF waves caught the wind, as evidenced by the observations of HF waves at the downwind end of the flume being significantly smaller in magnitude than at some upwind locations.

The nonlinearity of wind input distribution between HF and LF waves suggests a fundamental change takes place in the wind flow regime once LF waves have caught the wind. The most likely cause of this nonlinearity is wind separation at LF wave crests, which is consistent with the present experiments in its dependence on both LF wave steepness and wind velocity (Donelan et al., 2006). This wind separation forces the wind field to be coherent with the LF wave, provides strong momentum input to the LF waves, and shelters HF waves along parts of the LF wave phase, all of which assist the LF waves to catch the wind at the expense of HF waves.

The presence of HF wave enhancement, or negative suppression, by following paddle waves of low steepness and small fetch cannot be denied, based on measurements and observations performed in LAB2016. This observation has not been discussed in wind-wave literature, although it may have been measured and overlooked by Mitsuyasu (1966). Some of this enhancement existed by broadening of the HF wave spectrum, and shifting it to lower frequencies. It was also clear that a large portion of this enhancement occurs within the harmonic frequencies. This enhancement of HF energy in harmonic frequencies, completely unbound to the paddle wave, often more than an order of magnitude greater than the energy in these harmonics in absence of wind, was not anticipated by the writer. This suggests a very strong amplification mechanism, with LF waves and their harmonics providing seeding to assist incipient HF waves to reach a point of Kelvin-Helmholst instability, or ripple formation, earlier. The marginally accelerated wind at LF wave crests of even very low steepness may assist this threshold to be reached earlier. HF energy appears to latch onto energy in these initially tiny harmonics, yet is able to drift in phase after having developed, to spread over the entire LF wave phase. This effect was discovered as a result of generating paddle waves of height and steepness lower than what is typically generated in laboratory wind-wave conditions. Future laboratory research should be performed to probe further into the nature of this unexpected behaviour with paddle waves of very low steepness and small fetch.

It is possible that the physics of early wave inception investigated by Jeffreys (1925) and discussed by Phillips (1957) play a more significant role in the enhancement of HF waves than those of form drag growth discussed by Miles (1957). The initial disturbance from a flat surface performed by paddle waves of low steepness appears to assist capillary waves to overcome initial skin tension and form into ripples sooner than they would have in absence of the paddle waves. Fluctuations in the wind stress coherent with the paddle waves is likely what speeds up this initial Kelvin-Helmholst instability, while at early fetches these HF waves have likely not yet reached the Phillips (1958) equilibrium limit, and consequently grow rapidly.

Stepping aside from the core focus of the present research, the statement by Plant and Wright (1977), that the longest waves to grow primarily by wind input are ca. 0.1m in length may be challenged by measurements made in the current study. A several-fold increase in $H_{LF_{w+p}}$ was sometimes observed, with wavelengths of order 1m, with minimal HF energy present from which energy could be extracted, indicating the growth was from coupling to the wind input. Indeed, the conditions in Figure 5.24 (c) revealed an almost 10-fold increase

of the height of LF waves with very low initial steepness. These observations casts doubt on that hypothesis.

Measurements of lake spectra were less conclusive than those made in the laboratory flume during the present study. Wave spectra were overall observed to evolve with a JONSWAP like spectral shape. Collectively, the relationship obtained by means of a multivariate first order regression did not prove that HF waves were being significantly suppressed, and if anything proved that the effect, if it was occurring throughout the dataset, was small in magnitude. The examination of distinct clusters of time periods with very low LF wave energy versus clusters with average LF wave energy also did not exhibit strong suppression. However, it must be kept in mind that this comparison of clusters was performed at ca. 2.0-2.2m/s wind velocity, and Figure 5.15 revealed that suppression in the laboratory flume tended to be weaker or even negative with lower wind velocity. The relatively small range of wind-wave conditions encountered in this coastal lake significantly reduced the scope of observation. The fact that HF energy was less suppressed in laboratory conditions by LF waves of low steepness, and sometimes was even enhanced, suggests, as was discussed by Chen and Belcher (2000), that suppression will rarely be as measurable in ocean conditions where swell waves interact with a wind-wave field, as what is apparent in laboratory conditions with steep paddle waves. Future field experiments focused on suppression should include samples of both swell and LF wind-waves for comparison, with measurements of strong wind forcing in conditions of both high and low LF wave steepness. This full range of conditions was not encountered in the present study.

7 Conclusion

Experimental observations have been made on the effect of LF waves on HF wind-waves, mostly in laboratory conditions but also in field conditions. The careful study of WO to W+P transitions provides compelling evidence that HF waves are actively destroyed by LF waves, more so than merely being inhibited in their development. While wind field modulation effects were observed in the flume, their importance in the suppression process was deemed to be secondary to that of enhanced dissipation. Observations indicated that the enhanced dissipation mechanism appears to be coupled to strong wind at LF wave crests and on the windward face, which caused preferential breaking. This mechanism should be reviewed theoretically, and additional insights may be gained by future laboratory measurements in facilities with paddle waves opposing the wind. The lake experiments performed were inconclusive regarding the identification of suppression in the field, suggesting that, at least in wind-wave fields at small fetch and small C/u^*, HF wave suppression is not a dominant contributor to wind-wave evolution, although future experiments may prove it to be present in other oceanic conditions.

It was observed that in conditions of low paddle wave steepness, the distribution of wind input between HF and LF waves, or specifically the LF waves' ability to absorb wind input, exhibited substantial nonlinearity. They absorbed negligible wind input until reaching a steepness and/or wind velocity sufficient to force the wind field to be coherent with the LF waves rather than HF waves, which allowed the LF waves to catch the wind. This nonlinearity suggests a change in the wind regime caused by wind separation at LF wave crests, indicating strongly that the Jeffreys (1924) mechanism of separated sheltering may deserve more attention than it typically receives in contemporary wave modelling. Further experiments should be performed in laboratory conditions with paddle waves of low steepness and varying wind velocity, to better quantify the point at which dominant (LF) waves catch the wind, combined with a closer examination of the wind field before and after this point.

One other novel finding in the present study was that of HF wave enhancement in conditions of low paddle wave steepness, which has not been discussed in past studies. This also included focused enhancement of HF energy in LF wave harmonic frequencies, while being unbound to the paddle wave. This also has not been documented previously, and neither of these enhancements is explained by present wave theories. The writer encourages the wind-wave community to perform further experimentation with wind applied

to paddle waves of very low steepness in other experimental flumes, to verify the replicability of these results. Verification of this effect will stimulate re-consideration of the theories surrounding initial inception of HF waves (Phillips, 1957).

References

Alves, J.H.G., Banner, M.L. and Young, I.R., 2003. Revisiting the pierson–moskowitz asymptotic limits for fully developed wind waves. Journal of physical oceanography, 33(7): 1301-1323.

Ardhuin, F., Chapron, B. and Collard, F., 2009. Observation of swell dissipation across oceans. Geophysical Research Letters, 36(6).

Babanin, A.V., 2011. Breaking and dissipation of ocean surface waves. Cambridge University Press, Cambridge, UK.

Babanin, A.V., Chalikov, D., Young, I.R. and Savelyev, I., 2010. Numerical and laboratory investigation of breaking of steep two-dimensional waves in deep water. J. Fluid Mech., 644: 433-463.

Babanin, A.V. and Young, I.R., 2005. Two-phase behaviour of the spectral dissipation of wind waves.

Badulin, S.I., Korotkevich, A.O., Resio, D. and Zakharov, V.E., 2008. Wave-wave interactions in wind-driven mixed seas. Proceedings of the Rogue Waves 2008 Workshop, Brest, France (ed. M. Olagnon & M. Prevosto), pp. 77-86.

Baldock, T.E. and Simmonds, D.J., 1999. Separation of incident and reflected waves over sloping bathymetry. Coastal Engineering, 38(3): 167-176.

Banner, M. and Melville, W., 1976. On the separation of air flow over water waves. Journal of Fluid Mechanics, 77(04): 825-842.

Banner, M.L., 1990. The influence of wave breaking on the surface pressure distribution in wind-wave interactions. Journal of Fluid Mechanics, 211(1): 463-495.

Banner, M.L. and Phillips, O., 1974. On the incipient breaking of small scale waves. Journal of Fluid Mechanics, 65(04): 647-656.

Belcher, S.E., Harris, J.A. and Street, R.L., 1994. Linear dynamics of wind waves in coupled turbulent air-water flow. Part 1. Theory. Journal of Fluid Mechanics, 271: 119-151.

Belcher, S.E. and Hunt, J.C.R., 1993. Turbulent shear flow over slowly moving waves. Journal of Fluid Mechanics, 251(1): 109-148.

Belcher, S.E., Newley, T. and Hunt, J., 1993. The drag on an undulating surface induced by the flow of a turbulent boundary layer. Journal of fluid mechanics, 249: 557-596.

Benjamin, T.B. and Feir, J.E., 1967. The disintegration of wave trains on deep water part 1. Theory. Journal of Fluid Mechanics, 27(3): 417-430.

Bliven, L.F., Huang, N.E. and Long, S.R., 1986. Experimental study of the influence of wind on benjamin-feir sideband instability. Journal of Fluid Mechanics, 162(1): 237-260.

Bole, J.B. and Hsu, E.Y., 1969. Response of gravity water waves to wind excitation. Journal of Fluid Mechanics, 35(4): 657-675.

Bonmarin, P., 1989. Geometric properties of deep-water breaking waves. Journal of Fluid Mechanics, 209: 405-433.

Booij, N., Holthuijsen, L.H. and Haagsma, I., 2001. The effect of swell on the generation and dissipation of wind sea. Proc. 4th International Symposium Waves 2001, pp. 501-506.

Booij, N., Ris, R.C. and Holthuijsen, L.H., 1999. A third-generation wave model for coastal regions 1. Model description and validation. Journal of Geophysical Research C: Oceans, 104(4): 7649-7666.

Buckley, M. and Veron, F., 2010. Dynamics of the airflow above breaking and non-breaking waves.

Caulliez, G., 2002. Self-similarity of near-breaking short gravity wind waves. Physics of Fluids, 14(8): 2917-2920.

Caulliez, G., 2013. Dissipation regimes for short wind waves. Journal of Geophysical Research: Oceans, 118(2): 672-684.
Caulliez, G. and Guerin, C.A., 2012. Higher-order statistical analysis of short wind wave fields. JOURNAL OF GEOPHYSICAL RESEARCH-OCEANS, 117(C6).
Cavaleri, L. et al., 2007. Wave modelling–the state of the art. Progress in Oceanography, 75(4): 603-674.
Cavaleri, L., Luciana, B., Jean-Raymond, B. and Cavaleri, L., 2015. Waving in the rain.
Cavaleri, L. and Rizzoli, P.M., 1981. Wind wave prediction in shallow water: Theory and applications. Journal of Geophysical Research, 86(C11): 10961-10973.
Chen, G. and Belcher, S.E., 2000. Effects of long waves on wind-generated waves. Journal of Physical Oceanography, 30(9): 2246-2256.
Cheng, Z. and Mitsuyasu, H., 1992. Laboratory studies on the surface drift current induced by wind and swell. Journal of Fluid Mechanics, 243(1): 247-259.
Cho, I. and Kim, M., 2008. Wave absorbing system using inclined perforated plates. Journal of Fluid Mechanics, 608: 1-20.
Collard, F., Ardhuin, F. and Chapron, B., 2005. Extraction of coastal ocean wave fields from sar images. IEEE Journal of Oceanic Engineering, 30(3): 526-533.
Crapper, G.D., 1957. An exact solution for progressive capillary waves of arbitrary amplitude. J. Fluid Mech., 2(6): 532-540.
Dobson, F.W., 1971. Measurements of atmospheric pressure on wind-generated sea waves. Journal of Fluid Mechanics, 48(01): 91-127.
Donelan, M. et al., 2004. On the limiting aerodynamic roughness of the ocean in very strong winds. Geophysical Research Letters, 31(18).
Donelan, M.A., 1987. Effects of swell on the growth of wind waves. Johns Hopkins APL Technical Digest (Applied Physics Laboratory), 8(1): 18-23.
Donelan, M.A., 2001. A nonlinear dissipation function due to wave breaking.
Donelan, M.A., Babanin, A.V., Young, I.R. and Banner, M.L., 2006. Wave-follower field measurements of the wind-input spectral function. Part ii: Parameterization of the wind input. Journal of Physical Oceanography, 36(8): 1672-1689.
Donelan, M.A., Babanin, A.V., Young, I.R., Banner, M.L. and McCormick, C., 2005. Wave-follower field measurements of the wind-input spectral function. Part i: Measurements and calibrations. JOURNAL OF ATMOSPHERIC AND OCEANIC TECHNOLOGY, 22(7): 799-813.
Donelan, M.A., Drennan, W. and Magnusson, A.K., 1996. Nonstationary analysis of the directional properties of propagating waves. Journal of Physical Oceanography, 26(9): 1901-1914.
Donelan, M.A., Drennan, W.M. and Katsaros, K.B., 1997. The air-sea momentum flux in conditions of wind sea and swell. JOURNAL OF PHYSICAL OCEANOGRAPHY, 27(10): 2087-2099.
Donelan, M.A., Haus, B.K., Plant, W.J. and Troianowski, O., 2010. Modulation of short wind waves by long waves. Journal of Geophysical Research-Oceans, 115.
Donelan, M.A. and Plant, W.J., 2009. A threshold for wind-wave growth. Journal of Geophysical Research - Oceans, 114(C7): C07012.
Duncan, J., Keller, W. and Wright, J., 1974. Fetch and wind speed dependence of doppler spectra. Radio Science, 9(10): 809-819.
Elliott, J., 1972. Microscale pressure fluctuations near waves being generated by the wind. Journal of Fluid Mechanics, 54(03): 427-448.
Forristall, G., 1981. Measurements of a saturated range in ocean wave spectra. Journal of Geophysical Research: Oceans, 86(C9): 8075-8084.
Fuchs, J.U., 2014. Wave flume - wave absorber. Personal communication emailed 4/03/2014.

Gent, P. and Taylor, P., 1976. A numerical model of the air flow above water waves. Journal of Fluid Mechanics, 77(1): 105-128.
Greco, M., Bordoni, F. and Gini, F., 2004. X-band sea-clutter nonstationarity: Influence of long waves. Oceanic Engineering, IEEE Journal of, 29(2): 269-283.
Groeneweg, J., van Gent, M., van Nieuwkoop, J. and Toledo, Y., 2015. Wave propagation into complex coastal systems and the role of nonlinear interactions. Journal of Waterway, Port, Coastal, and Ocean Engineering, 141(5).
Hanson, J., 1997. Wind sea growth and swell evolution in the gulf of alaska. ProQuest Dissertations Publishing.
Hara, T. and Belcher, S.E., 2002. Wind forcing in the equilibrium range of wind-wave spectra. Journal of Fluid Mechanics, 470: 223-245.
Hara, T. and Plant, W.J., 1994. Hydrodynamic modulation of short wind‐wave spectra by long waves and its measurement using microwave backscatter. Journal of Geophysical Research: Oceans (1978–2012), 99(C5): 9767-9784.
Hasselmann, K., 1962. On the non-linear energy transfer in a gravity-wave spectrum part 1. General theory. Journal of Fluid Mechanics, 12(4): 481-500.
Hasselmann, K., 1963. On the non-linear energy transfer in a gravity-wave spectrum. Part 3. Evaluation of the energy flux and swell-sea interaction for a neumann spectrum. Journal of Fluid Mechanics, 15(3): 385-398.
Hasselmann, K. et al., 1973. Measurements of wind-wave growth and swell decay during the joint north sea wave project (jonswap), Deutches Hydrographisches Institut.
Hasselmann, S. and Hasselmann, K., 1985. Computations and parameterizations of the nonlinear energy transfer in a gravity-wave spectrum. Part 1: A new method for efficient computations of the exact nonlinear transfer integral. Journal of Physical Oceanography, 15(11): 1369-1377.
Hatori, M., Tokuda, M. and Toba, Y., 1981. Experimental study on strong interaction between regular waves and wind waves-i. Journal of the Oceanographical Society of Japan, 37(3): 111-119.
Holthuijsen, L.H., Ris, R.C., Booij, N. and Cecchi, E., 2000. Swell and whitecapping, a numerical experiment.
Hunter, J.D., 2007. Matplotlib: A 2d graphics environment. Computing in Science & Engineering, 9: 90-95.
Hwang, P.A., 2002. Phase distribution of small-scale ocean surface roughness. Journal of Physical Oceanography, 32(11): 2977-2987.
Imai, Y., Hatori, M., Tokuda, M. and Toba, Y., 1981. Experimental study on strong interaction between regular waves and wind waves—ii. in Tohoku Geophysical Journal, 27.
Janssen, P.A., 1991. Quasi-linear theory of wind-wave generation applied to wave forecasting. Journal of Physical Oceanography, 21(11): 1631-1642.
Jeffreys, H., 1925. On the formation of water waves by wind. Proceedings of the Royal Society of London. Series A, 107(742): 189-206.
Jones, E., Oliphant, E., Peterson, P. and al, e., 2001-. Scipy: Open source scientific tools for python.
Kato, H. and Tsuruya, H., 1978. Experimental study of wind waves generated on currents. In: M.o.T. Port and Harbour Research Institute, Yokosuka, Japan (Editor), Japan.
Kawai, S., Okada, K. and Toba, Y., 1977. Field data support of three-seconds power law andgu* σ− 4-spectral form for growing wind waves. Journal of the Oceanographical Society of Japan, 33(3): 137-150.
Keller, W., Larson, T. and Wright, J., 1974. Mean speeds of wind waves at short fetch. Radio Science, 9: 1091-1100.

Keller, W.C., Plant, W.J., Petitt Jr, R.A. and Terray, E.A., 1994. Microwave backscatter from the sea: Modulation of received power and doppler bandwidth by long waves. Journal of Geophysical Research, 99(5): 9751-9766.
Keller, W.C. and Wright, J.W., 1975. Microwave scattering and the straining of wind‐generated waves. Radio Science, 10(2): 139-147.
Kelvin, L., 1871. Mathematical and physical papers. Cambridge University Press (1910), 4: 76-85.
Kitaigorodskii, S., 1983. On the theory of the equilibrium range in the spectrum of wind-generated gravity waves. Journal of Physical Oceanography, Boston, 13(5): 816-827.
Komen, G. et al., 1994. Dynamics and modelling of ocean waves. Cambridge University Press, New York.
Komen, G., Hasselmann, K. and Hasselmann, K., 1984. On the existence of a fully developed wind-sea spectrum. Journal of Physical Oceanography, 14(8): 1271-1285.
Komen, G.J., Komen, G.J. and Oost, W.A., 1989. Radar scattering from modulated wind waves : Proceedings of the workshop on modulation of short wind waves in the gravity-capillary range by non-uniform currents / edited by g. J. Komen and w. A. Oost. Dordrecht, Netherlands ; Boston, Massachusetts ; London, England : Kluwer Academic Publishers, Dordrecht, Netherlands ; Boston, Massachusetts ; London, England.
Kudryavtsev, V. and Makin, V., 2002. Coupled dynamics of short waves and the airflow over long surface waves. Journal of Geophysical Research: Oceans, 107(C12).
Kudryavtsev, V., Mastenbroek, C. and Makin, V., 1997. Modulation of wind ripples by long surface waves via the air flow: A feedback mechanism. Boundary-Layer Meteorology, 83(1): 99-116.
Lake, B.M., Yuen, H.C., Rungaldier, H. and Ferguson, W.E., 1977. Nonlinear deep-water waves: Theory and experiment. Part 2. Evolution of a continuous wave train. Journal of Fluid Mechanics, 83(1): 49-74.
Lighthill, M.J., 1962. Physical interpretation of the mathematical theory of wave generation by wind. Journal of Fluid Mechanics, 14(3): 385-398.
Liu, P.C., 1993. Estimating breaking wave statistics from wind-wave time series data. ANNALES GEOPHYSICAE-EUROPEAN GEOPHYSICAL SOCIETY, pp. 970-970.
Liu, P.C. and Babanin, A.V., 2004. Using wavelet spectrum analysis to resolve breaking events in the wind wave time series. Annales Geophysicae, pp. 3335-3345.
Longo, S. and Losada, M., 2012. Turbulent structure of air flow over wind-induced gravity waves. Experimental Methods and their Applications to Fluid Flow, 53(2): 369-390.
Longuet-Higgins, M.S., 1969. A nonlinear mechanism for the generation of sea waves. Proceedings of the Royal Society of London. Series A, Mathematical and Physical Sciences, 311(1506): 371-389.
Longuet-Higgins, M.S., Cartwright, D.E. and Smith, N.D., 1963. Observations of the directional spectrum of sea waves using the motions of a floating buoy. Deep-Sea Research and Oceanographic Abstracts, 12(1): 53-53.
Longuet-Higgins, M.S. and Smith, N.D., 1983. Measurement of breaking waves by a surface jump meter. Journal of Geophysical Research, 88(14): 9823-9831.
Longuet-Higgins, M.S. and Stewart, R.W., 1960. Changes in the form of short gravity waves on long waves and tidal currents. Journal of Fluid Mechanics, 8(04): 565-583.
Longuet, H., 1985. Accelerations in steep gravity waves. Journal of Physical Oceanography, 15(11): 1570-1579.
Masson, D., 1993. On the nonlinear coupling between swell and wind waves. Journal of Physical Oceanography, 23(6): 1249-1258.

Mastenbroek, C., Burgers, G. and Janssen, P., 1993. The dynamical coupling of a wave model and a storm surge model through the atmospheric boundary layer. Journal of Physical Oceanography, 23(8): 1856-1866.
McKinney, W., 2010. Data structures for statistical computing in python. Proceedings of the 9th Python in Science Conference, p.^pp. 51-56.
Melville, W., 1982. Instability and breaking of deep-water waves. Journal of Fluid Mechanics, 115(1): 165-185.
Miles, J.W., 1957. On the generation of surface waves by shear flows. Journal of Fluid Mechanics, 3(2): 185-204.
Miles, J.W., 1959. On the generation of surface waves by shear flows. Part 2. Journal of Fluid Mechanics, 6(4): 568-582.
Miller, S.J., Shemdin, O.H. and Longuet-Higgins, M.S., 1991. Laboratory measurements of modulation of short-wave slopes by long surface waves. Journal of Fluid Mechanics, 233(1): 389-404.
Mitsuyasu, H., 1966. Interactions between water waves and wind (i). Rep. Res. Inst. Appl. Mech. Kyushu Univ, 14: 67-88.
Mitsuyasu, H., 1977. Measurement of the high-frequency spectrum of ocean surface waves. Journal of Physical Oceanography, Boston, 7(6): 882-891.
Mitsuyasu, H., 2015. Reminiscences on the study of wind waves. Proceedings of the Japan Academy. Series B, Physical and biological sciences, 91(4): 109-130.
Mitsuyasu, H. and Honda, T., 1974. The high frequency spectrum of wind-generated waves. edited by The Oceanographic Society of Japan, 30(4): 185-198.
Mitsuyasu, H. and Yoshida, Y., 1989. Air-sea interactions under the existence of swell propagating against the wind. Bull. Res. Inst. Appl. Mech., Kyushu Univ, 63: 47-71.
Mitsuyasu, H. and Yoshida, Y., 1991. The effect of swell on the growth of wind waves. Elsevier oceanography series, 54: 381-392.
Mitsuyasu, H. and Yoshida, Y., 2005. Air-sea interactions under the existence of opposing swell. Journal of Oceanography, 61(1): 141-154.
Munk, W., 1950. Origin and generation of waves. 1st International Conference on Coastal Engineering, Long Beach, California, pp. 1-4.
Nayak, S., Bhaskaran, P.K., Venkatesan, R. and Dasgupta, S., 2013. Modulation of local wind-waves at kalpakkam from remote forcing effects of southern ocean swells. Ocean Engineering, 64: 23-35.
Nielsen, P., 2009. Coastal and estuarine processes, 29. World Scientific, Singapore.
Nielsen, P. and You, Z.-J., 1996. Eulerian mean velocities under non-breaking waves on horizontal bottoms. Proceedings of the Coastal Engineering Conference, 4: 4066-4077.
Ochi, M. and Tsai, C.-H., 1983. Prediction of occurrence of breaking waves in deep water. Journal of Physical Oceanography, Boston, 13(11): 2008-2019.
Olfateh, M., 2014. Momentum and energy transfer under wind waves, wave organised motion contribution, University of Queensland, Brisbane, Australia.
Olfateh, M., Ware, P., Callaghan, D.P., Nielsen, P. and Baldock, T.E., 2017. Momentum transfer under laboratory wind waves. Coastal Engineering, 121: 255-264.
Ouellet, Y. and Datta, I., 1986. A survey of wave absorbers. Journal of Hydraulic Research/Journal de Recherches Hydraulique, 24(4): 265-280.
Pedregosa, F. et al., 2011. Scikit-learn: Machine learning in python. Journal of Machine Learning Research, 12: 2825-2830.
Peirson, W.L. and Garcia, A.W., 2008. On the wind-induced growth of slow water waves of finite steepness. Journal of Fluid Mechanics, 608: 243-274.
Peirson, W.L., Garcia, A.W. and Pells, S.E., 2003. Water wave attenuation due to opposing wind. Journal of Fluid Mechanics, 487(487): 345-365.

Phillips, O. and Banner, M., 1974. Wave breaking in the presence of wind drift and swell. Journal of Fluid Mechanics, 66(04): 625-640.
Phillips, O.M., 1957. On the generation of waves by turbulent wind. Journal of Fluid Mechanics, 2(5): 417-445.
Phillips, O.M., 1958. The equilibrium range in the spectrum of wind-generated waves. J. Fluid Mech., 4(4): 426-434.
Phillips, O.M., 1960. On the dynamics of unsteady gravity waves of finite amplitude part 1. The elementary interactions. J. Fluid Mech., 9(2): 193-217.
Phillips, O.M., 1966. The dynamics of the upper ocean. Cambridge University Press.
Phillips, O.M., 1985. Spectral and statistical properties of the equilibrium range in wind-generated gravity waves. J. Fluid Mech., 156(-1): 505-531.
Pierson Jr, W.J. and Moskowitz, L., 1964. A proposed spectral form for fully developed wind seas based on the similarity theory of sa kitaigorodskii. Journal of geophysical research, 69(24): 5181-5190.
Plant, W., Dahl, P., Giovanangeli, J. and Branger, H., 2004. Bound and free surface waves in a large wind-wave tank. Journal of Geophysical Research - Oceans, 109(C10): C10002.
Plant, W., Keller, W. and Cross, A., 1983. Parametric dependence of ocean wave‐radar modulation transfer functions. Journal of Geophysical Research: Oceans, 88(C14): 9747-9756.
Plant, W.J., 1982. A relationship between wind stress and wave slope. Journal of Geophysical Research: Oceans (1978–2012), 87(C3): 1961-1967.
Plant, W.J. and Alpers, W., 1994. An introduction to saxon‐fpn. Journal of Geophysical Research: Oceans, 99(C5): 9699-9703.
Plant, W.J. and Wright, J.W., 1977. Growth and equilibrium of short gravity waves in a wind-wave tank. Journal of Fluid Mechanics, 82(4): 767-793.
Ramberg, S.E. and Griffin, O.M., 1987. Laboratory study of steep and breaking deep water waves. Journal of Waterway, Port, Coastal, and Ocean Engineering, 113(5): 493-506.
Rapp, R.J. and Melville, W.K., 1990. Laboratory measurements of deep-water breaking waves. Philosophical Transactions of the Royal Society of London. Series A, Mathematical and Physical Sciences, 331(1622): 735-800.
Reece Jr, A.M., 1978. Modulation of short waves by long waves. Boundary-Layer Meteorology, 13(1-4): 203-214.
Rogers, W., Babanin, A. and Wang, D., 2012. Observation-consistent input and whitecapping dissipation in a model for wind-generated surface waves: Description and simple calculations. Journal of Atmospheric and Oceanic Technology, 29(9): 1329-1346.
Rogers, W.E. et al., 2007. Forecasting and hindcasting waves with the swan model in the southern california bight. Coastal Engineering, 54(1): 1-15.
Russell, J.S., 1844. Report on waves. 14th meeting of the British Association for the Advancement of Science, pp. 390.
Schwarz, K.T., 2008. Wind dispersion of carbon dioxide leaking from underground sequestration, and outlier detection in eddy covariance data using extreme value theory. University of California, Berkeley.
Shabani, B., 2013. Nearshore and surf zone wind stress, The University of Queensland, School of Civil Engineering U6 - ctx_ver=Z39.88-2004&ctx_enc=info%3Aofi%2Fenc%3AUTF-8&rfr_id=info:sid/summon.serialssolutions.com&rft_val_fmt=info:ofi/fmt:kev:mtx:dissertation&rft.genre=dissertation&rft.title=Nearshore+and+Surf+Zone+Wind+Stress&rft.DBID=VQ8&rft.au=Shabani%2C+Behnam&rft.date=2013-01-01&rft.pub=The+University+of+Queensland%2C+School+of+Civil+Engineering&rft.

externalDBID=n%2Fa&rft.externalDocID=oai_espace_library_uq_edu_au_UQ_331937&paramdict=en-US U7 - Dissertation.
Shabani, B., Babanin, A.V. and Baldock, T.E., 2016. Observations of the directional distribution of the wind energy input function over swell waves. Journal of Geophysical Research: Oceans, 121(2): 1174-1193.
Shabani, B., Nielsen, P. and Baldock, T., 2014. Direct measurements of wind stress over the surf zone. Journal of Geophysical Research: Oceans, 119(5): 2949-2973.
Shemdin, O.H. and Hsu, E.Y., 1967. Direct measurement of aerodynamic pressure above a simple progressive gravity wave. Journal of Fluid Mechanics, 30(02): 403-416.
Smith, J., 1986. Short surface waves with growth and dissipation. Journal of Geophysical Research, 91(2): 2616-2632.
Smith, J.A., 1990. Modulation of short wind waves by long waves, Surface waves and fluxes. Springer, pp. 247-284.
Snyder, R., 1974. Field study of wave-induced pressure-fluctuations above surface gravity-waves. Journal of Marine Research, 32(3): 497-531.
Snyder, R., Smith, L. and Kennedy, R., 1983. On the formation of whitecaps by a threshold mechanism. Part iii: Field experiment and comparison with theory. Journal of physical oceanography, 13(8): 1505-1518.
Snyder, R.L. and Cox, C.S., 1966. A field study of the wind generation of ocean waves. J. mar. Res., 24: 141-178.
Snyder, R.L., Dobson, F.W., Elliott, J.A. and Long, R.B., 1981. Array measurements of atmospheric pressure fluctuations above surface gravity waves. Journal of Fluid Mechanics, 102(1): 1-59.
Stanton, T.E., Marshall, D. and Houghton, R., 1932. The growth of waves on water due to the action of the wind. Proc. R. Soc. Lond. A, 137(832): 283-293.
Tamura, H., Waseda, T. and Miyazawa, Y., 2009. Freakish sea state and swell‐windsea coupling: Numerical study of the suwa‐maru incident. Geophysical Research Letters, 36(1).
Tamura, H., Waseda, T., Miyazawa, Y. and Komatsu, K., 2008. Current-induced modulation of the ocean wave spectrum and the role of nonlinear energy transfer. Journal of physical oceanography, 38(12): 2662-2684.
Teixeira, M.A.C. and Belcher, S.E., 2002. On the distortion of turbulence by a progressive surface wave. J. Fluid Mech., 458: 229-267.
Thais, L. and Magnaudet, J., 1996. Turbulent structure beneath surface gravity waves sheared by the wind. Journal of Fluid Mechanics, 328(1): 313-344.
The-SWAN-team, 2018. Swan scientific and technical documentation. Delft University of Technology, Faculty of Civil Engineering and Geosciences, Environmental Fluid Mechanics Section, The Netherlands.
The-Wamdi-Group, 1988. The wam model—a third generation ocean wave prediction model. Journal of Physical Oceanography, 18(12): 1775-1810.
Toba, Y., 1973. Local balance in the air-sea boundary processes - iii. On the spectrum of wind waves. Journal of the Oceanographical Society of Japan, 29(5): 209-220.
Tolman, H.L., 1991. A third-generation model for wind waves on slowly varying, unsteady, and inhomogeneous depths and currents. Journal of Physical Oceanography, 21(6): 782-797.
Tolman, H.L., 1992. Effects of numerics on the physics in a third-generation wind-wave model. Journal of Physical Oceanography, 22(10): 1095-1111.
Tolman, H.L., Krasnopolsky, V.M. and Chalikov, D.V., 2005. Neural network approximations for nonlinear interactions in wind wave spectra: Direct mapping for wind seas in deep water. Ocean Modelling, 8(3): 253-278.
Townsend, A.A., 1980. The response of sheared turbulence to additional distortion. Journal of Fluid Mechanics, 98(1): 171-191.

Tulin, M. and Landrini, M., 2001. Breaking waves in the ocean and around ships. Twenty-Third Symposium on Naval HydrodynamicsOffice of Naval Research, Bassin d'Essais des CarenesNational Research Council.
van der Walt, S., Colbert, S.C. and Varoquaux, G., 2011. The numpy array: A structure for efficient numerical computation. Computing in Science & Engineering, 13: 22-30.
Van Duin, C. and Janssen, P., 1992. An analytic model of the generation of surface gravity-waves by turbulent air-flow. J. Fluid Mech., 236: 197-215.
Violante-Carvalho, N., Babanin, A., Liu, Q., Nascimento, F. and Parente, C., 2017. Wave observations from an array of directional buoys over the southern brazilian coast. Ocean Dynamics, 67(12): 1577-1591.
Violante-Carvalho, N., Ocampo-Torres, F. and Robinson, I., 2004. Buoy observations of the influence of swell on wind waves in the open ocean. Applied Ocean Research, 26(1-2): 49-60.
Waseda, T. and Tulin, M.P., 1999. Experimental study of the stability of deep-water wave trains including wind effects. Journal of Fluid Mechanics, 401: 55-84.
WAVEWATCH III Development Group, 2016. User manual and system documentation of wavewatch iii version 5.16.
White, F.M., 2011. Fluid mechanics. McGraw-Hill, New York.
Willmarth, W.W. and Wooldridge, C.E., 1962. Measurements of the fluctuating pressure at the wall beneath a thick turbulent boundary layer. J. Fluid Mech., 14(2): 187-210.
Wright, J.W., 1976. The wind drift and wave breaking. Journal of Physical Oceanography, 6(3): 402-405.
Wu, J., 1968. Laboratory studies of wind-wave interactions. Journal of Fluid Mechanics, 34(1): 91-111.
Wu, J., 1977. Effects of long waves on wind boundary layer and on ripple slope statistics. Journal of Geophysical Research, 82(9): 1359-1362.
Wu, J., 1982. Wind‐stress coefficients over sea surface from breeze to hurricane. Journal of Geophysical Research: Oceans (1978–2012), 87(C12): 9704-9706.
Young, I.R., 1999. Wind generated ocean waves, 2. Elsevier, Amsterdam.
Young, I.R. and Babanin, A., 2006a. Spectral distribution of energy dissipation of wind-generated waves due to dominant wave breaking. Journal of Physical Oceanography, 36(3): 376-394.
Young, I.R. and Babanin, A.V., 2006b. The form of the asymptotic depth‐limited wind wave frequency spectrum. Journal of Geophysical Research: Oceans, 111(C6).
Young, I.R. and Sobey, R.J., 1985. Measurements of the wind-wave energy flux in an opposing wind. Journal of fluid mechanics, 151: 427-442.
Zakharov, V.E. and Badulin, S.I., 2012. The generalized phillips' spectra and new dissipation function for wind-driven seas.
Zavadsky, A. and Shemer, L., 2012. Characterization of turbulent airflow over evolving water‐waves in a wind‐wave tank. Journal of Geophysical Research: Oceans (1978‐2012), 117(C11).
Zhang, X., 1995. Capillary-gravity and capillary waves generated in a wind-wave tank - observations and theories. Journal of Fluid Mechanics, 289(1): 51-82.
Zieger, S., Babanin, A.V., Rogers, W.E. and Young, I.R., 2015. Observation-based source terms in the third-generation wave model wavewatch. Ocean Modelling, 96: 2-25.